Dosimetry and Biological Studies for Microbeam Radiation Therapy at the Canadian Light Source

by

Danielle Anderson

A thesis submitted in partial fulfillment of the requirements for the degree of

Doctor of Philosophy

in

Medical Physics

Department of Oncology
University of Alberta

Abstract

Microbeam radiation therapy (MRT) is a pre-clinical type of radiation therapy that uses an array of high-dose microbeams to treat solid tumours. An intense, quasi-parallel synchrotron beam is collimated to create microbeams several 10s of μm wide, and separated by 100s of μm. Animal studies over the past two decades have demonstrated that the extreme spatial fractionation employed in MRT leads to an unusual normal tissue sparing, while being effective for tumour palliation, and in some cases, ablation.

This work considers both physical and biological questions remaining in MRT, with a focus on preparation for MRT experimentation on the two BioMedical Imaging and Therapy (BMIT) beamlines at the Canadian Light Source (CLS). A variety of techniques and detectors were employed to investigate the geometric and relative dosimetric characteristics of the 05B1-1 and 05ID-2 beamlines as a basis for further dosimetry. The absolute air kerma rate on the 05B1-1 beamline was measured for several beam qualities (monoenergetic and filtered polyenergetic x-ray beams) using a cylindrical, variable-length free-air ionization chamber and Monte Carlo simulations were carried out to determine correction factors. Air kerma rates between 4.5 mGy/s and 5.2 Gy/s were measured. Additionally, reference dosimetry was performed using a cavity ionization chamber by applying a geometric correction based on the non-uniform beam profile and the ion chamber response function in the broad synchrotron x-ray beam. This allowed the determination of peak (at the most intense point in the beam) and mean air kerma rates for several beam qualities, with a range from 1.9 cGy/s to 1.9 Gy/s.

The MRT dose distributions delivered by the 05ID-2 beamline were investigated theoretically using the Monte Carlo package PENELOPE. This work demonstrated that the 05ID-2 beamline has the necessary energy characteristics to provide the spatial fractionation and penetration required for MRT experimentation. The dose distributions in cubic head phantoms representing small, medium and large animals were also determined to understand the considerations required for moving from small (*e.g.*, rodent) animal experimentation to larger (*e.g.*, cat and dog) animals. The spatial fractionation of MRT dose distributions will necessitate unconventional methods for treatment plan optimization. To explore this requirement, four dose-volume metrics, the peak-to-valley dose ratio, the peak-to-mean-valley dose ratio, the mean dose and the percentage volume below a threshold dose, were explored with changing microbeam array geometry and phantom size.

To investigate the DNA damage response in cell cultures to synchrotron-generated microbeams, the formation of γH2AX foci (a marker of DNA double-strand breaks), rates of foci clearance and apoptosis in cultured normal human fibroblasts and malignant glioma cells were examined on the 05B1-1 beamline. The two cell types demonstrated similar trends in γH2AX foci formation and clearance with dose and time after irradiation. Additionally, despite elevated levels of γH2AX foci at late times (up to 72 hours after irradiation), both cell types showed very low levels of apoptosis. The results also highlighted the importance of understanding the DNA damage response specific to cell type, and the consideration of non-apoptotic responses even at high doses.

The research in this thesis establishes a foundation in experimental dosimetry, theoretical dosimetry, and cell culture studies for future MRT research on the BMIT beamlines at the Canadian Light Source.

Preface

The entirety of this thesis work represents original research motivated by the objectives of my Ph.D. project. This research was supervised by Drs. E.A. Siegbahn, B.G. Fallone, and B. Warkentin (primary supervisor). The research was made possible with the significant additional input and assistance of several collaborators. A summary of these contributions is given in the following.

The characterization of the BioMedical Imaging and Therapy beamlines and cavity and free air ionization chamber dosimetry described in Chapters 3, 4 and 5 represents work that I performed, initiated and led. This work included a large amount of data collection and analysis. B. Warkentin assisted with the collection and interpretation of this data, and in project conceptualization; he also provided project guidance and oversight. E.A. Siegbahn and B.G. Fallone provided general guidance. Dr. M. McEwen, Dr. E. Mainegra-Hing, and Mr. H. Shen of the National Research Council of Canada assisted with various aspects of the free air ion chamber work, including initial chamber testing, aperture fabrication, and expert guidance on Monte Carlo simulation of device response.

A slightly altered version of Chapter 6 was published as D.A. Anderson, E.A. Siegbahn, R. Serduc, B.G. Fallone, and B. Warkentin, "Evaluation of dose-volume metrics for microbeam radiation therapy dose distributions in head phantoms of various sizes using Monte Carlo simulations, " *Phys. Med. Biol.* **57**, 3223-48 (2012). I was responsible for the computer simulations, analysis of data, and manuscript composition. E.A. Siegbahn conceived of the initial study as well as the initial version of the simulation code and manuscript edits. R. Serduc and B.G. Fallone provided manuscript edits and general guidance. B. Warkentin was the supervising author, involved in concept and methodology development, manuscript edits, and project oversight.

The material presented in Chapter 7 has been published in two articles: D.L. Anderson, R. Mirzayans, B. Andrais, E.A. Siegbahn, B.G. Fallone and B. Warkentin, 'Spatial and temporal distribution of γH2AX fluorescence in human cell cultures following synchrotron-generated X-ray microbeams: lack of correlation between persistent γH2AX foci and apoptosis," *J. Synch. Rad*. **21**, 801-810 (2014), and D.

Anderson, B. Andrais, R. Mirzayans, E.A. Siegbahn, B.G. Fallone and B. Warkentin, "Comparison of two methods for measuring γ-H2AX nuclear fluorescence as a marker of DNA damage in cultured human cells: applications for microbeam radiation therapy," *J. Inst*. **8**, C06008 (2013). I led and was responsible for all aspects of the project, including: project conceptualization; handling (*e.g.* transport of equipment between the Canadian Light Source (Saskatoon, SK) and the Cross Cancer Institute (Edmonton, AB), growing, irradiating, immunostaining and imaging our cell culture samples; developing original software for image analysis; and manuscript composition. B. Andrais assisted in planning the logistics of the experiments, initiating cell culture and preparing materials for transport, and assisted in immunostaining. R. Mirzayans was involved in concept formation, experiment planning, imaging the samples, analyzing and interpreting the data, and manuscript composition. E.A. Siegbahn and B.G. Fallone were involved with manuscript edits and general guidance. B. Warkentin was responsible for project conceptualization and oversight, and assisted with methodology development, sample irradiation, and other guidance.

The literature review and description of the Canadian Light Source in Chapters 1 and 2, as well as the concluding Chapter 8 were conceived and written independently, with editorial suggestions from my supervisors and supervising committee.

Acknowledgements

There are many people that have been invaluable in the completion of this research, and my general medical physics education. First, I am incredibly thankful for the guidance, supervision and constant encouragement provided by Dr. Brad Warkentin. Dr. Warkentin far exceeded his responsibilities as a supervisor in every way possible. He not only cared about my success within the graduate program, but also my overall happiness. I would also like to thank my two co-supervisors. Dr. Albert Siegbahn offered expertise in the field of microbeam radiation therapy (MRT), and also facilitated my introduction to the international MRT community, which greatly enriched my research experience. Dr. Siegbahn consistently provided helpful comments, and always did so in a supportive manner. Dr. Gino Fallone's vast experience and expertise in medical physics were important for directing the aims of this unique project, as well as my general development as a researcher in medical physics, and providing funding.

A large portion of my research involved investigating the response of cell cultures to ionizing radiation, and this was only possible through the direct involvement of Dr. Razmik Mirzayans. Dr. Mirzayans was always very generous with his time – we had many discussions on biological concepts, literature, planning experiments, and interpreting results. In addition to the science that he taught me, he was also a great role model in terms of demonstrating dedication and integrity. I need to thank Bonnie Andrais for patiently teaching me laboratory skills, helping plan experiments, preparing the considerable amount of materials required for the biological experiments at the Canadian Light Source, and being a friend.

Dr. Tomasz Wysokinski and Dr. George Belev, as well as the rest of the BioMedical Imaging and Therapy scientists and staff, were very important for completing the experimental measurements. Drs. Wysokinski and Belev provided assistance with applying for beamtime, planning and setting up experiments, and allowed us to use commissioning time. They also encouraged collaborations and connections within the synchrotron community, and provided valuable comments on part of this thesis. In addition, I'd like to thank Dr. Les Dallin for his helpful comments on the thesis, and for giving me my first introduction to and education in synchrotron light sources.

I am appreciative of the involvement of Dr. Malcolm McEwen, Dr. Ernesto Mainegra-Hing and Mr. Hong Shen, who were all involved in the free air ionization chamber measurements described in this thesis. This included the refurbishment and testing of the free air ionization chamber, packing and shipping the chamber to the Canadian Light Source, many discussions on the proper use of the chamber, as well as important guidance for Monte Carlo simulations.

I am very grateful to my supervisory committee, Dr. Satyapal Rathee, Dr. Ron Sloboda, Dr. Razmik Mirzayans, and (briefly) Dr. Alasdair Syme, for their helpful comments and criticisms over the course of my research. I am grateful to those who took part in my candidacy exam, Dr. Atiyah Yahya and Dr. Richard Sydora and supervisory committee. Similarily, a huge thank you is extended to those were were also involved in my defense, including the chair, Dr. Don Robinson, and the examiners: my supervisors, supervisory committee, Dr. Geetha Menon, and Dr. Sha Chang. I am very grateful for the time spent preparing for the exam and providing important corrections for this thesis.

More generally, I am thankful for my experience with the physicists and staff in the Medical Physics department at the Cross Cancer Institute, who were all involved in my education in some way. I feel fortunate to have been in an environment with so many excellent teachers, researchers and clinical medical physicists. I'm also very grateful for the friendships that I've developed with the other graduate students.

I am extremely appreciative for the financial support I have received during my time at the University of Alberta. This has included funding from many sources, including the Natural Science Engineering Research Council of Canada, Alberta Innovates – Health Solutions, the Canadian Federation of University Women, the University of Alberta, and Vanier Canada Graduate Scholarships. This funding not only allowed me the freedom to only work minimally, and thus focus on research, but also travel internationally to attend conferences, visit other synchrotron light sources, and meet other MRT researchers.

Aside from those directly involved in my education, I am very thankful to my friends and family for their support and encouragement during my many years as a student, and much celebration upon completion of this thesis.

TABLE OF CONTENTS

List of Figures

List of Tables

List of Abbreviations

ATM	Ataxis telangiectasia mutated
BM	Bending magnet
BMIT	BioMedical Imaging and Therapy
CF	Cross-fired
CLS	Canadian Light Source
CNS	Central nervous system
CT	Computed tomography
DAPI	4',6-diamidino-2-phenylindole
DDR	DNA damage response
DEI	Diffraction enhanced imaging
DNA	Deoxyribose nucleic acid
DSB	Double strand break
EBRT	External beam radiation therapy
ESRF	European Synchrotron Radiation Facility
EUD	Equivalent uniform dose
FAC	Free-air ionization chamber
FWHM	Full width at half maximum
HVL	Half-value layer
ID	Insertion device
KES	K-edge subtraction
LAPS	Large animal positioning system
MBRT	Mini beam radiation therapy
MGC	Malignant glioma cell
MLC	Multi leaf collimator
MRT	Microbeam radiation therapy
MSC	Multi slit collimator
NHF	Normal human fibroblast
NRC	National Research Council of Canada
PBS	Phosphate-buffered saline
PDD	Percent depth dose
PMMA	Poly(methyl methacrylate)
PMVDR	Peak to mean valley dose ratio
PVDR	Peak to valley dose ratio
RF	Radio frequency
SIPS	Stress-induced premature senescence
SR	Synchrotron radiation
SSB	Single strand break
WIP1	Wild-type p53-induced phosphatase 1

1 INTRODUCTION

1.1 Radiation therapy

1.1.1 Cancer incidence and treatment

In Canada two in every five people (45% of men and 41% of women) will develop cancer at some point in their lifetime.[1] Figure 1.1 shows the lifetime probability of incidence and mortality for males and females in Canada for several types of cancers.[1] Approximately 60% of patients with cancer will be treated with radiation therapy, often in conjunction with surgery, chemotherapy or other types of treatment.[2] Radiation therapy is thus a vital tool in treating cancer.

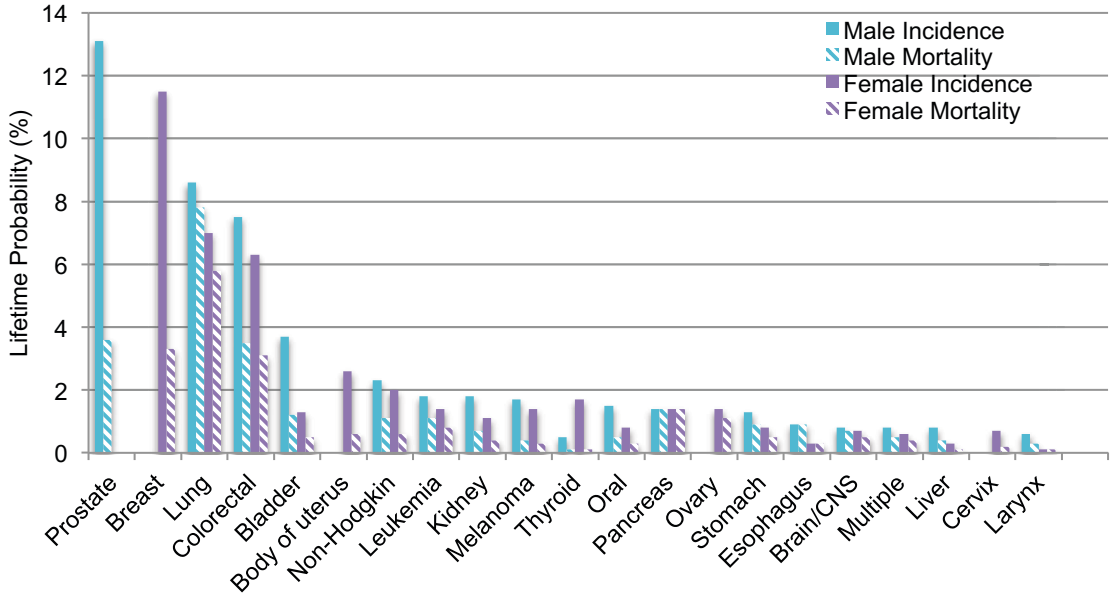

Figure 1.1 The lifetime probability of incidence and mortality for various types of cancer in Canada for males and females. Data compiled from *Canadian Cancer Statistics 2014*.[1]

There are two main types of radiotherapy: external beam radiation therapy (EBRT) and brachytherapy. With EBRT, treatment is delivered by a radiation beam

emitted from a source outside of the patient's body, and is the most commonly used type of radiation therapy. With brachytherapy, a sealed radioactive source is placed as close as possible to the malignancy by interstitial, intracavitary, or surface application.[3] EBRT usually provides treatment using high-energy (> ~1 MeV) photons (*i.e.*, x-rays or gamma-rays) or electrons, although other types of radiation can be used for specific applications (*e.g.*, protons, ions, neutrons, etc.). Today in North America, high energy x-rays and electrons are most often produced by clinical linear accelerators. Medium energy x-rays (~ 40 – 400 kV) are also occasionally used to treat superficial cancers, and are produced by x-ray tubes.

Although the treatment for an individual patient will vary based on a number of factors, the majority of conventional high-energy EBRT treatments share commonalities. Treatment plans are designed to maximize radiation dose to the whole treatment volume. Typically a uniform coverage of this treatment volume is desired, while minimizing the dose to the surrounding tissue. Total doses (D) delivered to the treatment volume depend on the tumour site, but are usually in the range of 50 – 80 Gray (Gy, Gy = J/kg). The total dose is delivered over weeks, with 1.8 – 2.0 Gy delivered per day for conventionally fractionated treatments. This temporal fractionation of the delivered dose leads to reduced normal tissue toxicity for an equivalent rate of tumour control than a single large dose.[4-6] With a clinical linear accelerator, standard dose rates are in the order of 1 - 6 Gy/minute.

1.1.2 Biological basis of radiation therapy

The earliest radiation therapy treatments, which first occurred only months after the discovery of x-rays by Roentgen in 1895, were performed with very limited understanding of the biological effects, or even the physical characteristics, of radiation.[7] For many decades, clinicians made therapeutic choices based predominantly on empirical data, which resulted in poor tumour control and significant toxicity.[7] Developments in radiobiology, as well as accumulated clinical experience and technological advances, gradually led to improved efficacy and reduced morbidity in radiation therapy.

Radiation therapy relies on the principle that ionizing radiation, at a sufficient dose, will lead to cell killing or the inhibition of proliferation. For many years, there existed a "DNA-centric" understanding surrounding cellular damage caused by ionizing radiation,[8] particularly that nuclear DNA is the principle site for ionizing radiation-induced cell death. Ionizing radiation can produce several types of damage in DNA, but DNA double strand breaks (DSBs) are thought to be the most important type of radiation-induced lesion in DNA.[4] A simplified model taken from Prise *et al.* (2009)[9] is shown in Fig. 1.2. After the initiation of a DSB, the break can be repaired properly, which will prevent any deleterious effects. Alternatively, unrepaired DSBs can cause chromosomal aberrations, and lead to the loss of clonogenic potential through cell death (*e.g.*, apoptosis) or growth arrest (*e.g.*, premature senescence). Another alternative is that repair is attempted, but is carried through incorrectly or incompletely, which can lead to mutation, and potentially transformation to a cancer cell.

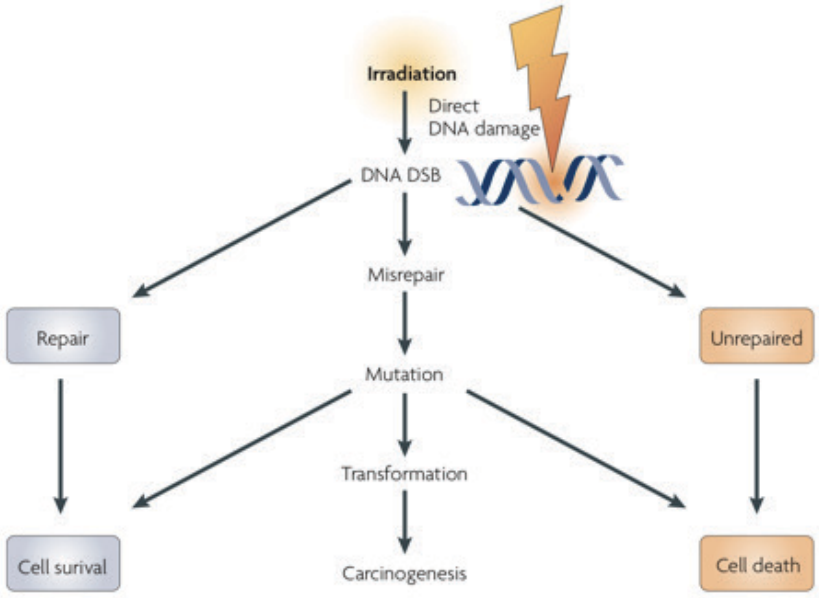

Figure 1.2 A general model for direct DNA damage by ionizing radiation. In this figure, 'Cell death' includes both lethality (*e.g.,* apoptosis) or growth arrest (*e.g.,* premature senescence). (Reprinted by permission from Macmillan Publishers Ltd: K.M. Prise and J.M. O'Sullivan, "Radiation-induced bystander signalling in cancer therapy," Nature Reviews Cancer **9**, 351-360 (2009).[9])

Current radiobiology has shown evidence that, in addition to a single cell's response to damage caused directly to DNA, there is important signalling between cells

and within tissue in response to ionizing radiation.[8] For example, the bystander response,[4,9,10] defined as "the induction of biologic effects in cells that are not directly traversed by a charged particle, but are in close proximity to cells that are;"[4] adaptive responses[11] that increase radioresistance after a very low dose "conditioning" exposure to ionizing radiation; the enhanced cell killing at very low doses of ionizing radiation referred to as low dose hypersensitivity;[4,8,12] and systemic abscopal effects[13,14] after irradiation. The impact of the extra-nuclear targets for ionizing radiation-induced damage, and the potential for systemic effects after exposure to ionizing radiation on modern radiation therapy is not yet understood.

DNA damage, and other biological effects of ionizing radiation, occurs in both normal and tumour tissue. Thus, not only does radiotherapy require sufficient radiation dose to cause tumour cell killing, it also requires that surrounding normal tissue is better able to repair, or at least tolerate, radiation damage than the targeted cancerous tissue. The concept of the therapeutic index, which is based on the tumour control probability (TCP) and normal tissue complication probability (NTCP), is used to predict the success of a treatment. Examples of potential TCP and NTCP curves are shown in Fig. 1.3. If the TCP if high (*e.g.* ~ 86%) for low doses relative to the acceptable NTCP (*e.g.* 5% in Fig. 1.3(a), the therapeutic index is favourable. However, if the TCP is low (*e.g.* ~ 20% in Fig. 1.3(b) with an acceptable NTCP, the probability of a successful treatment is very low. TCP and NTCP are affected by numerous parameters, including the radiosensitivity of the involved tissues, the dose-time fractionation and the type of radiation therapy used.

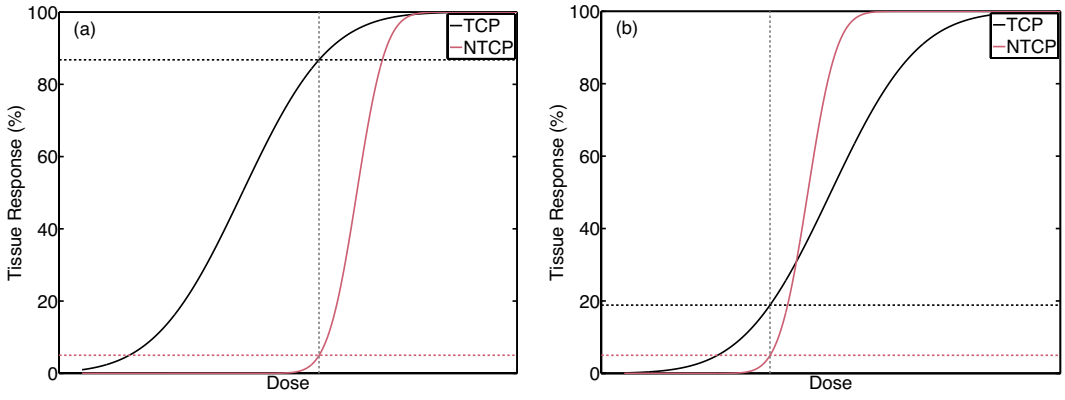

Figure 1.3 Examples of tumour control probability (TCP) and normal tissue complication probability (NTCP) curves. (a) An example that has a more favourable therapeutic index with respect to (b).

1.1.3 The volume effect

As stated above, one of the main goals in radiation therapy planning is to minimize the volume of normal tissue irradiated based on the expectation that with a decrease in irradiated volume comes a decrease in the probability of normal tissue complications. This purpose has motivated many new techniques and technology in EBRT to enable more precise targeting of the treatment volume, such as conformal radiation therapy (CRT), intensity modulated radiation therapy (IMRT), volumetric modulated arc therapy (VMAT), image guided radiation therapy (IGRT), respiratory gating, image guided adaptive radiotherapy (IGART), stereotactic radiosurgery (SRS), and stereotactic body radiation therapy (SBRT).

Physicians in radiotherapy have exploited the dose-volume effect, the increase in the threshold dose for some end point as irradiated volume decreases, for many decades despite limited tissue-specific experimental evidence and the difficulty of generalizing the data that does exist.[15,16] A lot of the applied clinical knowledge surrounding dose-volume relationships is based on anecdotes and best judgement of clinicians.[15,17]

Hopewell and Trott, in a review on the volume effect, discuss its complex nature and warn of the quantification of existing data for the purpose of treatment planning.[16] The authors separate the volume effect for structural versus functional radiation damage, and claim that there is little or no volume effect when considering structural radiation damage. The apparent volume effect observed in very small irradiation fields is attributed to cell migration of non-irradiated periphery cells into the damaged region during the healing process and not intrinsic radiosensitivity.[16,18] On the other hand, the authors present evidence for volume effects in terms of functional end points. The authors summarize the work of Herrmann *et al.*, who irradiated pig lung.[19] Their results showed no change in structural damage with varying irradiated volumes, but a decrease in lung function was observed as the volume of lung irradiated increased.[19] Hopewell and Trott state that the "relationship between anatomical/structural radiation damage and failure of organ function is different for different organs, and more related to organ physiology than to basic radiobiological concepts of cell survival."[16]

In a model developed by Withers *et al.*, the dose-volume response of a type of tissue depends on the architecture of the tissue itself.[20] The authors introduced the

concept of a functional subunit (FSU), and two types of FSU arrangement in tissues. In an organ with series architecture (*e.g.*, spinal cord), each individual FSU is vital to function, and the elimination of one, or a small number of FSUs, will lead to a complication.[20] These organs will respond to radiation in a binary fashion: below a threshold dose there is normal function, but above there is significant loss of function. Alternatively, an organ's FSUs can be arranged in parallel (*e.g.*, skin). In this case, organ toxicity will not occur if a small number of FSUs are irradiated to a high dose. Instead, a critical volume must be eliminated before there is a loss of function.[20]

The dose-volume effect of ionizing radiation on the microscopic scale was first investigated in the 1950's and 1960's.[21-25] Zeman *et al.* used a 22 MeV deuteron beam to irradiate the visual cortex of mice to simulate the effect of cosmic rays on brain tissue in preparation for manned space flight.[23] The diameter of the cylindrical microbeam was decreased from 1 mm down to 25 μm. The researchers defined a threshold dose as the smallest dose at which practically all of the nerve cells within the path disappeared by 24 days following irradiations. Dose rates were varied between 0.125 and 9000 Gy/s. Although no dose rate effect was observed, it was determined that doses required to cause cellular destruction are strongly dependent on the volume of tissue irradiated. Figure 1.4 shows the threshold dose as a function of field size. The error bars indicate the variability between individual animals, which was only stated for the two largest beams, although the authors mentioned that variability continued decreasing with beam size. For a beam diameter of 1 mm, not only were all nerve cells obliterated in the beam path after a 140 Gy dose, there was complete destruction of the brain tissue (Fig. 1.5(a)). There was evidence of vascular damage (e.g. haemorrhage, edema and vasodilation). As the beam size was reduced, the threshold dose increased to a maximum of 4000 Gy for the smallest (25 μm) beam. For this beam size, the 4000 Gy dose caused no lasting effects except the removal of nerve cells within the beam track (Fig. 1.5(b)). Additionally the scale and occurrence of vascular damage decreased with beam size. For the 25 μm beam, disruptions in circulation were practically absent up to 50,000 Gy.

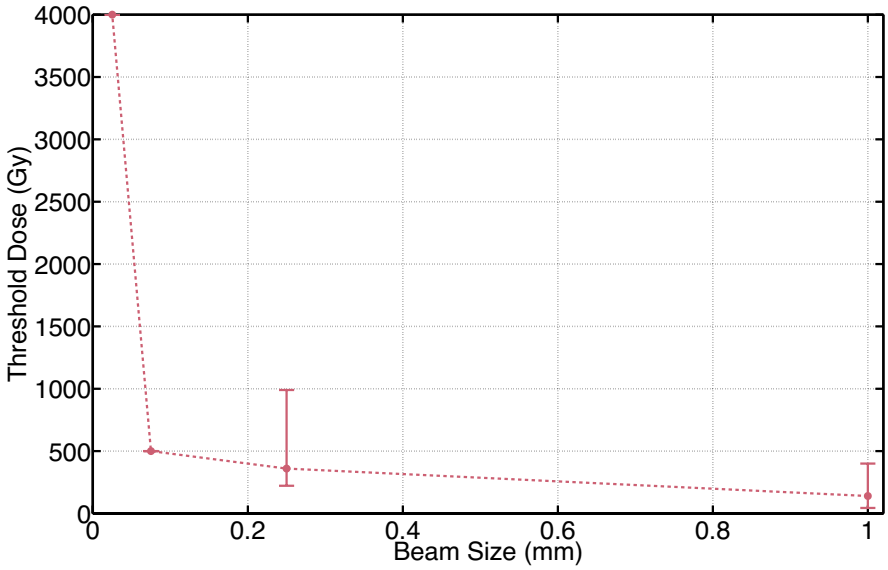

Figure 1.4 The change in threshold dose as a function of beam size after irradiation with a 22 MeV deuteron beam. Data points taken from Zeman *et al.* 1961.[23]

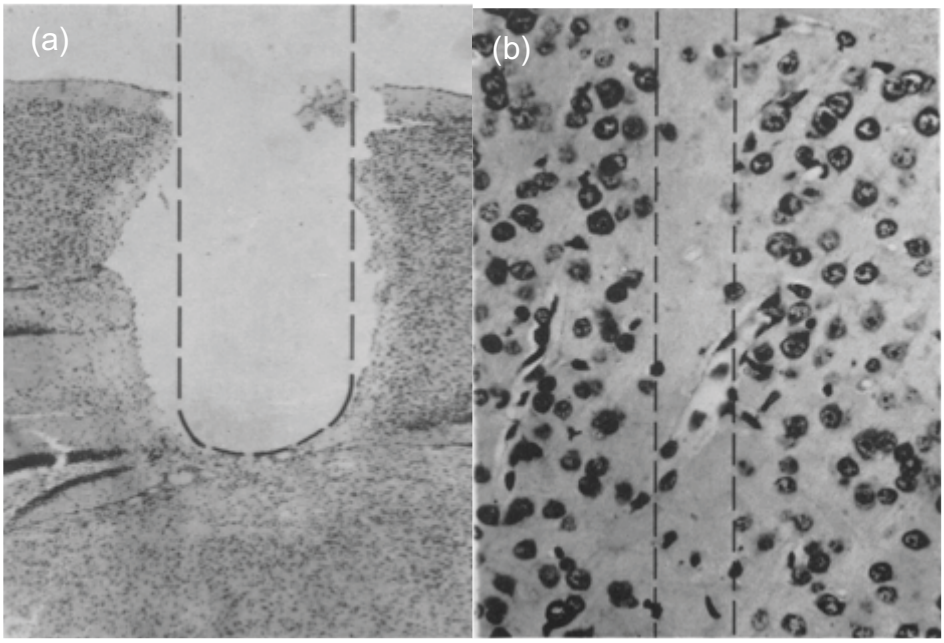

Figure 1.5 Histological images of a mouse visual cortex following irradiation with a 22 MeV deuteron beam. (a) The cavity present 120 days after a 280 Gy irradiation with the 1 mm beam. (b) The loss of nerve cells along the beam track can be seen 24 days after a 4000 Gy irradiation with the 0.025 mm beam. (Image reproduced from W. Zeman *et al.*, "Histopathologic Effect of High-Energy-Particle Microbeams on Visual Cortex of Mouse Brain," Radiation Research, **15**, 496-514 (1961)[23] with permission of Radiation Research).

Two explanations for the rapid increase in tolerance at the smallest beam size were proposed. First, the small microbeam has a high likelihood of passing through the tissue without intersecting many capillaries based on the size of the beam and the spacing of the capillaries, and thus little vascular damage is produced. For the broad beam, vasculature cannot be avoided and is destroyed, which leads to necrosis.[23,25] An alternative explanation is that damaged cells can release cell-damaging enzymes that, in a small irradiated volume would quickly diffuse and their effects would be minimized, while in a large irradiated volume the enzymes would remain concentrated and cause further damage.[23]

The biological effects of an x-ray microbeam on mouse skin were investigated by Straile and Chase.[26] The authors examined the damage caused by a 5 mm diameter beam (60 Gy $\leq D \leq$ 100 Gy) versus a 150 μm planar beam (60 $\leq D \leq$180 Gy) produced by a 200 kV x-ray tube. The authors reported a similar amount of initial cellular damage by both beams, but observed superior healing after irradiation with the microbeam. The hypothesis offered to explain the more efficient healing of the smaller lesions was the greater surface area to volume ratio of the lesion, which allows a greater number of undamaged cells at the periphery to migrate into the lesion and facilitate healing.[26]

1.1.4 Spatial fractionation in radiation therapy

In the early days of radiation therapy, because very little was known about the biological effects of radiation or dosimetry, a high incidence of morbidity and poor tumour control occurred.[7] In an attempt to reduce normal tissue complications, particularly skin effects that were especially problematic due to the low x-ray energies available, clinicians exploited the dose-volume effect, in the form of spatial fractionation. Spatial fractionation of the dose distribution was initially conceived in 1909 in Germany. Köhler used a grid of 1 mm thick iron wires spaced 3.0 – 3.5 mm apart applied to the patient's skin during irradiations to reduce normal tissue complications.[27] With the grid, doses were 10 – 20 times higher than typically delivered with an open field.[28] The use of a perforated lead sheet to prevent skin injury during the treatment of deep lesions was independently developed in the United States by Liberson in 1933.[29] Liberson noted that

the lattice of normal skin protected by lead acted as centers of healing for the heavily irradiated regions. The popularity of grid therapy to enhance the healing process of radiodermatitis escalated in the 1950s with improvements in grid materials and geometry (ratio of covered to open area).[28,30,31]

Spatial fractionation was largely abandoned as megavoltage sources, whose dose build-up from skin surface to deeper tissue improved skin sparing, became available.[32] Over the last few decades grid therapy has been reintroduced as a treatment for large, bulky tumours ($\geq$ 6 cm).[32-36] Treatment may be applied to offer palliation to sites that have already reached tolerance, or used to debulk large tumours in preparation for a more conventional course of open field radiation therapy.[35] Spatial fractionation with high-energy linear accelerators is achieved with a solid grid (cerrobend or brass), or a multileaf collimator (MLC). Typically, the grid has equal areas blocked and unblocked, with ~ 1 cm diameter circular openings. Relatively high doses (~15 – 20 Gy) are delivered to the target in a single fraction with a palliative or curative goal. Despite the non-uniform dose distributions, uniform reduction in tumour mass has been observed. This uniform response has been explained by broad systemic effects following spatially fractionated therapy, such as the increase in ceramide[36,37] (which sensitizes cells to apoptosis) and perhaps a bystander effect.[35]

1.1.5 Challenges in the treatment of pediatric brain tumors

Pediatric central nervous system (CNS) tumours constitute one type of cancer with an unfavourable therapeutic index. Treatment offers significant challenges because of the sensitivity of the developing brain. Although the incidence of childhood (ages 0 – 14) cancer is low at 163.2 per million per year in Canada,[1] it is the second leading cause of death in children aged 1 – 14.[38] CNS malignancies are responsible for a greater proportion of deaths (34%) in children (ages 0 – 14) than any other type of cancer (Fig. 1.6).[1] It has been well established that the treatment of CNS tumours in children carries a high risk of complications. The developing brain is very sensitive to interventions, including any CNS-directed treatments.[39,40] Although surgery and certain chemotherapeutic agents carry risks of causing long-term effects, radiation therapy is

associated with the highest risks of long term cognitive deficits.[41,42] It is thought that these deficits may at least be partially explained by radiation-induced damage to the brain's white matter.[43] Other radiotherapy-related factors that increase the risk of unfavourable neurocognitive effects include the location of the tumour,[41,42,44] a higher delivered dose,[44] a greater volume of brain irradiated,[42,44] and a younger age at time of treatment.[42,44-47] Patients under the age of 5 experience the greatest impact on cognitive processes, and the influence of patient age at time of treatment has a greater effect on neurological deficits than the delivered dose.[48]

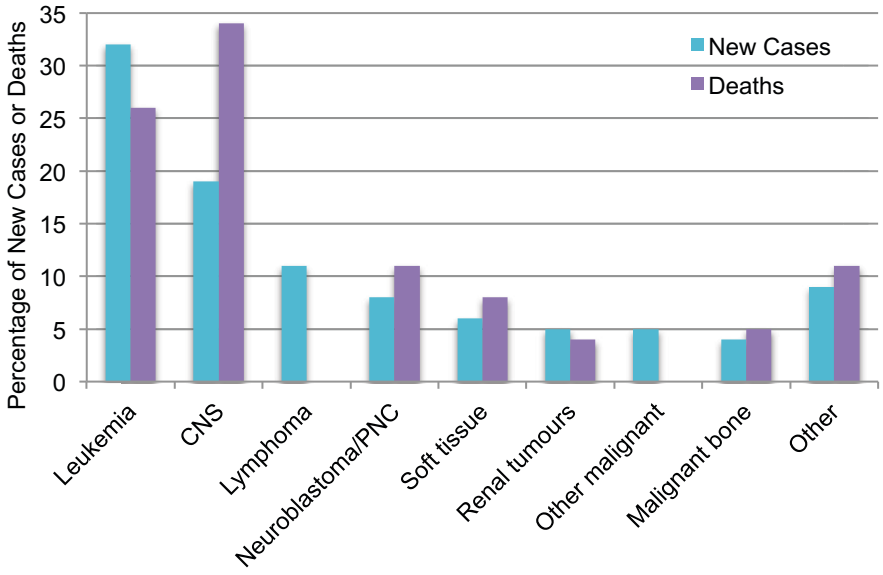

Figure 1.6 The distribution of new cancer cases for ages 0 – 14 in Canada from 2006 – 2010 (total number of cases = 4600), and the distribution of cancer deaths for ages 0 – 14 in Canada from 2005 – 2009 (total number of deaths = 640). CNS = central nervous system, PNC = peripheral nervous cell tumours. Data taken from *Canadian Cancer Statistics 2014*.[1]

Potential types of impairment include intelligence,[44,45,49-52] neurocognitive function (e.g. attention/processing, learning and memory, language visual perception, task efficiency[42,47,48]), endocrine dysfunction,[45,47,48] and behavioural or emotional effects.[47] When compared to other cancer survivors and a sibling cohort, childhood CNS malignancy survivors achieve lower educational status, less income, and less fulltime employment.[42] Despite the importance of radiation therapy in tumour control, there have been efforts to reduce radiation dose, reduce the volume of normal tissue irradiated, delay

the commencement of radiation treatments till the child is older, or omit radiotherapy altogether in an attempt to reduce the occurrence and severity of neurological sequelae.[39,44,47,51,53] However, for certain types of disease, delaying radiotherapy negatively impacts the rate of survival.[39] Extended or aggressive chemotherapy has been used to replace radiation treatments for standard risk disease, but high dose radiation can still be employed for high risk disease.[39,44,47,51] Many long-term studies considering the effects of radiation therapy on the developing brain were performed on patients treated decades ago. Technological advancements (such as conformal radiotherapy) may prove to offer improvements in terms of avoiding long-term deficits while achieving better tumour control probabilities.[44]

1.2 Microbeam radiation therapy: Overview and biological rationale

1.2.1 Introduction to microbeam radiation therapy

Microbeam radiation therapy (MRT) is an experimental technique that exploits the unusual tissue response to microbeams and may offer a treatment option for cases that would otherwise be limited by normal tissue toxicity. This method employs synchrotron x-rays shaped into an array of quasi-parallel microbeams to treat solid tumours (Fig. 1.7). MRT differs markedly from conventional therapies in three key aspects: (1) the dose distribution delivered to the tumours is extremely spatially fractionated (microbeams are typically 25 – 100 μm wide and separated by 100 – 400 μm), (2) extremely high doses (hundreds of Gy) are delivered in the microbeam paths in a single, high dose rate (thousands of Gy/s) fraction, and (3) the polyenergetic synchrotron x-rays are relatively low in energy (~50 – 600 keV).[54-57] Third-generation synchrotrons are used as x-ray sources for MRT because they can provide the high dose rates and minimally divergent beams necessary to produce the extremely spatially fractionated high dose microbeams characteristic of MRT.[57]

In the late 1980's researchers at the National Synchrotron Light Source in Upton, New York were attempting to perform microtomography of a mouse head with a synchrotron x-ray microbeam approximately 30 μm in diameter. To maximize contrast

the dose was increased during the imaging procedure to approximately 200 Gy. The mouse recovered normally, and histological analysis a month later revealed no evidence of damage along the beam path.[57] This prompted the researchers to investigate the possibility of using an array of microscopic synchrotron x-ray beams in radiotherapy. In 1995, Slatkin *et al.* first demonstrated the high tolerance of normal rat brain to extreme doses of synchrotron x-ray microbeams, and discussed a microbeam array's potential application in radiation therapy.[55] Since then, animal studies have demonstrated that MRT can achieve similar or improved tumour control while resulting in reduced normal tissue toxicity when compared to single fraction broad beam irradiations.[56-58]

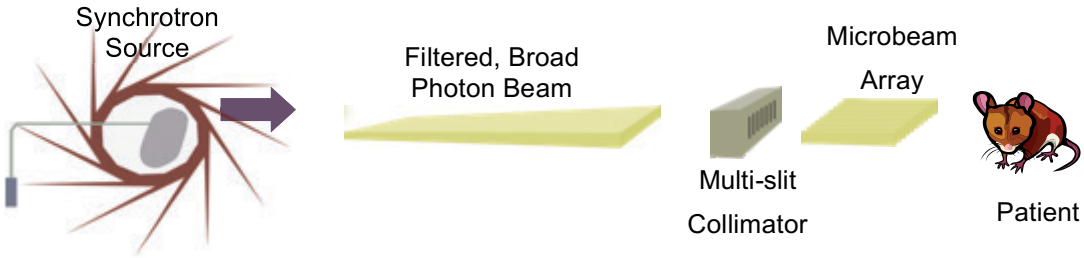

Figure 1.7 Schematic of microbeam radiation therapy. Synchrotron x-rays are shaped by a multi-slit collimator into a microbeam array to treat a solid tumour.

1.2.2 Irradiation conditions

Currently only synchrotron radiation (SR) produced in synchrotron light sources (to be discussed in more detail in Chapter 2) can provide the geometric conditions required for MRT. There are two unique characteristics of SR that allow MRT experimentation. Firstly, SR is minimally divergent (on the order of 1 milliradian (mrad)), and thus the width of the microbeam widens only minimally as it travels several centimetres in the medium. Secondly, SR is extremely intense: for typical energies used for MRT experiments, dose rates of up to approximately 20,000 Gy/s are achievable. The high dose rates mean that the high doses associated with MRT can be delivered within a fraction (*e.g.,* a few hundredths) of a second, which is important to prevent both macroscopic and microscopic (cardiosynchronous tissue movement) patient motion from blurring out the dose distribution during irradiation. Additionally, although not unique to SR, the x-rays produced are relatively low in energy (mean energy ~ 100 keV). The

released secondary electrons have limited ranges in tissue, and thus help maintain the peak and valley patterned dose distribution. Increasing the beam's energy will increase the penetrability of the microbeam array, but will also lead to further scatter between the microbeams. The spatially fractionated dose distribution must be preserved to exploit the high normal tissue sparing effect observed with MRT.

A synchrotron beam used for MRT is wide horizontally, but very narrow vertically. The desired horizontal array size is achieved by simply collimating the beam. In the vertical direction, the array size is achieved by vertically scanning the phantom/animal/patient through the small, stationary beam. The vertical scan rate and dose rate determine the delivered dose. The width and separation of the microbeams within the array are determined by the microbeam collimator. Originally, a single slit collimator composed of tantalum was used, and multiple beams were produced by the horizontal translation of the phantom or animal.[55] To rapidly irradiate an animal with a full microbeam array, a collimator with multiple slits is required. The collimator must be accurately machined for microbeam uniformity, must be made of a material that can withstand the heat load from the intense beam without expansion, and must provide sufficient attenuation to create the microbeam pattern. The first multi-slit collimator (MSC) was made of alternating leaves of ~150 – 165 μm wide aluminum (high x-ray permeability) and ~ 50 μm wide gold (low x-ray permeability) leaves.[59] The design included two identical pieces that could be offset with respect to each other to alter the microbeam width (Fig. 1.8(a)). More recent designs offer improved uniformity with more precise machining methods.[60,61]

Like conventional radiation therapy that uses multiple beams, MRT experimentation often employs more than a single microbeam array. Geometric arrangements utilized thus far include a single unidirectional array[55,56,58,62-70] (Fig.1.8(b)), cross-fired geometry[56,69,71-76] (Fig. 1.8(c)), cross-hatched geometry[64,70] (Fig.1.8(d)) and interlaced microbeams[77,78] (Fig. 1.8(e)). Additionally, an extension of MRT, mini-beam radiation therapy (MBRT), has been developed by increasing the scale of the microbeam array. In MBRT, the width of the microbeams is approximately 200 - 700 μm, and the centre-to-centre separation is approximately 1 – 4 mm.[79,80] These mini-beams maintain

some of the sparing effect of microbeams, but are technically simpler to produce and work with, and thus may be easier to implement clinically.

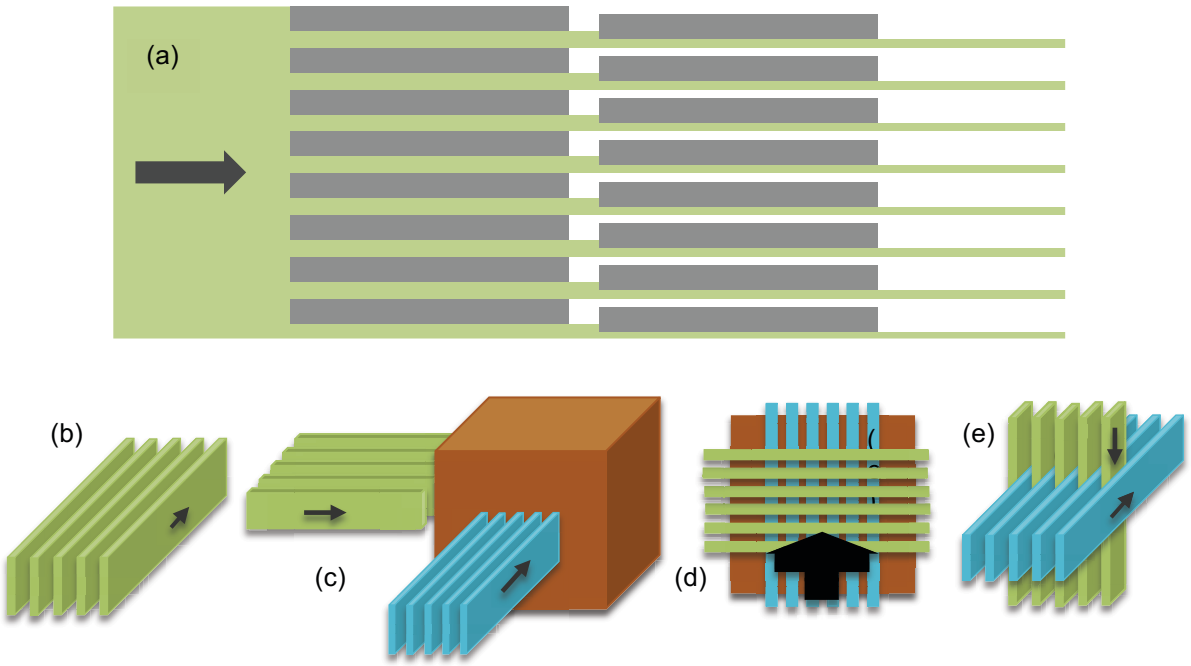

Figure 1.8 (a) A cross-sectional view (through a horizontal plane) of the stacked MSC design common to many MRT experiments. An offset between one stack with respect to the other allows variable microbeam width. The black arrow indicates the direction of the x-ray beam. The dimensions of the MSC are not to scale. Various irradiation geometries are portrayed in the bottom row: (b) unidirectional irradiation, (c) cross-fire irradiation, (d) cross-hatched geometry and (e) interlaced geometry.

1.2.3 Animal studies demonstrating normal tissue sparing

Multiple experiments have demonstrated an unusual normal tissue tolerance to high dose microbeam arrays. In the first *in vivo* study, Slatkin *et al.* investigated the response of adult rat brain to entrance doses of between 312 and 10000 Gy and beam widths of 20, 37 or 44 μm.[55] Histological analysis of brain tissue irradiated with doses ≤ 625 Gy appeared normal. A dose of 2000 Gy led to loss of cell neuronal and astrocytic nuclei in the beam path within 1 month in 50% of rats, but no other kind of damage was evident for entrance doses ≤ 5000 Gy. Necrosis was not observed until a dose of 10000 Gy.[55] To consider the effects on particularly sensitive structures, multiple experiments were performed on

immature CNS tissue. The brains of suckling rats,[81] weanling piglets[62] and duck embryos[58] have been irradiated. The hindbrains of 11 – 13 day old rats were irradiated with 28 μm wide microbeams, separated by either 105 or 210 μm in a cross-fired arrangement, and doses between 50 and 150 Gy. Although histological analysis revealed loss of cell nuclei in the microbeam path, there were no rat deaths attributed to radiation damage, normal tissue architecture was maintained, and no haemorrhaging was observed during the 15 month follow up. Weight loss, motor disturbances and behavioural changes were observed in some rats, and were associated with higher doses and more closely spaced microbeams.[81]

A similar study was performed using 42 – 48 day old piglets irradiated unidirectionally with 20 – 30 μm wide microbeams separated by 210 μm and entrance doses between 150 and 600 Gy.[62] These larger animals better represented the brain size of a human infant, and again demonstrated the high normal tissue tolerance of the young cerebellum. In this study, where animals were observed for over a year after irradiation, magnetic resonance imaging, behavioural and neurological assessment, and eventual necroscopy revealed no changes between irradiated piglets and their unirradiated litter mates except for loss of nuclei in the beam path (Fig. 1.9). Finally, duck embryos *in ovo* were irradiated with both microbeam and broad beam synchrotron radiation.[58] The study again showed elevated tolerance to microbeams, and suggested that the dose threshold seems to depend on the valley dose, the dose in between the microbeams, and not the peak dose, or the dose in the microbeam path. All of these studies concluded that their results supported the possibility of MRT as a potential for the treatment of neoplasms in the immature CNS tissue of infants.[55,58,62,81]

Aside from brain tissue, the elevated tolerance of the spinal cord to microbeams[82] (35 μm × 210 μm, 253 Gy) and minibeams[83] (0.68 mm × 4 mm, 400 Gy) has been established. Similarly, the resistance of mouse skin[84] (25 μm × 200 μm) and rat skin[85] (90 μm × 300 μm) to high dose microbreams has been demonstrated. The researchers suggested a 6 to 9-fold increase in skin tolerance when comparing the mean dose delivered by the microbeam array to the mean dose causing moist desquamation in rats. In mice, the study concluded that the integrated dose better predicted tissue tolerance than either peak or valley doses.[84]

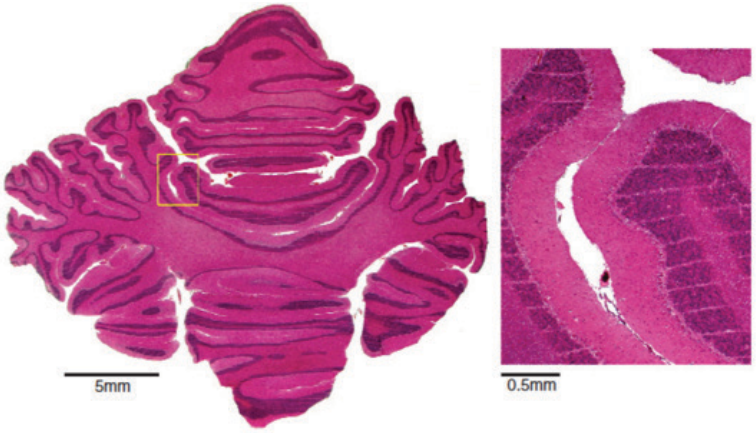

Figure 1.9 A section of the piglet cerebellum after irradiation with microbeam array (~ 25 μm wide, 210 μm spacing) and an entrance dose of 300 Gy. The lighter stripes indicate the path of the microbeams, where some cells and nuclei were destroyed.[62] (Image reprinted from: J.A. Laissue *et al.*, "Prospects for microbeam radiation therapy of brain tumours in children to reduce neurological sequelae," Dev. Med. Child Neurol. **49**, 577-581 (2007) with permission from John Wiley and Sons.)

1.2.4 Animal studies demonstrating tumourcidal effects

To study tumour response to MRT, animal models (most commonly rats and mice) have been inoculated with intracranial and subcutaneous tumours of a variety of cell lines and treated with microbeam arrays. In these MRT experiments the growth of nearly every tumour was suppressed, at least temporarily, and many tumours were ablated.[57] This is despite the fact that only a fraction of the tumour volume was directly irradiated by the microbeams.

Data from two experiments examining the response of intracranial 9L gliosarcoma (9LGS) in adult rats are summarized in Table 1.1. In 1998, Laissue *et al.* treated the rats with 25 μm wide microbeams separated by 100 μm.[56] MRT was responsible for ablating 22/36 tumours overall, and notably 4/11 of those treated by unidirectional irradiation only. The comparison to broad beam irradiation was extrapolated from a previously published result. Despite the increased survival times and ablation of tumours, significant damage was observed in the cross-fired regions. The same animal and tumour models were investigated by Dilmanian *et al.* (2002)[63] with a unidirectional array of 27 μm wide microbeams that delivered doses between 150 and

500 Gy. The beam spacing was either 50, 75 or 100 μm. The results included both tolerable and intolerable irradiation configurations. It was observed that the sparing of normal brain tissue was lost when the valley dose approached the tissue tolerance to broad beams. The study demonstrated that, under the right irradiation conditions, single fraction unidirectional MRT may offer a higher therapeutic index than single fraction broad beam irradiations. A number of other studies have supported the ability of high-dose microbeam treatments to prolong survival time in animals with intracranial 9LGS tumours.[65,67-69,72,75,76,86,87]

Table 1.1 The median survival time (days) for 9LGS-bearing rats following microbeam irradiation and broad beam irradiation. Tabulated data from Laissue *et al.*[56] and Dilmanian *et al.*[63]

Irradiation Protocol	Median Survival Time (d)
Laissue *et al.* 1998[56]	
Controls, 0 Gy	20
Unidirectional, 625 Gy (n = 11)	24
Cross-fire, 625 Gy x 2 (n = 14)	139
Cross-fire, 312.5 Gy x 2 (n = 11)	96
Broad beam (250 kVp), 22.5 Gy[88]	35
Dilmanian *et al.* 2002[63]	
Controls, 0 Gy	19
Tolerable dose MRT	170
High dose MRT	60
Broad Beam, 22.5 Gy[89]	33.5

For subcutaneous EMT-6[64] and EMT-6.5[70] (mammary) tumours in the legs of mice it has also been shown that unidirectional and cross-hatched MRT treatment can achieve similar or better tumour control compared to broad beam irradiation, with less acute and delayed normal tissue toxicity (Fig. 1.10).[64,70] The achieved therapeutic index was better for cross-hatched versus unidirectional irradiations, and when the integrated dose is taken into account, MRT offers an approximately six-fold increase in tolerance over broad beam irradiations.[64] Because there are so many parameters in MRT (Section 1.2.2), the optimal geometric and dosimetric parameters have not yet been deduced.

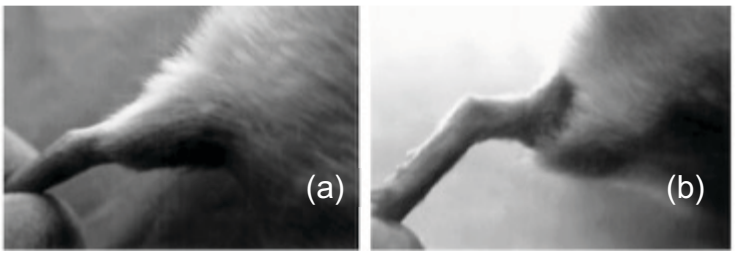

Figure 1.10 The hair regrowth in mice following (a) cross-hatched microbeam array irradiation, with an entrance dose of 520 Gy, and (b) after a 38 Gy broad beam irradiation at least 6 months after treatment. The image shows better regrowth, and a slightly higher rate of tumour ablation in the microbeam treated animal. (Image reproduced with a slight modification from: F.A. Dilmanian *et al.*, "Murine EMT-6 carcinoma: High therapeutic efficacy of microbeam radiation therapy," Radiat. Res. **159**, 632-641 (2003)[64] with permission from Radiation Research.)

In addition to the effects of MRT alone, the efficacy of MRT combined with adjuvant therapies has also been examined. Dose enhancement in the tumour has been suggested through the use of high atomic number agents, including iodine,[90] gadolinium (Gd-DTPA),[68] Gd-based nanoparticles[86] and gold nanoparticles.[91,92] The high-Z compounds can be preferentially delivered to the tumour because of the enhanced permeability of the tumour vasculature.[93] The dose enhancement is attributed to an increase in the cross-section for the photoelectric effect (increases with $\sim Z^3$ [94]). The generated photoelectrons have a short range and deposit their energy near the high-Z material, and thus predominantly in the malignant tissue. Additionally, the high-Z compounds provide enhanced contrast for X-ray-based imaging, or magnetic resonance imaging for the case of gadolinium.[86] Gene-mediated immunotherapy was shown to increase survival over MRT alone for 9LGS-bearing rats.[65] Also, the combination of MRT and chemotherapeutic agents has been investigated.[68,73,76,95] Schultke *et al.* demonstrated the benefit of buthione-SR-sulfoximine (BSO, a radiosensitizer) in combination with MRT in prolonging survival in rats with intracranial C6 and F98 gliomas.[73] Bouchet *et al.* showed that JAI-51, an anti-mitotic drug, prolonged the survival of rats with intracranial 9LGS in combination with MRT, but not alone.[76] It was suggested that MRT induced a temporary disruption of the blood brain barrier that enhanced drug uptake over the treatment with JAI-51 alone.[76] Griffin *et al.* used anginex, an anti-angiogenic peptide, to further delay tumour growth over MRT alone.[95]

1.2.5 Biological mechanism behind microbeam radiation therapy

The detailed biological response to high dose microbeams, particularly how such high sparing is achieved in normal tissue and what causes the differential response between normal and cancerous tissues, is not yet fully understood. A better fundamental understanding of these tissue responses would advance the present preclinical state of MRT, and may lead to translational advancements in conventional therapies. There are two main hypotheses that have been proposed to explain this "microbeam effect" in tissues. First, the enhanced normal tissue sparing observed following microbeam irradiations has long been associated with unusually high radioresistance of microvasculature,[23,25,55-57,63,64,96-98] and several experimental results support this connection. Spatially fractionated irradiation of normal brain results in limited tissue damage.[55,56,97] Slatkin *et al.* suggested that damaged blood vessels are repaired by the immigration of nearby, minimally irradiated cells, which would be facilitated by the large area at the interface between highly irradiated tissues in need of repair, and minimally irradiated tissues that could provide restorative cells.[55,97] The absence of necrosis at late times after the delivery of such high doses associated with MRT suggests that the microvasculature must either maintain or restore at least partial functionality.[85] Evidence of normal tissue microvasculature repair has been observed.[63,64,66,96,99] Figure 1.11 shows a "vasculature bridge" formed 24 hours after microbeam irradiation in chick chorioallontoic membrane. It has been demonstrated that tissue injury following MRT depends on blood supply, and particularly on the stage of capillary maturation.[96,100]

In addition, researchers observed the "absence of important cerebral edema,"[101] and a transient and dose-dependent disruption of the blood brain barrier[66] following MRT. This absence of edema could offer significant advantages of MRT over broad beam treatments. Although changes in normal vasculature following unidirectional microbeam irradiation have included an increase in vessel inter-distances, the normal tissue has still maintained an adequate blood supply; in contrast, MRT leads to hypoxia in intracerebral 9LGS tumours.[75,87] To explain the differential effect, it was proposed that the disorganized tumour vasculature is less efficient at repair following destructive irradiation compared to the ordered vasculature found in normal tissues.[57]

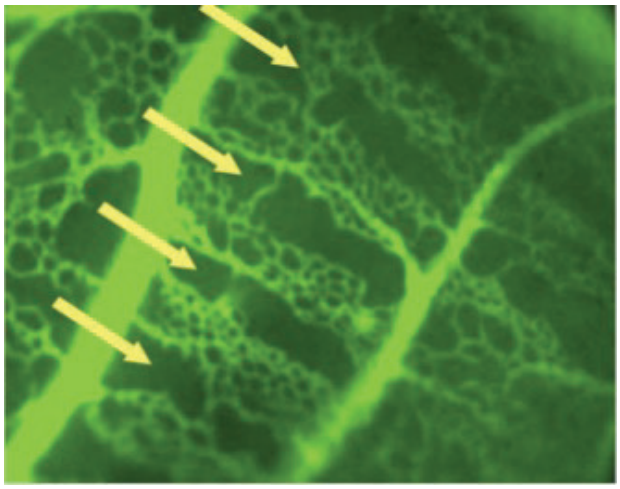

Figure 1.11 The formation of "vascular bridge" 24 h following a 300 Gy peak dose in the immature microvasculature of a chick chorioallantoic membrane. The yellow arrows indicate the path of the microbeams. (Image reprinted from Nuclear Instruments and Methods in Physics Research Section A: Accelerators, Spectrometers, Detectors and Associated Equipment, **548**, H. Blattmann *et al.,* "Applications of synchrotron X-rays to radiotherapy," 17-22, Copyright 2005, with permission from Elsevier [96])

The second proposed explanation is that differential responses in normal and tumour tissue are due to different ionizing radiation induced changes at the cellular level, and may include differences in cellular communication, cell mobility and gene expression.[70,102-106] Dilmanian *et al*. hypothesized that the bystander effect (Section 1.1.2) plays a role in the migration, proliferation and differentiation of cells neighbouring maximally-irradiated cells to facilitate repair following microbeam irradiation.[102] Direct evidence of the bystander effect-mediated damage in cell culture was demonstrated in C6 rat glioma cells and U251 human glioma cells.[107] DNA double strand breaks (DSBs) were detected in non-irradiated cultured cells after exposure to soluble factors collected in the medium of microbeam irradiated cells.

Differential cellular responses in normal tissue (skin) and EMT-6.5 subcutaneous tumours following MRT have been investigated in a rat model, and showed that skin demonstrated a greater capacity for repair and proliferation than the tumour tissue.[70] The authors also observed mixing of cells exhibiting maximal and minimal γ-H2AX-stained cells (stained brown in Fig. 1.12) 24 hours after irradiation. This distribution was attributed to "rapid intratumour migration of maximally and minimally irradiated cells."[70]

They suggested that the reduced distance between "peak" and "valley" cells could increase cell-mediated communication and perhaps increase overall damage to the tumour. In the same tumour model, infrared microspectroscopy was used to identify molecular composition after microbeam (560 Gy peak dose) and broad beam irradiations (11, 22, and 44 Gy).[108] The study showed differences between microbeam and broad beam-irradiated tissue, although it is not clear whether these differences are due to total dose differences or the geometric differences. Additionally, there were no spectroscopic differences between peak and valley doses, despite the valley dose being only ~ 2% of the peak dose, which the researchers claim suggests a uniform tissue response to the microbeams. Investigation of the differences in transcription following MRT versus broad beam irradiations shows that samples irradiated by these two irradiation geometries regulate genes differently in EMT-6.5 tumours.[103] Expression of immunity-related genes was higher following broad beam irradiation versus MRT, which may lead to a decreased inflammatory response following MRT and may influence the increased sparing seen in normal tissues.

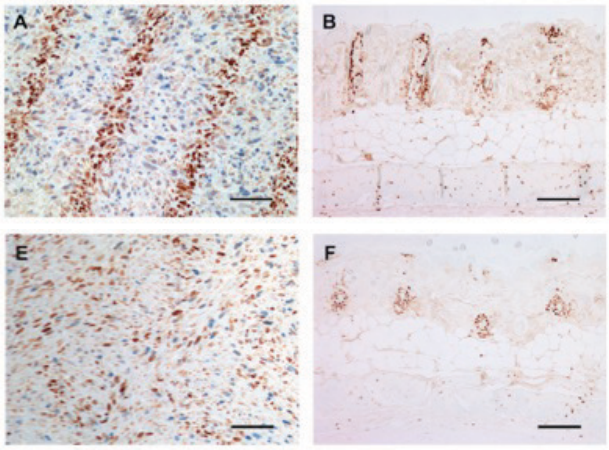

Figure 1.12 The EMT-6.5 (left column) and normal skin (right column) from mice euthanized at 4 h (top row) or 24 h (bottom row) post-irradiation with a 560 Gy microbeam (25 × 200 μm). Brown cells = DNA DSBs (γ-H2AX), blue cells are proliferating cells (BrdU). (Image reprinted from International Journal of Radiation Oncology Biology Physics, **77**, J.C. Crosbie *et al.*, "Tumor Cell Response to Synchrotron Microbeam Radiation Therapy Differs Markedly from Cells in Normal Tissues," 886-894, Copyright 2010, with permission from Elsevier.[70])

The effects of radiation-induced damage at greater distances from the site of irradiation have also been studied. It has been demonstrated that irradiation of one hemisphere of the rat brain will lead to dose-dependent abscopal effects in the contralateral brain and urinary bladder for both microbeam and broad beam irradiations.[104,105] The signals were significantly weaker in the bladder versus either brain hemisphere, which indicates either a distance or tissue dependence of this effect. Additionally, the researchers reported that the production of bystander effects was higher when tumour bearing rats were irradiated versus tumour free animals.[104] An extension of this work showed that these abscopal effects were also detected in non-irradiated cage mates of irradiated rats at 48 hours after irradiation for both broad beam and microbeam-irradiation protocol.[105] The effects in cage mates were independent of dose, but the deleterious effects were stronger after broad beam irradiations and were equal in the brain and the urinary bladder.[105] A better understanding of the cell-to-cell communication pathways implicated by these results could shed light on the optimum geometry and prescribed dose for MRT.

1.2.6 Applications of microbeam radiation therapy

The profound normal tissue tolerance and elevated therapeutic index of high dose microbeams may be advantageous for the treatment of malignancies that require more normal tissue preservation than can be offered from conventional methods, but are not restricted by the limited penetrability of the low energy x-rays. Since the earliest MRT publications, it was suggested that synchrotron x-ray microbeams could be used to treat brain tumours, and particularly to address the difficulty in treating pediatric brain tumours (Section 1.1.5).[54-56,58,62] MRT has the potential to spare the sensitive CNS tissues of childhood cancer patients, while inhibiting tumour growth in relatively shallow lesions.[55,97] Even if complete ablation of the tumour is not possible, a reduction in tumour size through microbeam irradiation could allow time for the brain to mature while postponing more aggressive treatments, and/or improve the efficacy of auxiliary treatments by reducing the number of malignant cells.[97] Aside from childhood malignancies, MRT could be used to treat tumours near particularly radiosensitive organs

(*e.g.*, eye, spinal cord),[79] or perhaps shallow tumours that require further palliation after being treated to tolerance by conventional methods.

Aside from the treatment of cancer, microbeam radiosurgery is being investigated as a treatment technique for other neurological conditions. Options include the treatment of vasculature malformations,[79] movement disorders[57,78,79,109] (*e.g.*, Parkinson's disease), epilepsy,[57,78,79,109,110] and behavioural disorders[109] (*e.g.*, depression).[109] The reduction in seizure duration over non-irradiated controls in rats using microbeams has been demonstrated without any related neurological deficits[78,110] (Fig. 1.13). Finally, microbeam irradiation may be used to temporarily disrupt the blood brain barrier for the delivery of drugs in the brain.[66,75,79]

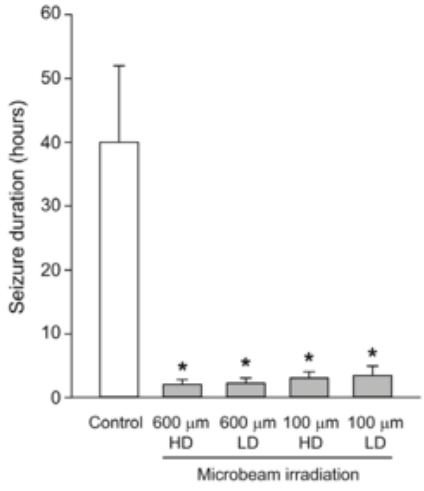

Figure 1.13 Reduction in seizure duration in control and microbeam-irradiated rats. Geometry (microbeam width × spacing): 100 μm × 400 μm or 600 μm × 1200 μm. Peak dose: HD = High dose protocol (360 Gy (100 μm) and 150 Gy (600 μm)). LD = low dose protocol (240 Gy (100 μm) and 100 Gy (600 μm)). (Image reproduced from: P. Romanelli *et al.*, "Synchrotron-Generated Microbeam Sensorimotor Cortex Transections Induce Seizure Control without Disruption of Neurological Functions," Plos One **8**, e53549 (2013).[110])

1.2.7 Future directions of microbeam radiation therapy

At the European Synchrotron Radiation Facility (ESRF), an expert panel recommended the treatment of spontaneous tumours in larger animals (cats and dogs) as the next step in progressing toward MRT clinical trials.[57,111] The knowledge gained from extending the geometric and dosimetric protocols for the treatment of rodents will hopefully provide

insight into the adaptation of MRT parameters from large animals to humans, if and when clinical trials are started. In preparation for large animal treatments, a dedicated MRT hutch was built on the ID17 beamline that included MRT-specific equipment and safety systems.[111] Although the ESRF has the most experience in MRT experimentation, similar plans for moving toward clinical trials are shared by the Australian Synchrotron and the Canadian Light Source.

Despite these plans, the progression of MRT research, and clinical implementation, is limited by the availability of alternative, more readily available x-ray sources capable of achieving the spatial fractionation required for MRT. One potential alternative source is a significantly smaller and less expensive accelerator compared to a synchrotron light source. High energy x-rays would be produced through inverse Compton scattering between a high-energy electron produced by the accelerator, and laser-generated low-energy photons.[112,113] It is estimated that the source could achieve dose rates of 10000 Gy/s, cost less than 15 million US dollars, and have a diameter of less than 5 m.[113] A more compact source based on carbon nanotube field emission is also being investigated.[114-118] The carbon nanotube source can produce microbeams that are approximately 300 μm wide, with an instantaneous dose rate of 2 Gy/s at 160 kVp.[115,116] To compensate for the low dose rate, the developers have demonstrated the potential for physiological gating to minimize motion-induced blurring.[116]

1.3 Microbeam radiation therapy: Dosimetry

Accurate dosimetry is important for the proper interpretation of animal studies, and for progress toward clinical trials in MRT. There are well-established dosimetric protocols for conventional radiotherapy, and overall uncertainties of less than 3 % are desired.[119] However, because MRT dose distributions and irradiation conditions are drastically different from conventional methods, MRT dosimetry is uniquely challenging. Firstly, MRT is performed at extremely high dose rates, up to several kGy/s, and thus any potential dosimeter must not become saturated by the rapidly accumulated signal. Secondly, a dosimeter with fine spatial resolution is required to accurately characterize the microbeam pattern, and particularly the sharp dose gradients at the edges of the

microbeams. Thirdly, a single dosimeter must have a wide dynamic range to measure the high doses (100s of Gy) in the microbeam path, and the low doses delivered between the microbeams. Finally, x-ray energies are relatively low (compared to conventional energies produced by a clinical linear accelerator), and in this region the energy response of many materials becomes non-linear. Presently, there is no single dosimeter that can sufficiently overcome these challenges.

1.3.1 Theoretical dosimetry for microbeam radiation therapy: Monte Carlo simulations

Monte Carlo is a statistical technique that employs random numbers and probability distributions to converge upon a solution. Monte Carlo has a wide range of applications including the transport of ionizing radiation in matter. For radiation transport, each particle sampled from a beam is simulated through successive interactions until it either exits the geometry or its energy reaches a pre-defined cut-off value. The trajectory of secondary particles created during the primary particle's interactions, are also followed in a similar step-by-step fashion. Monte Carlo simulations have been used extensively in the calculation of dose depositions in conventional radiotherapy. Because Monte Carlo methods are not limited by the physical challenges described in the previous section, theoretical dosimetry has been relied upon heavily since the earliest MRT studies. Instead of the physical limitations described above, Monte Carlo simulations are restricted by the accuracy of the implementation of the physical models, statistical uncertainty, and the representation of the x-ray source and geometry.

At the photon energies present in MRT (up to a few hundred keV), the important photon interactions are Rayleigh scattering, Compton scattering and the photoelectric effect. Secondary electron interactions include elastic scattering and inelastic scattering. The differential cross-sections for the various interactions are given in Table 1.2 (with the coordinate system shown in Fig. 1.14) for both non-polarized and polarized conditions. The details of how each of these interactions are implemented depends on the physical models implemented, and thus on the choice of Monte Carlo environment.

Table 1.2 The differential cross-sections for non-polarized and polarized x-rays for the three relevant interaction types for MRT. r_0 is the classical electron radius, θ/θ_e is the polar angle of photon/photoelectron, ϕ/ϕ_e is the aximuthal angle of the photon/photoelectron, $F(q,Z)$ is the atomic form factor, q is the momentum transfer, Z is the atomic number, $k_{i/f}$ is the initial/final wave vector, α is the fine structure constant, $\hbar$ is the reduced Planck's constant, c is the speed of light, a_0 is the Bohr radius for hydrogen, v_e is the velocity of the photoelectron, and m_0 is the electron mass.

Interaction	Cross-Section	Non-Polarized X-Rays	Polarized X-Rays
Rayleigh scattering	$\frac{d\sigma_{Ra}}{d\Omega}$	$\frac{r_0^2}{2}\left(1+\cos^2\theta\right)F^2(q,Z)$	$\mathrm{r}_0^2\left(1-\sin^2\theta\cos^2\varphi\right)\mathrm{F}^2(\mathrm{q},\mathrm{Z})$
Compton Scattering	$\frac{d\sigma_{KN}}{d\Omega}$	$\frac{r_0^2}{2}\left(\frac{k_f}{k_i}\right)^2\left(\frac{k_f}{k_i}+\frac{k_i}{k_f}-\sin^2\theta\right)$	$\frac{r_0^2}{2}\left(\frac{k_f}{k_i}\right)^2\left(\frac{k_f}{k_i}+\frac{k_i}{k_f}-2\sin^2\theta\cos^2\phi\right)$
Photoelectric Absorption	$\frac{d\sigma_{Ph}}{d\Omega}$	$16\cdot\alpha\cdot\left(\frac{\hbar}{m_0}\right)\cdot\frac{Z^5}{c\cdot k_i\cdot(k_e\cdot a_0)^5}\cdot\frac{\sin^2\theta_e}{\left(1-\frac{v_e}{c}\cdot\cos\theta_e\right)^4}$	$32\cdot\alpha\cdot\left(\frac{\hbar}{m_0}\right)\cdot\frac{Z^5}{c\cdot k_i\cdot(k_e\cdot a_0)^5}\cdot\frac{\sin^2\theta_e\cdot\cos^2\phi_e}{\left(1-\frac{v_e}{c}\cdot\cos\theta_e\right)^4}$

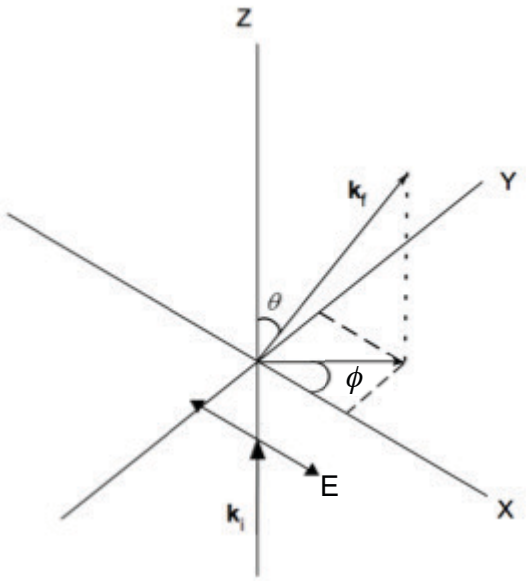

Figure 1.14 The coordinate system for the differential cross-sections given in Table 1.2 where $k_{i/f}$ is the initial/final wave vector, E is the electric field vector, θ is the polar angle, and ϕ is the azimuthal angle.

There are multiple options for Monte Carlo packages for the transport of ionizing radiation, and many have been used for the calculation of MRT dose distributions: EGS4,[54,120-124] EGS5,[124,125] PSI-GEANT,[126] GEANT4,[127-130] PENELOPE,[77,131-138] and MCNPX.[71,139] Comparisons of the deposited dose from cylindrical and planar microbeams in water and PMMA were calculated with different MC codes (PENELOPE,[140] EGS4,[141] MCNPX[142] and GEANT4[143]).[144] The differences between the results from PENELOPE and any other code were within 3 % in the peak regions, and did not exceed ± 20 %, and discrepancies were largest in the distance range 10 – 1000 μm (at the edge of the microbeam and extending into the valley region), where the transport of electrons is the dominant mechanism for dose deposition.[122] A separate study showed excellent agreement between PENELOPE and GEANT4-Penelope (shares an analytical approach with PENELOPE for low energy applications). The version of GEANT4 using its own low energy model (the original evaluated data libraries) shows a much greater difference (up to 65%) from PENELOPE's results.[127] Again, the differences are attributed to the cross-sections and the algorithms for tracking secondary particle interactions.[127]

Accurate description of the x-ray beam source is critical to the overall accuracy of a Monte Carlo calculation. This description requires information on each particle's energy, polarization, position and direction. The energy spectrum of the synchrotron x-ray beam is challenging to obtain experimentally. The incident photon beam is too intense to directly measure the energy spectrum with, for example, a semiconductor detector. One indirect method uses x-ray powder diffraction[145] to reconstruct the incident beam energy spectrum based on the measured energy spectrum scattered into a given solid angle after interaction with a crystalline powder. Alternatively, the energy spectrum can be determined analytically with software packages (*e.g.,* SPECTRA[146] and PHOTON[147]) based on the theoretical description of synchrotron radiation (Chapter 2). Early Monte Carlo studies have systematically studied the effect of the incident photon energy on the resultant dose distribution.[54,124,126,127,132,134] Increasing initial energy provides greater penetration, potentially allowing the treatment of deeper lesions. However, increasing energy also leads to a wider penumbra and consequently more dose delivered in the valley region. This reduces the degree of spatial fractionation delivered by the microbeams, thus diminishing the MRT sparing effect. The optimum energy for MRT would provide the best compromise between spatial fractionation and beam penetration.

The synchrotron x-rays produced for MRT experimentation are linearly polarized in the horizontal plane, orthogonal to the direction of propagation. The polarization introduces an angular dependence on the azimuthal angle (ϕ, Fig. 1.14) for the direction of scattered photons or photoelectrons. Figure 1.15 demonstrates the angular dependence of scattered photons or emitted photoelectrons for a 100 keV incident photon undergoing Rayleigh scattering, Compton scattering, and the photoelectric effect for non-polarized (top row) and polarized (bottom row) conditions based on the formulae in Table 1.2. The photon is traveling in the z-direction, with linear polarization directed along the x-axis. For Rayleigh and Compton scattering, the photons are preferentially scattered along the height of the microbeam or in the direction of propagation, while the photoelectrons are preferentially scattered into the valley regions. There have been a few studies on the effect of polarization on dose distributions with unclear results.[122,130,148] The most recent report employing Geant4 demonstrated differences in deposited dose of no more than 3%

in the microbeam path between polarized and unpolarized incident photons, and thus it was concluded that polarization has relatively little impact on dose calculations for clinical trials. [130]

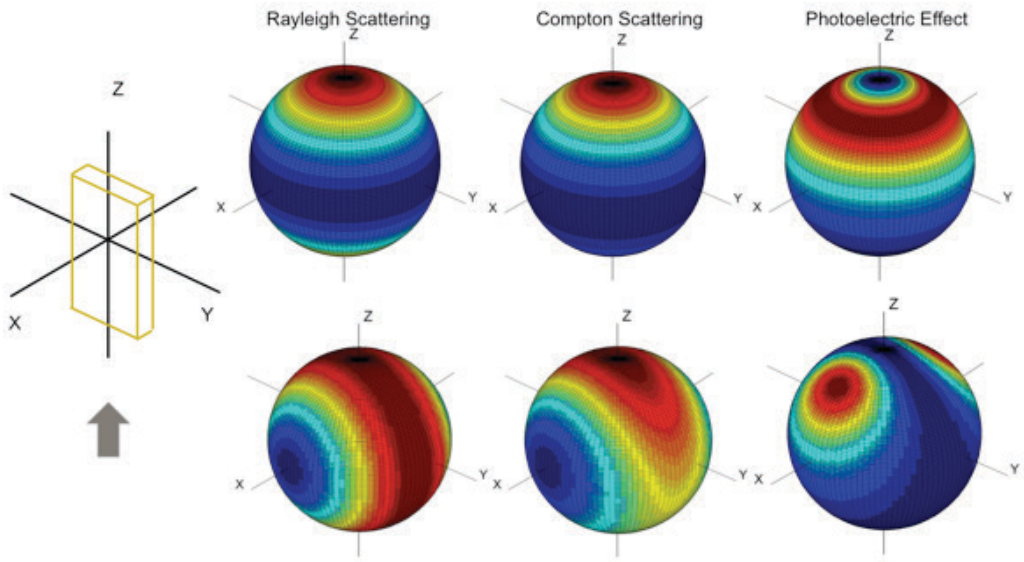

Figure 1.15 The angular distribution of 100 keV incident photons for non-polarized (top row) and linearly polarized (bottom row). The distributions correspond to a microbeam traveling in the Z-direction, with height in the Y-direction, width in the X-direction, and polarization along the X-axis. The associated differential cross-sections are given in Table 1.2. For each case, red and blue indicate the maximum and minimum cross-section values, respectively.

The majority of MRT Monte Carlo simulations have been performed with idealized microbeam geometry. A single, uniform, parallel microbeam is modeled at the surface of the phantom.[54,120,121,126,127,132,134,136] This reduces the simulation time, but means the source size, photon beam divergence, scatter and interactions with the collimator, and scatter in the air are ignored. The transition from a single microbeam dose distribution to a microbeam array dose distribution has most often been performed by a simple superposition procedure. Individual microbeam dose distributions are added with an incremental shift equal to the desired center-to-center spacing of the microbeam array.[127,132,134,136] The first study on the effect of more realistic geometry in Monte Carlo dose distribution calculations was published by Nettelbeck *et al.* in 2009.[149] The authors considered the effect of modeling the distributed photon beam source, the photon beam

divergence, the multi-slit collimator (MSC), and the array model. The authors demonstrated that the distributed photons source resulted in an up to ~30% change in dose, but only in the very narrow penumbral region. The explicit modeling of the beam's divergence had the greatest effect on penumbra and valley dose, out to ~ 200 μm from the center of a 50 μm microbeam, where the results are shown in Fig. 1.16.[149] The asymmetry of the stacked MSC (Fig. 1.8) affected the FWHM of off-centre microbeams by up to 4 μm. Finally, for a symmetric MSC, the superposition of a single microbeam dose distribution to achieve a full array dose distribution was deemed to be sufficient.[149]

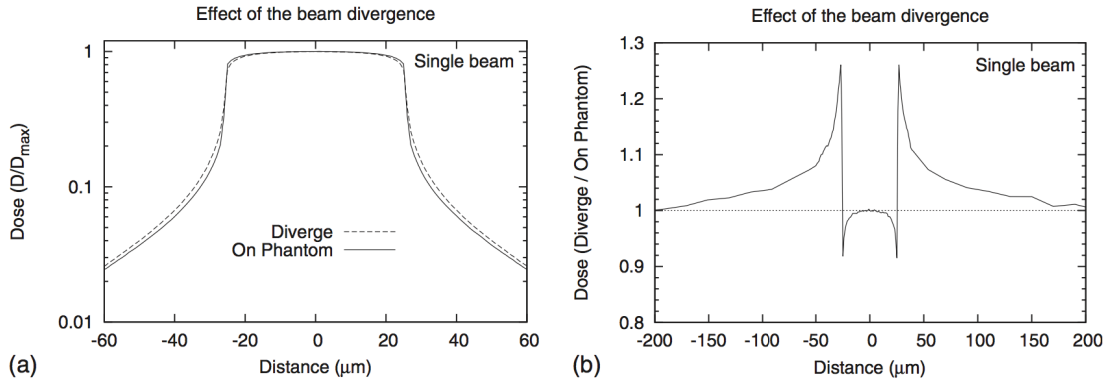

Figure 1.16 The impact of modeling beam divergence (42 m source to phantom distance) versus parallel photons incident on the phantom surface for a 50 μm wide microbeam. (Image reproduced from: H. Nettelbeck *et al.*, "Microbeam radiation therapy: A Monte Carlo study of the influence of the source, multislit collimator, and beam divergence on microbeams," Med. Phys. **36**, 447-456 (2009)[149] with permission from the American Association of Physicists in Medicine and the author).

Martinez-Rovira *et al.* moved further from the ideal microbeam model by developing a model specific to the ESRF ID17 beamline.[137] The beamline model followed the photons from source to patient position using a synchrotron ray-tracing program and Monte Carlo simulations, to create a phase space file for subsequent Monte Carlo simulations. The model was validated by comparing the computed dose distributions against measurements using Gafchromic® film (Ashland Specialty Ingredients, Inc., Bridgewater, NJ). The phase space file created by Martinez-Rovira *et al.* was further analyzed by Bartzsch *et al.* (2014), and demonstrated that Monte Carlo

simulations using the phase space information versus without resulted in an approximate 10% increase in the valley dose.[130] Differences were attributed to a non-uniform flux profile across the uncollimated beam, the geometrical effects of the beam traversing the edges of the MSC, and the inadequate absorption of the MSC's attenuating material.[130] The authors concluded that the ideal microbeam is not an adequate approximation for MRT dose distribution calculations.[130]

The beamline model developed by Martinez-Rovira *et al.*[137] was incorporated into a Monte Carlo-based treatment planning system (TPS).[138] The optimized and parallelized TPS computes dose distribution based on voxelized CT data for upcoming clinical trials on pets in a reasonable time (~ 1 day, 60 cores).[138] An alternative analytical approach to an MRT TPS that could reduce computation times down to a few minutes has been developed by Bartzsch and Oelfke (2013).[129] The authors established an analytic approach to the calculation of dose kernels for 40 – 200 keV photons, and validated them by comparing to Monte Carlo generated dose kernels using the Geant4 toolkit and showed a deviation of the analytically and Monte Carlo-calculated dose kernels of less than 5% for doses greater than 1% of the maximum dose.[129]

1.3.2 Experimental MRT dosimetry

Experimental dosimetry for MRT is often separated into two domains. First, absolute or reference dosimetry is determined in the non-collimated x-ray beam. Although the demands for spatial resolution and dynamic range are relaxed in broad beam dosimetry, the dosimeter's energy dependence and response to high flux must be suitable for the synchrotron x-ray beam. Second, a relative or reference dosimetric system to characterize the peak and valley doses in the collimated beam is required.

1.3.2.1 Broad beam synchrotron dosimetry

Even before collimation, the synchrotron photon beam used for MRT experimentation is wide in the horizontal direction, but narrow (< 1 cm) in the vertical direction due to synchrotron radiation's low natural divergence (described further in Chapter 2). The x-ray beam is often collimated in the vertical direction (to < 1 mm) to

reduce the non-uniformity of the roughly Gaussian-shaped beam. The phantom or animal is scanned vertically through the beam to increase the effective field size. Dosimeters in the homogeneous field must withstand the high dose rates, and must have a correctable energy response. Additionally, in preparation for clinical trials, they must provide an absolute or reference measurement traceable to a primary standards institute.

At the European Synchrotron Radiation Facility (ESRF), cavity ionization chambers are used for broad beam dosimetry by vertically scanning the chamber through the collimated field.[57,150] Cavity ionization chambers measure the charge produced as x-rays interact with the cavity medium (usually air), which can be related to dose under specified calibration conditions. Ionization chamber dosimetry is accurate, reproducible, and provides real-time measurements. For low energy photons, the energy dependence of an ion chamber is an important consideration. This energy response is a function of the chamber's material construction, most specifically that of the wall and central electrode. The spatial resolution of an ion chamber depends on its geometry, particularly the size of its active volume. The dynamic range of an ion chamber is limited by the range of the associated electrometer. The greatest challenge in cavity chamber dosimetry for microbeam radiation therapy conditions is the reduction in ion collection efficiency in the high dose rate synchrotron beam. Ion recombination corrections can be determined experimentally (*e.g.*, two-voltage method[151]), or theoretically with Boag's treatment.[152]

The dose rate on the Australian Synchrotron's imaging and medical beamline has been investigated using two free-air ionization chambers.[153] Free-air ionization chamber dosimetry is performed by directly measuring exposure, and converting that to dose using the average energy required to produce an ion pair in air. The greatest advantage of using a free air ionization chamber over a cavity chamber is that there is no calibration required, and it thus provides an absolute dose measurement.[152] However, a free air ionization chamber requires a number of experimentally and theoretically determined correction factors. Additionally, like for cavity ionization chambers, at sufficiently high dose rates recombination corrections become increasingly difficult to apply accurately.

Alanine has also been used as a dosimeter for the high intensity synchrotron x-ray beam at the European Synchrotron Radiation Facility (ESRF).[150,154] Alanine dosimeters consist of finely dispersed microcrystals of the amino acid alanine suspended in a binder,

typically available in the form of pellets or rods of varying sizes. Upon exposure to ionizing radiation the chemical becomes de-aminated, leaving a free radical.[155] The absorbed dose is proportional to the concentration of these unpaired electrons, and is quantified via electron spin resonance (ESR) or electron paramagnetic resonance (EPR) spectrometry.[155] Alanine is an appropriate dosimeter for broad beam dosimetry in synchrotron radiation under the conditions used for microbeam radiation therapy because it can cover wide dose ranges (~ 0.5 – 100,000 Gy)[155-157] and is unaffected by the extreme dose rates.[155,158] Additionally, alanine dosimetry is trusted; EPR readouts of the dosimeters are used as a dosimetric reference standard by several institutions.[159] The spatial resolution of the dosimeter is limited by the smallest available pellet size, which is approximately 1 mm in the smallest dimension.[160,161] The greatest disadvantage of the dosimeter is its energy dependence. In Waldeland and Malinen (2011), the experimental and Monte Carlo-predicted energy response correction of an alanine dosimeter was determined for medium-energy x-rays, and clinical electrons and photons.[162] The dose-to-water energy response (with reference to Co-60 γ-rays) was found to be between 0.725 and 0.935 for x-rays between 50 and 200 kV.[162] Additionally, the dosimeter readout is typically achieved by mailing the dosimeter to the vendor, which is an expensive and delayed process.

Finally, graphite calorimetry has been assessed for the absolute dosimetry on the Imaging and Medical Beamline (IMBL) at the Australian Synchrotron.[163] Calorimetry allows absolute dosimetry by equating a rise in temperature to energy deposition after exposure to ionizing radiation.[164,165] The major advantage of calorimeters is that they require no dose rate correction; for this reason, calorimeters may prove more accurate than free air chambers at the high dose rates possible in a synchrotron x-ray beam. Calorimeters do require a conversion from absorbed dose to graphite to absorbed dose in water, which can be determined from Monte Carlo calculations based on the energy spectrum of the photon beam.[163] After this conversion, the graphite calorimetry results of Harty *et al.* agreed within 1 – 3 % to measurements taken with a free air ionization chamber.[163]

1.3.2.2 Microbeam dosimetry

Like the broad beam dosimeters, an appropriate dosimetry system for MRT must be able to withstand dose rates up to approximately 20,000 Gy/s, and must have a well-understood energy dependence in the energy range of interest. In microbeam dosimetry, a potential complication in terms of energy dependence is introduced due to a slight shift in energy spectrum between the x-rays depositing dose in the peak versus the valley regions.[133] In addition to the requirements common to broad beam dosimetry, additionally a very high spatial resolution (on the order of 1 μm) is required to characterize the dose distribution in, not only the peak and valley regions, but also in the high dose gradient region at the interface of these two regions. Finally, a dosimeter for microbeams must be able to measure the high doses in the peak region (up to ~ 1000 Gy) and the lower doses in the valley regions (down to approximately 1 Gy). A thorough review of potential dosimeters for MRT is given by Bräuer-Krisch *et al.* (2010);[150] selected dosimeters will be presented next.

Gafchromic radiochromic film (Ashland Specialty Ingredients, Inc., Bridgewater, NJ) has many advantages for MRT dosimetry, and has been used in this field for many years. Upon exposure to ionizing radiation, radiochromic film undergoes a self-developing color change due to a chemical change in its radiosensitive layer. A quantitative measure of the net optical density is achieved through digitization with a transmission densitometer, a flat bed scanner or a spectrophotometer. The optical density can be related to absorbed dose based on the sensitometric curve of the radiochromic film. The greatest advantage of radiochromic film for MRT is its very high spatial resolution. The effective spatial resolution is usually limited by the digitization process and not by the film itself. Different types of film have different sensitivities that are appropriate for the wide range of doses in a microbeam array dose distribution. In previous studies Gafchromic EBT film (now EBT2 and EBT3 models available), with a dose range of ~ 0.01 – 40 Gy,[166,167] has been used to measure lower doses. Higher doses have been measured with Gafchromic HD810 and the newer HDV2, which has a dose range of ~ 10 – 1000 Gy.[168,169] The peak-to-valley dose ratio (PVDR) has been measured with film in two ways: pieces of the higher-sensitivity EBT2 film and the lower sensitivity HD-810 film are placed back to back to simultaneously measure the valley

dose with EBT2 and the peak dose with HD-810.[128] Alternatively, the peak and valley dose can both be measured with HD-810 film if the peak dose is measured, then a second exposure is taken, scaled up by the expected PVDR, to measure the valley dose.[170] There is little published on the dose rate dependence of radiochromic film response, particularly at the high dose rates produced at a synchrotron. However, to this point there has been no evidence of a dose rate effect causing problems. Other advantages of radiochromic film are that it is relatively simple to handle and is relatively inexpensive.

There are some limitations of radiochromic film for MRT dosimetry. Although radiochromic films are nearly tissue equivalent (the effective atomic number of HD-810 is between 6.0 and 6.5[171] and is 6.98 for EBT[172]), there is an energy dependence at low energies. Varying values are given for the energy dependence of EBT,[172] EBT2,[173,174] and EBT3,[175,176] but all indicate the strongest energy dependence in the energy range of approximately 20 – 100 keV, which is highly relevant for MRT. With a 30% decrease in response from 1710 to 28 keV, a greater energy dependence was demonstrated for HD-810.[177] Another limitation is the loss in spatial resolution through digitization. A single sheet of radiochromic film has non-uniformity of up to 7% for HD-810,[177] while EBT3 has a uniformity of better than 3%.[166] Finally, while valuable qualitative measurements can be taken at the time of irradiation, quantitative measurements should be delayed by at least 8 hours to allow the film response to stabilize.[178]

Research into the use of semiconductors for MRT dosimetry has also been ongoing for over a decade.[133,179-183] Early studies investigated the use of MOSFET (metal oxide semiconductor field effect transistor) chips in the "edge-on" orientation to achieve the high resolution (< 1 μm) required for MRT.[182] MOSFETs also provide a nearly instantaneous "online" reading, and their sensitivity can be adjusted based on the application.[181] Although they can demonstrate radiation damage after some time, they show no dose rate dependence.[181] There are, however, two major drawbacks of MOSFETs for MRT dosimetry. First, because they are composed primarily of silicon, they exhibit a strong energy dependence at the low energies of interest. Additionally, the alignment of the chip to achieve high resolution is difficult and time-consuming.[182] PVDR measurements using edge-on MOSFETS were within 5% of the Monte Carlo calculated values for several depths within a PMMA phantom.[182] Discrepancies were

attributed to the energy dependence of the detector and the change in energy spectrum with depth.[182]

An alternative semiconductor device is the silicon strip detector under development specifically for MRT dosimetry.[184-186] The silicon strip detector is one component in the two-module X-Tream quality assurance system (Fig. 1.17(a, b)).[186] The detector scans a microstrip silicon diode laterally across the microbeam array and calculates the peak and valley doses and positions, the PVDR, and the peak shape. The strip thickness (10 μm) dictates the spatial resolution of the system, which provides sufficient resolution for measurements in the peak and valley regions, but not the high dose gradient regions. The device has a large dynamic range (10 – 50000 Gy),[150] satisfying the requirements for the measurement of both peak and valley doses. Another advantage is that the design allows the detector to measure dose distributions in a water tank or Solid Water phantoms.[186] Like MOSFETS, the greatest inherent disadvantage of the silicon strip detector is its high energy dependence at low energies. A measurement of the PVDR at the ESRF with depth in PMMA, compared to Monte Carlo calculated values, is shown in Fig. 1.17(c).[184] The results show similar trends between the theoretical and experimental values, but the experimental PVDRs were 4.5 times less than the calculated values, which may be attributed to recombination effects, energy dependence, and partial volume effects.[184] The second component of the X-Tream system is a real-time beam monitoring system positioned between the MSC and the patient during treatment. It monitors the peak and valley flux across the array, and generates a trigger to disrupt the synchrotron beam if there is a reduction in the quality of the microbeam array distribution.[186]

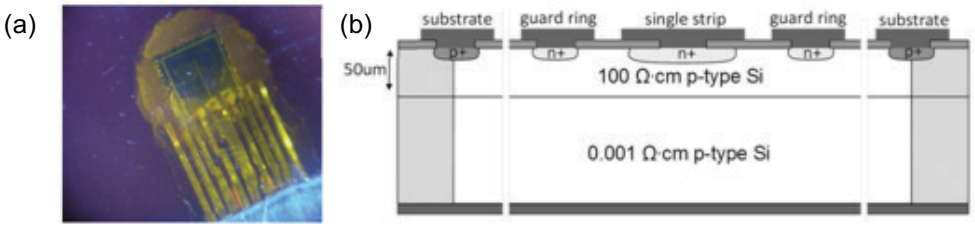

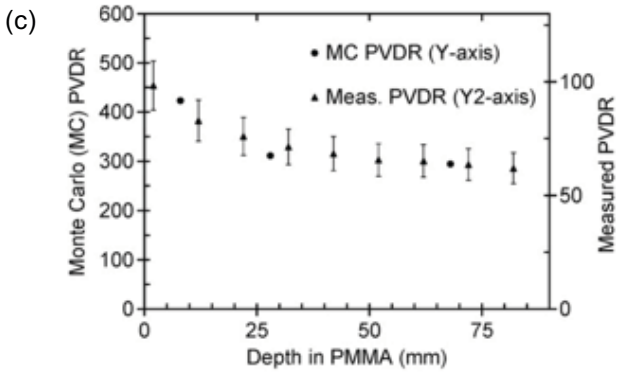

Figure 1.17 (a) A close up of the single microstrip silicon diode detector, and (b) a schematic of the detector's cross-section (Images reproduced from: M. Petasecca *et al.*, "X-Tream: a novel dosimetry system for Synchrotron Microbeam Radiation Therapy," Journal of Instrumentation **7**, P07022 (2012) [186] with permission from the copyright holder and author.) (c) The PVDR measured with the Si strip detector compared with Monte Carlo calculations of the PVDR (Reprinted from Radiation Measurements, **46**, M.L.F. Lerch *et al.*, "Dosimetry of intensive synchrotron microbeams," 1560-1565, Copyright 2011, with permission from Elsevier. [184]).

Like radiochromic film, PRESAGE radiochromic plastic undergoes a color change following exposure to ionizing radiation. Combining PRESAGE phantoms with an optical computed tomography (CT) readout system has been investigated as a potential three-dimensional MRT dosimeter.[187,188] The degree of color change, quantified as the change in optical density, is linear with the absorbed dose.[187] PRESAGE has a dose range appropriate for MRT (~ 10 – 500 Gy).[150] However, the energy dependence of PRESAGE in the kilovoltage energy range requires correction, and its magnitude changes with different formulations.[189] The dosimeter is also limited by the optical CT readout technique, which has shown a maximum spatial resolution of 37 μm thus far.[190] Annabell *et al.* achieved an extremely high spatial resolution (78 nm) using confocal fluorescence readout of PRESAGE gel after microbeam irradiations.[191] The authors claimed that PRESAGE has better intrinsic spatial resolution than Gafchromic film, and is thus a superior method of characterizing MRT dose distributions.[191]

Fluorescent nuclear track detectors (FNTDs) are a new type of luminescent detector made of fluorescent aluminum oxide single crystals doped with carbon and magnesium.[192,193] The FNTDs are read with a scanning confocal fluorescence readout

system (0.85 μm resolution).[194] The dose response to gamma and x-rays is linear up to nearly 30 Gy, and doesn't completely saturate until 100 Gy.[194] They can also withstand dose rates up to 10^8 Gy/s.[150] The detectors are simple to handle in that they are not light sensitive, they do not fade with time, and they are thermally stable up to 600°C. A drawback of these detectors is their over-response with respect to water.[150]

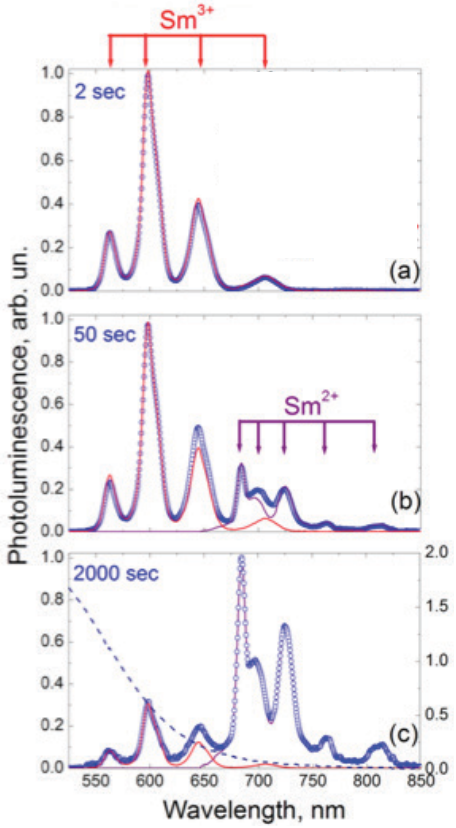

Figure 1.18 The photoluminescence spectra after x-ray irradiations of the SM-doped fluorophosphates glass lasting 2, 50 and 200 seconds. (Reprinted with permission from G. Okada *et al.*, "Spatially resolved measurement of high doses in microbeam radiation therapy using samarium doped fluorophosphate glasses," Appl. Phys. Lett. **99**, 121105 (2011).[195] Copyright 2011, AIP Publishing LLC.)

Another high spatial resolution dosimeter relying on fluorescence confocal microscopy readout is samarium-doped fluorophosphate or fluoroaluminate glasses, or glass ceramic.[195-198] The dosimeter is based on the conversion of the oxidation state of samarium (Sm^{3+} to Sm^{2+}) upon exposure to ionizing radiation. The change in the oxidation state leads to changes in the photoluminescence spectrum of the irradiated material (Fig. 1.18). The intensity of the lines is proportional to the concentration of their

respective ions, which can be related to the amount of dose delivered to the dosimeter. The dynamic range of the materials depends on their make up and doping levels, but a range of up to 0.1 – 10000 Gy is possible.[197,198] The ability to characterize microbeam array dose distributions with a spatial resolution in the micrometer range has been demonstrated.[195,197] Additionally, the detector can be reused after thermal annealing or exposure to ultraviolet light.[197,198] A potential draw-back is the lack of tissue-equivalence and energy dependence of the material (not yet quantified).

1.4 Thesis outline

The research presented in this thesis was motivated by the development of two biomedical beamlines at the Canadian Light Source (CLS). These BioMedical Imaging and Therapy (BMIT) beamlines were constructed to provide the opportunity for novel imaging and therapy research, including MRT, in Canada. Initially, our research plans focused on the development of dosimetry for MRT on the higher energy, higher flux BMIT beamline (05ID-2) based on the expectation of a forthcoming MRT research program on the beamline. Long delays limited access to this beamline, but the lower energy, lower flux BMIT beamline allowed our research, with shifted and broadened goals, to continue.

This chapter provided the context and background on microbeam radiation therapy necessary to motivate our work. In Chapter 2, a general description of a synchrotron light source and synchrotron radiation is provided. Additionally, an overview of the Canadian Light Source (CLS) and its two BioMedical Imaging and Therapy (BMIT) beamlines, where the experimental work has taken place, is given. In Chapter 3, a general description of the BMIT beamlines' characteristics, as determined theoretically and experimentally, are described. The information in this chapter formed an important basis for the rest of the thesis work. Chapters 4 and 5 will discuss broad beam dosimetry on the 05B1-1 BMIT beamline using a free air ionization chamber and cavity ionization chamber, respectively. This work applied clinical dosimetric frameworks to the pre-clinical radiation environment at the BMIT beamlines. Chapter 6 will describe theoretical dosimetry for the 05ID-2 beamline using Monte Carlo simulations in cubic

head phantoms. The Monte Carlo-generated dose distributions were used to evaluate potential dose-volume metrics for MRT. This work demonstrated the potential for the BMIT 05ID-2 to host MRT research. Finally, Chapter 7 will present a biological study that employs γ-H2AX immunostaining and cell morphology to investigate the DNA damage response and cell fate, in terms of apoptosis and growth arrest, in human cell cultures following microbeam irradiations. Chapter 8 is a concluding chapter to the thesis.

1.5 References

[1] Canadian Cancer Society's Advisory Committee on Cancer Statistics, *Canadian Cancer Statistics 2014* (Canadian Cancer Society, Toronto, ON, 2014).

[2] Canadian Cancer Society, "Childhood cancer," http://www.cancer.ca/en/cancer-information/cancer-type/childhood-cancer-information/treatment/radiation-therapy/ Accessed 4/19/2015.

[3] F.M. Khan, *The Physics of Radiation Therapy*, 4th ed. (Lippincott Williams & Wilkins, Philadelphia, PA, USA, 2010).

[4] E.J. Hall and A.J. Giaccia, *Radiobiology for the Radiologist*, 6th Edition ed. (Lippincott Williams & Wilkins, Philadelphia, PA, USA, 2006).

[5] C. Regaud and R. Ferroux, "Discordance of the effects of X rays of one part in the skin and of the other part in the testicle, by the fraction of the dosage: Reduction of the efficiency in the skin." C. R. Seances Soc. Biol. Fil. **97**, 431-434 (1927).

[6] H. Coutard, "Principles of X ray therapy of malignant diseases," Lancet **2**, 1-8 (1934).

[7] H.S. Kaplan, "Basic Principles in Radiation Oncology," Cancer **39**, 689-693 (1977).

[8] K.M. Prise, G. Schettino, M. Folkard, K.D. Held, "New insights on cell death from radiation exposure," Lancet Oncology **6**, 520-528 (2005).

[9] K.M. Prise and J.M. O'Sullivan, "Radiation-induced bystander signalling in cancer therapy," Nature Reviews Cancer **9**, 351-360 (2009).

[10] C. Mothersill and C. Seymour, "Radiation-induced bystander effects: Past history and future directions," Radiat. Res. **155**, 759-767 (2001).

[11] S. Wolff, "The adaptive response in radiobiology: Evolving insights and implications," Environ. Health Perspect. **106**, 277-283 (1998).

[12] M.C. Joiner, B. Marples, P. Lambin, S.C. Short, I. Turesson, "Low-dose hypersensitivity: Current status and possible mechanisms," International Journal of Radiation Oncology Biology Physics **49**, 379-389 (2001).

[13] G.W. Morgan and S.N. Breit, "Radiation and the Lung - a Reevaluation of the Mechanisms Mediating Pulmonary Injury," International Journal of Radiation Oncology Biology Physics **31**, 361-369 (1995).

[14] K. Camphausen, M.A. Moses, C. Menard, M. Sproull, W.D. Beecken, J. Folkman, M.S. O'Reilly, "Radiation abscopal antitumor effect is mediated through p53," Cancer Res. **63**, 1990-1993 (2003).

[15] A.J. Vanderkogel, "Dose-Volume Effects in the Spinal-Cord," Radiotherapy and Oncology **29**, 105-109 (1993).

[16] J.W. Hopewell and K.R. Trott, "Volume effects in radiobiology as applied to radiotherapy," Radiotherapy and Oncology **56**, 283-288 (2000).

[17] B. Emami, J. Lyman, A. Brown, L. Coia, M. Goitein, J.E. Munzenrider, B. Shank, L.J. Solin, M. Wesson, "Tolerance of Normal Tissue to Therapeutic Irradiation," International Journal of Radiation Oncology Biology Physics **21**, 109-122 (1991).

[18] R.J. Yaes and A. Kalend, "Local Stem-Cell Depletion Model for Radiation Myelitis," Math. Comput. Model. **11**, 1041-1046 (1988).

[19] T. Herrmann, M. Baumann, L. Voigtmann, A. Knorr, "Effect of irradiated volume on lung damage in pigs," Radiotherapy and Oncology **44**, 35-40 (1997).

[20] H.R. Withers, J.M.G. Taylor, B. Maciejewski, "Treatment Volume and Tissue Tolerance," International Journal of Radiation Oncology Biology Physics **14**, 751-759 (1988).

[21] W. Zeman, H.J. Curtis, E.L. Gebhard, W. Haymaker, "Tolerance of Mouse-Brain Tissue to High-Energy Deuterons," Science **130**, 1760-1761 (1959).

[22] C.P. Baker, R.G. Woodley, H.J. Curtis, W. Zeman, "Design and Calibration of a Deuteron Microbeam for Biological Studies," Radiat. Res. **15**, 489-& (1961).

[23] W. Zeman, C.P. Baker, H.J. Curtis, "Histopathologic Effect of High-Energy-Particle Microbeams on Visual Cortex of Mouse Brain," Radiat. Res. **15**, 496-514 (1961).

[24] J.M. Ordy, W. Zeman, T. Samorajski, H.J. Curtis, R.L. Collins, "Long-Term Pathologic and Behavioral Changes in Mice After Focal Deuteron Irradiation of Brain," Radiat. Res. **20**, 30-& (1963).

[25] H.J. Curtis, "The use of deuteron microbeam for simulating the biological effects of heavy cosmic-ray particles." Radiation research.Supplement **7**, 250-7 (1967).

[26] W.E. Straile and H.B. Chase, "Use of Elongate Microbeams of X-Rays for Simulating Effects of Cosmic Rays on Tissues - a Study of Wound Healing and Hair Follicle Regeneration," Radiat. Res. **18**, 65-& (1963).

[27] J.A. Laissue, H. Blattmann, D.N. Slatkin, "Alban Kohler (1874-1947): Inventor of grid therapy," Zeitschrift Fur Medizinische Physik **22**, 90-99 (2012).

[28] H. Marks, "Clinical Experience with Irradiation through a Grid," Radiology **58**, 338-342 (1952).

[29] F. Liberson, "The Value of a Multi-perforated Screen in Deep X-ray Therapy," Radiology **20**, 186-195 (1933).

[30] B. Jolles, "Radiotherapy of Accessible Malignant Tumours by Alternating Chess-Board Method," Lancet **257**, 603-606 (1949).

[31] W.V. Tenzel, "Experience with Grid Therapy," Radiology **59**, 399-408 (1952).

[32] M. Mohiuddin, D.L. Curtis, W.T. Grizos, L. Komarnicky, "Palliative Treatment of Advanced Cancer using Multiple Nonconfluent Pencil Beam Radiation - a Pilot-Study," Cancer **66**, 114-118 (1990).

[33] J.E. Reiff, M.S. Huq, M. Mohiuddin, N. Suntharalingam, "Dosimetric Properties of Megavoltage Grid Therapy," International Journal of Radiation Oncology Biology Physics **33**, 937-942 (1995).

[34] M. Mohiuddin, M. Fujita, W.F. Regine, A.S. Megooni, G.S. Ibbott, M.M. Ahmed, "High-dose spatially-fractionated radiation (GRID): A new paradigm in the management of advanced cancers," International Journal of Radiation Oncology Biology Physics **45**, 721-727 (1999).

[35] R.D. Zwicker, A. Meigooni, M. Mohiuddin, "Therapeutic advantage of grid irradiation for large single fractions," International Journal of Radiation Oncology Biology Physics **58**, 1309-1315 (2004).

[36] J.A. Penagaricano, E.G. Moros, V. Ratanatharathorn, Y. Yan, P. Corry, "Evaluation of Spatially Fractionated Radiotherapy (Grid) and Definitive Chemoradiotherapy with Curative Intent for Locally Advanced Squamous Cell Carcinoma of the Head and Neck: Initial Response Rates and Toxicity," International Journal of Radiation Oncology Biology Physics **76**, 1369-1375 (2010).

[37] S. Sathishkumar, B. Boyanovsky, A.A. Karakashian, K. Rozenova, N.V. Giltiay, M. Kudrimoti, M. Mohiuddin, M.M. Ahmed, M. Nikolova-Karakashian, "Elevated sphingomyelinase activity and ceramide concentration in serum of patients undergoing high dose spatially fractionated radiation treatment - Implications for endothelial apoptosis," Cancer Biology & Therapy **4**, 979-986 (2005).

[38] R. Siegel, D. Naishadham, A. Jemal, "Cancer statistics, 2012," CA Cancer. J. Clin. **62**, 10-29 (2012).

[39] B. Timmermann, R.D. Kortmann, J. Kuhl, S. Rutkowski, K. Dieckmann, C. Meisner, M. Bamberg, "Role of radiotherapy in anaplastic ependymoma in children under age of 3 years: Results of the prospective German brain tumor trials HF-SKK 87 and 92," Radiotherapy and Oncology **77**, 278-285 (2005).

[40] S. Rutkowski, N.U. Gerber, K. von Hoff, A. Gnekow, U. Bode, N. Graf, F. Berthold, G. Henze, J.E. Wolff, M. Warmuth-Metz, N. Soerensen, A. Emser, H. Ottensmeier, F. Deinlein, P.G. Schlegel, R.D. Kortmann, T. Pietsch, J. Kuehl, German Pediatric Brain Tumor Study Group, "Treatment of early childhood medulloblastoma by postoperative chemotherapy and deferred radiotherapy," Neuro Oncol. **11**, 201-210 (2009).

[41] T.S. Reimers, S. Ehrenfels, E.L. Mortensen, M. Schmiegelow, S. Sonderkaer, H. Carstensen, K. Schmiegelow, Muller J., "Cognitive deficits in long-term survivors of childhood brain tumors: Identification of predictive factors," Med. Pediatr. Oncol. **40**, 26-34 (2003).

[42] L. Ellenberg, L. Qi, G. Gioia, Y. Yasui, R.J. Packer, A. Mertens, S.S. Donaldson, M. Stovall, N. Kadan-Lottick, G. Armstrong, L.L. Robison, L.K. Zeltzer, "Neurocognitive status in long-term survivors of childhood CNS malignancies: a report from the childhood cancer survivor study," Neuropsychology **23**, 705-717 (2009).

[43] R.K. Mulhern, H.A. White, J.O. Glass, L.E. Kun, L. Leigh, S.J. Thompson, W.E. Reddick, "Attentional functioning and white matter integrity among survivors of malignant brain tumors of childhood," Journal of the International Neuropsychological Society **10**, 180-189 (2004).

[44] R.K. Mulhern, T.E. Merchant, A. Gajjar, W.E. Reddick, L.E. Kun, "Late neurocognitive sequelae in survivors of brain tumours in childhood," Lancet Oncology **5**, 399-408 (2004).

[45] E. Suc, C. Kalifa, R. Brauner, J.L. Habrand, M.J. Terrier-Lacombe, G. Vassal, J. Lemerle, "Brain tumours under the age of three. The price of survival. A retrospective study of 20 long-term survivors," Acta Neurochir. (Wien) **106**, 93-98 (1990).

[46] H.P. Wagner, "Cancer in childhood and supportive care," Supportive Care in Cancer **7**, 293-294 (1999).

[47] K. Ribi, C. Relly, M.A. Landolt, F.D. Alber, E. Boltshauser, M.A. Grotzer, "Outcome of medulloblastoma in children: Long-term complications and quality of life," Neuropediatrics **36**, 357-365 (2005).

[48] T.E. Merchant, H.M. Conklin, S. Wu, R.H. Lustig, X. Xiong, "Late effects of conformal radiation therapy for pediatric patients with low-grade glioma: prospective evaluation of cognitive, endocrine, and hearing deficits," J. Clin. Oncol. **27**, 3691-3697 (2009).

[49] J.H. Silber, J. Radcliffe, V. Peckham, G. Perilongo, P. Kishnani, M. Fridman, J.W. Goldwein, A.T. Meadows, "Whole-brain irradiation and decline in intelligence: the influence of dose and age on IQ score," J. Clin. Oncol. **10**, 1390-1396 (1992).

[50] S.L. Palmer, O. Goloubeva, W.E. Reddick, J.O. Glass, A. Gajjar, L. Kun, T.E. Merchant, R.K. Mulhern, "Patterns of intellectual development among survivors of pediatric medulloblastoma: A longitudinal analysis," Journal of Clinical Oncology **19**, 2302-2308 (2001).

[51] M.D. Ris, R. Packer, J. Goldwein, D. Jones-Wallace, J.M. Boyett, "Intellectual outcome after reduced-dose radiation therapy plus adjuvant chemotherapy for medulloblastoma: a Children's Cancer group study," J. Clin. Oncol. **19**, 3470-76 (2001).

[52] J.E. Schreiber, J.G. Gurney, S.L. Palmer, J.K. Bass, M. Wang, S. Chen, H. Zhang, M.L. Chapieski, M.J. Bonner, D.J. Mabbott, S.J. Knight, C.L. Armstrong, R. Boyle, A. Gajjar, "Examination of risk factors for intellectual and academic outcomes following treatment for pediatric medulloblastoma," Neuro. Oncol. **16**, 1129-36 (2014).

[53] S. Rutkowski, N.U. Gerber, K. von Hoff, A. Ghekow, U. Bode, N. Graf, F. Berthold, G. Henze, J.E.A. Wolff, M. Warmuth-Metz, N. Soerensen, A. Emser, H. Ottensmeier, F. Deinlein, P.-. Schlegel, R.-. Kortmann, T. Pietsch, J. Kuehl, "Treatment of early childhood medulloblastoma by postoperative chemotherapy and deferred radiotherapy," Neuro. Oncol. **11**, 201-210 (2009).

[54] D.N. Slatkin, P. Spanne, F.A. Dilmanian, M. Sandborg, "Microbeam Radiation Therapy," Med. Phys. **19**, 1395-1400 (1992).

[55] D.N. Slatkin, P. Spanne, F.A. Dilmanian, J.O. Gebbers, J.A. Laissue, "Subacute Neuropathological Effects of Microplanar Beams of X-Rays from a Synchrotron Wiggler," Proc. Natl. Acad. Sci. U. S. A. **92**, 8783-8787 (1995).

[56] J.A. Laissue, G. Geiser, P.O. Spanne, F.A. Dilmanian, J.O. Gebbers, M. Geiser, X.Y. Wu, M.S. Makar, P.L. Micca, M.M. Nawrocky, D.D. Joel, D.N. Slatkin, "Neuropathology of ablation of rat gliosarcomas and contiguous brain tissues using a microplanar beam of synchrotron-wiggler-generated X rays," International Journal of Cancer **78**, 654-660 (1998).

[57] E. Braeuer-Krisch, R. Serduc, E.A. Siegbahn, G. Le Duc, Y. Prezado, A. Bravin, H. Blattmann, J.A. Laissue, "Effects of pulsed, spatially fractionated, microscopic synchrotron X-ray beams on normal and tumoral brain tissue," Mutat. Res. - Rev. Mut. Res. **704**, 160-166 (2010).

[58] F.A. Dilmanian, G.M. Morris, G. Le Duc, X. Huang, B. Ren, T. Bacarian, J.C. Allen, J. Kalef-Ezra, I. Orion, E.M. Rosen, T. Sandhu, P. Sathe, X.Y. Wu, Z. Zhong, H.L. Shivaprasad, "Response of avian embryonic brain to spatially segmented X-ray microbeams," Cell Mol. Biol. **47**, 485-493 (2001).

[59] D.W. Archer, "Collimator for producing an array of microbeams," United States Patent **813,547** (1998).

[60] E. Brauer-Krisch, A. Bravin, L. Zhang, E. Siegbahn, J. Stepanek, H. Blattmann, D.N. Slatkin, J.O. Gebbers, M. Jasmin, J.A. Laissue, "Characterization of a tungsten/gas multislit collimator for microbeam radiation therapy at the European Synchrotron Radiation Facility," Rev. Sci. Instrum. **76**, 064303 (2005).

[61] E. Braeuer-Krisch, H. Requardt, T. Brochard, G. Berruyer, M. Renier, J.A. Laissue, A. Bravin, "New technology enables high precision multislit collimators for microbeam radiation therapy," Rev. Sci. Instrum. **80**, 074301 (2009).

[62] J.A. Laissue, H. Blattmann, M. Di Michiel, D.N. Slatkin, N. Lyubimova, R. Guzman, W. Zimmermann, S. Birrer, T. Bley, P. Kircher, R. Stettler, R. Fatzer, A. Jaggy, H.M. Smilowitz, E. Brauer, A. Bravin, G. Le Duc, C. Nemoz, M. Renier, W. Thomlinson, J. Stepanek, H.P. Wagner, "The weanling piglet cerebellum: a surrogate for tolerance to MRT (microbeam radiation therapy) in pediatric neuro-oncology," Penetrating Radiation Systems and Applications III **4508**, 65-73 (2001).

[63] F.A. Dilmanian, T.M. Button, G. Le Duc, N. Zhong, L.A. Pena, J.A.L. Smith, S.R. Martinez, T. Bacarian, J. Tammam, B. Ren, P.M. Farmer, J. Kalef-Ezra, P.L. Micca, M.M. Nawrocky, J.A. Niederer, F.P. Recksiek, A. Fuchs, E.M. Rosen, "Response of rat intracranial 9L gliosarcoma to microbeam radiation therapy," Neuro-oncology **4**, 26-38 (2002).

[64] F.A. Dilmanian, G.M. Morris, N. Zhong, T. Bacarian, J.F. Hainfeld, J. Kalef-Ezra, L.J. Brewington, J. Tammam, E.M. Rosen, "Murine EMT-6 carcinoma: High therapeutic efficacy of microbeam radiation therapy," Radiat. Res. **159**, 632-641 (2003).

[65] H.M. Smilowitz, H. Blattmann, E. Brauer-Krisch, A. Bravin, M. Di Michiel, J.-. Gebbers, A.L. Hanson, N. Lyubimova, D.N. Slatkin, J. Stepanek, J.A. Laissue, "Synergy of gene-mediated immunoprophylaxis and microbeam radiation therapy for advanced intracerebral rat 9L gliosarcomas," J. Neurooncol. **78**, 135-143 (2006).

[66] R. Serduc, P. Verant, J.C. Vial, R. Farion, L. Rocas, C. Remy, T. Fadlallah, E. Brauer, A. Bravin, J. Laissue, H. Blattmann, B. Van der Sanden, "In vivo two-photon microscopy study of short-term effects of microbeam irradiation on normal mouse brain microvasculature," International Journal of Radiation Oncology Biology Physics **64**, 1519-1527 (2006).

[67] P. Regnard, G. Le Duc, E. Brauer-Krisch, I. Tropres, E.A. Siegbahn, A. Kusak, C. Clair, H. Bernard, D. Dallery, J.A. Laissue, A. Bravin, "Irradiation of intracerebral 9L gliosarcoma by a single array of microplanar x-ray beams from a synchrotron: balance between curing and sparing," Phys. Med. Biol. **53**, 861-878 (2008).

[68] P. Regnard, E. Brauer-Krisch, I. Tropres, J. Keyrilainen, A. Bravin, G. Le Duc, "Enhancement of survival of 9L gliosarcoma bearing rats following intracerebral delivery of drugs in combination with microbeam radiation therapy," Eur. J. Radiol. **68**, S151-S155 (2008).

[69] R. Serduc, A. Bouchet, E. Braeuer-Krisch, J.A. Laissue, J. Spiga, S. Sarun, A. Bravin, C. Fonta, L. Renaud, J. Boutonnat, E.A. Siegbahn, F. Esteve, G. Le Duc, "Synchrotron microbeam radiation therapy for rat brain tumor palliation-influence of the microbeam width at constant valley dose," Phys. Med. Biol. **54**, 6711-6724 (2009).

[70] J.C. Crosbie, R.L. Anderson, K. Rothkamm, C.M. Restall, L. Cann, S. Ruwanpura, S. Meachem, N. Yagi, I. Svalbe, R.A. Lewis, B.R.G. Williams, P.A.W. Rogers, "Tumor Cell Response to Synchrotron Microbeam Radiation Therapy Differs Markedly from Cells in Normal Tissues," International Journal of Radiation Oncology Biology Physics **77**, 886-894 (2010).

[71] M. Miura, H. Blattmann, E. Brauer-Krisch, A. Bravin, A.L. Hanson, M.M. Nawrocky, P.L. Micca, D.N. Slatkin, J.A. Laissue, "Radiosurgical palliation of aggressive murine SCCVII squamous cell carcinomas using synchrotron-generated X-ray microbeams," Br. J. Radiol. **79**, 71-75 (2006).

[72] R. Serduc, T. Christen, J. Laissue, R. Farion, A. Bouchet, B. van der Sanden, C. Segebarth, E. Braeuer-Krisch, G. Le Duc, A. Bravin, C. Remy, E.L. Barbier, "Brain tumor vessel response to synchrotron microbeam radiation therapy: a short-term in vivo study," Phys. Med. Biol. **53**, 3609-3622 (2008).

[73] E. Schultke, B.H.J. Juurlink, K. Ataelmannan, J. Laissue, H. Blattmann, E. Brauer-Krisch, A. Bravin, J. Minczewska, J. Crosbie, H. Taherian, E. Frangou, T. Wysokinsky, L.D. Chapman, R. Griebel, D. Fourney, "Memory and survival after microbeam radiation therapy," Eur. J. Radiol. **68**, S142-S146 (2008).

[74] R. Serduc, E. Braeuer-Krisch, A. Bouchet, L. Renaud, T. Brochard, A. Bravin, J.A. Laissue, G. Le Duc, "First trial of spatial and temporal fractionations of the delivered dose using synchrotron microbeam radiation therapy," Journal of Synchrotron Radiation **16**, 587-590 (2009).

[75] A. Bouchet, B. Lemasson, G. Le Duc, C. Maisin, E. Brauer-Krisch, E.A. Siegbahn, L. Renaud, E. Khalil, C. Remy, C. Poillot, A. Bravin, J.A. Laissue, E.L. Barbier, R. Serduc, "Preferential Effect of Synchrotron Microbeam Radiation Therapy on Intracerebral 9l Gliosarcoma Vascular Networks," International Journal of Radiation Oncology Biology Physics **78**, 1503-1512 (2010).

[76] A. Bouchet, A. Boumendjel, E. Khalil, R. Serduc, E. Braeuer, E.A. Siegbahn, J.A. Laissue, J. Boutonnat, "Chalcone JAI-51 improves efficacy of synchrotron microbeam radiation therapy of brain tumors," Journal of Synchrotron Radiation **19**, 478-482 (2012).

[77] E. Brauer-Krisch, H. Requardt, P. Regnard, S. Corde, E.A. Siegbahn, G. LeDuc, H. Blattmann, J. Laissue, A. Bravin, "Exploiting geometrical irradiation possibilities in MRT application," Nuclear Instruments & Methods in Physics Research Section A-Accelerators Spectrometers Detectors and Associated Equipment **548**, 69-71 (2005).

[78] R. Serduc, E. Braeuer-Krisch, E.A. Siegbahn, A. Bouchet, B. Pouyatos, R. Carron, N. Pannetier, L. Renaud, G. Berruyer, C. Nemoz, T. Brochard, C. Remy, E.L. Barbier, A. Bravin, G. Le Duc, A. Depaulis, F. Esteve, J.A. Laissue, "High-Precision Radiosurgical Dose Delivery by Interlaced Microbeam Arrays of High-Flux Low-Energy Synchrotron X-Rays," Plos One **5**, e9028 (2010).

[79] F.A. Dilmanian, Z. Zhong, T. Bacarian, H. Benveniste, P. Romanelli, R.L. Wang, J. Welwart, T. Yuasa, E.M. Rosen, D.J. Anschel, "Interlaced x-ray microplanar beams: A radiosurgery approach with clinical potential," Proc. Natl. Acad. Sci. U. S. A. **103**, 9709-9714 (2006).

[80] D.J. Anschel, P. Romanelli, H. Benveniste, B. Foerster, J. Kalef-Ezra, Z. Zhong, F.A. Dilmanian, "Evolution of a focal brain lesion produced by interlaced microplanar X-rays," Minimally Invasive Neurosurgery **50**, 43-46 (2007).

[81] J.A. Laissue, N. Lyubimova, H.P. Wagner, D.W. Archer, D.N. Slatkin, M. Di Michiel, C. Nemoz, M. Renier, E. Brauer, P.O. Spanne, J.O. Gebbers, K. Dixon, H. Blattmann, "Microbeam radiation therapy," Medical Applications of Penetrating Radiation **3770**, 38-45 (1999).

[82] J.A. Laissue, S. Bartzsch, H. Blattmann, E. Braeuer-Krisch, A. Bravin, D. Dallery, V. Djonov, A.L. Hanson, J.W. Hopewell, B. Kaser-Hotz, J. Keyrilainen, P.P. Laissue, M. Miura, R. Serduc, A.E. Siegbahn, D.N. Slatkin, "Response of the rat spinal cord to X-ray microbeams," Radiotherapy and Oncology **106**, 106-111 (2013).

[83] F.A. Dilmanian, Z. Zhong, T. Bacarian, H. Benveniste, J. Kalef-Ezra, P. Romanelli, R. Wang, T. Yuasa, P.L. Micca, M.M. Nawrocky, M. Testa, M. Worth, E.M. Rosen, D.J. Anschel, "Microbeam radiation

therapy in an interlaced geometry: Potential applicability to neuro-oncology and radiosurgery," Neuro-oncology **8**, 484-485 (2006).

[84] R.C.U. Priyadarshika, J.C. Crosbie, B. Kumar, P.A.W. Rogers, "Biodosimetric quantification of short-term synchrotron microbeam versus broad-beam radiation damage to mouse skin using a dermatopathological scoring system," Br. J. Radiol. **84**, 833-842 (2011).

[85] N. Zhong, G.M. Morris, T. Bacarian, E.M. Rosen, E.A. Dilmanian, "Response of rat skin to high-dose unidirectional X-ray microbearns: A histological study," Radiat. Res. **160**, 133-142 (2003).

[86] G. Le Duc, I. Miladi, C. Alric, P. Mowat, E. Braeuer-Krisch, A. Bouchet, E. Khalil, C. Billotey, M. Janier, F. Lux, T. Epicier, P. Perriat, S. Roux, O. Tillement, "Toward an Image-Guided Microbeam Radiation Therapy Using Gadolinium-Based Nanoparticles," Acs Nano **5**, 9566-9574 (2011).

[87] A. Bouchet, B. Lemasson, T. Christen, M. Potez, C. Rome, N. Coquery, C. Le Clec'h, A. Moisan, E. Braeuer-Krisch, G. Leduc, C. Remy, J.A. Laissue, E.L. Barbier, E. Brun, R. Serduc, "Synchrotron microbeam radiation therapy induces hypoxia in intracerebral gliosarcoma but not in the normal brain," Radiotherapy and Oncology **108**, 143-148 (2013).

[88] J.A. Coderre, T.M. Button, P.L. Micca, C.D. Fisher, M.M. Nawrocky, H.B. Liu, "Neutron-Capture Therapy of the 9L Rat Gliosarcoma using the P-Boronophenylalanine-Fructose Complex," International Journal of Radiation Oncology Biology Physics **30**, 643-652 (1994).

[89] D.D. Joel, R.G. Fairchild, J.A. Laissue, S.K. Saraf, J.A. Kalefezra, D.N. Slatkin, "Boron Neutron-Capture Therapy of Intracerebral Rat Gliosarcomas," Proc. Natl. Acad. Sci. U. S. A. **87**, 9808-9812 (1990).

[90] F.A. Dilmanian, G.M. Morris, J.F. Hainfeld, "Methods for implementing microbeam radiation therapy," United States Patent **11/054,001** (2007).

[91] C. Alric, R. Serduc, C. Mandon, J. Taleb, G. Le Duc, A. Le Meur-Herland, C. Billotey, P. Perriat, S. Roux, O. Tillement, "Gold nanoparticles designed for combining dual modality imaging and radiotherapy," Gold Bulletin **41**, 90-97 (2008).

[92] W.N. Rahman, R. Davidson, N. Yagi, M. Geso, I. Darby, "Influence of gold nanoparticles on radiation dose enhancement and cellular migration in microbeam-irradiated cells," BioNanoSci. **1**, 1-13 (2011).

[93] A.K. Iyer, G. Khaled, J. Fang, H. Maeda, "Exploiting the enhanced permeability and retention effect for tumor targeting," Drug Discov. Today **11**, 812-818 (2006).

[94] H.E. Johns and J.R. Cunningham, *The Physics of Radiology*, 4th Edition ed. (Charles C Thomas, Springfield, IL, USA, 1983).

[95] R.J. Griffin, N.A. Koonce, R.P.M. Dings, E. Siegel, E.G. Moros, E. Braeuer-Krisch, P.M. Corry, "Microbeam Radiation Therapy Alters Vascular Architecture and Tumor Oxygenation and is Enhanced by a Galectin-1 Targeted Anti-Angiogenic Peptide," Radiat. Res. **177**, 804-812 (2012).

[96] H. Blattmann, J.O. Gebbers, E. Brauer-Krisch, A. Bravin, G. Le Duc, W. Burkard, M. Di Michiel, V. Djonov, D.N. Slatkin, J. Stepanek, J.A. Laissue, "Applications of synchrotron X-rays to radiotherapy," Nuclear Instruments & Methods in Physics Research Section A-Accelerators Spectrometers Detectors and Associated Equipment **548**, 17-22 (2005).

[97] J.A. Laissue, H. Blattmann, H.P. Wagner, M.A. Grotzer, D.N. Slatkin, "Prospects for microbeam radiation therapy of brain tumours in children to reduce neurological sequelae," Dev. Med. Child Neurol. **49**, 577-581 (2007).

[98] B. van der Sanden, E. Braeuer-Krisch, E.A. Siegbahn, C. Ricard, J. Vial, J. Laissue, "Tolerance of Arteries to Microplanar X-Ray Beams," International Journal of Radiation Oncology Biology Physics **77**, 1545-1552 (2010).

[99] F.A. Dilmanian, Y. Qu, S. Liu, C.D. Cool, J. Gilbert, J.F. Hainfeld, C.A. Kruse, J. Laterra, D. Lenihan, M.M. Nawrocky, G. Pappas, C.I. Sze, T. Yuasa, N. Zhong, Z. Zhong, J.W. McDonald, "X-ray microbeams: Tumor therapy and central nervous system research," Nuclear Instruments & Methods in Physics Research Section A-Accelerators Spectrometers Detectors and Associated Equipment **548**, 30-37 (2005).

[100] S. Sabatasso, J.A. Laissue, R. Hlushchuk, W. Graber, A. Bravin, E. Braeuer-Krisch, S. Corde, H. Blattmann, G. Gruber, V. Djonov, "Microbeam Radiation-Induced Tissue Damage Depends on the Stage of Vascular Maturation," International Journal of Radiation Oncology Biology Physics **80**, 1522-1532 (2011).

[101] R. Serduc, Y.V. de Looij, G. Francony, O. Verdonck, B. Van der Sanden, J. Laissue, R. Farion, E. Braeuer-Krisch, E.A. Siegbahn, A. Bravin, Y. Prezado, C. Segebarth, C. Remy, H. Lahrech, "Characterization and quantification of cerebral edema induced by synchrotron x-ray microbeam radiation therapy," Phys. Med. Biol. **53**, 1153-1166 (2008).

[102] F.A. Dilmanian, Y. Qu, L.E. Feinendegen, L.A. Pena, T. Bacarian, F.A. Henn, J. Kalef-Ezra, S. Liu, Z. Zhong, J.W. McDonald, "Tissue-sparing effect of x-ray microplanar beams particularly in the CNS: Is a bystander effect involved?" Exp. Hematol. **35**, 69-77 (2007).

[103] C.N. Sprung, Y. Yang, H.B. Forrester, J. Li, M. Zaitseva, L. Cann, T. Restall, R.L. Anderson, J.C. Crosbie, P.A.W. Rogers, "Genome-Wide Transcription Responses to Synchrotron Microbeam Radiotherapy," Radiat. Res. **178**, 249-259 (2012).

[104] C. Fernandez-Palomo, E. Schueltke, R. Smith, E. Braeuer-Krisch, J. Laissue, C. Schroll, J. Fazzari, C. Seymour, C. Mothersill, "Bystander effects in tumor-free and tumor-bearing rat brains following irradiation by synchrotron X-rays," Int. J. Radiat. Biol. **89**, 445-453 (2013).

[105] C. Mothersill, C. Fernandez-Palomo, J. Fazzari, R. Smith, E. Schueltke, E. Braeuer-Krisch, J. Laissue, C. Schroll, C. Seymour, "Transmission of Signals from Rats Receiving High Doses of Microbeam Radiation to Cage Mates: an Inter-Mammal Bystander Effect," Dose-Response **12**, 72-92 (2014).

[106] R.W. Smith, J. Wang, E. Schueltke, C.B. Seymour, E. Braeuer-Krisch, J.A. Laissue, H. Blattmann, C.E. Mothersill, "Proteomic changes in the rat brain induced by homogenous irradiation and by the bystander effect resulting from high energy synchrotron X-ray microbeams," Int. J. Radiat. Biol. **89**, 118-127 (2013).

[107] G. Kashino, T. Kondoh, N. Nariyama, K. Umetani, T. Ohigashi, K. Shinohara, A. Kurihara, M. Fukumoto, H. Tanaka, A. Maruhashi, M. Suzuki, Y. Kinashi, Y. Liu, S. Masunaga, M. Watanabe, K. Ono, "Induction of Dna Double-Strand Breaks and Cellular Migration through Bystander Effects in Cells Irradiated with the Slit-Type Microplanar Beam of the Spring-8 Synchrotron," International Journal of Radiation Oncology Biology Physics **74**, 229-236 (2009).

[108] M. Sharma, J.C. Crosbie, L. Puskar, P.A.W. Rogers, "Microbeam-irradiated tumour tissue possesses a different infrared absorbance profile compared to broad beam and sham-irradiated tissue," Int. J. Radiat. Biol. **89**, 79-87 (2013).

[109] D.J. Anschel, A. Bravin, P. Romanelli, "Microbeam radiosurgery using synchrotron-generated submillimetric beams: a new tool for the treatment of brain disorders," Neurosurg. Rev. **34**, 133-141 (2011).

[110] P. Romanelli, E. Fardone, G. Battaglia, E. Braeuer-Krisch, Y. Prezado, H. Requardt, G. Le Duc, C. Nemoz, D.J. Anschel, J. Spiga, A. Bravin, "Synchrotron-Generated Microbeam Sensorimotor Cortex Transections Induce Seizure Control without Disruption of Neurological Functions," Plos One **8**, e53549 (2013).

[111] H. Requardt, A. Bravin, Y. Prezado, E. Braeuer-Krisch, M. Renier, T. Brochard, P. Berkvens, F. Esteve, H. Elleaume, J.-. Adam, H. Blattmann, J.A. Laissue, B. Kaser-Hotz, C. Nemoz, G. Berruyer, "The Clinical Trials Program at the ESRF Biomedical Beam line ID17: Status and Remaining Steps," Sri 2009: the 10th International Conference on Synchrotron Radiation Instrumentation **1234**, 161-164 (2010).

[112] J. Alder and M. Wright, "Method of performing microbeam radiosurgery," US Patent Application Publication **13/453,338** (2013).

[113] M. Wright, "High energy microbeam radiosurgery," US Patent Application Publication **13/492,412** (2013).

[114] E.C. Schreiber and S.X. Chang, "Monte Carlo simulation of a compact microbeam radiotherapy system based on carbon nanotube field emission technology," Med. Phys. **39**, 4669-4678 (2012).

[115] M. Hadsell, J. Zhang, P. Laganis, F. Sprenger, J. Shan, L. Zhang, L. Burk, H. Yuan, S. Chang, J. Lu, O. Zhou, "A first generation compact microbeam radiation therapy system based on carbon nanotube X-ray technology," Appl. Phys. Lett. **103** (2013).

[116] P. Chtcheprov, L. Burk, H. Yuan, C. Inscoe, R. Ger, M. Hadsell, J. Lu, L. Zhang, S. Chang, O. Zhou, "Physiologically gated microbeam radiation, using a field emission x-ray source array," Med. Phys. **41**, 88-95 (2014).

[117] L. Zhang, H. Yuan, L.M. Burk, C.R. Inscoe, M.J. Hadsell, P. Chtcheprov, Y.Z. Lee, J. Lu, S. Chang, O. Zhou, "Image-guided microbeam irradiation to brain tumour bearing mice using a carbon nanotube x-ray source array," Phys. Med. Biol. **59** (2014).

[118] L. Zhang, H. Yuan, C. Inscoe, P. Chtcheprov, M. Hadsell, Y. Lee, J. Lu, S. Chang, O. Zhou, "Nanotube x-ray for cancer therapy: a compact microbeam radiation therapy system for brain tumor treatment," Expert Review of Anticancer Therapy **14**, 1411-1418 (2014).

[119] A. Brahme, "Dosimetric Precision Requirements in Radiation-Therapy," Acta Radiologica Oncology **23**, 379-391 (1984).

[120] F.Z. Company and B.J. Allen, "Calculation of microplanar beam dose profiles in a tissue/lung/tissue phantom," Phys. Med. Biol. **43**, 2491-2501 (1998).

[121] I. Orion, A.B. Rosenfeld, F.A. Dilmanian, F. Telang, B. Ren, Y. Namito, "Monte Carlo simulation of dose distributions from a synchrotron-produced microplanar beam array using the EGS4 code system," Phys. Med. Biol. **45**, 2497-2508 (2000).

[122] M. De Felici, R. Felici, M.S. del Rio, C. Ferrero, T. Bacarian, F.A. Dilmanian, "Dose distribution from x-ray microbeam arrays applied to radiation therapy: An EGS4 Monte Carlo study," Med. Phys. **32**, 2455-2463 (2005).

[123] A. De Felici, R. Felici, C. Ferrero, A. Bravin, A. Tartari, M. Gambaccini, "Monte Carlo assessment of peak-to-valley dose ratio for MRT," Nuclear Instruments & Methods in Physics Research Section A-Accelerators Spectrometers Detectors and Associated Equipment **580**, 489-492 (2007).

[124] F.Z. Company, "Calculation of dose profiles in stereotactic synchrotron microplanar beam radiotherapy in a tissue-lung phantom," Australasian Physical & Engineering Sciences in Medicine **30**, 33-41 (2007).

[125] R.P. Hugtenburg, A.S. Adegunloye, D.A. Bradley, "X-ray microbeam radiation therapy calculations, including polarisation effects, with the Monte Carlo code EGS5," Nuclear Instruments & Methods in Physics Research Section A-Accelerators Spectrometers Detectors and Associated Equipment **619**, 221-224 (2010).

[126] J. Stepanek, H. Blattmann, J.A. Laissue, N. Lyubimova, M. Di Michiel, D.N. Slatkin, "Physics study of microbeam radiation therapy with PSI-version of Monte Carlo code GEANT as a new computational tool," Med. Phys. **27**, 1664-1675 (2000).

[127] J. Spiga, E.A. Siegbahn, E. Braeuer-Krisch, P. Randaccio, A. Bravin, "The GEANT4 toolkit for microdosimetry calculations: Application to microbeam radiation therapy (MRT)," Med. Phys. **34**, 4322-4330 (2007).

[128] J.C. Crosbie, I. Svalbe, S.M. Midgley, N. Yagi, P.A.W. Rogers, R.A. Lewis, "A method of dosimetry for synchrotron microbeam radiation therapy using radiochromic films of different sensitivity," Phys. Med. Biol. **53**, 6861-6877 (2008).

[129] S. Bartzsch and U. Oelfke, "A new concept of pencil beam dose calculation for 40-200 keV photons using analytical dose kernels," Med. Phys. **40**, 111714 (2013).

[130] S. Bartzsch, M. Lerch, M. Petasecca, E. Braeuer-Krisch, U. Oelfke, "Influence of polarization and a source model for dose calculation in MRT," Med. Phys. **41**, 041703 (2014).

[131] E. Brauer-Krisch, H. Requardt, P. Regnard, S. Corde, E. Siegbahn, G. LeDuc, T. Brochard, H. Blattmann, J. Laissue, A. Bravin, "New irradiation geometry for microbeam radiation therapy," Phys. Med. Biol. **50**, 3103-3111 (2005).

[132] E.A. Siegbahn, J. Stepanek, E. Brauer-Krisch, A. Bravin, "Determination of dosimetrical quantities used in microbeam radiation therapy (MRT) with Monte Carlo simulations," Med. Phys. **33**, 3248-3259 (2006).

[133] E.A. Siegbahn, E. Braeuer-Krisch, A. Bravin, H. Nettelbeck, M.L.F. Lerch, A.B. Rosenfeld, "MOSFET dosimetry with high spatial resolution in intense synchrotron-generated x-ray microbeams," Med. Phys. **36**, 1128-1137 (2009).

[134] Y. Prezado, G. Fois, G. Le Duc, A. Bravin, "Gadolinium dose enhancement studies in microbeam radiation therapy," Med. Phys. **36**, 3568-3574 (2009).

[135] I. Martinez-Rovira, J. Sempau, J.M. Fernandez-Varea, A. Bravin, Y. Prezado, "Monte Carlo dosimetry for forthcoming clinical trials in x-ray microbeam radiation therapy," Phys. Med. Biol. **55**, 4375-4388 (2010).

[136] I. Martinez-Rovira and Y. Prezado, "Monte Carlo dose enhancement studies in microbeam radiation therapy," Med. Phys. **38**, 4430-4439 (2011).

[137] I. Martinez-Rovira, J. Sempau, Y. Prezado, "Development and commissioning of a Monte Carlo photon beam model for the forthcoming clinical trials in microbeam radiation therapy," Med. Phys. **39**, 119-131 (2012).

[138] I. Martinez-Rovira, J. Sempau, Y. Prezado, "Monte Carlo-based treatment planning system calculation engine for microbeam radiation therapy," Med. Phys. **39**, 2829-2838 (2012).

[139] G. Gokeri, C. Kocar, M. Tombakoglu, "Monte Carlo simulation of microbeam radiation therapy with an interlaced irradiation geometry and an Au contrast agent in a realistic head phantom," Phys. Med. Biol. **55**, 7469-7487 (2010).

[140] F. Salvat, J.M. Fernandez-Varea, J. Sempau, "PENELOPE, a Code System for Monte Carlo Simulation of Electron and Photon Transport," OECD NEA France (2003).

[141] W.R. Nelson, H. Hirayama, D.W.O. Rogers, "The EGS4 Code System," SLAC Report 265 **265** (1985).

[142] J.S. Hendricks, G.W. McKinney, J.W. Durkee, M.R. James, D.B. Pelowitz, H.R. Trellue, "The MCNPX Radiation Transport Code," Los Alamos National Laboratory Report **LA-UR-05-0683** (2005).

[143] S. Agostinelli, J. Allison, K. Amako, J. Apostolakis, H. Araujo, P. Arce, M. Asai, D. Axen, S. Banerjee, G. Barrand, F. Behner, L. Bellagamba, J. Boudreau, L. Broglia, A. Brunengo, H. Burkhardt, S. Chauvie, J. Chuma, R. Chytracek, G. Cooperman, G. Cosmo, P. Degtyarenko, A. Dell'Acqua, G. Depaola, D. Dietrich, R. Enami, A. Feliciello, C. Ferguson, H. Fesefeldt, G. Folger, F. Foppiano, A. Forti, S. Garelli, S. Giani, R. Giannitrapani, D. Gibin, J.J.G. Cadenas, I. Gonzalez, G.G. Abril, G. Greeniaus, W. Greiner, V. Grichine, A. Grossheim, S. Guatelli, P. Gumplinger, R. Hamatsu, K. Hashimoto, H. Hasui, A. Heikkinen, A. Howard, V. Ivanchenko, A. Johnson, F.W. Jones, J. Kallenbach, N. Kanaya, M. Kawabata, Y. Kawabata, M. Kawaguti, S. Kelner, P. Kent, A. Kimura, T. Kodama, R. Kokoulin, M. Kossov, H. Kurashige, E. Lamanna, T. Lampen, V. Lara, V. Lefebure, F. Lei, M. Liendl, W. Lockman, F. Longo, S. Magni, M. Maire, E. Medernach, K. Minamimoto, P.M. de Freitas, Y. Morita, K. Murakami, M. Nagamatu, R. Nartallo, P. Nieminen, T. Nishimura, K. Ohtsubo, M. Okamura, S. O'Neale, Y. Oohata, K. Paech, J. Perl, A. Pfeiffer, M.G. Pia, F. Ranjard, A. Rybin, S. Sadilov, E. Di Salvo, G. Santin, T. Sasaki, N. Savvas, Y. Sawada, S. Scherer, S. Seil, V. Sirotenko, D. Smith, N. Starkov, H. Stoecker, J. Sulkimo, M. Takahata, S. Tanaka, E. Tcherniaev, E.S. Tehrani, M. Tropeano, P. Truscott, H. Uno, L. Urban, P. Urban, M. Verderi, A. Walkden, W. Wander, H. Weber, J.P. Wellisch, T. Wenaus, D.C. Williams, D. Wright, T. Yamada, H. Yoshida, D. Zschiesche, "GEANT4-a simulation toolkit," Nuclear Instruments & Methods in Physics Research Section A-Accelerators Spectrometers Detectors and Associated Equipment **506**, 250-303 (2003).

[144] M. de Felici, E.A. Siegbahn, J. Spiga, A.L. Hanson, R. Felici, C. Ferrero, A. Tartari, M. Gambaccini, J. Keyrilaeinen, E. Braeuer-Krisch, P. Randaccio, A. Bravin, "Monte Carlo code comparison of dose delivery prediction for Microbeam Radiation Therapy," International Workshop on Monte Carlo Techniques in Radiotherapy Delivery and Verification - Third McGill International Workshop **102**, 012005 (2008).

[145] J. Als-Nielsen and D. McMorrow, *Elements of Modern X-Ray Pysics* (John Wiley & Sons, Ltd., Singapore, 2001).

[146] T. Tanaka and H. Kitamura, "SPECTRA: a synchrotron radiation calculation code," Journal of Synchrotron Radiation **8**, 1221-1228 (2001).

[147] D. Chapman, N. Gmur, N. Lazarz, W. Thomlinson, "Photon - a Program for Synchrotron Radiation-Dose Calculations," Nuclear Instruments & Methods in Physics Research Section A-Accelerators Spectrometers Detectors and Associated Equipment **266**, 191-194 (1988).

[148] J. Spiga, Y. Prezado, E. Braeuer-Krisch, V. Fanti, P. Randaccio, A. Bravin, "The Effect of Beam Polarization in Microbeam Radiation Therapy (MRT): Monte Carlo Simulations Using Geant4," 2009 IEEE Nuclear Science Symposium Conference Record, Vols 1-5, 2170-2173 (2009).

[149] H. Nettelbeck, G.J. Takacs, M.L.F. Lerch, A.B. Rosenfeld, "Microbeam radiation therapy: A Monte Carlo study of the influence of the source, multislit collimator, and beam divergence on microbeams," Med. Phys. **36**, 447-456 (2009).

[150] E. Braeuer-Krisch, A. Rosenfeld, M. Lerch, M. Petasecca, M. Akselrod, J. Sykora, J. Bartz, M. Ptaszkiewicz, P. Olko, A. Berg, M. Wieland, S. Doran, T. Brochard, A. Kamlowski, G. Cellere, A. Paccagnella, E.A. Siegbahn, Y. Prezado, I. Martinez-Rovira, A. Bravin, L. Dusseau, P. Berkvens, "Potential High Resolution Dosimeters For MRT," 6th International Conference on Medical Applications of Synchrotron Radiation **1266**, 89-97 (2010).

[151] P.R. Almond, P.J. Biggs, B.M. Coursey, W.F. Hanson, M.S. Huq, R. Nath, D.W.O. Rogers, "AAPM's TG-51 protocol for clinical reference dosimetry of high-energy photon and electron beams," Med. Phys. **26**, 1847-1870 (1999).

[152] F.H. Attix, *Introduction to Radiological Physics and Radiation Dosimetry* (John Wiley & Sons, Inc., New York, 1986).

[153] J.C. Crosbie, P.A.W. Rogers, A.W. Stevenson, C.J. Hall, J.E. Lye, T. Nordstrom, S.M. Midgley, R.A. Lewis, "Reference dosimetry at the Australian Synchrotron's imaging and medical beamline using free-air ionization chamber measurements and theoretical predictions of air kerma rate and half value layer," Med. Phys. **40**, 062103 (2013).

[154] P. Fournier, A.H. Clavel, I. Cornelius, P. Berkvens, J.C. Crosbie, M.L.F. Lerch, A.B. Rosenfeld, E. Brauer-Krisch, "Determination of ion recombination for absolute dosimetry in microbeam radiation therapy," European Journal of Medical Physics **29**, e42 (2013).

[155] D.F. Regulla and U. Deffner, "Dosimetry by Electron-Spin-Resonance Spectroscopy of Alanine," Int. J. Appl. Radiat. Isot. **33**, 1101-& (1982).

[156] J.W. Hansen, K.J. Olsen, M. Wille, "The Alanine Radiation Detector for High and Low Let Dosimetry," Radiat. Prot. Dosimet. **19**, 43-47 (1987).

[157] F. Coninckx, H. Schonbacher, A. Bartolotta, S. Onori, A. Rosati, "Alanine Dosimetry as the Reference Dosimetric System in Accelerator Radiation Environments," Applied Radiation and Isotopes **40**, 977-983 (1989).

[158] M.F. Desrosiers, J.M. Publ, S.L. Cooper, "An absorbed-dose/dose-rate dependence for the alanine-EPR dosimetry system and its implications in high-dose ionizing radiation metrology," Journal of Research of the National Institute of Standards and Technology **113**, 79-95 (2008).

[159] R.B. Hayes, E.H. Haskell, J.K. Barrus, G.H. Kenner, A.A. Romanyukha, "Accurate EPR radiosensitivity calibration using small sample masses," Nuclear Instruments & Methods in Physics Research Section A-Accelerators Spectrometers Detectors and Associated Equipment **441**, 535-550 (2000).

[160] A. Mack, S.G. Scheib, J. Major, S. Gianolini, G. Pazmandi, H. Feist, H. Czempiel, H.J. Kreiner, "Precision dosimetry for narrow photon beams used in radiosurgery - Determination of Gamma Knife ® output factors," Med. Phys. **29**, 2080-2089 (2002).

[161] F. Chen, C.F.O. Graeff, O. Baffa, "K-band EPR dosimetry: small-field beam profile determination with miniature alanine dosimeter," Applied Radiation and Isotopes **62**, 267-271 (2005).

[162] E. Waldeland and E. Malinen, "Review of the dose-to-water energy dependence of alanine and lithium formate EPR dosimeters and LiF TL-dosimeters - Comparison with Monte Carlo simulations," Radiat. Measur. **46**, 945-951 (2011).

[163] P.D. Harty, J.E. Lye, G. Ramanathan, D.J. Butler, C.J. Hall, A.W. Stevenson, P.N. Johnston, "Absolute x-ray dosimetry on a synchrotron medical beam line with a graphite calorimeter," Med. Phys. **41**, 052101 (2014).

[164] C.K. Ross and N.V. Klassen, "Water calorimetry for radiation dosimetry," Phys. Med. Biol. **41**, 1-29 (1996).

[165] J. Seuntjens and S. Duane, "Photon absorbed dose standards," Metrologia **46**, S39-S58 (2009).

[166] "Gafchromic EBT3," http://www.ashland.com/Ashland/Static/Documents/ASI/Advanced%20materials/gafchromic-ebt3.pdf Accessed 4/19/2015.

[167] "Gafchromic EBT2," http://www.ashland.com/Ashland/Static/Documents/ASI/Advanced%20materials/ebt2.pdf Accessed 4/19/2015.

[168] "GAFCHROMIC HD-V2 Dosimetry Film," http://www.ashland.com/Ashland/Static/Documents/ASI/Advanced%20materials/gafchromic-hdv2.pdf Accessed 4/19/2015.

[169] "GAFCHROMIC HD-810 Radiochromic Dosimetry Film," http://www.meditest.fr/pdf/GAFCHROMIC%20HD-810.pdf Accesed 4/19/2015.

[170] E. Brauer-Krisch, E.A. Siegbahn, A. Bravin, "GafChromic film measurements for Microbeam Radiation Therapy (MRT)," IFMBE Proceedings **25**, 174-177 (2009).

[171] A. Niroomand-Rad, C.R. Blackwell, B.M. Coursey, K.P. Gall, J.M. Galvin, W.L. McLaughlin, A.S. Meigooni, R. Nath, J.E. Rodgers, C.G. Soares, "Radiochromic film dosimetry: Recommendations of AAPM Radiation Therapy Committee Task Group 55," Med. Phys. **25**, 2093-2115 (1998).

[172] M.J. Butson, T. Cheung, P.K.N. Yu, "Weak energy dependence of EBT gafchromic film dose response in the 50 kVp-10 MVp X-ray range," Applied Radiation and Isotopes **64**, 60-62 (2006).

[173] M.J. Butson, P.K.N. Yu, T. Cheung, H. Alnawaf, "Energy response of the new EBT2 radiochromic film to x-ray radiation," Radiat. Measur. **45**, 836-839 (2010).

[174] B. Arjomandy, R. Tailor, A. Anand, N. Sahoo, M. Gillin, K. Prado, M. Vicic, "Energy dependence and dose response of Gafchromic EBT2 film over a wide range of photon, electron, and proton beam energies," Med. Phys. **37**, 1942-1947 (2010).

[175] T.A.D. Brown, K.R. Hogstrom, D. Alvarez, K. Ham, J.P. Dugas, K.L. Matthews II, "Dose-response curve of EBT, EBT2 and EBT3 radiochromic films to a synchrotron-produced monochromatic x-ray beam," Med. Phys. **39**, 3738-3739 (2012).

[176] J.E. Villarreal-Barajas and R.F.H. Khan, "Energy response of EBT3 radiochromic films: implications for dosimetry in kilovoltage range," Journal of Applied Clinical Medical Physics **15**, 331-338 (2014).

[177] P.J. Muench, A.S. Meigooni, R. Nath, W.L. Mclaughlin, "Photon Energy-Dependence of the Sensitivity of Radiochromic Film and Comparison with Silver-Halide Film and Lif TLDs used for Brachytherapy Dosimetry," Med. Phys. **18**, 769-775 (1991).

[178] S. Devic, "Radiochromic film dosimetry: Past, present, and future," Physica Medica-European Journal of Medical Physics **27**, 122-134 (2011).

[179] A.B. Rosenfeld, G.I. Kaplan, T. Kron, B.J. Allen, A. Dilmanian, I. Orion, B. Ren, M.L.F. Lerch, A. Holmes-Siedle, "MOSFET dosimetry of an X-ray microbeam." IEEE Trans. Nucl. Sci. **46**, 1774-1780 (1999).

[180] G.I. Kaplan, A.B. Rosenfeld, B.J. Allen, J.T. Booth, M.G. Carolan, A. Holmes-Siedle, "Improved spatial resolution by MOSFET dosimetry of an x-ray microbeam," Med. Phys. **27**, 239-244 (2000).

[181] A.B. Rosenfeld, "MOSFET dosimetry on modern radiation oncology modalities," Radiat. Prot. Dosimet. **101**, 393-398 (2002).

[182] E. Brauer-Krisch, A. Bravin, M. Lerch, A. Rosenfeld, J. Stepanek, M. Di Michiel, J.A. Laissue, "MOSFET dosimetry for microbeam radiation therapy at the European Synchrotron Radiation Facility," Med. Phys. **30**, 583-589 (2003).

[183] A.B. Rosenfeld, E.A. Siegbahn, E. Brauer-Krish, A. Holmes-Siedle, M.L.F. Lerch, A. Bravin, I.M. Cornelius, G.J. Takacs, N. Painuly, H. Nettelback, T. Kron, "Edge-on face-to-face MOSFET for synchrotron microbeam dosimetry: MC modeling," IEEE Trans. Nucl. Sci. **52**, 2562-2569 (2005).

[184] M.L.F. Lerch, M. Petasecca, A. Cullen, A. Hamad, H. Requardt, E. Braeuer-Krisch, A. Bravin, V.L. Perevertaylo, A.B. Rosenfeld, "Dosimetry of intensive synchrotron microbeams," Radiat. Measur. **46**, 1560-1565 (2011).

[185] A. Cullen, M. Lerch, M. Petasecca, A. Rosenfeld, "Monte Carlo modelling of a silicon strip detector for microbeam radiation therapy," Radiat. Measur. **46**, 1646-1649 (2011).

[186] M. Petasecca, A. Cullen, I. Fuduli, A. Espinoza, C. Porumb, C. Stanton, A.H. Aldosari, E. Braeuer-Krisch, H. Requardt, A. Bravin, V. Perevertaylo, A.B. Rosenfeld, M.L.F. Lerch, "X-Tream: a novel dosimetry system for Synchrotron Microbeam Radiation Therapy," Journal of Instrumentation **7**, P07022 (2012).

[187] S.J. Doran, T. Brochard, J. Adamovics, N. Krstajic, E. Braeuer-Krisch, "An investigation of the potential of optical computed tomography for imaging of synchrotron-generated x-rays at high spatial resolution," Phys. Med. Biol. **55**, 1531-1547 (2010).

[188] A.T. Abdul Rahman, E. Brauer-Krisch, T. Brochard, J. Adamovics, S.K. Clowes, D. Bradley, S.J. Doran, "Sophisticated test objects for the quality assurance of optical computed tomography scanners." Phys. Med. Biol. **56**, 4177-99 (2011).

[189] T. Gorjiara, R. Hill, Z. Kuncic, J. Adamovics, S. Bosi, J. Kim, C. Baldock, "Investigation of radiological properties and water equivalency of PRESAGE ® dosimeters," Med. Phys. **38**, 2265-2274 (2011).

[190] S.J. Doran, A.T.A. Rahman, E. Braeuer-Krisch, T. Brochard, J. Adamovics, A. Nisbet, D. Bradley, "Establishing the suitability of quantitative optical CT microscopy of PRESAGE radiochromic dosimeters for the verification of synchrotron microbeam therapy," Phys. Med. Biol. **58**, 6279-6297 (2013).

[191] N. Annabell, N. Yagi, K. Umetani, C. Wong, M. Geso, "Evaluating the peak-to-valley dose ratio of synchrotron microbeams using PRESAGE fluorescence," Journal of Synchrotron Radiation **19**, 332-339 (2012).

[192] G.M. Akselrod, M.S. Akselrod, E.R. Benton, N. Yasuda, "A novel Al_2O_3 fluorescent nuclear track detector for heavy charged particles and neutrons," Nuclear Instruments & Methods in Physics Research Section B-Beam Interactions with Materials and Atoms **247**, 295-306 (2006).

[193] M.S. Akselrod, R.C. Yoder, G.M. Akselrod, "Confocal fluorescent imaging of tracks from heavy charged particles utilising new Al_2O_3 : C,Mg crystals," Radiat. Prot. Dosimet. **119**, 357-362 (2006).

[194] J.A. Bartz, G.J. Sykora, E. Braeuer-Krisch, M.S. Akselrod, "Imaging and dosimetry of synchrotron microbeam with aluminum oxide fluorescent detectors," Radiat. Measur. **46**, 1936-1939 (2011).

[195] G. Okada, B. Morrell, C. Koughia, A. Edgar, C. Varoy, G. Belev, T. Wysokinski, D. Chapman, S. Kasap, "Spatially resolved measurement of high doses in microbeam radiation therapy using samarium doped fluorophosphate glasses," Appl. Phys. Lett. **99**, 121105 (2011).

[196] G. Belev, G. Okada, D. Tonchev, C. Koughia, C. Varoy, A. Edgar, T. Wysokinski, D. Chapman, S. Kasap, "Valency conversion of samarium ions under high dose synchrotron generated X-ray radiation," Physica Status Solidi C: Current Topics in Solid State Physics, **8**(9) (2011).

[197] S. Vahedi, G. Okada, B. Morrell, E. Muzar, C. Koughia, A. Edgar, C. Varoy, G. Belev, T. Wysokinski, D. Chapman, S. Kasap, "X-ray induced Sm^{3+} to Sm^{2+} conversion in fluorophosphate and fluoroaluminate glasses for the monitoring of high-doses in microbeam radiation therapy," J. Appl. Phys. **112**, 073108 (2012).

[198] G. Okada, J. Ueda, S. Tanabe, G. Belev, T. Wysokinski, D. Chapman, D. Tonchev, S. Kasap, "Samarium-Doped Oxyfluoride Glass-Ceramic as a New Fast Erasable Dosimetric Detector Material for Microbeam Radiation Cancer Therapy Applications at the Canadian Synchrotron," J. Am. Ceram. Soc. **97**, 2147-2153 (2014).

2 THE PRODUCTION OF SYNCHROTRON RADIATION AND THE BIOMEDICAL IMAGING AND THERAPY BEAMLINES AT THE CANADIAN LIGHT SOURCE

2.1 Introduction to synchrotron radiation

Synchrotron radiation (SR) is the general term for the electromagnetic radiation emitted by a relativistic charged particle deflected in a magnetic field. SR was first recognized, and the name coined, in 1947 at the USA's General Electric synchrotron,[1-3] a type of accelerator that synchronously changes magnetic field strength as particle energy is increased. Originally SR was considered a nuisance for researchers at particle accelerators because it was an energy loss mechanism of the accelerated charged particle, but the potential of SR for research was eventually recognized due to its unique characteristics. Experimentation with SR was first performed in a parasitic fashion on accelerators used for particle physics. These are described as first generation SR sources. In the 1980's, specialized particle accelerators, called synchrotron light sources, were built for the sole purpose of producing SR from dipole magnets, and these are referred to as second generation sources.[1] Current designs (third generation sources) use insertion devices to optimize SR spectral brightness (photons$\cdot s^{-1}\cdot mrad^{-2}\cdot mm^{-2}\cdot$(0.1 % bandwidth)$^{-1}$). Today there are approximately 40 third generation synchrotron light sources around the world.[4]

2.2 Overview of a synchrotron light source

A synchrotron light source consists of multiple major components that enable a beam of relativistic charged particles to circulate in a closed orbit for an extended period of time producing SR whenever the particles follow a curved path. A generic schematic for a synchrotron is shown in Fig. 2.1. Essentially, to produce useful SR, an intense beam of high-energy charged particles traveling through large magnetic fields is required. A synchrotron light source accelerates either electrons or positrons (although for simplicity, only electrons will be referred to from now on) to nearly the speed of light, and stores

them in an evacuated pipe (vacuum chamber) composing a closed orbit that is established through a magnet lattice. A description of a synchrotron light source, from initial beam production in the injector, through storage at a constant energy in the storage ring, and experimentation using SR in a beamline, will be discussed in the following subsections.

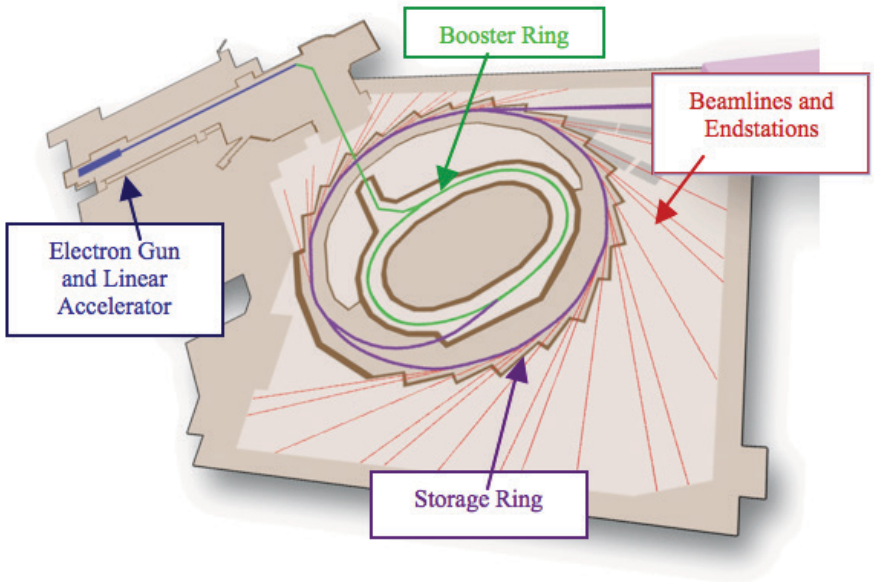

Figure 2.1 A schematic of a synchrotron light source highlighting the major components: the linear accelerator, booster ring, storage ring, and beamlines. (Image courtesy of Canadian Light Source, Inc.)

2.2.1 Injector

The injector system produces an electron beam and accelerates it to its target energy after which the electrons are transferred to the storage ring. There are different types of injectors, but all must accomplish five functions: the production of free electrons, an initial acceleration of the non-relativistic electrons to relativistic energies, a second acceleration to the target energy, extraction from the injector, and injection to the storage ring.[5]

The electrons originate at an electron gun. Often, this is a cathode with a high voltage applied under vacuum that generates electrons via thermionic emission. Electric and/or magnetic fields are used to focus and accelerate the free electrons into the next stage of the injector. For many synchrotron light sources that operate in the GeV energy

range, the injector is composed of both a linear accelerator, which can accelerate non-relativistic electrons to several hundred MeV, and a booster synchrotron (referred to as the booster ring) that can achieve energies up to several GeV.

The linear accelerator consists of a series of cavities in which the electrons gain energy as they travel a linear path. The accelerating energy is provided by klystrons generating high power radiofrequency (RF) fields. Typically the electrons are accelerated to a few hundred MeV before being transported to the booster ring.[6] The booster ring is a cyclic accelerator, and thus allows the electron beam to gain energy as it repeatedly traverses the same accelerating section. The closed orbit is maintained through the presence of dipole magnets, which cause the electrons' trajectories to curve due to the Lorentz force. Because the electrons are constantly gaining energy as they circulate in the booster ring, the magnetic and RF fields must increase concurrently. Once the electrons reach their target energy (several GeV), they are "kicked" using magnetic fields out of the booster ring and into the storage ring.[5] For many light sources, the injector is only operated for a short time with long intervals between the injection of electrons into the storage ring. The injector refills the storage ring current to its maximum value after decay of the current or after some interruption in operation. Alternatively, the synchrotron light source may operate in "top-up" mode: the injector is used to maintain the storage ring current at a near constant level by frequent injections.

2.2.2 Storage ring

In the storage ring (Fig. 2.2) the electrons circulate within a vacuum tube and produce SR upon each deflection in a magnetic field. The storage ring consists of straight sections connected at nodes where bending magnets (BMs), which are dipole magnets, are situated to curve the electron paths into the adjoining straight section. The angle at which the electron paths are bent as they pass through each dipole depends on the number of nodes and straight sections. The BMs are required to keep the electron beam in a closed orbit, and thus the total bending from the dipole magnets will sum to 360°. In third generation synchrotron light sources, SR is produced as electrons pass through the magnetic fields of BMs at the nodes, as well as in magnetic arrays known as insertion

devices (IDs), which are placed in the straight sections of the storage ring. The characteristics of the various magnetic structures and the radiation they produce will be discussed in more detail in section 2.4.

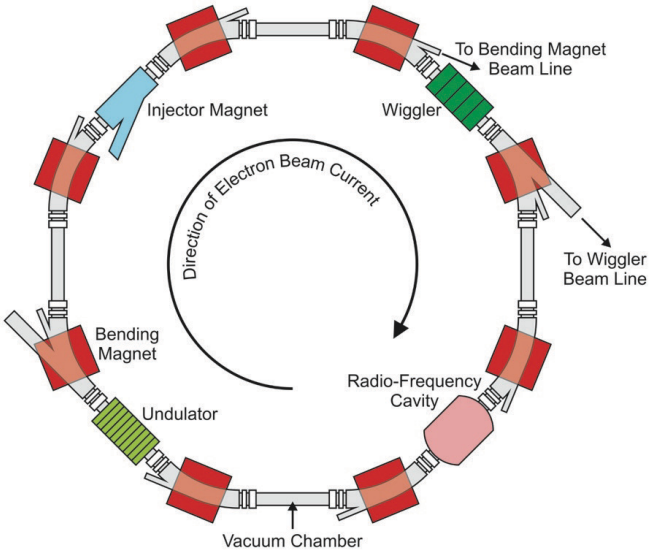

Figure 2.2 A schematic for a storage ring highlighting some main features, including the injection magnet, BMs, IDs (undulators and wigglers), the RF cavity, and vacuum chamber. (Image used with permission from "How do synchrotrons work?" http://pd.chem.ucl.ac.uk/pdnn/inst2/work.htm.[7])

There are several other magnet types distributed around the storage ring that serve multiple functions. The arrangement of the magnets in the ring compose its lattice, which affects both electron and photon beam parameters. Quadrupole magnets are required to focus the electron beam. Sextupoles, and possibly even higher pole order magnets, are present to account for energy-dependent focusing (*e.g.*, the increase in focal length with increasing particle energy) in dipoles and quadrupoles.[8] Additionally, there are small orbit corrector magnets to correct the electron beam trajectory, and magnets present to manage injection from the injector into the storage ring.

There is ultra high vacuum ($< 10^{-13}$ atm) in the storage ring to reduce interactions between electrons and air molecules. The vacuum system is composed of many parts, including the vacuum tube, ion pumps to sweep away molecules and maintain the high vacuum, gauges to monitor the pressure, and a valve system designed to rapidly contain any detected vacuum leaks to a limited section of the storage ring. Beam lifetime (the

time it takes for the storage ring current to reduce to 1/*e* of its initial value) is heavily influenced by electron interactions with air (and other gas) molecules. Interactions between electrons and gas molecules include Coulomb scattering and the production of bremsstrahlung radiation.[9] These interactions may cause the electrons to be lost from the beam if the energy loss is large enough. Alternatively, collisions involving minimal energy loss cause an increase in the electron beam's transverse size. The electron beam itself is the greatest source of molecules within the vacuum tube. The electron beam, or the SR produced, causes desorption of gas molecules from the vacuum tube's surface.[9] Although the interaction with air molecules is usually the most significant mechanism for the reduction in storage ring current, it is not the only mechanism. There are losses due to the quantum nature of SR emission, specifically if the energy lost by the electron during emission is great enough that the electron will lose its place in the stable orbit, and consequently the electron beam.[9] Additionally, there are electron-electron interactions within the electron bunch (Touschek scattering) that can also lead to large energy losses, and thus lost particles. Touschek scattering increases with increasing electron density within the beam, and thus occurs to the greatest extent at high storage ring currents.[9] Beam lifetime determines the rate at which the storage ring current decreases, the time between refills, and thus how frequently the injector system is required.

Radiofrequency cavities located in one or more straight sections are another necessary feature of the storage ring.[10] They are required to maintain the electron beam energy at its target value following losses due to radiation emission and interactions with air molecules or other electrons. The lost energy is replaced as the electrons cross the accelerating gap of the RF cavity during each lap around the storage ring. The direction of the electric field within the resonant cavity alternates with time, which bunches the beam.[10] This bunching is required to ensure that individual electrons remain within a stable interval in terms of their energy and phase with respect to the RF so that they continue circulating in the storage ring. The regions of stability (in longitudinal phase space) are known as RF buckets (Fig. 2.3). The RF system's frequency and voltage influences the maximum number of bunches in the storage ring, the bunch length, and the minimal distance between consecutive bunches.[10] The bunch characteristics, in turn, determine the time structure of the emitted SR, which is relevant for time-resolved

experiments (*e.g.*, ultra-fast spectroscopy). The voltage across the accelerating gap of a cavity must not only account for the energy lost due to the production of SR in the BMs and IDs, but must account for the quantum nature of SR production, losses to the vacuum tube, and for losses in the RF system itself.[10]

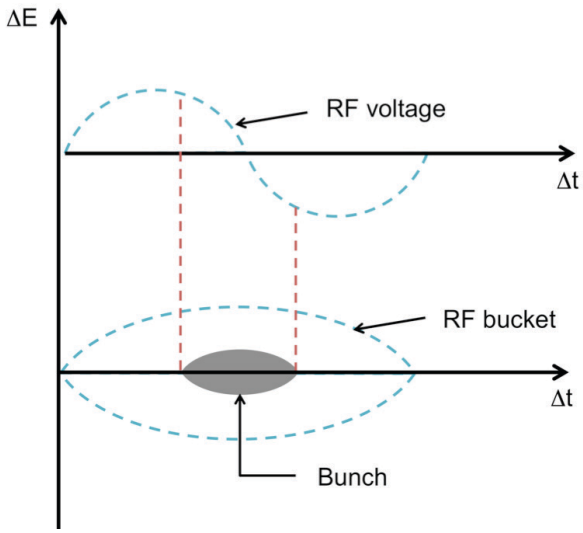

Figure 2.3 A representation of the RF voltage, RF bucket and electron bunch in longitudinal phase space. (Image adapted from: S. Baird, "Accelerators for Pedestrians," European Organization for Nuclear Research, CERN AB-Note-2007-014 OP (2007).[11])

2.2.3 Beamlines

Beamlines are built tangential to the storage ring and capture the SR emitted at BMs or IDs so it can be used for research. Beamlines are composed of three distinct sections that are typically contained in different hutches (shielded areas): an optics section, an experimental section, and a control area. The optics hutch contains beam-modifying devices under vacuum, such as shutters, filters for modifying the energy spectrum, collimators for defining the beam size, mirrors for focusing, and monochromators for energy selection. Often these components require cooling to withstand the high heat loads of the powerful SR beams. The components of the experimental hutch may be under vacuum or not, depending on the energy of the photon beam. Its components vary depending on the application, but normally contain specialized chambers to control

experimental conditions (*e.g.*, pressure, atmosphere), motorized sample stages, radiation detectors and a beam stop to absorb what remains of the photon beam. The control room or hutch contains the controls for the beamline components and experimental end station, and computers for data collection.

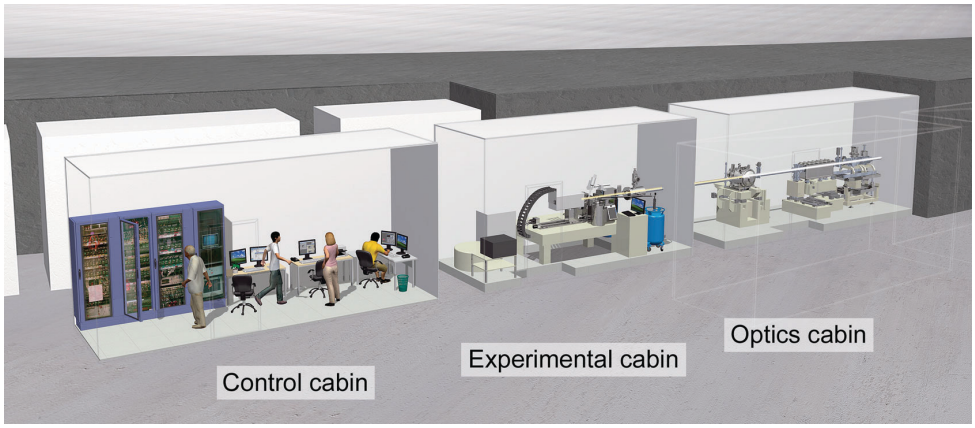

Figure 2.4 A schematic of a beamline's optics, experimental and control hutches. (Image from www.esrf.eu.[12])

2.3 Characteristics of synchrotron radiation

The radiation produced from a synchrotron light source is valuable for research due to its unique properties that can be manipulated for a wide variety of applications. These unique characteristics will be described qualitatively below, and their physical origins discussed in section 2.4.

2.3.1 Brightness

The intensity of photons produced from a synchrotron light source is several orders of magnitude higher than that produced with conventional sources, such as x-ray tubes. In addition to the overall intensity, synchrotrons in particular have extreme brightness (photons $\cdot s^{-1} \cdot mrad^{-2} \cdot mm^{-2} \cdot (0.1\ \%\ bandwidth)^{-1}$), which means that their incredible intensity is concentrated in a very small spatial and angular distribution. Low emittance (a measure of electron beam transverse size and angular divergence) is a design feature of third generation sources to achieve high brightness. The great number of photons allows

better statistics and shorter experimentation times using SR compared to conventional sources. Additionally, narrow energy bandwidths may be selected from the broad energy spectrum, and still allow for sufficient flux. Figure 2.5 shows the brightness of x-ray tubes, various magnet sources used in synchrotron light sources, and x-ray FELs (free electron lasers).

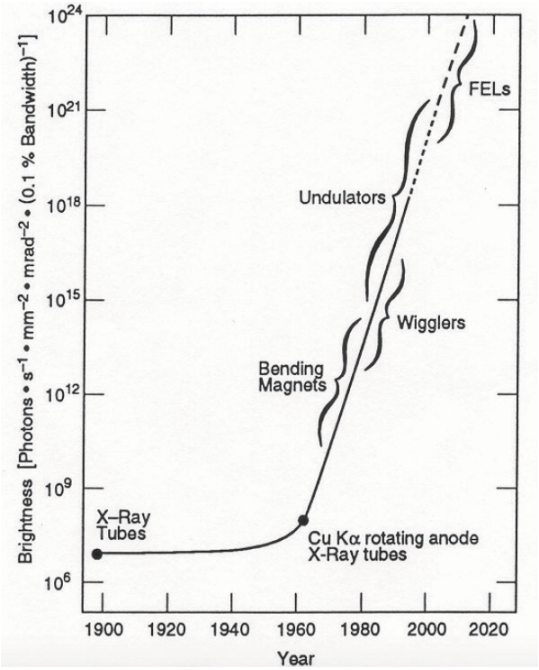

Figure 2.5 A plot of brightness for various x-ray producing devices, including x-ray tubes, the three types of magnetic devices used to produce SR, and free electron lasers (FELs). (Image reproduced from: *Synchrotron Radiation Sources: A Primer, Vol. 1*, H. Winick, World Scientific Publishing Co. Pte. Ltd., Singapore, 1994[13] with permission from World Scientific Publishing Co. (www.worldscientific.com/worldscibooks/10.1142/2444).)

2.3.2 Energy range

The energy of SR depends on the energy of the electrons in the storage ring and the strength of the magnetic field in which they are deflected. Bending magnet and wiggler radiation (Sections 2.4.2 and 2.4.3, respectively) is produced with a broad energy spectrum that can extend from the far infrared (< 1 meV) to hard x-ray regions (several hundred keV) of the electromagnetic spectrum. The radiation produced in an undulator (Section 2.4.4) has a quasi-monochromatic energy spectrum composed of a fundamental

frequency and higher order harmonics. The broad energy spectrum covered by a synchrotron facility allows applications in a wide range of scientific disciplines.

2.3.3 Natural collimation

Due to the ultra-relativistic speeds of the electrons in the storage ring, the familiar dipole angular distribution of emitted radiation for non-relativistic particles is collapsed into a narrow cone whose opening angle is inversely proportional to the electron energy (Fig. 2.6). The extreme natural collimation, in combination with the high intensity, allows for the tunability of SR using either grating or crystal monochromators.

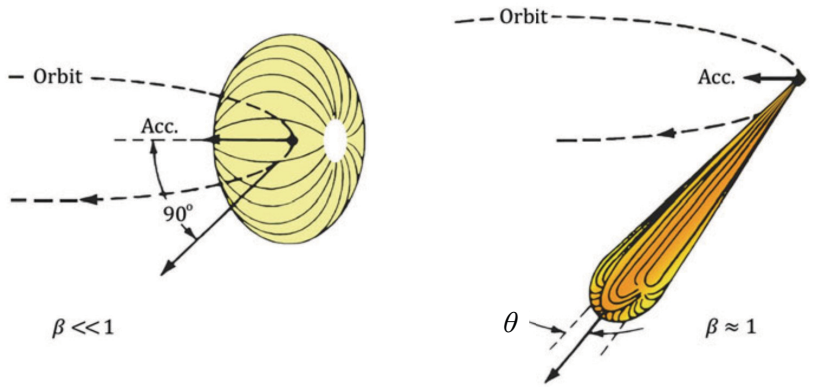

Figure 2.6 The emission of radiation from a non-relativistic (left) and relativistic (right) charged particle undergoing circular motion. (Image reproduced from: A. Balerna and S. Mobilio, "Introduction to Synchrotron Radiation," in *Synchrotron Radiation: Basics, Methods and Applications*, edited by S. Mobilio, F. Boscherini, C. Meneghini (Springer-Verlag Berlin Heidelberg, 2015)[6] with permission of Springer Science+Business Media and the authors).

2.3.4 Polarization

Synchrotron radiation has a strong degree of polarization (Fig. 2.7). The photon beam produced in a BM is 100% linearly polarized in the horizontal plane. Above and below the horizontal plane, the photon beam has some vertical component, which results in elliptical polarization. The photon beam exiting a wiggler is 100% linearly polarized everywhere. The polarization of the photon beam can be altered using specially designed IDs, and can be used to study dichroic materials, such as some organic molecules and

magnetic materials.[14,15] Additionally, the polarization will introduce an additional angular dependence in the interactions between photons in matter which must be considered in dosimetry, as discussed in Section 1.3.1.

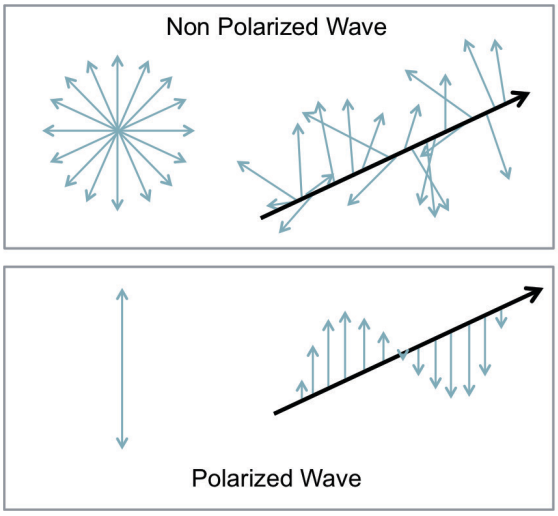

Figure 2.7 Schematic demonstrating the concept of polarization for electromagnetic radiation. The black arrows indicate the direction of beam propagation, and the blue arrows indicate the direction of the electric field.

2.3.5 Coherence

Some SR exhibits coherence, and this in turn allows for diffraction and interference studies. Lateral (or spatial) coherence improves as the source size decreases and the collimation increases.[16] Longitudinal (or temporal) coherence improves with the degree of monochromatization.[16] The minimal divergence and high brightness of SR allows monochromators to select narrow energy bandwidths, consequently producing beams with longitudinal coherence. Coherence allows novel phase-based x-ray imaging techniques to be investigated.[17-19]

2.3.6 Time Structure

The temporal structure of the SR beam is dependent on the storage ring's RF system. As a bunch of electrons passes through a BM, a pulse of photons can be detected on the beamline. Usually, multiple buckets within the storage ring are populated with electrons.

The time between successive pulses depends on the longitudinal distance between electron bunches, which depends only on the frequency of the RF field. The time between bunches (if all RF buckets are populated) can be calculated by $\Delta t = f_{RF}^{-1}$, where f_{RF} is the frequency of the RF field.[10] With a typical RF frequency of several hundred MHz, this separation is on the order of ns. If only one bunch in the storage ring is filled, the time between light pulses will equal the time it takes for the electron bunch to travel around the storage ring: $\Delta t = C/c$, where C is the circumference of the storage ring, and c is the speed of light. The manner in which bunches are filled within the storage ring can be controlled through the injection system, and thus can be optimized for certain experiments.

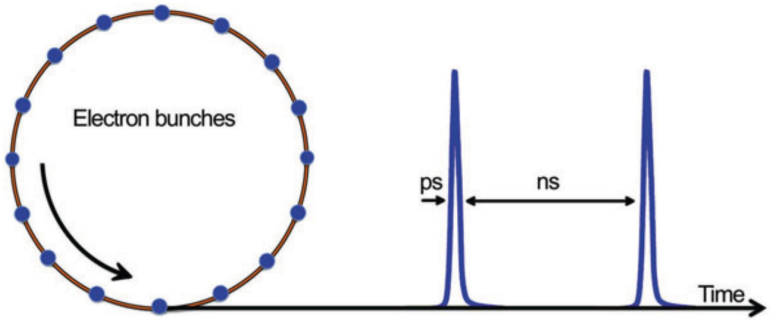

Figure 2.8 A schematic illustrating the bunching of electrons in the storage ring, and the resulting temporal pattern of the emitted SR. Typically individual pulses have a duration of tens of picoseconds, and are separated by nanoseconds. (Image reproduced from: A. Balerna and S. Mobilio, "Introduction to Synchrotron Radiation," in *Synchrotron Radiation: Basics, Methods and Applications*, edited by S. Mobilio, F. Boscherini, C. Meneghini (Springer-Verlag Berlin Heidelberg, 2015)[6] with permission of Springer Science+Business Media and authors.)

The temporal length of each individual pulse of light is slightly more complicated to determine, and depends on the magnetic lattice and the RF system. Typically bunches are between 0.5 and 5 cm long, which results in a temporal pulse length of L_{bunch}/c, where L_{bunch} is the bunch length. This results in a pulse length on the order of 10s of picoseconds.

2.4 Production of synchrotron radiation

2.4.1 Radiation from a charged particle undergoing circular motion

The acceleration of a charged particle causes a disruption of the electromagnetic field that travels away from its origin at the speed of light. Radiation will be emitted as a result of acceleration applied parallel to the particle's velocity such that its speed changes (*e.g.* bremsstrahlung radiation), or perpendicular resulting in a change in the particle's direction. An electron traveling through a uniform magnetic field in the absence of an electric field will be acted upon by the Lorentz force:[20,21]

$$\boldsymbol{F} = \frac{d\boldsymbol{p}}{dt} = e(\boldsymbol{v} \times \boldsymbol{B}) \tag{2.1}$$

where e is the electron's charge, v is its velocity, and B is the magnetic field. If the magnetic field and velocity are perpendicular, the resulting force will be perpendicular to both, and the electron will undergo circular motion. For non-relativistic particles, the Lorentz force can be related to the angular acceleration to obtain an expression for the angular frequency

$$\omega_{cyc} = \frac{v}{\rho} = \frac{eB}{m_e} \tag{2.2}$$

where ρ is the radius of curvature and m_e is the mass of the electron. For the non-relativistic case ($\beta \ll 1$, where $\beta = v/c$), the emitted radiation will have a single frequency component given by ω_{cyc}. The total power emitted by the accelerated electron is given by the Larmor formula:[20,21]

$$P = \frac{e^2 a^2}{6\pi\varepsilon_0 c^3} \tag{2.3}$$

where a is the acceleration, and ε_0 is the permittivity of free space. The radiation is emitted with the spatial distribution of the familiar dipole pattern characterized by a $sin^2 \Theta$ dependence (Fig. 2.6), where Θ is measured with respect to the direction of acceleration. No radiation is emitted at $\Theta = 0$.

As the electron's velocity approaches c, relativistic effects become important. For an ultra-relativistic charged particle, this results in a drastic change in the frequency, power, and angular distribution of the emitted SR from the non-relativistic case described above. The power emitted from an ultra-relativistic particle in circular motion is given by the Liénard's generalization of the Larmor formula[20]

$$P=\frac{e^2a^2}{6\pi\varepsilon_0c^3}\gamma^4 \tag{2.4}$$

where γ is the Lorentz factor given by

$$\gamma=\sqrt{1/\left(1-\beta^2\right)}=\frac{E_e}{m_ec^2}. \tag{2.5}$$

The emitted power is thus proportional to the fourth power of the particle's energy, E_e, and inversely proportional to the fourth power of the particle's mass. Since present day synchrotron light sources have storage ring energies that correspond to γ on the order of 10^3 to 10^4, the power is increased by a factor of 10^{12} to 10^{16} compared to non-relativistic electrons.

The angular distribution of emitted radiation in the electron's frame of reference is the dipole pattern characteristic of the non-relativistic case. A Lorentz transformation applied to the $sin^2\Theta$ dependence results in the SR being collapsed into an extremely forward peaked cone in the laboratory frame of reference (Fig. 2.6). This cone of radiation has a half-angle opening given by

$$\theta \approx 1/2\gamma. \tag{2.6}$$

For storage rings in the GeV range the resultant opening angle is sub-milliradian. The radiation cone emitted down a beamline is reminiscent of a sweeping searchlight as the electron moves along the radius of curvature. The divergence of the SR produced from an electron beam will have a slightly greater divergence than that for a single electron (Eq. 2.6) due to the angular dispersion of the electron beam itself.

The rapidly sweeping, narrowing cone creates a very short pulse of radiation as it circulates as seen by a stationary observer in the laboratory frame of reference (Fig. 2.6). A simple geometric analysis considering the opening angle of the photon beam ($2\theta \approx 1/\gamma$)

and the time it takes for the photons to reach the observer, can be made[6,14,16,22] to show that the pulse of radiation has a temporal length given by

$$\Delta\tau \approx m_e/Be\gamma^2. \tag{2.7}$$

Based on Fourier theory, this short pulse will correspond to a broad energy spectrum of frequency components up to a critical energy given by[6,14,16,20,22]

$$E \sim \frac{1}{\Delta\tau} \sim Be\gamma^2/m_e. \tag{2.8}$$

The transition from the monoenergetic cyclotron radiation spectrum (Equation 2.2) to the broad SR emission spectrum (Equation 2.8) as the particle's energy increases from non-relativistic to highly relativistic energies is demonstrated in Fig. 2.9. As the energy of an electron increases, and the pulse length decreases, the radiation emitted from the electron becomes dominated by harmonics of a fundamental frequency until it becomes nearly continuous.[6,23] The SR spectrum becomes truly continuous due to the energy spread of radiating electrons within the bunch, oscillations around the ideal orbit, and the statistical nature of radiation emission. [6]

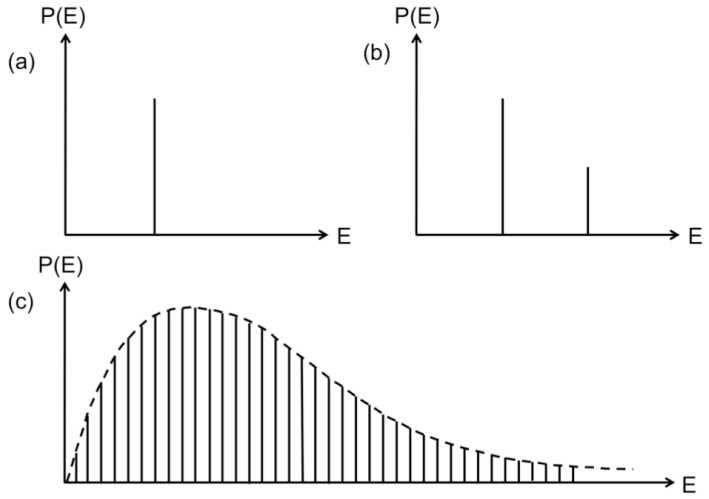

Figure 2.9 The power spectrum for a (a) non-relativistic, (b) intermediate energy, and (c) highly relativistic charged particle's emitted radiation as a function of photon energy, E. The images demonstrate the increased contribution of harmonics as the particle's speed increases. (Image adapted from: G.B. Rybicki and A.P. Lightman, *Radiative Processes in Astrophysics* (WILEY-VCH Verlag CmbH & Co. KGaA, Weinheim, 2004).[23] Reproduced with permission.)

In addition to the extreme broadening of the energy spectrum at relativistic energies, the simple geometric approximation of the pulse length and cut-off energy (Eq. 2.7 and 2.8, respectively) also indicate that there is a significant increase in the emitted photon frequencies. This transformation to higher energies is due to relativistic length contraction (increases frequency by a factor of γ), as well as the relativistic Doppler effect, given by:[24]

$$f=f_0\gamma(1+\beta\cos\alpha) \tag{2.9}$$

where f is the frequency of the emitted radiation in the laboratory frame of reference, f_0 is the frequency in the electron frame of reference, and α is the emission angle, with respect to the electron trajectory, in the electron's frame of reference. On axis (α=0) and for $\beta\approx1$, the Doppler effect increases the frequency by an additional factor of 2γ. The magnitude of the Doppler effect falls off with angle, and this results in the highest frequency photons emitted at the center of the narrow cone of radiation.

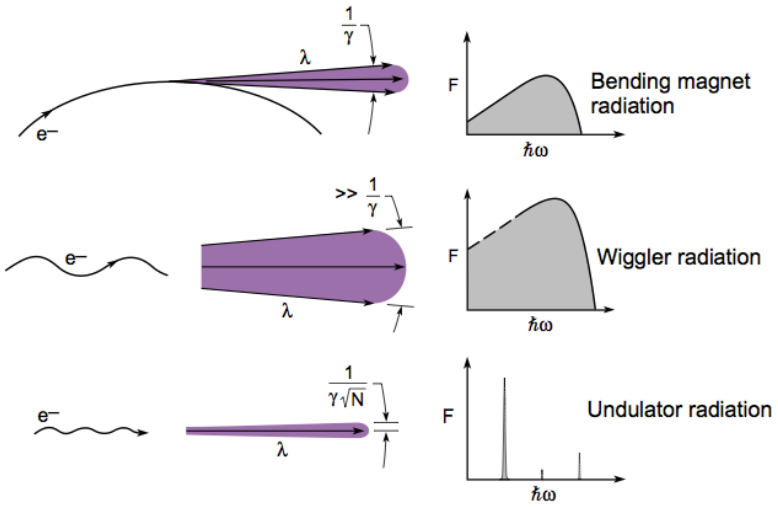

Figure 2.10 General representations of the spatial and energy distributions (flux, F, versus energy, $\hbar\omega$) produced by the three different types of magnetic devices, BMs, wigglers and undulators, used in storage rings for SR production. (Image reproduced from: D.T. Attwood, *Soft X-Rays and Extreme Ultraviolet Radiation: Principles and Applications* (Cambridge University Press, New York, NY, USA, 2007). Reprinted with the permission of Cambridge University Press and consent of the author.[22])

The specific characteristics of the emitted radiation depend on a number of factors. The emitted energy, power and degree of collimation depend strongly on the

electron energy. The emitted energy spectrum and power also depend on the strength of the magnetic field through which the electron beam passes. The size of the beam, and its polarity, will depend on the electron trajectory through the magnetic device, and thus on its dimensions. The basic characteristics of SR produced in a BM, wiggler and undulator (Fig. 2.10) will be discussed next.

2.4.2 Bending magnet radiation

A BM is simply a dipole magnet with a uniform magnetic field, and thus electrons passing through the magnet's field are deflected onto a circular arc. As the electrons travel through the field of the BM, the narrow cone of emitted photons sweeps along the horizontal plane of the orbit (Figs. 2.10 & 2.11). This creates a wide beam horizontally, but maintains the narrow opening angle in the vertical direction. The horizontal photon beam size is limited by a mask at the front end of the beamline.

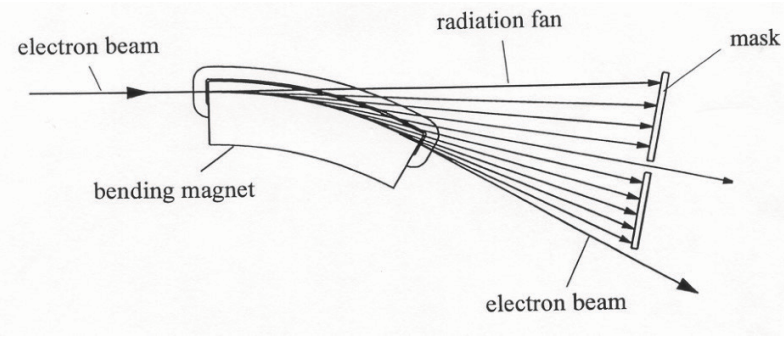

Figure 2.11 The trajectory of an electron beam and the emitted radiation fan produced in a BM. (Image reproduced from: K. Wille, The Physics of Particle Accelerators, an Introduction (Oxford University Press, Oxford, U.K., 2000.)[25] Used with permission from Oxford University Press).

While the exact energy spectrum of SR from a BM source depends on the storage ring energy and BM field, its general shape follows the "universal" functions illustrated in Fig. 2.12. The function G_1 (Fig. 2.12) provides the dependence of the photon flux, F, vertically integrated over the photon beam as a function of the beam energy with respect to a critical energy, E_c. The function H_2 provides the same dependence except for only the on-axis photons (ψ=0, where ψ is the observation angle in the vertical plane). The

critical energy is defined as the energy at which half of the radiated power is emitted at an energy above E_c and half is emitted below. The expression for the critical energy is[22]

$$E_c = \frac{3\hbar e B \gamma^2}{2\pi m_e}, \tag{2.10}$$

or in commonly used units[13,16,22]

$$E_c[keV] = 0.665\, B[T]\, E_e^2[GeV]. \tag{2.11}$$

The critical energy increases linearly with the magnetic field, and with the square of the electron beam energy. The expression for E_c shows the same dependencies on B, γ, and m_e as was determined for E (Equation 2.8) from the simple geometric analysis based on the temporal pulse length in.

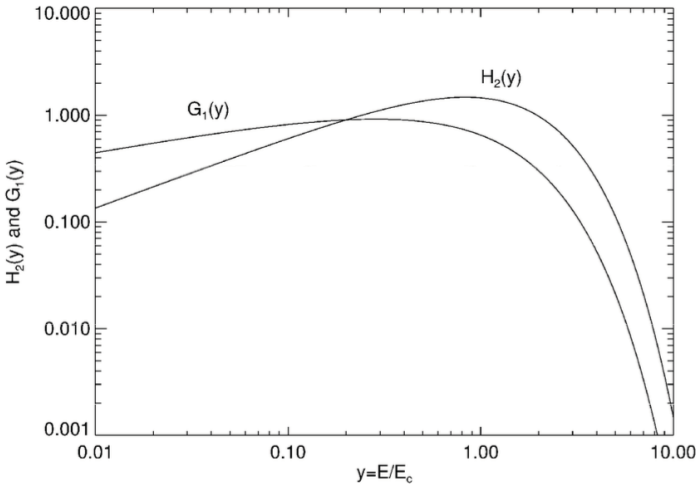

Figure 2.12 The universal brightness function, $H_2(y)$ and flux function $G_1(y)$ for the radiation emitted from a BM. The curves fall off rapidly above the critical energy, and fall off much more slowly below the critical energy. (Figure reproduced from: T.K. Sham and M.L. Rivers, A brief overview of synchrotron radiation, Reviews in Mineralogy and Geochemistry, 49, 117-147 (2002).[26] Image reprinted with permission from the Mineralogical Society of America.)

Using the critical energy and the universal curves, the photon flux from a BM source in the plane of the orbit can be calculated as[26,27]

$$\left.\frac{d^2F(E)}{d\theta d\psi}\right|_{\psi=0} = 1.327\times10^{13}\ E_e^2[GeV]\ I[A]\ H_2(y)\left[\frac{photons}{s\cdot mrad^2\cdot 0.1\%\ BW}\right] \quad (2.12)$$

where E is the photon energy, θ is the observational angle in the horizontal plane, I is the storage ring current in Amperes, $y=E/E_c$, $H_2(y)= y^2\cdot K_{2/3}^2(y/2)$ and $K_{2/3}$ is the K-type Bessel function of 2/3 fractional order. The vertically integrated flux is given by[26,27]

$$\frac{d^2F(E)}{d\theta} = 2.457\times10^{13}\ E_e[GeV]\ I[A]\ G_1(y)\left[\frac{photons}{s\cdot mrad\cdot 0.1\%\ BW}\right] \quad (2.13)$$

where $G_1=y\int_y^\infty K_{5/3}(y')dy'$. Finally, the total irradiated power from a BM over a length L of the electron beam orbit is given by[16]

$$P[kW]=1.266\ E_e^2[GeV]\ B^2[T]L[m]\ I[A]. \quad (2.14)$$

Beamlines fed by a BM have certain advantages. The beamlines are relatively inexpensive, can be more common at some facilities, and are not as bright, which generally means that there is less competition for access. Another advantage is that they produce a broad energy spectrum, and either the filtered polyenergetic beam (referred to as pink beam) can be used, or a monochromator can be employed to select a single energy from the spectrum. Disadvantages are that they are less tunable than ID beamlines because the magnetic field is fixed in order to maintain the closed orbit in the storage ring. Additionally, they are not as bright as wiggler or undulator sources.

2.4.3 Wiggler radiation

The introduction of IDs to the straight sections of a storage ring allowed a significant gain in SR brightness, and defined the development of third generation synchrotron light sources. An ID consists of a series of alternating magnetic poles that cause the electrons to follow an approximate sinusoidal path (Fig. 2.13). The multiple deflections of the charged particles lead to an increase in the SR produced compared to a BM. Additionally, because the devices can be fabricated such that the electron beam exiting the ID has no net change in position or trajectory, the magnetic field can be different than

that of a BM, and it can be adjustable, thus allowing a variable energy spectrum. An ID can be characterized by its deflection parameter, K, which is given by[14,16,26]

$$K = \frac{e}{2\pi m_e c}\lambda_u B = 0.934\ \lambda_u[cm]\ B[T]. \qquad (2.15)$$

Physically, the deflection parameter is the maximal angular deflection of the electron trajectory in units of γ^{-1} ($\theta_{max} = K\gamma$). The essential difference between the two types of IDs, wigglers and undulators, is in their K value: wigglers have $K \gg 1$, while undulators have $K \sim 1$.

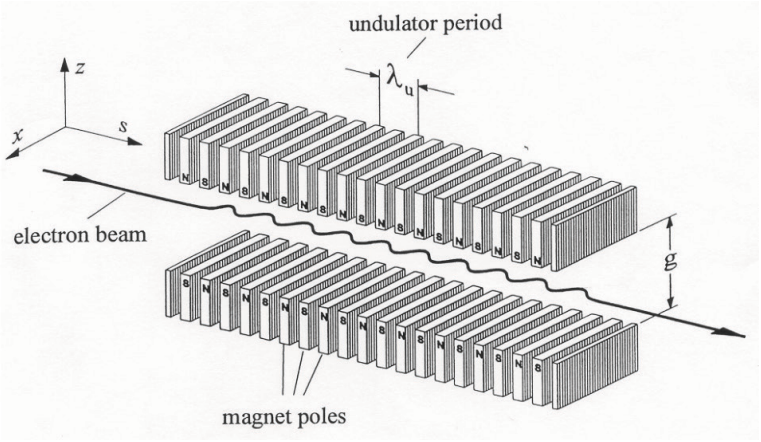

Figure 2.13 A schematic of an ID, consisting of an array of alternating magnetic poles. The electron beam oscillates as it moves through the ID. The degree of deviation from the s-axis (in the figure) determines whether the ID is a wiggler or an undulator. (Image reproduced from: K. Wille, *The Physics of Particle Accelerators, an Introduction* (Oxford University Press, Oxford, U.K., 2000.)[25] Used with permission from Oxford University Press).

The large deflections (with respect to the natural opening angle of the SR) of wigglers are accomplished by large magnetic fields and relatively long magnetic periods. The SR produced from a wiggler approximates the superposition of the emission from N_{poles} BMs, where N_{poles} is the number of magnetic poles in the array.[26] The on axis and integrated photon flux can be calculated from equations 2.12 and 2.13, respectively, with the extra factor of N_{poles}. Also, the magnetic field of a wiggler is typically greater in magnitude than that of the storage ring's BMs, which leads to higher flux and higher photon energies (Fig. 2.5). The required strong magnetic fields of a wiggler mean that

these magnetic devices are much more expensive than a BM. The natural collimation in the vertical direction (~1/γ) is maintained, but the additional transverse motion of the electron beam in the wiggler is observed by the experimenter as an effective increase in the horizontal beam divergence (by the factor K) (Fig. 2.10).

Wiggler beamlines are more difficult to gain access to compared to BM beamlines because they are brighter and in higher demand. Like a BM beamline, the energy spectrum is broad, and can be used in both polyenergetic and monoenergetic modes, but wigglers provide higher flux and higher energies, and are completely linearly polarized. Also, the energy can often be tuned by changing the magnetic field strength.

2.4.4 Undulator radiation

An undulator has a weaker magnetic field and shorter periods to achieve deflections on the order of the opening angle of the radiation cone. For certain wavelengths, as determined by the pole period of the undulator, the emitted radiation constructively interferes, and in contrast to the broad energy spectrum produced in a BM or wiggler, the undulator energy spectrum is quasi-monoenergetic (Fig. 2.10). The wavelengths of SR produced in an undulator are longer than those produced in a wiggler or BM, but the extreme collimation in both the vertical and horizontal directions, as well as the constructive inference between poles, leads to greatly enhanced brightness (Fig. 2.5).

Like a wiggler, undulator beamlines are more difficult to access than BM beamlines because they are expensive to build and less common. Unlike BM and wiggler beamlines, the undulator beamline emits narrow spectral lines, and a monochromator or collimators can be used to reduce the energy bandwidth further. Also, the emitted radiation is brighter and has a smaller spot size than any other magnetic source.

2.5 Canadian Light Source

The experimental work in this thesis was carried out at Canada's only synchrotron light source, the Canadian Light Source (CLS). The CLS (Fig. 2.14) is located on the University of Saskatchewan campus in Saskatoon, Saskatchewan. The CLS has a storage

ring that is 170.88 m in circumference, and an electron energy of 2.9 GeV (γ = 5675). Currently, the storage ring has one RF cavity operating with a 500 MHz frequency and a potential of 2.4 MV, which results in a 2 ns separation between consecutive electron bunches, each with a 34 ps (1 σ) pulse length.[28] The horizontal and vertical emittances are 22.7 nm·rad and 0.102 nm·rad, respectively.[28] These low emittances allow the high brilliances typical of third generation sources. The transverse horizontal and vertical electron beam sizes (1 σ) are 485 and 16.1 μm, respectively. The storage ring has a maximum current of 250 mA, a lifetime (1/e) of approximately 21 hours, and receives regular injections every 12 hours.

The storage ring has a double bend achromatic design consisting of 12 straight sections (9 available for IDs) and 24 BMs that each have a 1.354 T field and a 15° bend angle.[29] There are 72 quadrupoles and 36 sextupoles.[29] The CLS has the potential to feed 40 beamlines, but currently there are 14 commissioned beamlines and 3 under development.

Figure 2.14 The exterior and interior of the Canadian Light Source. (Images courtesy of the Canadian Light Source, Inc.)

2.6 BioMedical Imaging and Therapy (BMIT) beamlines

The BMIT facility at the CLS was designed to facilitate imaging and radiotherapy applications of SR. The facility consists of two beamlines, one with a BM source (05B1-1) and one with a wiggler ID source (05ID-2) (Fig. 2.15). The beamlines were designed to offer several imaging techniques in either planar or tomographic configurations:

absorption, K-edge subtraction, diffraction enhanced, and phase contrast imaging. Planned therapy techniques include microbeam radiation therapy, stereotactic synchrotron radiation therapy and photo-activation therapy.[30] These techniques serve a wide variety of biomedical applications, including cancer diagnosis and treatment, circulatory and respiratory disease, neurological disease, reproductive health, musculoskeletal conditions, and dental illnesses.

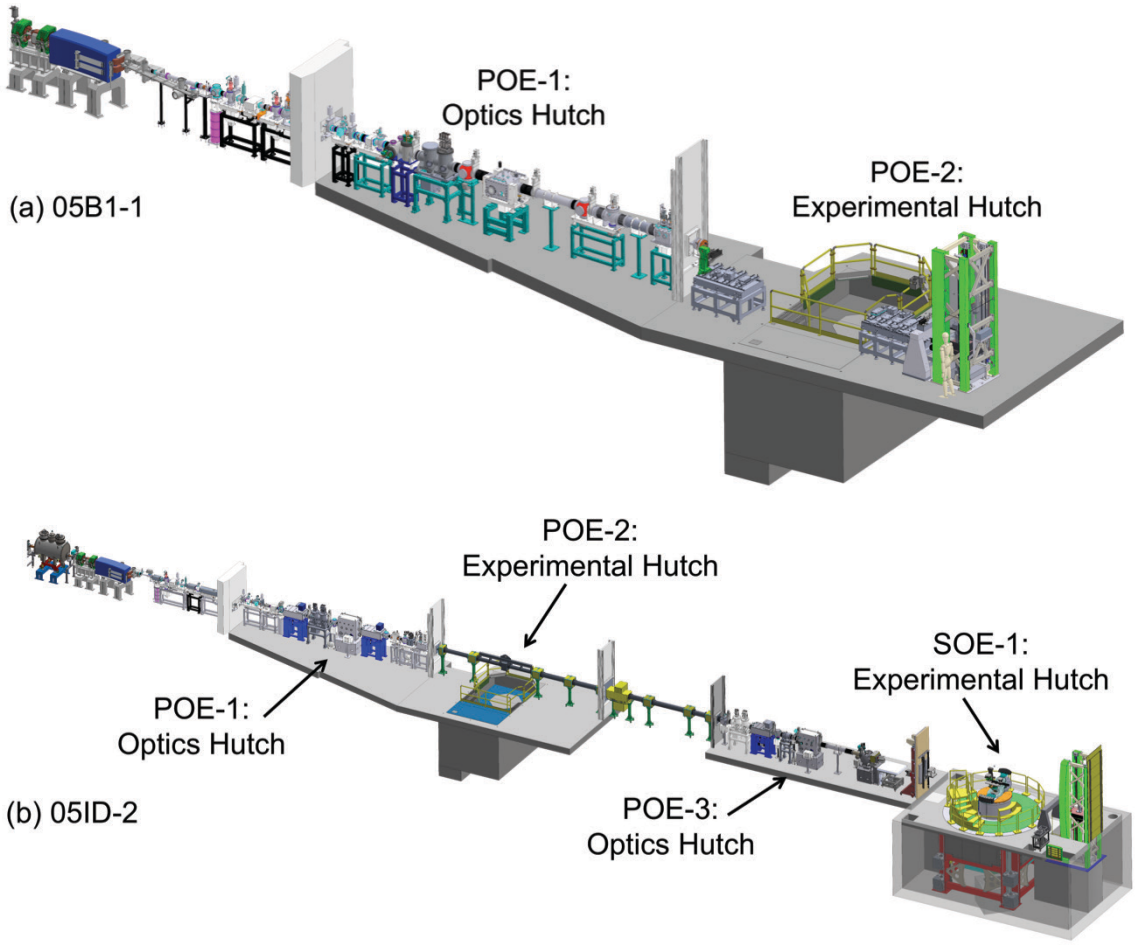

Figure 2.15 A schematic layout of the (a) 05B1-1 and (b) 05ID-2 BMIT beamlines. The POE-1 hutch houses optics equipment for both beamlines. The POE-2 hutch is presently the experimental area for the 05B1-1 beamline, and in the future will also be for the 05ID-2 beamline. The POE-3 hutch houses more optics for the 05ID-2 beamline, and the SOE-1 hutch is for monoenergetic 05ID-2 experimentation. (Images courtesy of the BMIT staff.)

2.6.1 The 05B1-1 beamline

The 05B1-1 beamline source is one of the storage ring's BMs (1.354 T, 7.14 m radius of curvature). The important parameters of the beamline are noted in Table 2.1. The distance between the BM and the end of the vacuum tube is 19.5 m. The distance from the source to the center of the optics table used to mount samples is 25.7 m. The first primary optics enclosure (POE-1) contains several components for beam modification, including collimators, filters, photon shutters, safety shutters, and ion pumps.[31] A double crystal silicon Bragg monochromator enables both monoenergetic and polyenergetic beams in the POE-2 hutch. The second optics hutch (POE-2) contains a monitor chamber, imaging shutters and experimental, motorized, precision stages. The 05B1-1 beamline has been in use since 2008, and normal operation began in 2011.[32]

Table 2.1 BMIT 05B1-1 beamline parameters[31,33-35]

Energy range	~ 8 – 60 keV
Critical energy, E_c	7.57 keV
Photon flux	1.5×10^{11} ph/s/mA/mrad^2/0.1%BW at 10 keV
Total radiated power	697.2 W @ 500mA, 2.9 GeV
Beamline length	28.5 m
Electron beam source size	173 μm (H) × 30.8 μm (V)
Horizontal divergence	10 mrad
Vertical divergence	0.2 mrad
Beam Size	240 mm (H) × 7 mm (V) at 23 m

2.6.2 The 05ID-2 beamline

The 05ID-2 beamline source is a superconducting multi-pole wiggler (Budker Institute of Nuclear Physics, Novosibirsk, Russia). The wiggler's physical parameters are given in Table 2.2. The 05ID-2 beamline has a higher flux and higher energy photon beam than the 05B1-1 beamline due to the wiggler's higher magnetic field and multiple poles. The beamline passes through several BMIT areas (Fig. 2.15) – POE-1, POE-2, the POE-2 control area (shielded), POE-3, and the secondary optics enclosure (SOE-1). Various

beam modifiers are located in the three primary optics enclosures, including masks, photon shutters, safety shutters, vacuum windows, ion pumps, collimators, filters, beryllium and Kapton windows, and three monochromators.[36] There are two potential sample positions for the 05ID-2 beamline. In the current set up, SOE-1 is used for experimentation, and only with a monoenergetic beam. The second option, for both poly- and monoenergetic applications, is in the POE-2 hutch shared with the 05B1-1 beamline. The beamline components have been installed and initial radiation testing has been performed,[32] but use of this end station would disrupt research on the active 05B1-1 beamline, and is thus presently not available.

Table 2.2 Characteristics of BMIT's superconducting wiggler that produces photons for the 05ID-2 beamline.[32,36]

Maximum magnetic field, B	4.3 T
Maximum deflection parameter, K	19.3
Period length	4.8 cm
Number of poles	25 full-field + 2 half-field poles
Gap	14.5 mm
Total radiated power	30.1 kW (500mA, 2.9 GeV)

Table 2.3 BMIT 05ID-2 beamline parameters[32,34-37]

Energy range	~ 20 – 100 + keV
Critical energy, E_c	24 keV
Photon flux	3.0×10^{12} ph/s/mA/mrad^2/0.1%BW at 20 keV
Beamline length	61 m
Electron beam source size	441 μm (H) × 16.6 μm (V)
Horizontal divergence	4 mrad
Vertical divergence	0.2 mrad
Beam Size	106 mm (H) × 5 mm (V) at 26.5 m 224 mm (H) × 11 mm (V) at 55 m

The main components of the SOE-1 hutch are: a moveable support platform for detectors, the Large Animal Positioning System (LAPS), and a granite stand offering

high stability. Currently the MRT Lift is installed on the LAPS for small to medium samples. The LAPS can travel over 2.7 m vertically at a speed of up to 20 cm/s, and has an accuracy of 100 μm.[32] The LAPS can move samples/subjects up to ~ 900 kg.[32] Experimentation on the ID beamline can occur in two hutches: the POE-2 hutch that is shared with the BM beamline, and the further downstream SOE-1 hutch.

2.6.3 Microbeam radiation therapy at the CLS

Originally an experimental MRT program was planned for the 05ID-2 beamline in the POE-2 hutch using a filtered polyenergetic beam. This would include filters to produce a mean energy of 99 keV[38] and an estimated dose rate of approximately 3000 Gy/s.[36] However, as described above, currently only a monoenergetic beam is available on the 05ID-2 beamline. The current two options for MRT experimentation are: (1) a monoenergetic beam (energies from 20 – 150 keV) on the 05ID-2 beamline in the SOE-1 hutch, or (2) a filtered polyenergetic beam on the 05B1-1 beamline with lower mean energies up to ~20 – 60 keV in the POE-2 hutch. Due to the prolonged commissioning period for the 05ID-2 beamline, the vast majority of our measurements were performed on the 05B1-1 beamline.

A mult-islit collimator (MSC) (Usinages et Nouvelles Technologies, Morbier, France) was fabricated for MRT at BMIT. The collimator is fabricated from tungsten alloy (Fig. 2.16). There are 75 slits that are each 50 μm wide, and separated by 400 μm centre-to-centre, and 8 mm thick. The MRT lift, a precise positioning system with 6 degrees of freedom, has been installed in SOE-2 for use on the 05ID-2 beamline, but could be installed in POE-2 in the future for high dose rate polyenergetic MRT experimentation.

Figure 2.16 The multi-slit collimator at the CLS. The tungsten alloy collimator has 75 50 μm wide slits separated by 400 μm centre-to-centre, and is 8 mm thick. (Image courtesy of BMIT staff.)

2.7 References

[1] A.L. Robinson, "History of Synchrotron Radiation," in *Center for X-Ray Optics Advanced Light Source X-Ray Data Booklet*, Second ed., edited by A.C. Thompson and D. Vaughan (Lawrence Berkeley National Laboratory, University of California, Berkeley, California 94720, 2001).

[2] F.R. Elder, A.M. Gurewitsch, R.V. Langmuir, H.C. Pollock, "A 70-Mev Synchrotron," J. Appl. Phys. **18**, 810-818 (1947).

[3] F.R. Elder, A.M. Gurewitsch, R.V. Langmuir, H.C. Pollock, "Radiation from Electrons in a Synchrotron," Physical Review **71**, 829-830 (1947).

[4] F. Frommberger, "Particle Accelerators Around the World," http://www-elsa.physik.uni-bonn.de/accelerator_list.html (2014) Accessed 2/23/2015.

[5] G. Muelhaupt, "Chapter 3: Injector Systems," in *Synchrotron Radiation Sources: A Primer, Vol. 1*, edited by H. Winick (World Scientific Publishing Co. Pte. Ltd., Singapore, 1994), p. 59.

[6] A. Balerna and S. Mobilio, "Introduction to Synchrotron Radiation," in *Synchrotron Radiation: Basics, Methods and Applications*, edited by S. Mobilio, F. Boscherini, C. Meneghini (Springer-Verlag Berlin Heidelberg, 2015), p. 3.

[7] P. Barnes, J.K. Cockcroft, S. Jacques, M. Vickers, "How do synchrotrons work?" http://pd.chem.ucl.ac.uk/pdnn/inst2/work.htm Accessed 2/23/2015.

[8] N. Marks, "Chapter 5: Magnet Design," in *Synchrotron Radiation Sources: A Primer, Vol. 1*, edited by H. Winick (World Scientific Publishing Co. Pte. Ltd., Singapore, 1994), p. 119.

[9] J. Noonan and D. Walters, "Chapter 8: Vacuum Systems," in *Synchrotron Radiaiton Sources: A Primer, Vol. 1*, 1st ed., edited by H. Winick (World Scientific Publishing Co. Pte. Ltd., Singapore, 1994), p. 197.

[10] D.J. Thompson and D.M. Dykes, "Chapter 4: R.F. Systems," in *Synchrotron Radiation Sources: A Primer, Vol. 1*, edited by H. Winick (World Scientific Publishing Co. Pte. Ltd., Singapore, 1994), p. 87.

[11] S. Baird, "Accelerators for Pedestrians," European Organization for Nuclear Research, CERN AB-Note-2007-014 OP (2007).

[12] "What is a beamline?" http://www.esrf.eu/about/synchrotron-science/beamline Accessed 2/23/2015.

[13] H. Winick, "Chapter 1: Introduction and Overview," in *Synchrotron Radiation Sources: A Primer, Vol. 1*, edited by H. Winick (World Scientific Publishing Co. Pte. Ltd., Singapore, 1994), p. 1.

[14] G. Margaritondo, *Elements of Synchrotron Light for Biology, Chemistry, and Medical Research* (Oxford University Press, New York, NY, USA, 2002).

[15] R.D. Schleuter, "Chapter 14: Wiggler and Undulator Insertion Devices," in *Synchrotron Radiation Sources: A Primer, Vol. 1*, edited by H. Winick (World Scientific Publishing Co. Pte. Ltd., Singapore, 1994), p. 377.

[16] J. Als-Nielsen and D. McMorrow, *Elements of Modern X-Ray Pysics* (John Wiley & Sons, Ltd., Singapore, 2001).

[17] R. Lewis, "Medical applications of synchrotron radiation x-rays," Phys. Med. Biol. **42**, 1213-1243 (1997).

[18] P. Suortti and W. Thomlinson, "Medical applications of synchrotron radiation," Phys. Med. Biol. **48**, R1-R35 (2003).

[19] A. Bravin, P. Coan, P. Suortti, "X-ray phase-contrast imaging: from pre-clinical applications towards clinics," Phys. Med. Biol. **58**, R1-R35 (2013).

[20] J.D. Jackson, *Classical Electrodynamics* (John Wiley & Sons, Inc., New York, NY, USA, 1962).

[21] D.J. Griffiths, *Introduction to Electrodynamics*, 3rd ed. (Prentice-Hall, Inc., Upper Saddle River, NJ, USA, 1999).

[22] D.T. Attwood, *Soft X-Rays and Extreme Ultraviolet Radiation: Principles and Applications* (Cambridge University Press, New York, NY, USA, 2007).

[23] G.B. Rybicki and A.P. Lightman, *Radiative Processes in Astrophysics* (WILEY-VCH Verlag CmbH & Co. KGaA, Weinheim, 2004).

[24] P.J. Duke, *Synchrotron Radiation: Production and Properties* (Oxford University Press, New York, NY, USA, 2009).

[25] K. Wille, *The Physics of Particle Accelerators, an Introduction* (Oxford University Press, Oxford, U.K., 2000).

[26] T.K. Sham and M.L. Rivers, "A brief overview of synchrotron radiation," Applications of Synchrotron Radiation in Low-Temperature Geochemistry and Environmental Sciences **49**, 117-147 (2002).

[27] K. Kwang-Je, "Characteristics of Synchrotron Radiation," in *X-Ray Data Booklet*, 2nd ed., edited by A.C. Thompson, D.T. Attwood, E.M. Gullikson, M.R. Howells, J.B. Kortright, A.L. Robinson, J.H. Underwood (Lawrency Berkeley National Laboratory, Berkeley, CA, USA, 2001).

[28] "Storage Ring Status," http://www.lightsource.ca/operations/storageRing_status.php Accessed 2/23/2015.

[29] L.O. Dallin, "Synchrotron Light Source Magnets," CLS Design Note 5.2.31.2 Rev.0 (2001).

[30] D. Chapman, "BioMedical Imaging and Therapy Beamline Preliminary Design Report," CLSI Document 26.2.1.2 Rev. 0 (2006).

[31] T.W. Wysokinski, D. Chapman, G. Adams, M. Renier, P. Suortti, W. Thomlinson, "Beamlines of the biomedical imaging and therapy facility at the Canadian light source - Part I," Nuclear Instruments & Methods in Physics Research Section A-Accelerators Spectrometers Detectors and Associated Equipment **582**, 73-76 (2007).

[32] T.W. Wysokinski, D. Chapman, G. Adams, M. Renier, P. Suortti, W. Thomlinson, "Beamlines of the biomedical imaging and therapy facility at the Canadian light source - Part 3," Nuclear Instruments & Methods in Physics Research Section A-Accelerators Spectrometers Detectors and Associated Equipment **775**, 1-4 (2015).

[33] "Biomedical Imaging and Therapy (BMIT-BM) 05B1-1,**"** http://www.lightsource.ca/beamlines/bmit.php Accessed 2/23/2015.

[34] "BioMedical Imaging and Therapy Facility (BMIT) at the Canadian Light Source," http://ex.lightsource.ca/bmit/images/Trifold-Poster-WEB.pdf Accessed 2/23/2015.

[35] "Beamline Status Update," http://www.lightsource.ca/uso/beamline_status.php Accessed 2/23/2015.

[36] T.W. Wysokinski, D. Chapman, G. Adams, M. Renier, P. Suortti, W. Thomlinson, "Beamlines of the Biomedical Imaging and Therapy Facility at the Canadian Light Source - Part 2." 11th International Conference on Synchrotron Radiation Instrumentation (SRI 2012) **425**, UNSP 072013 (2013).

[37] "Biomedical Imaging and Therapy (BMIT-ID) 05ID-2," http://www.lightsource.ca/beamlines/bmit_2.php Accessed 2/23/2015.

[38] D. Anderson, E.A. Siegbahn, B.G. Fallone, R. Serduc, B. Warkentin, "Evaluation of dose-volume metrics for microbeam radiation therapy," Med. Phys. **39**, 4645-4645 (2012).

3 CHARACTERIZATION OF THE BIOMEDICAL IMAGING AND THERAPY BEAMLINES

3.1 Introduction

It is necessary to have a thorough understanding of a photon beam's characteristics before it is used for radiation therapy or imaging applications to maximize the efficacy of a treatment, to properly interpret an image, and particularly for the safety of the patient. The photon beams produced by x-ray sources used for conventional radiation therapy and imaging are described in terms of energy spectrum, geometric qualities (*e.g.*, beam profiles, divergence), and absolute dose. Similarly, these same features of a synchrotron x-ray beam used for imaging and therapy are required. Although theory (Chapter 2) can be used to predict the detailed characteristics of radiation produced by a synchrotron light source, these calculations must be validated by measurement. In this chapter, the BioMedical Imaging and Therapy (BMIT) beamlines' output reproducibility, energy, geometry and relative dosimetry will be described. For imaging and therapy applications that have been performed and planned on the BMIT beamlines, determination of the absolute magnitude of the dose rate is also vital. Absolute and reference dosimetry of the wide beam using ionization chambers will be discussed in Chapters 4 and 5.

The 05B1-1 BMIT beamline has been available for experimentation since 2010, in both monoenergetic and polyenergetic modes. Various beam energies, produced using either a crystal monochromator to select a single energy or by introducing copper or aluminum filtration into the polyenergetic beam, have been considered to match the conditions used for various imaging or therapy techniques on the beamlines, or to simply vary the dose rate and mean energy of the beam. Measurements were taken to characterize both the broad beam and microbeam configurations. Access to the 05ID-2 BMIT beamline has been considerably more limited due to the long process of commissioning this more complex and more powerful beamline. Only monoenergetic, broad beam conditions have been available for measurements on the 05ID-2 beamline. Additionally, stability issues have limited the reproducibility and therefore value of some measurements.

The description of the wide synchrotron beam is both important for microbeam radiation therapy (MRT) dosimetry, and for the other imaging and therapy applications on the BMIT beamlines. The wide beam characterization includes the examination of output stability and reproducibility, profiles vertically over the height of the non-uniform beam, theoretical and experimental investigations into beam quality, and relative dose deposition at depth in water. A study of the microbeam array, created by introducing the multi-slit collimator (MSC) into the filtered 05B1-1 beam, was also undertaken. This included investigating the alignment of the MSC, the horizontal and vertical profiles across a single microbeam, the change in profile shape, dose and width with depth in solid water, and the variation of relative peak and valley dose across the whole MSC. Several detectors were used to characterize the broad beam, including cavity ionization chambers, a free air ionization chamber, a solid state diamond detector and radiochromic film. Selected measurements were compared with theoretical values derived from analytical calculations and Monte Carlo simulations.

3.2 Materials and methods

3.2.1 Beamlines and experimental sessions

Several experimental sessions occurred on the 05B1-1 beamline between May 2010 and July 2014. The majority of characterization was done for the polyenergetic beam with filtrations of 0.938 mm Cu and 1.103 mm Cu, but testing was also done for a minimum of no added filtration and a maximum of 2.210 mm Cu. Aluminum or copper filtration was added to the beam to increase the mean energy and decrease the dose rate. The majority of filtration was achieved using the *in vacuo* beamline filters, positioned at an angle of 25° with respect to the direction of x-ray propagation. The 05B1-1 beamline is also capable of producing monoenergetic beams through the insertion of a Bragg double crystal Si (1,1,0) monochromator ($\Delta E/E = 5\times10^{-5}$).[1] Single energies are selected by varying the angle of the crystals with respect to the horizontal x-ray beam. We studied monoenergetic energies of 20.0 keV, which is commonly used for imaging applications, and 33.3 keV, chosen because it is near the K-edge of iodine (for K-edge subtraction

imaging). A filtration of 0.110 mm Al was used with the monoenergetic beams to remove low energy photons and reduce the heat load on beamline components. Measurements were taken for both broad beam and microbeam configurations. The broad beam dimensions were controlled by the beamline jaws. The microbeam array was created by using the MSC (Section 2.6.3, Fig. 2.16). The collimator is made of 8 mm thick (in beam direction) tungsten alloy sheets separated by air gaps to create the array. The gaps are 50 μm wide and 4 mm in height, and have a centre-to-centre spacing of 400 μm. Measurements were taken in POE-1 (Fig. 2.15) at distances between 25 and 28.3 m from the bending magnet (BM) source.

Experiments on the 05ID-2 beamline were performed in August 2013 and June 2014, during which time the beamline was still being commissioned. Only monoenergetic x-ray beams were available for experimentation. Two monochromators were used to produce the monoenergetic beams: the K-edge subtraction (KES) monochromator single crystal bent Laue Si (1,1,1) ($\Delta E/E = 10^{-3}$) and the computed tomography (CT) monochromator double crystal bent Laue Si (1,1,1) ($\Delta E/E = 10^{-2}$).[1] Filtration was introduced into the beam to protect the optics equipment and reduce dose rates. Measurements on the 05ID-2 beamline were only performed for the broad beam configuration in SOE-1 (Fig. 2.15). The detectors were positioned on the Large Animal Positioning System (LAPS) and MRT Lift (Section 2.6.2), located at a distance of 55.0 m from the insertion device (ID) source.

3.2.2 Description of detectors

A variety of detectors were used to experimentally examine the x-ray beam parameters including ionization chambers, a solid state diamond detector, and radiochromic film. The dimensions of the three cavity chambers are given in Table 3.1. The Capintec PR06C (Capintec, Inc., Ramsey, New Jersey, USA) was used for the majority of the ionization chamber measurements. The Wellhofer IC10 (IBA, Louvain-La-Neuve, Belgium) has a waterproof sleeve, and was used for percent depth dose measurements in a water phantom. The PTW 23343 (PTW, Freiburg, Germany), a parallel plate ionization chamber, was chosen for its rating for low energy photon beams, and its spatial resolution

in the depth direction (0.03 mm thick entrance window, 1 mm thick sensitive volume). The three cavity chambers were operated at 300 V.

Table 3.1 The dimensions and materials of the cavity chambers used for beamline characterization.

Manufacturer and Model	Cavity volume (cm^3)	Cavity radius (cm)	Wall material	Wall thickness (g/cm^2)	Central electrode
Capintec PR06C	0.65	0.32	C-552	0.050	C-552
Wellhofer IC10	0.14	0.30	C-552	0.070	C-552
PTW 23342	0.02	0.15	Polyethylene	0.003	---

A PTW 60003 diamond detector (PTW, Freiburg, Germany) was used for its high spatial resolution along the detector's longitudinal axis. The detector's active volume is a diamond wafer with a radius of 1.47 mm, and a thickness of 0.25 mm, embedded in polystyrene. The irradiation of the active volume leads to the excitation of electrons from the valence to the conduction band, and the produced charges are collected by an applied voltage (100 V). The cavity ionization chambers and diamond detector were used in conjunction with a Unidos E (PTW, Freiburg, Germany) electrometer.

A Victoreen 480 free air ionization chamber (The Victoreen Instrument Co., Cleveland, OH (no longer commercially available)) was primarily used for absolute air kerma rate measurements (Chapter 4), but was also used to determine beam quality. This Attix-type free air chamber[2] (described in detail in Chapter 4) has telescoping cylindrical electrodes that extend between 32 and 62 cm, and are used to define the active volume. The outer aluminum electrodes have a 30 cm diameter, and the off-centre aluminum collecting electrode has a diameter of 0.95 cm. The chamber was operated between 3000 and 5000 V, and the collected charge was measured using a Keithley 6517A (Keithley Instruments, Inc., Cleveland, Ohio, USA) electrometer.

Three types of radiochromic film, Gafchromic EBT2, EBT3 and HD810 (Ashland Inc., Covington, KY, USA), were used to measure two-dimensional dose distributions (Table 3.2). The film was digitized using either an Epson V700 Perfection or Epson Expression 10000XL (Epson, Suwa, NGN, Japan) flatbed scanner. The films were scanned at the center of the flatbed scanner to reduce variation in pixel values due to

position-dependent scanner sensitivity across the scanner bed.[3] The film was consistently scanned in the same orientation with respect to the scanner's CCD array, which is necessary due to the change in absolute pixel values (up to ~10 %[4]) in the resulting image when the film is scanned in landscape versus portrait orientations for certain CCD scanners. This is attributed to the anisotropic scattering from the rod-like active particles that tend to align themselves with the coating direction.[5] The film was scanned at a nominal resolution of 4800 dots per inch (dpi) (=5.3 μm) and a color depth of 48 bits (16 per colour channel). The red channel image was analyzed as recommended by the manufacturer because the film exhibits the highest absorption at "red" wavelengths, but does not allow for heterogeneity corrections available with triple-channel methods.[4-6] A calibration curve was created using a polynomial fit in MATLAB, and was used to convert pixel value to dose.

Table 3.2 Gafchromic film characteristics[5,7-11]

Model	Thickness of film / active layer (μm)	Dose range (Gy)	Uniformity	Effective atomic number
EBT2	278/ 28	0.01 - 40	< 3 %	6.84
EBT3	280 / 30	0.01 - >40	< 3 %	6.7
HD-810	97 / 6.5	10 - 1000	< 8%	6.0 – 6.5

3.2.3 Output: Linearity with current-time product (05B1-1)

As described in Sections 2.2.1 and 2.2.2, the electron beam current in the storage ring of a synchrotron light source decays with time, and the beam's dose rate decays proportionally. At the CLS, the dose rate can change by nearly a factor of two between storage ring injections. To deliver equivalent doses, the irradiation time must increase as the storage ring current decays. For this purpose, beamline controls allow selection of the mAs, the product of the ring current and beam-on time.

The BMIT beamlines have a series of shielded shutters to control the transport of the x-ray beam from the BM or wiggler source through the hutches. For experiments requiring rapid control of the 05B1-1 x-ray beam, a set of fast imaging shutters are used. The minimum dose that can be delivered in a reproducible manner is limited by the speed and precision of the imaging shutter control. To investigate the lower limits of

deliverable doses, the linearity between ion chamber reading (Capintec PR06C) and the storage ring current-time product (mAs) was measured. The shutters are located at approximately 21 m, and the ion chamber was positioned at approximately 25 m from the BM source on the 05B1-1 beamline. The polyenergetic beam was used with a filtration of 0.938 mm Cu.

3.2.4 Output: CT monochromator stability (05ID-2)

Crystal monochromators are used to produce monoenergetic x-ray beams on the 05ID-2 beamline. The high heat load of the intense synchrotron x-ray beam on the monochromator crystals can cause temperature drifts, and a change in output. To investigate the stability of the 05ID-2 double crystal monochromator (relatively newly installed at time of measurement), the Victoreen 480 free air ionization chamber was used to take readings over several hours (Fig. 3.1). The measurements were taken with an energy of 100 keV and a magnetic field of 4.007 T.

Figure 3.1 The Victoreen 480 free air ionization chamber mounted on the MRT Lift in the SOE-1 hutch on the 05ID-2 beamline for beam stability and quality measurements.

3.2.5 Broad beam geometric characteristics: Vertical profile, beam size as a function of collimator setting, and divergence (05B1-1)

A synchrotron x-ray beam is non-uniform in both intensity and energy spectrum in the vertical direction. The highest x-ray energies lie in the horizontal plane. The mean

energy and intensity decrease when moving in the positive or negative vertical y-direction. The vertical profile on the 05B1-1 beamline was measured most extensively for the 0.938 mm Cu filtered beam. The profile in the vertical direction was characterized by three methods:

1) A 100 μm vertical beam defined by a slit between polished steel blocks was stepped across the full height of the beam in unison with the PR06C ion chamber, which was centered with respect to the slit beam (Fig. 3.2).

2) A two-dimensional measurement with Gafchromic EBT2 film, subsequently scanned with an Epson Perfection V700 flatbed scanner.

3) The PTW diamond detector aligned such that the thin wafer dimension is vertical, providing a spatial resolution of 250 μm.

Multiple methods were used to determine the profile due to uncertainty in the detectors' energy dependence in the low energy beam. Because the beam's energy changes with vertical position, the detector response potentially also changes with vertical position, which would compromise the accuracy of the profile measurement. Additional measurements using the beam defining slit and the PR06C ion chamber were taken for the unfiltered polyenergetic beam, the polyenergetic beam filtered with 1.103 mm Cu, and two monoenergetic energies (20.0 and 33.3 keV, 0.110 mm Al filtration).

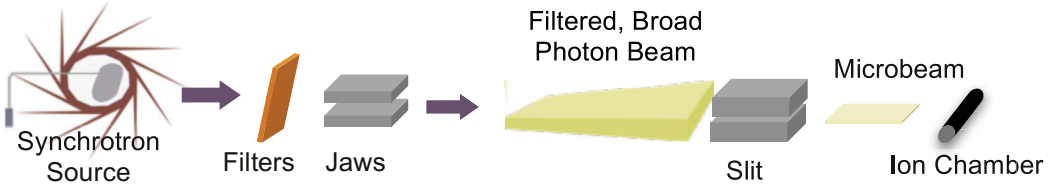

Figure 3.2 Schematic for the experimental set up of measuring the broad beam profile using the PR06C ion chamber. The filtered broad beam passed through a 100 μm slit to create a horizontal microbeam. The slit and ionization chamber were then stepped vertically through the broad beam.

The beam size with respect to nominal beamline collimator settings in both the horizontal and vertical planes was measured using Gafchromic EBT2 film. The film was placed at 26.13 m from the BM source. For the polyenergetic beam filtered with 0.938

mm Cu, the full width at half maximum (FWHM) sizes were measured for several vertical collimator settings between the smallest 0.1 mm and the maximum of 8.7 mm.

The broad beam's divergence was investigated by measuring the difference in beam size at a distance of 25.0 m versus 28.3 m from the BM source. The measurements were made on the unfiltered 05B1-1 beamline using Gafchromic HD-810 film.

3.2.6 Broad beam energy: Theoretical energy spectra (05B1-1 and 05ID-2)

The energy spectra of the 05B1-1 and 05ID-2 beamlines were calculated using SPECTRA (Version 10.0) (Fig. 3.3), free software specifically designed for the analytical calculation of synchrotron radiation (SR) characteristics developed by Tanaka and Kitamura.[12] SPECTRA requires several storage ring and beamline parameters to calculate the energy spectrum. The storage ring parameters include the electron energy and current, the circumference, the number of electron bunches, the length of the bunch, the emittance, the coupling constant, the energy spread, the alpha and beta functions (Twiss parameters; describe beam shape and angular deviation as function of position in storage ring[13]), and the dispersion. For a BM beamline, the magnetic field and bending radius are required. For a wiggler source, the magnetic field, pole length, and number of poles must be provided.

All spectra calculations also accounted for beam filtration and attenuation in air. Each beamline used in our experiments includes fixed filtration from multiple beamline windows: the 05B1-1 beamline has a 0.1 mm thick Kapton window and two 0.25 mm beryllium windows, while the full 05ID-2 beamline going to the SOE-1 hutch has a 1.5 mm Kapton window and three beryllium windows totaling 0.75 mm. The proposed configuration of the beam used for a future MRT program at the CLS would be a polyenergetic 05ID-2 beam terminating in POE-2 that would pass through 0.75 mm of beryllium (three windows) and 0.1 mm of aluminum (one window). Because of the relatively low X-ray energies and large distances between the exit window (before which the beam is under high vacuum) and the point of measurement, air attenuation cannot be ignored. On the 05B1-1 beamline, the energy spectrum was calculated at a distance of 25.17 m from the BM source, with 5.68 m of air. Additional calculations were obtained

for various filter combinations to match experimental conditions. For the 05ID-2 beamline, calculations were done at 27.5 m from the wiggler source with 2.5 m of air, and at a distance of 55.0 m with 7.0 m of air for the POE-2 and SOE-1 hutches, respectively.

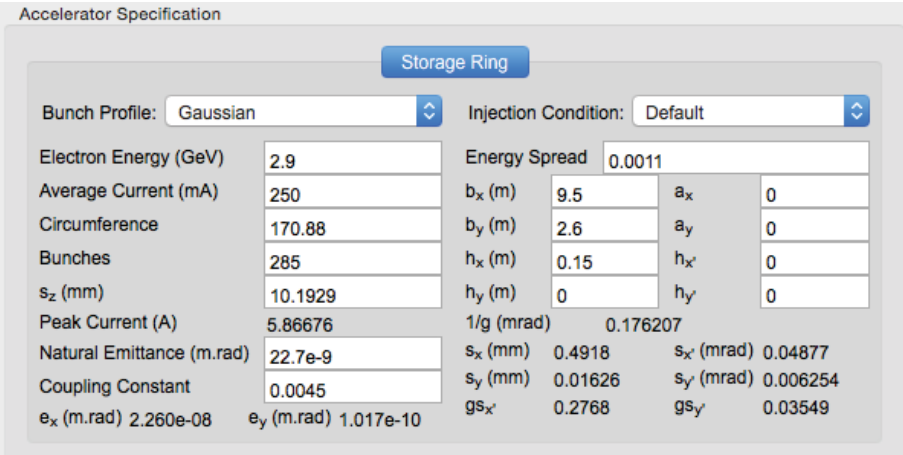

Figure 3.3 A screenshot displaying the required storage ring information for the calculation of SR energy spectra using the SPECTRA software.

Since the energy and intensity of these synchrotron beams change rapidly as a function of vertical position, beam collimation affects the calculated spectra. Calculations were done for beams passing through either of two collimations. For the first, a 0.52 mm diameter circular opening represented the small aperture used for measurements with the free air ion chamber. The second configuration is a 32 mm (x) × 0.5 mm (y) rectangular slit, corresponding to the width of our multi-slit collimator, and a height approximating the vertical collimation that has been used for MRT animal experiments at the European Synchrotron Radiation Facility.

To determine the sensitivity of the output to uncertainties in the storage ring or beamline parameters, each variable was assessed individually to determine its effect on the mean energy and total flux. This was done for the 05B1-1 beamline for two scenarios - with only the permanent beamline filtration (vacuum windows), and with an additional 1.103 mm Cu filtration (chosen as a mid-range amount of filtration).

3.2.7 Broad beam energy: Half-value layer values (05B1-1 and 05ID-2)

The direct measurement of the energy spectrum of SR is challenging due to the high intensity of many beams. To experimentally validate the predicted beam energy we instead chose to measure the half-value layer (HVL) using aluminum and copper filters (Inovision Radiation Measurements, LLC., Cleveland, OH, USA). For clinical x-ray beams with energy lower than the megavoltage range, the HVL is often used to describe beam quality.[14] On the 05B1-1 beamline, HVL measurements were done for the polyenergetic beam with the following filtrations: 0.552 mm Cu, 0.552 mm Cu + 13 mm Al, 0.938 mm Cu, 1.103 mm Cu, and 2.210 mm Cu. Monochromatic 20.0 and 33.3 keV photon beams were also evaluated. On the 05ID-2 beamline, measurements were taken with 40, 80, 100, and 150 keV monoenergetic beams generated at a magnetic field of 4.0 T. Our initial HVL measurements were made with the Capintec PR06C on the 05B1-1 beamline using 0.938 mm Cu filtration. The beam was collimated to 4 mm horizontally, and was not collimated vertically. For all other beam configurations, the HVL was determined during later experimental sessions using the Victoreen 480 with a 0.52 mm diameter aperture, which approximated narrow beam geometry.

To determine the first half-value layer, the experimental data were fit by a two term exponential function using MATLAB's curve fitting toolbox (MathWorks, Natick, MA, USA). The experimental HVLs were compared to the predicted values based on either the computed energy spectrum obtained from SPECTRA (Section 3.2.6) or the nominal monoenergetic energy based on the monochromator's crystal angle.

3.2.8 Broad beam energy: Spectroscopy (05ID-2)

The energy of four monoenergetic x-ray beams on the 05ID-2 beamline was measured using a X-123CdTe spectrometer (Amptek, Inc., Bedford, MA, USA). The nominal energies were 40, 80, 100 and 150 keV. The ID magnetic field was set at 4.0 T. The spectrometer was placed directly below the window between the POE-3 and SOE-1 hutches through which the x-ray beam passes. Thus, the majority of photons reaching the detector must undergo Compton scattering in air with a scattering angle of 90°. The Compton peak was determined as the central energy of the resulting histogram of counts

versus energy. The incident photon energy was calculated from the equation for the energy of the scattered photon (hv') following a Compton interaction[15]

$$hv' = hv \cdot \frac{1}{1+\frac{hv}{m_e c^2}(1-\cos\theta)} \tag{3.1}$$

where hv is the energy of the incident photon, hv' is the energy of the scattered photon, θ is the angle between the propagating initial photon and the scattered photon, m_e is the mass of an electron, and c is the speed of light. By substituting 90° for θ, and the scattered x-ray energy from the spectrometer results, it is possible to solve for the incident x-ray energy.

3.2.9 Broad beam energy: Percent depth dose (05B1-1)

To characterize beam penetration in water, the percent depth dose (PDD) was measured on the 05B1-1 beamline for different configurations. The most thorough determination was for the polyenergetic beam filtered by 0.938 mm Cu. The measurements were taken at a distance of 27.5 m from the BM source with a 32 mm wide beam (uncollimated vertically). The Wellhofer IC10 was used to measure dose in an in-house built water phantom (Fig. 3.4). The water phantom was built to accommodate the horizontal beam, and has a thin Mylar window and a jig to hold the ionization chamber. The chamber dimensions limit the shallowest depth that can be measured to 4.1 mm. The PDD was also measured with the PTW 23342, in a Lucite jig and slabs of Solid Water (Gammex, Inc., Middleton, WI, USA). There was no adjustment to the PTW PDD to account for potential changes in scatter due to the presence of the Lucite. The parallel plate chamber provides improved spatial resolution in the depth direction, which was particularly beneficial for measuring the dose near the surface. Finally, Gafchromic EBT2 film was used to measure the PDD at depth in Solid Water. The EBT2 PDD was measured for three exposures: 100, 500 and 1000 mAs. The experimental PDDs were compared to a PENELOPE[16] Monte Carlo simulation of the PDD in a 16 cm diameter, 16 cm long cylindrical water phantom. The simulation input was a SPECTRA-generated photon spectrum for the 05B1-1 beamline with 0.938 mm of copper filtration (Section 3.3.6, Fig. 3.9(a)). The beam was approximated as a 1 x 1 cm^2 beam uniform in the vertical and

horizontal directions. The number of histories used was 10^8, and the resolution in the depth direction was 2 mm. The PENELOPE transport parameters are discussed in more detail in Chapter 6, but briefly, the cut-off energy loss for hard elastic collisions (W_{CC}) and hard bremsstrahlung emission (W_{CR}) for both electrons and photons were set to 1 keV. The mixed simulation parameters that define the allowed average angular deflection and maximum fractional energy loss between consecutive hard elastic events (C1 and C2) were set to small values (0.01) so that simulations were almost completely done in detail. Because there was either missing data or a large amount of uncertainty for the surface dose for most measurement methods, the experimental and Monte Carlo curves were normalized at a depth of 2 cm.

The Wellhofer IC10 and water phantom were used to measure the PDDs for additional 05B1-1 beams: polyenergetic with 1.103 mm Cu filtration and monoenergetic 20.0 and 33.3 keV. Measurements were made at 26.0 m from the BM source, and with a horizontal beam size of 70 mm (uncollimated vertically). Since the shallowest depth measured was 4.1 mm, the dose at the surface of the water phantom was estimated from a polynomial fit of the experimental data using the MATLAB curve-fitting toolbox.

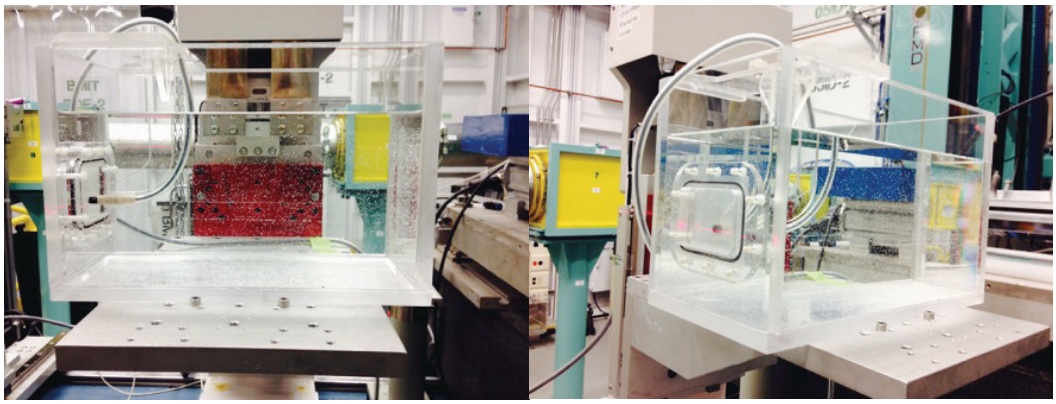

Figure 3.4 The experimental set up for the PDD measurement using our in-house built water phantom, with a thin Mylar window and Welhoffer IC10 cavity ionization chamber on the 05B1-1 beamline.

3.2.10 Microbeam array: Monte Carlo dose distributions (05B1-1 and 05ID-2)

The Monte Carlo code PENELOPE was used to simulate the microbeam array dose distributions in a 16 cm long, 16 cm diameter cylindrical water phantom. As has been done in previous work,[17-20] a single, rectangular, parallel microbeam was modeled at the surface of the cylindrical water phantom. The dose was tallied in parallelepipeds that were the height of the microbeam (4 mm) in the vertical (y) direction, were 2 mm in the depth (z) direction, and varied in width (x-direction). The lateral bins were smallest (1 μm) within and at the edges of the microbeam, and increased in size as the lateral displacement from the center of the beam increased, in order to reduce statistical uncertainties as the dose decreases. Each simulation used 10^8 histories, and the same transport parameters as described in Section 3.2.9. The full microbeam array dose distribution was generated from the single planar microbeam distribution using the discrete convolution:

$$D_{tot}(x) = \sum_{i=1}^{N} D_s(x) \cdot \delta(x-x_i) \tag{3.2}$$

where $D_s(x)$ is the dose distribution as a function of lateral displacement for a single microbeam (interpolated to a 1 μm spacing to facilitate the convolution), N is the number of microbeams in the array and the x_i's are the relative position of the centers of the different microbeams in the array. This approach assumes that the dose profile used in the convolution is position invariant. Nettelbeck *et al* (2009) showed that modeling of a single microbeam and subsequent superposition is an adequate approximation if the construction of the MSC is symmetric.[21] More recent studies,[22,23] have demonstrated the limitations of this approach, as described in Section 1.3.1.

Simulations for the 05B1-1 beamline used the SPECTRA-generated energy spectrum for the setup with 0.938 mm Cu filtration (Fig. 3.9(a)). To match our MSC, the microbeam dimensions were 50 μm wide by 4 mm tall with centre-to-centre spacing of 400 μm. The 05ID-2 energy spectrum (Fig. 3.9(b)) was calculated with SPECTRA using a wiggler magnet field set to 4.3 T, and with the filters originally suggested for the planned MRT experimental program at BMIT: 1.15 mm carbon, 0.8 mm aluminum nitride, and 2.3 mm copper at an angle of 25°. This is in addition to the 0.1 mm

aluminum and 0.75 mm total beryllium of the beamline windows. The resulting beam has a mean energy of 99 keV. Microbeam dose distributions were also calculated using the energy spectrum for the European Synchrotron Radiation Facility (ESRF) ID17 beamline, which has a slightly higher mean energy of 107 keV.[17] This facilitated a comparison of the potential dose distributions on the BMIT 05ID-2 beamline to the distributions already commonly used for MRT experimentation at the ESRF. The BMIT 05ID-2 and ESRF ID17 simulations were both done with 25 μm wide x 4 mm tall microbeams separated by 200 μm.

The simulations were used to compile the percent depth dose curve for the 05B1-1, 05ID-2 and ESRF ID17 beamlines for both the peak dose (dose delivered at the center of the microbeam path) of the central microbeam, and the valley dose (dose delivered directly between two microbeams) adjacent to the central microbeam. Additionally, the peak-to-valley dose ratio (PVDR) was tabulated as a function of depth in the phantom for the three beamlines. The PVDR is a commonly used metric used to predict biological response to a specific MRT geometry, with more normal tissue sparing expected with a higher PVDR. Further Monte Carlo simulations and examination of the PVDR will be presented in Chapter 6.

3.2.11 Microbeam array: Multi-slit collimator alignment (05B1-1)

For experimental irradiations, the MSC was used to create the microbeam pattern. The dependence of the output through the MSC on angular offset was investigated to better understand the accuracy required in aligning the MSC. The MSC was aligned on a precision stage allowing rotational adjustments in three orientations, as well as in the vertical and horizontal directions. The MSC was roughly centered and aligned using a fluorescent screen, followed by more precise adjustments made using either an ionization chamber or a beamline CCD camera as a detector. The coordinate system used to describe the beam propagation and dimensions is shown in Fig. 1.15. The x-axis lies in the horizontal plane (the plane of the storage ring), the y-axis is in the vertical direction, and the z-axis is along the direction of beam propagation. The dependence of output on angle in the pitch (rotation about the x-axis), yaw (rotation about the y-axis), and roll

(rotation about the z-axis) orientations was determined by measuring the relative reading of the PR06C chamber with changing angle.

3.2.12 Microbeam array: Vertical and horizontal profiles; microbeam width and peak dose with depth (05B1-1)

The dose distribution produced by the 75-microbeam array was characterized with EBT2 film over multiple experimental sessions on the 05B1-1 beamline. A filtered (0.938 mm Cu) polyenergetic broad beam was used for these experiments. After positioning and aligning the MSC (at 24.76 m from the BM source), film was placed in or on the surface of a Solid Water phantom (Fig. 3.5) at 25.70 m from the source. A vertical profile was analyzed from film placed on the surface exposed to a 3000 mAs irradiation. Horizontal dose profiles and corresponding peak doses and peak widths were extracted for the central microbeam as a function of depth using 500 mAs film exposures. Additionally, the relative peak and valley doses were scored for *each* microbeam in the array for exposures of 25 to 3000 mAs at the surface of the Solid Water. The change in the central microbeam width with distance from the collimator was investigated through film measurements (at the surface) with the phantom at distances of 24.88 and 25.89 m from the source.

For comparison to Monte Carlo prediction, a more accurate measurement of the horizontal dose profile at the surface was made using the two-film technique suggested by Crosbie *et al.*[24] (Section 1.3.2.2): Gafchromic HD810 and EBT2 radiochromic films were used to measure the high dose peak region and the low dose valley regions, respectively. The two types of film were stacked (EBT2 downstream) and placed on the surface of Solid Water.

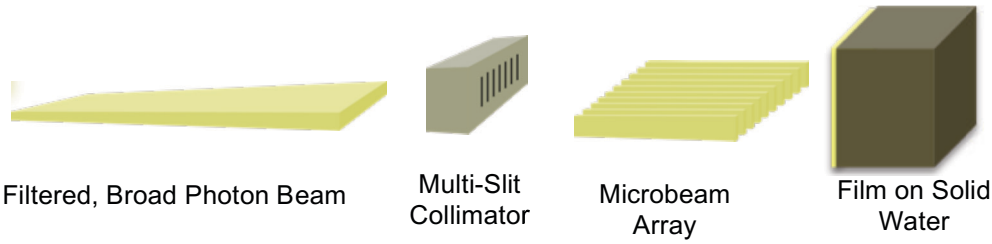

Figure 3.5 Experimental setup for film measurements of the microbeam array.

3.3 Results and discussion

3.3.1 Output: Linearity with current-time product (05B1-1)

The relationship between storage ring current-time product (as controlled via the fast imaging shutters) and the average ion chamber reading is reported in Table 3.3. The results indicate that the deviation from linearity is within 1.1% for an exposure of 20 mAs or greater. This corresponds to an irradiation time between 80 and 130 ms depending on the electron beam current in the storage ring. The percent difference between a linear fit and the measured ion chamber response increases rapidly from 10.9% to nearly 130% between 5 and 1 mAs, respectively. These values correspond to irradiation times between 4 and 33 ms. The large deviations indicate that for reproducibility, the current-time product must remain above 5 – 10 mAs depending on the required accuracy.

Table 3.3 Test for linearity between the current-time product and the ion chamber reading on the 05B1-1 beamline.

Current-time product (mAs)	Average ion chamber reading (nC)	Deviation from fit (%)
10000	86.50	0.0
2000	17.25	0.3
1000	8.68	0.4
500	4.33	0.1
200	1.73	0.0
100	0.866	0.1
50	0.436	0.8
20	0.175	1.1
10	0.089	2.8
5	0.048	10.9
2	0.021	21.0
1	0.020	129.7

3.3.2 Output: CT monochromator stability (05ID-2)

The relative change in the electron storage ring current and the 05ID-2 beam output as measured by the Victoreen 480 free air ionization chamber over nearly 6 hours is plotted in Fig. 3.6. The current in the storage ring decays in a regular manner. If the beamline output were stable, the free air chamber current would decay at the same rate as the

storage ring current. Instead, the output from the CT monochromator decays very rapidly over the first 2 hours.

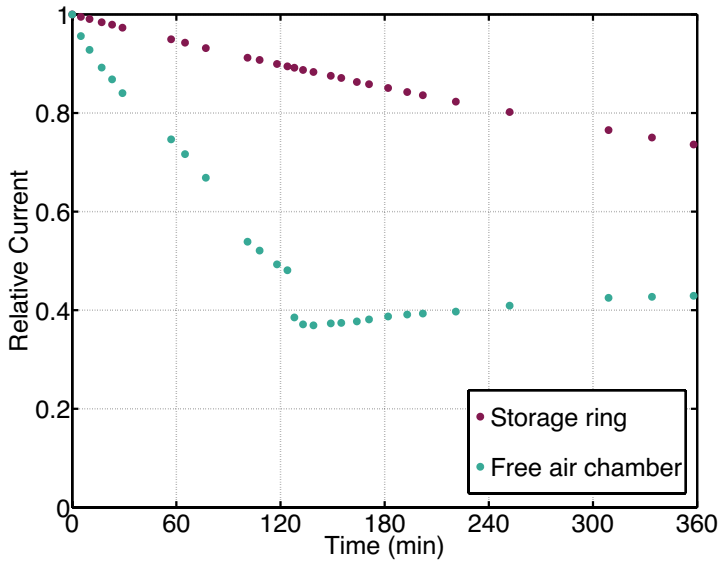

Figure 3.6 The relative storage ring current and CT monochromator output as measured by the Victoreen 480 free air chamber over several hours on the 05ID-2 beamline.

The discontinuity just after 120 minutes coincided with an adjustment of the monochromator parameters, after which the measured beamline output started slowly increasing. The non-linear and inconsistent relationship between the storage ring current and monochromator output limited the accuracy and repeatability of measurements on the 05ID-2 beamline. The unexpected output is likely predominantly due to thermal effects in the monochromator's crystal. Implementation of a feedback system to adjust the monochromator angle with changing output, as is available on the 05B1-1 monochromator, would mitigate this issue, and is planned for the future.

3.3.3 Broad beam geometric characterization: Vertical profile (05B1-1)

The three measurements of the vertical profile for the largest available nominal vertical collimator setting of 8.7 mm are shown in Figure 3.7(a). There is good agreement between the measurements except in the tails, where it appears that the ion chamber-slit system did not accurately characterize the beam edges, and the radiochromic film may be overestimating the dose. The profile measured using the ion chamber underestimates the

dose due to the additional collimation provided by the slit assembly which would reduce the in-air scatter and provide the greatest attenuation for the x-rays propagating at an angle with respect to the slit orientation, which are the lowest energy x-rays at the edges of the beam profile. The uncertainty of the edges of the beam profile measured with film is likely due to uncertainty in the film calibration at these low doses. The similarity between the three profiles suggests that energy dependence of the detectors is not significantly influencing the shape of the curve despite the changing energy spectrum across the beam height. The FWHM of the 0.938 mm Cu filtered x-ray beam is 2.57, 2.74 and 2.81 mm based on the ion chamber, film and diamond detector measurements, respectively. Relative to the film FWHM, this equates to -5.2 % for the ion chamber and +3.7 % for the diamond detector measurements.

Beam profile measurements using the ion chamber-slit method for four other energies are plotted in Fig. 3.7(b). In general, the beam height decreases as the mean energy increases. The FWHM of the 1.103 mm Cu filtered beam is slightly less than the 0.938 mm Cu filtration at 2.51 mm. The polyenergetic unfiltered beam has the lowest energy components, and thus provides the widest possible beam at 3.64 mm. Finally, the two monoenergetic beam widths are 3.32 and 2.95 mm for 20.0 and 33.3 keV, respectively.

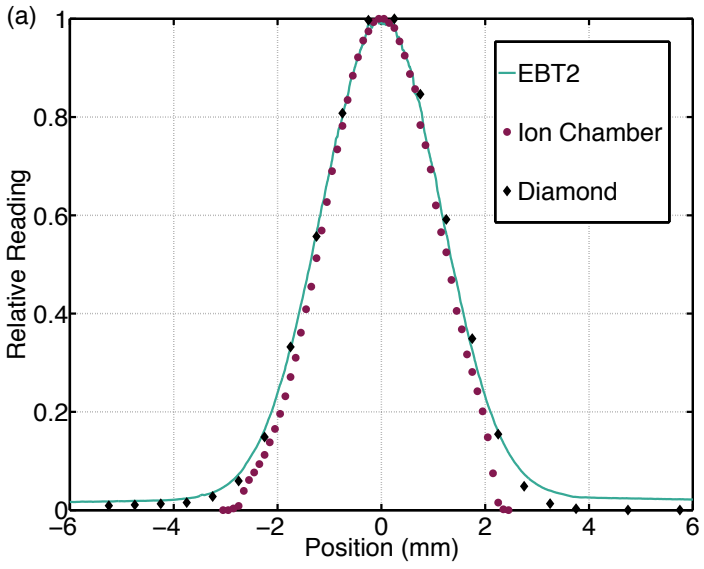

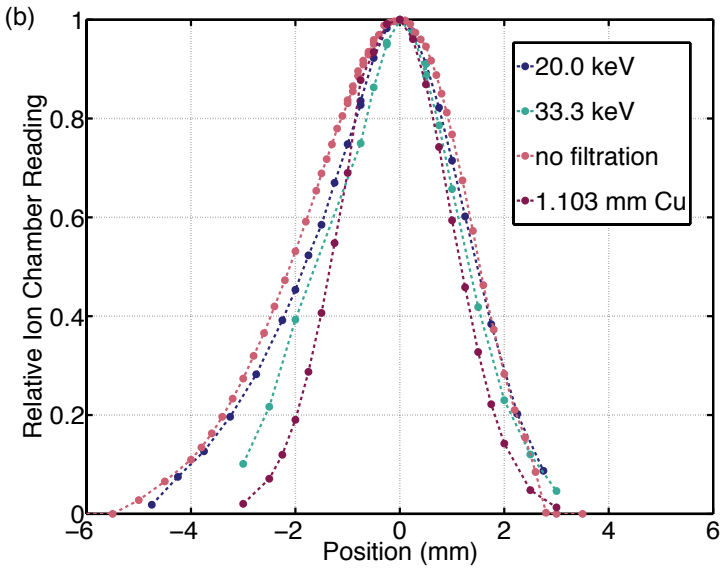

Figure 3.7 The 05B1-1 vertical beam profile. (a) The filtered (0.938 mm Cu) profile measured using EBT2 film, a Capintec PR06C cavity ionization chamber and a beam-defining slit, and a PTW diamond detector. (b) The beam profile measured with the PR06C ionization chamber for 20.0 and 33.3 keV monoenergetic beams, the unfiltered polyenergetic beam, and the beam after 1.103 mm Cu filtration.

3.3.4 Broad beam geometric characterization: Horizontal and vertical beam size with collimator setting (05B1-1)

The vertical beam profiles measured with EBT2 film as a function of nominal collimator settings are shown in Fig. 3.8 for the 0.938 mm Cu filtered 05B1-1 beam. The results demonstrate the asymmetry of the beam for all collimator settings below 8.7 mm, suggesting some misalignment of the collimators. The nominal setting also bears little correspondence to the true beam size, as shown by the measured FWHMs given in Table 3.4. For collimator settings of 2.0 mm or less, the deviation from the measured FWHM increases as the collimator size is decreased, with the greatest discrepancy of nearly 0.8 mm seen for the 0.1 mm setting. The differences between the collimated and measured beam width for settings of 5 mm and above reflect the natural shape of the beam, rather than inadequacies of the collimation. In general, the deviations highlight the necessity of independently verifying the beam size and symmetry for experimentation rather than relying on nominal beamline settings.

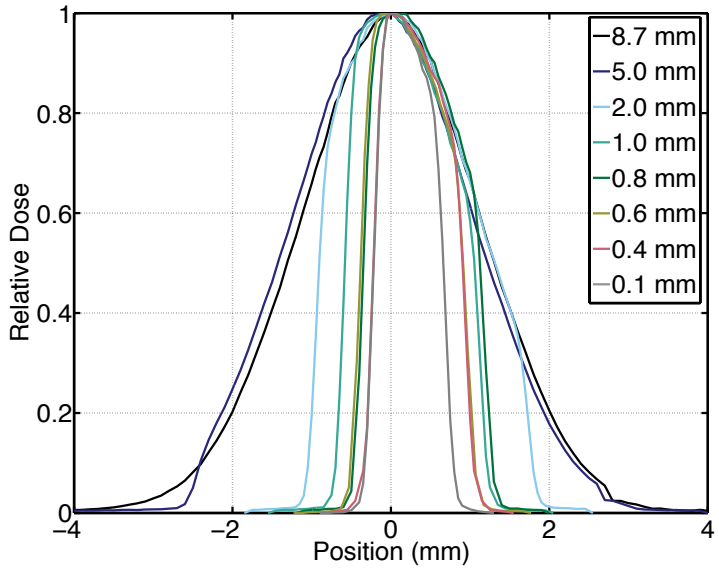

Figure 3.8 The vertical beam profiles measured with Gafchromic EBT2 film for various nominal vertical collimator settings. The measurements were taken with a beam filtration of 0.938 mm Cu. Each individual curve is self-normalized.

Measured beam widths as a function of horizontal collimator setting (and using the largest vertical setting of 8.7 mm) are presented in Table 3.4. The results show a deviation of approximately 0.3 mm for beam settings of 4 mm and smaller. At larger settings, the nominal collimation value and measured FWHM show excellent agreement (within ~ 0.1 mm).

Table 3.4 The 05B1-1 collimator settings and measured vertical and horizontal beam sizes (FWHM) for the 05B1-1 beamline.

Collimator Setting (mm)	Measured (FWHM)	Difference (mm)	Collimator Setting (mm)	Measured (FWHM)	Difference (mm)
	Vertical			Horizontal	
0.1	0.88	0.78	1.0	0.7	0.3
0.2	0.94	0.74	2.0	1.7	0.3
0.4	1.12	0.72	4.0	3.7	0.3
0.6	1.29	0.69	6.0	5.9	0.1
0.8	1.47	0.67	8.0	7.9	0.1
1.0	1.63	0.63	10.0	10.0	0.0
2.0	2.22	0.22	20.0	20.0	0.0
5.0	2.62	-2.38			
8.7	2.65	-6.05			

3.3.5 Broad beam geometric characterization: Divergence (05B1-1)

Based on the measurements of the vertical beam size of the uncollimated, unfiltered 05B1-1 beam at distances of 25.0 and 28.3 m from the source, the full beam height increases from 7.93 to 9.03 mm. From this, the full vertical opening angle was determined to be 0.32 ± 0.01 mrad.

3.3.6 Broad beam energy: Theoretical energy spectra (05B1-1 and 05ID-2)

The dependence of the energy spectrum calculated using SPECTRA on input parameters is quantified in Table 3.5. The percentage change in mean energy, first half-value layer (Cu), and air kerma rate are tabulated as a result of either a 2% or 0.5 mm (for vertical position with respect to the horizontal axis) increase in the storage ring, magnet source, or experimental condition parameters. These results are specific to the 05B1-1 beamline with the given filtration – either only the inherent beamline windows, or with an additional 1.103 mm Cu filtration. The factors that had the strongest influence on the beam energy, HVL and air kerma rate are the storage ring energy, magnetic field strength, the distance travelled in air, and the vertical position in the beam (with respect to the horizontal (x,z)-plane). The storage ring energy and magnetic field strength at the CLS are known precisely (< 0.01% and < 0.1% uncertainty in storage ring energy and magnetic field, respectively [25,26]), and thus will have a minimal impact on the energy spectra calculations. The strong dependence on the vertical position within the beam highlights the importance of careful alignment in the beam when taking point measurements.

The calculated energy spectra for the 05B1-1 beamline with a variety of filtrations are illustrated in Fig. 3.9(a), and the associated mean energies and relative flux are reported in Table 3.6. As expected, the mean energy increases with increasing filtration. The 05ID-2 beamline energy spectra are shown in Fig. 3.9(b). The reduction in intensity for the SOE-1 curve is due to the fact that the energy spectrum was calculated at a distance twice that for the POE-1 curves with the same sized rectangular slit, and is thus selecting a smaller angular section of the beam. The MRT filters referenced in Fig. 3.9(b) and Table 3.6 are those described in Section 3.2.6.

Table 3.5 Dependence on storage ring characteristics, magnet source parameters, and experimental conditions for the 05B1-1 beamline filtered with the beamline windows only (no added filtration) and an additional 1.103 mm Cu.

Category	Parameter (Δ = +2% or +0.5 mm)	Δ Mean Energy (%)		ΔHVL (%)		ΔAir kerma rate (%)	
		No added filtration	1.103 mm Cu	No added filtration	1.103 mm Cu	No added filtration	1.103 mm Cu
Storage ring characteristics	Energy	1.73	1.30	3.97	3.22	9.76	32.98
	Emittance	<0.01	<0.01	<0.01	<0.01	<0.01	-0.02
	β-function (x)	0	0	0	0	0	0
	β-function (y)	<0.01	<0.01	<0.01	<0.01	<0.01	0.02
	Energy spread	0	0	0	0	0	0
	Bunch length	0	0	0	0	0	0
	Dispersion	0	0	0	0	0	0
	Coupling	<0.01	<0.01	<0.01	<0.01	<0.01	-0.02
Source	Magnetic field	0.86	0.65	1.97	1.60	2.76	13.20
Experimental conditions	Source to calculation point	<0.01	<0.01	<0.01	<0.01	-3.87	-3.84
	Distance travelled in air	0.33	0.01	0.72	0.02	-2.23	-0.28
	Air density	0.33	0.01	0.72	0.02	-2.23	-0.28
	Vertical position	0.76	-0.56	-1.74	-1.38	-2.87	-11.02

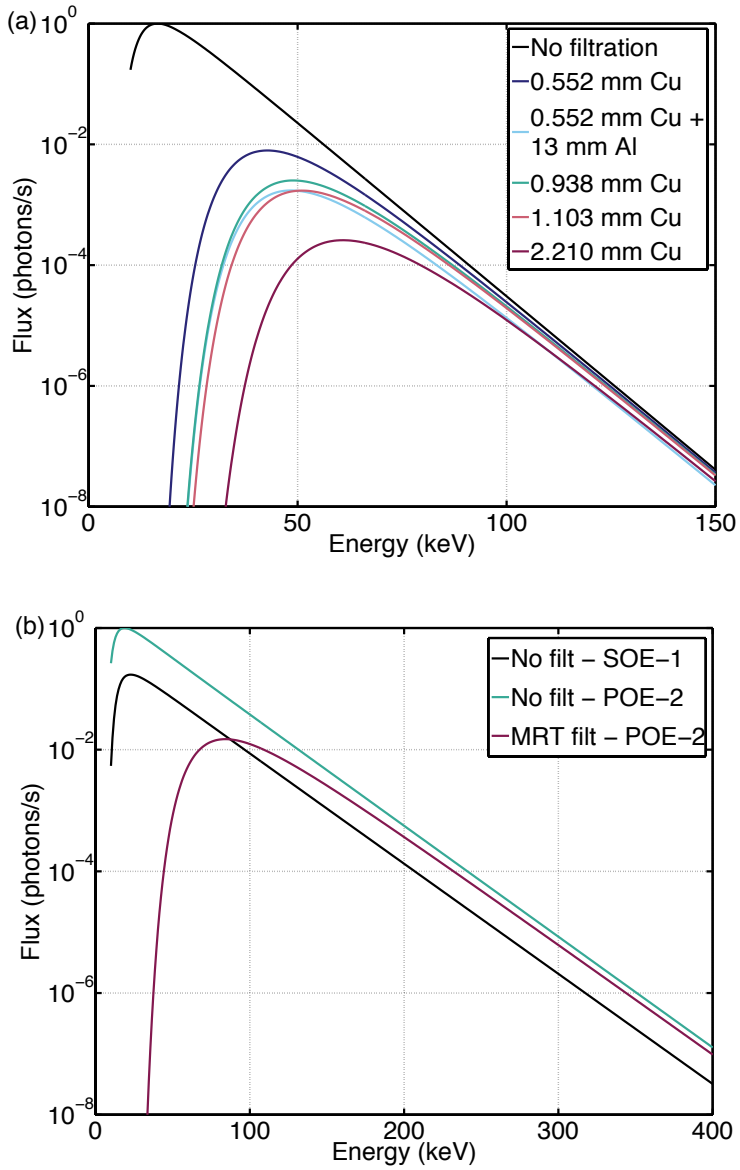

Figure 3.9 (a) The 05B1-1 beamline and (b) 05ID-2 beamline energy spectra on a log-linear plot. The energy spectra were calculated for various filtrations for both beamlines. The 05ID-2 beamline spectra were calculated for two beamline hutches.

Table 3.6 The mean energy and relative flux for the polyenergetic BMIT beamlines.

Filtration	Mean Energy (keV)	Normalized Total Photon Flux
	05B1-1	
None	21.9	≡ 1.00
0.552 mm Cu	47.8	1.23×10^{-2}
0.552 mm Cu + 13 mm Al	53.5	2.82×10^{-3}
0.938 mm Cu	54.0	4.14×10^{-3}
1.103 mm Cu	56.0	2.87×10^{-3}
2.210 mm Cu	65.9	4.69×10^{-4}
	05ID-2	
None (POE-2)	37.4	≡ 1.00
None (SOE-1)	41.2	1.86×10^{-1}
MRT filters (POE-2)	100.7	2.71×10^{-2}

3.3.7 Broad beam energy: Half-value layer values (05B1-1 and 05ID-2)

The theoretical and experimental transmission through copper and aluminum for the 05B1-1 beamline are shown in Fig. 3.10(a) and 3.10(b), respectively. The theoretical and fitted experimental first HVLs are tallied in Table 3.7. The agreement between the theoretical and measured HVLs for the 20.0 and 33.3 keV monoenergetic x-ray beams was 4.6% and 2.6%, respectively. The measured HVLs predict energies of 20.2 and 33.5 keV, which correspond to a 1.0 and 0.7% discrepancy in the predicted and measured energies, respectively. This agreement validates the nominal beam energy based on the monochromator angle. Additionally, the results demonstrate that the HVL measurements have the potential to be reasonably accurate.

The discrepancy between the theoretical and measured HVL for the polyenergetic beams was greater than for the monoenergetic beams. The theoretical HVL is consistently greater than the measured value, which means SPECTRA calculates a slightly higher energy polyenergetic beam than is measured. The discrepancy increased as the filtration, and thus the mean energy of the beam, decreased. This could mean that the HVL measurement has inherently more uncertainty at lower photon energies. The additional uncertainty at the low energies could be due to the thinner Al and Cu filters

used for the measurement, resulting in greater uncertainty in the dimensions of the filters due to mechanical stress. Additionally at lower energies, any impurities in the Al and Cu filters may cause greater attenuation than expected, and could help explain the lower penetrability of the measured beams, but is unlikely to explain the magnitude of the discrepancies. Due to the much better agreement achieved for the low energy, monoenergetic beams, it is likely that the theoretical energy spectrum calculated by SPECTRA is less accurate in the low energy components of the x-ray beam.

To further investigate the relationship between measured HVL and beam energy, the theoretical filtration of the beam was reduced until the theoretical and measured HVLs were equal. For the lowest energy filtered (0.552 mm Cu) polyenergetic beam with the greatest discrepancy between theoretical and experimental HVLs, this resulted in a decrease in mean energy of 5.2%. Following the same procedure for the other conditions, the discrepancies in mean energy were 3.4, 2.3, 2.3, and 1.0% for filtrations of 0.552mm Cu + 13 mm Al, 0.938 mm Cu, 1.103 mm Cu and 2.210 mm Cu, respectively. These results demonstrate that the percent error in the beam's mean energy is less than half of the corresponding percent error in the HVLs.

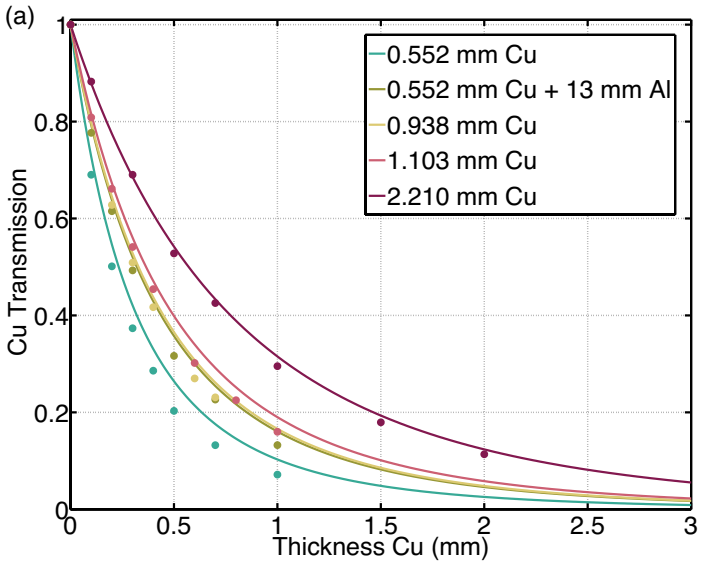

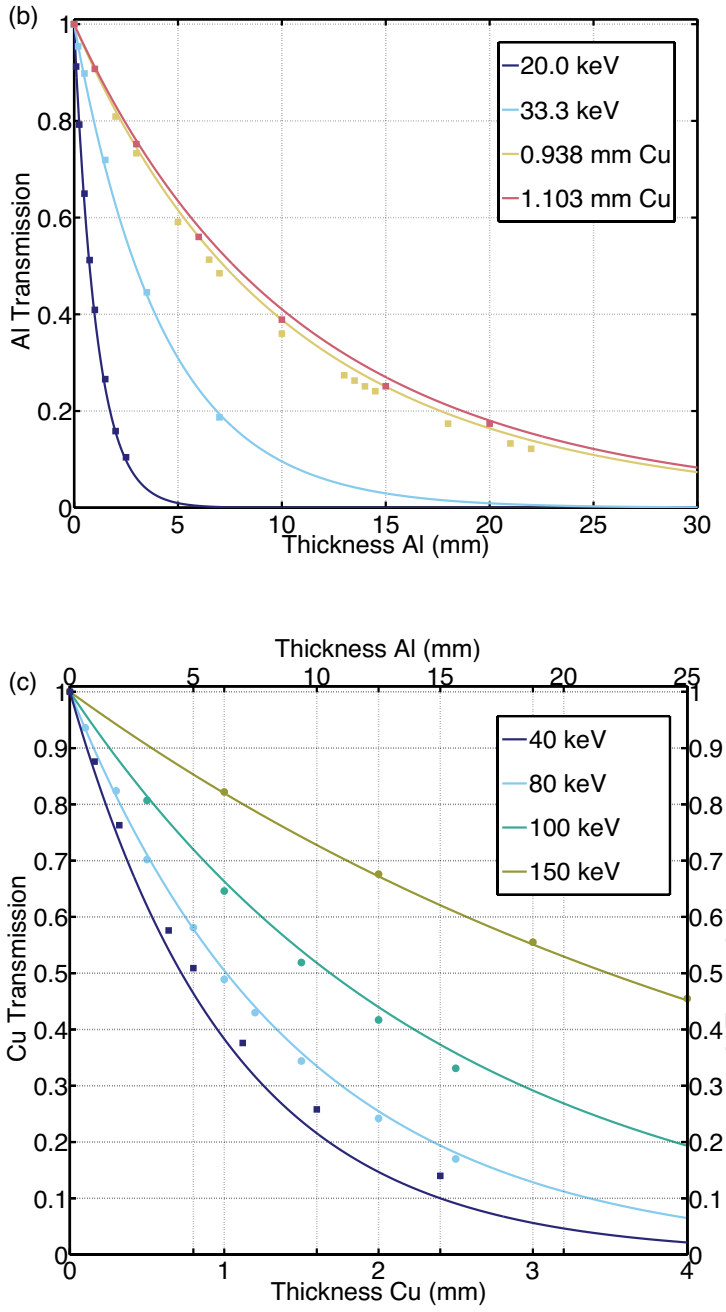

Figure 3.10 The HVL beam quality measurements in terms of (a) Cu and (b) Al thickness for various filtered polyenergetic and monoenergetic 05B1-1 beams. The experimental values are represented by discrete points and the theoretical values by solid lines. (c) The HVLs for monoenergetic 05ID-2 beams. Cu measurements are displayed as circles, and Al measurements as squares.

Table 3.7 The theoretical and measured first HVLs for both the 05B1-1 and 05ID-2 beamlines. The polyenergetic beam quality is specified by the filtration, while the monoenergetic beam quality is specified by the nominal energy.

Filtration or Energy	Theoretical HVL (mm)	Measured HVL (mm)	Percent Difference (%)
	05B1-1 Beamline		
20.0 keV	0.75 (Al)	0.78 (Al)	4.6
33.3 keV	2.96 (Al)	3.03 (Al)	2.6
0.552 mm Cu	0.23 (Cu)	0.20 (Cu)	-14.2
0.552 mm Cu + 13 mm Al	0.32 (Cu)	0.29 (Cu)	-9.1
0.938 mm Cu	7.23 (Al)	6.72 (Al)	-7.1
	0.33 (Cu)	0.31 (Cu)	-6.4
1.102 mm Cu	7.71 (Al)	7.26 (Al)	-5.9
	0.37 (Cu)	0.34 (Cu)	-6.3
2.210 mm Cu	0.57 (Cu)	0.56 (Cu)	-2.5
	05ID-2 Beamline		
40 keV	4.52 (Al)	5.06 (Al)	11.9
80 keV	1.01 (Cu)	0.99 (Cu)	-2.6
100 keV	1.69 (Cu)	1.58 (Cu)	-6.2
150 keV	3.49 (Cu)	3.53 (Cu)	1.1

The 05ID-2 beamline monoenergetic results are shown in Fig. 3.10(c), and the tabulated results are shown in Table 3.7. The agreement between experiment and theory was best for the highest energy beam (150 keV) and worst for the lowest energy beam (40 keV). The measured HVL for 40 keV indicated a higher energy beam than the theoretical predictions, and corresponds to a discrepancy of 2 keV. A possible contribution to the discrepancy is the influence of higher order harmonics from the monochromator, in this case expected at 120 keV, contaminating the monoenergetic beam. There is evidence of harmonics for the 40 keV beam in the spectroscopy results (Section 3.3.8).

3.3.8 Broad beam energy: Spectroscopy (05ID-2)

Histograms of the spectroscopic measurements of four monoenegetic x-ray beams on the 05ID-2 beamline are shown in Fig. 3.11. The measured Compton peak and corresponding calculated incident beam energy (Eq. 3.1) are given in Table 3.8. The

agreement between the measured and expected energies was less than 1 % for all energies except the highest energy beam at 150 keV, which had a percent difference of 3.3 %.

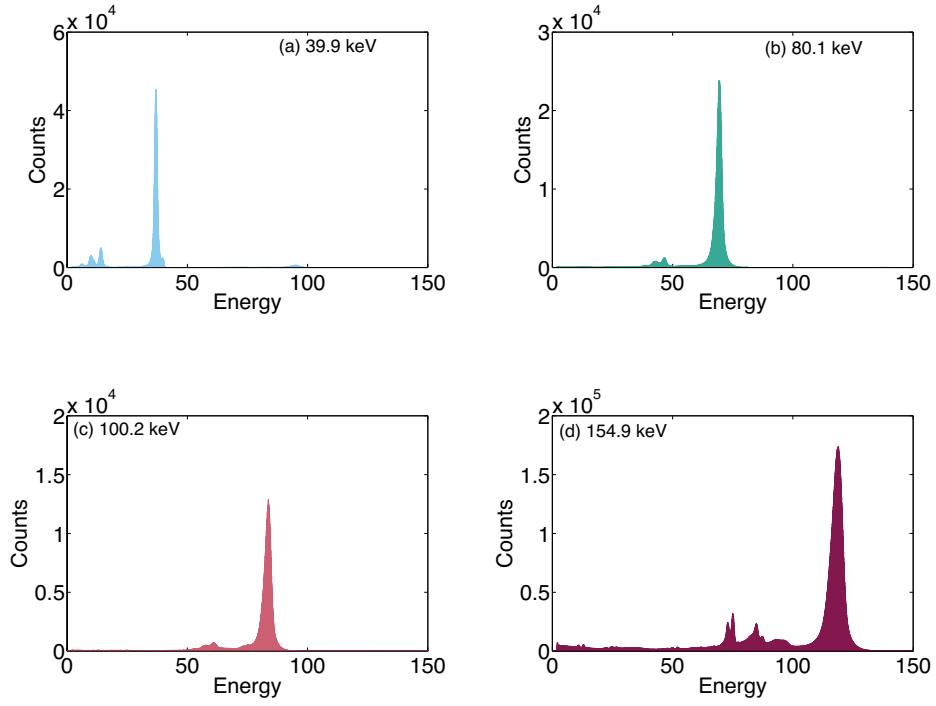

Figure 3.11 The spectrometer output of counts versus energy for the Compton scattered photons from the 05ID-2 beamline. The measured beam energy was determined based on the position of the Compton peaks.

The nature of a monochromator (*i.e.* the diffraction from a crystal) allows not only the fundamental desired frequency to be emitted, but also higher order harmonics that are multiples of the fundamental frequency. At the lowest monoenergetic beam (40 keV), the second and third harmonic would be 80 and 120 keV, respectively, but for the specific crystal in the monochromator the second harmonic corresponds to a forbidden reflection. It can be seen that there are non-negligible components at higher energies, and the 40 keV spectroscopic measurements (Fig. 3.11(a)) show evidence of harmonics. Above the fundamental Compton peak at 37 keV, the other most prominent Compton peak corresponds to an incident energy of ~ 117 keV, which is similar to the expected energy of the third harmonic. The peak at 117 keV has an area of ~3.6 % of the fundamental peak's area.

Table 3.8 The nominal, Compton peak, and measured incident x-ray energies (via Eq. 3.1) for the four monoenergies examined on the 05ID-2 beamline.

Nominal Energy (keV)	Compton Peak (keV)	Measured Energy (keV)	Difference (%)
40	37.02	39.91	0.22
80	69.23	80.29	0.37
100	83.74	100.15	0.15
150	118.89	154.94	3.29

3.3.9 Broad beam energy: Percent depth dose (05B1-1 and 05ID-2)

The experimental (Wellhofer IC10, PTW 23342, and EBT2 film) and theoretical (Monte Carlo) percent depth dose curves for the 05B1-1 beamline filtered with 0.938 mm Cu are shown in Fig. 3.12(a). Past 5 mm, the deviation between any two of the curves was a maximum of 2.4 %. The greatest deviation, 5.4 %, occurred at a depth of 1 mm. This was expected due to the difficulty in accurate measurements near the surface. The Monte Carlo predicted PDD is slightly more penetrating than the measured curves. This is consistent with our HVL measurements, which yielded values approximately 7 % lower than the theoretical HVL (for this particular polyenergetic beam). The depth in water at which the PDD drops to 50 % (*D50*) for the five measurements and Monte Carlo prediction are given in Table 3.9. The mean experimental value is 34.7 ± 0.7 mm, which is 3.6 % lower than the predicted value of 36.0 mm.

The PDD curves for the 05B1-1 beamline were measured with the Welhoffer IC10 and water phantom for an additional polyenergetic beam (1.103 mm Cu filtration), and two monoenergetic beams (33.3 and 20.0 keV). The curves are plotted in Fig. 3.12(b), normalized to the shallowest measurement depth of 4.1 mm. Tabulated (Table 3.9) *D50* doses are based on the polynomial fits to the measured PDDs. As expected, the 1.103 mm Cu filtered beam is slightly more penetrating than the 0.938 mm Cu filtered beam. There is approximately a three-fold increase in the *D50* value from the monoenergetic 20.0 keV beam (1.29 cm) to the polyenergetic 1.103 mm Cu beam (3.72 cm). The uncertainty in Table 3.9 takes into account the uncertainty in the polynomial fit performed in MATLAB to estimate the surface dose (which could not be measured using our horizontal water phantom (Fig. 3.4)).

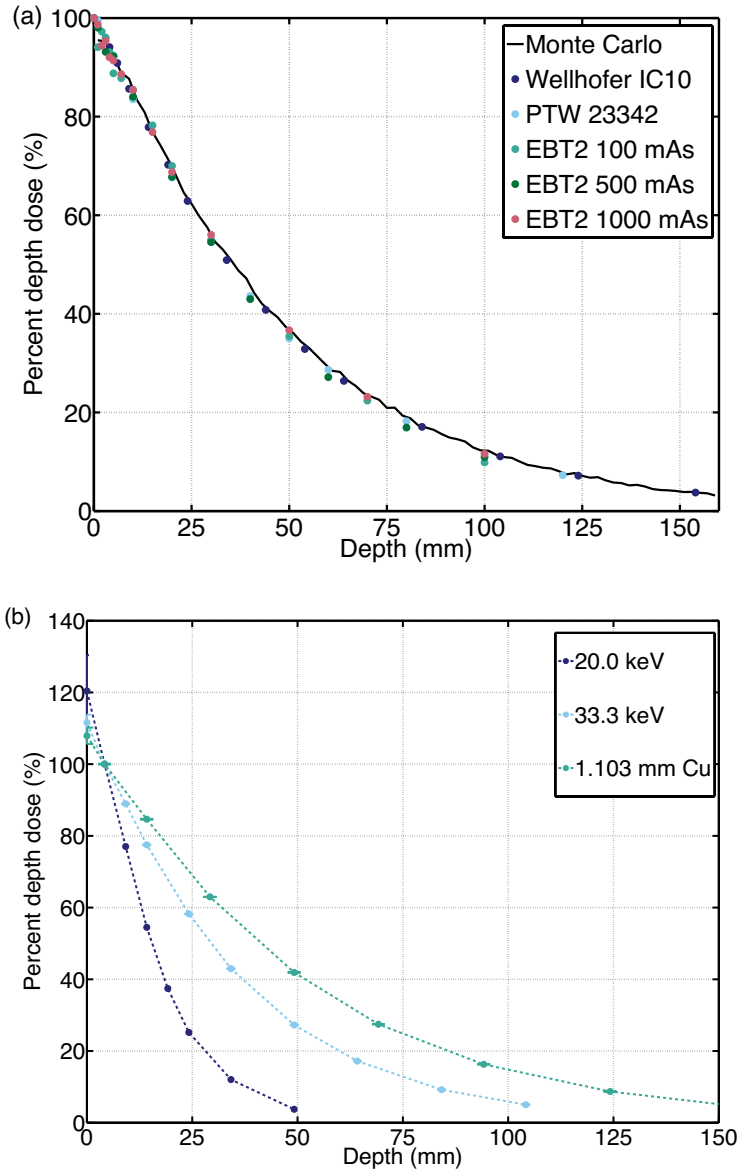

Figure 3.12 (a) For the 05B1-1 beamline with 0.938 mm Cu filtration, comparison of measured PDDs in water or Solid Water for three different detectors to Monte Carlo prediction. (b) PDDs for three different beam qualities (two monoenergetic, one polyenergetic) on the 05B1-1 beamline measured with the Welhoffer IC10 chamber in the in-house built water phantom. The curves were normalized at the shallowest measurement depth (4.1 mm), and a polynomial fit was used to predict the dose at shallower depths.

Table 3.9 The depth at which the dose falls to 50 % (*D50*) in water for various energies or filtrations on the 05B1-1 beamline.

Energy or Filtration	Dosimeter	*D50* (mm)
0.938 mm Cu	Monte Carlo	36.0
	Wellhofer IC10	35.0
	PTW 23342	34.2
	EBT2 100 mAs	35.0
	EBT2 500 mAs	33.9
	EBT2 1000 mAs	35.6
1.103 mm Cu	Wellhofer IC10	37.2 ± 1.4
33.3 keV	Wellhofer IC10	25.8 ± 0.9
20.0 keV	Wellhofer IC10	12.9 ± 1.5

3.3.10 Microbeam array: Monte Carlo dose distributions (05B1-1 and 05ID-2)

The Monte Carlo-simulated microbeam horizontal dose profiles as a function of depth are shown in Fig. 3.13 for the filtered 05B1-1 and 05ID-2 beamlines. Corresponding peak and valley PDDs for these beamlines and additionally for the ESRF ID17 beamline are given in Fig. 3.14(a). The lower energy 05B1-1 peak dose falls off more rapidly than the 05ID-2 or ESRF ID17 beams: *D50* is 31.7 mm for 05B1-1, 43.3 mm for 05ID-2, and 44.3 mm for ESRF ID17. Although it is not visible on the plot, the valley dose for all beamlines has a build-up region over the first 11 mm. The valley dose increases by approximately 30 % of its maximum over the build-up region, then monotonically decreases with depth. Even at its maximum, the valley dose does not exceed 2 % of the entrance peak dose.

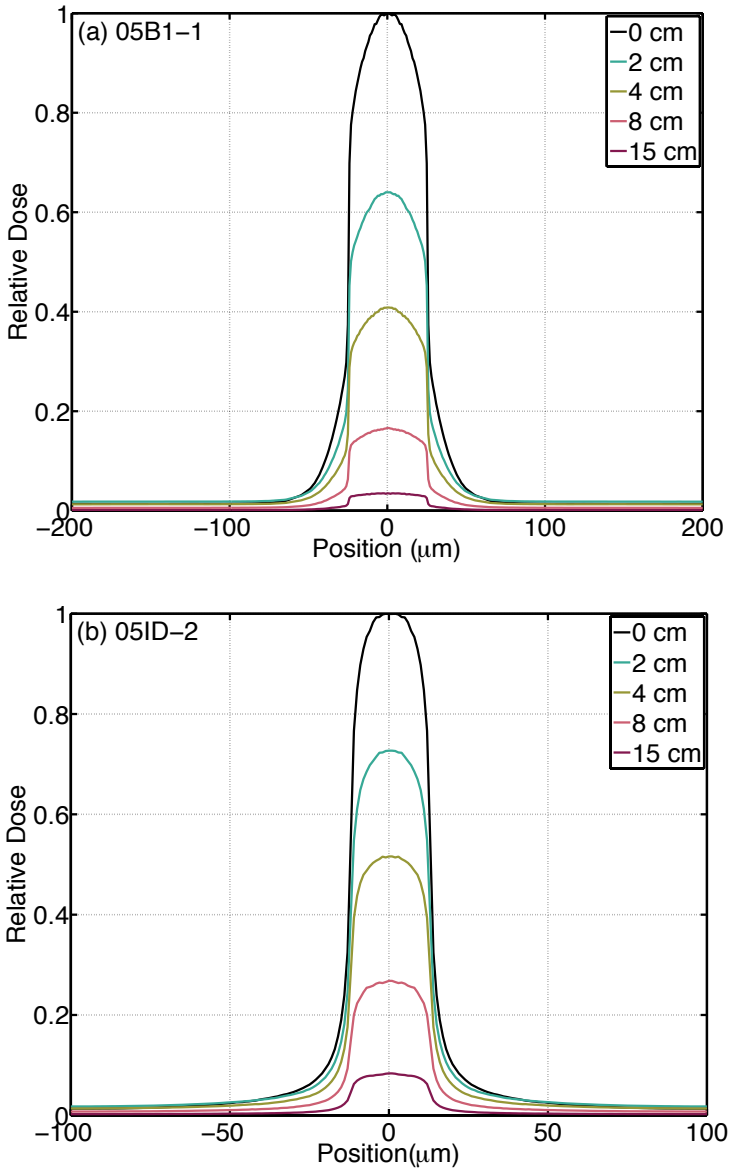

Figure 3.13 The horizontal dose profiles for the (a) filtered 05B1-1 beamline and (b) filtered 05ID-2 beamline for various depths in a cylindrical water phantom. The simulations were performed assuming microbeam widths of 50 μm and 25 μm for the 05B1-1 and 05ID-2 beamlines, respectively.

Fig. 3.14(b) shows the peak-to-valley-dose ratio (PVDR) as a function of depth. The similarity between the 05ID-2 and ESRF ID17 PVDRs suggests that the appropriately filtered BMIT 05ID-2 beamline has the potential to create the spatially fractionated dose distribution necessary to achieve the high normal tissue sparing characteristic of microbeam irradiations. Further Monte Carlo calculations in a cubic head phantom for the 05ID-2 beamline energy spectrum are reported in Chapter 6.

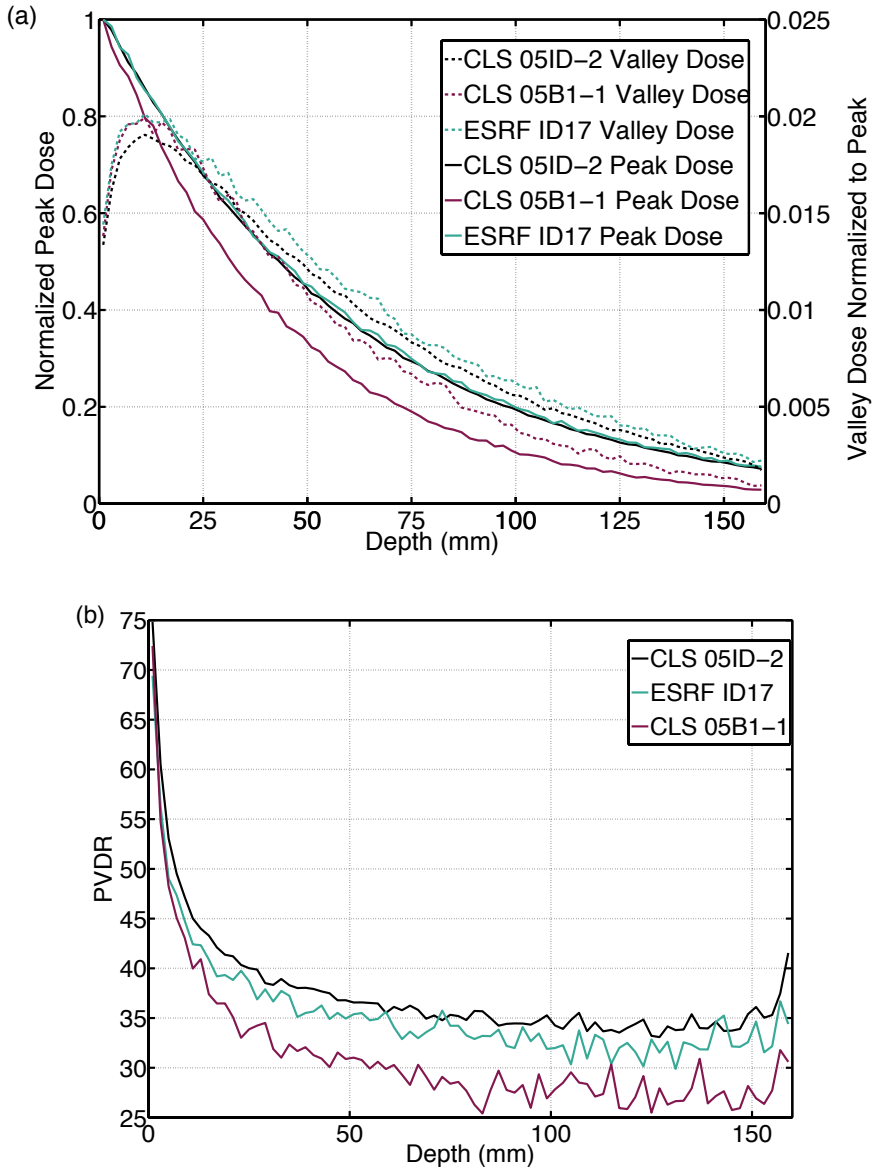

Figure 3.14 The depth dose distributions of the two BMIT beamlines and the ESRF ID17 beamline. (a) Peak (solid lines) and valley doses (dashed lines) with depth. (b) The peak-to-valley dose ratio (PVDR) is plotted with depth.

3.3.11 Microbeam array: Multi-slit collimator alignment

Output through the MSC with changing angular position in the yaw, pitch, and roll orientations is shown in Fig. 3.15. The results confirm the expectation that the output is strongly dependent on rotation of the MSC in the yaw orientation (about the vertical axis) (Fig. 3.15(a)) – no output was detected by the PR06C ion chamber after a misalignment

of only 0.4°. The effect was confirmed with EBT2 Gafchromic film measurements. There was a gradual reduction in microbeam height and width as the MSC was rotated, until the microbeams vanished between a yaw angle of 0.35° and 0.4°. Based on geometric consideration of a perfectly parallel beam and perfectly constructed collimator ('Predicted' line in Fig. 3.15(a)), complete obstruction of the SR beam would be predicted for a rotation of approximately 0.05° less than our measured values. Although there is a strong dependence on the MSC alignment in the yaw direction, reproducible alignment can be achieved with the rotating stage and an ionization chamber.

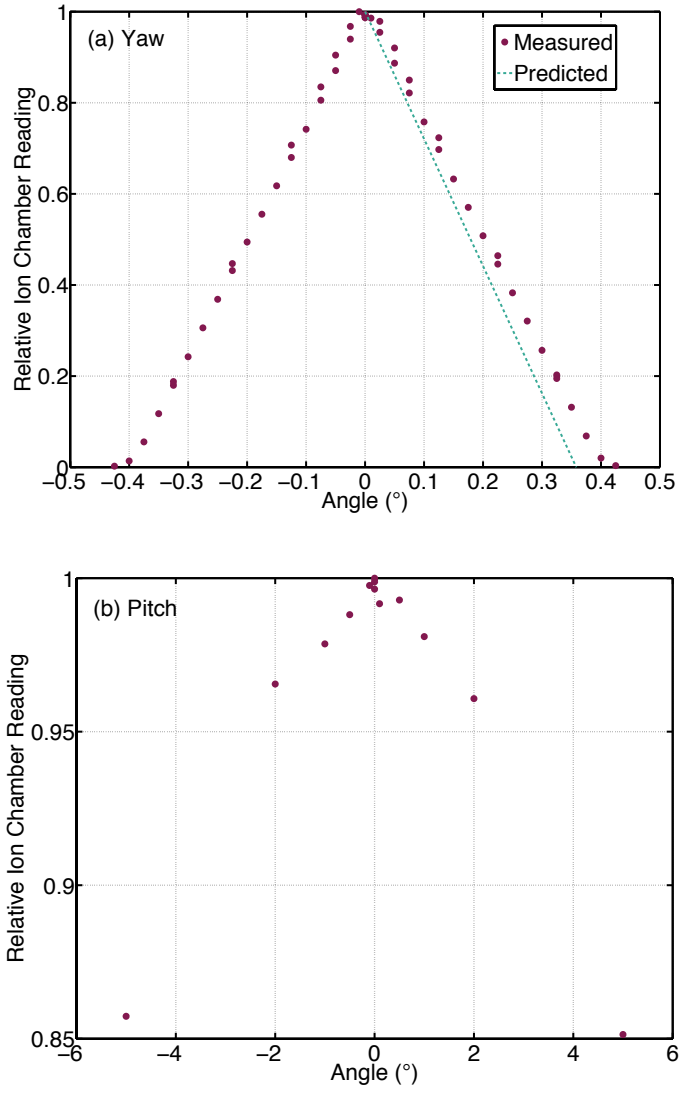

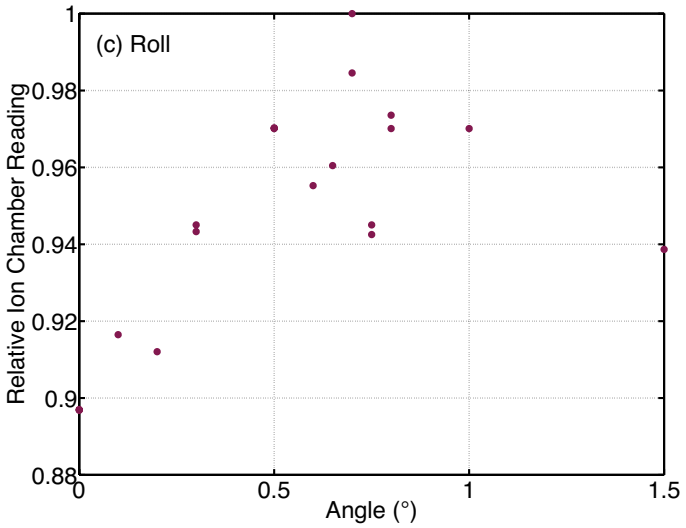

Figure 3.15 The relative ion chamber output through the multi-slit collimator (MSC) with adjustments in the MSC's (a) yaw, (b) pitch and (c) roll.

The alignment of the MSC's pitch and roll is simpler. As seen in Figure 3.15(b) and 3.15(c), the output is less sensitive to small angular misalignments in these orientations, and the alignment can be aided with a level.

3.3.12 Microbeam array: Horizontal and vertical profiles (05B1-1)

The horizontal dose profile (at zero depth in phantom) across a single microbeam in the array is shown for two distances from the BM source in Fig. 3.16. The upstream microbeam profile has a width of 48.3 μm and the downstream profile has a width of 52.5 μm. The change in microbeam width was 4.2 μm as a result of traveling 1.01 m farther in air, which is likely due to both beam divergence and scattering in air. Horizontal profiles, such as those in Fig. 3.16, were averaged over the central 2 mm of the beam vertically to reduce the pixel fluctuations.

The vertical microbeam profile is shown in Fig. 3.17. The profile shows the fall off of dose when moving away from the central axis, as was demonstrated in the vertical profile of the broad beam (Fig. 3.7). The film reading was smoothed in MATLAB using a moving average filter to reduce signal noise.

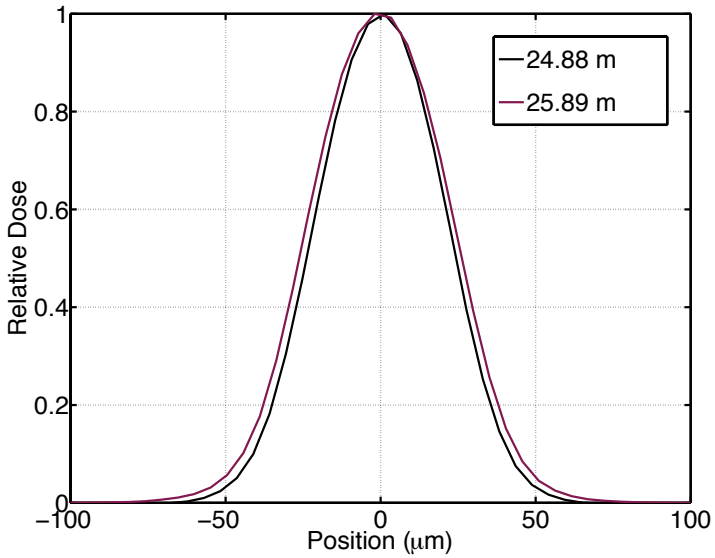

Figure 3.16 The change in microbeam profile resulting from moving 1.01 m farther from the source, as measured with Gafchromic EBT2 film.

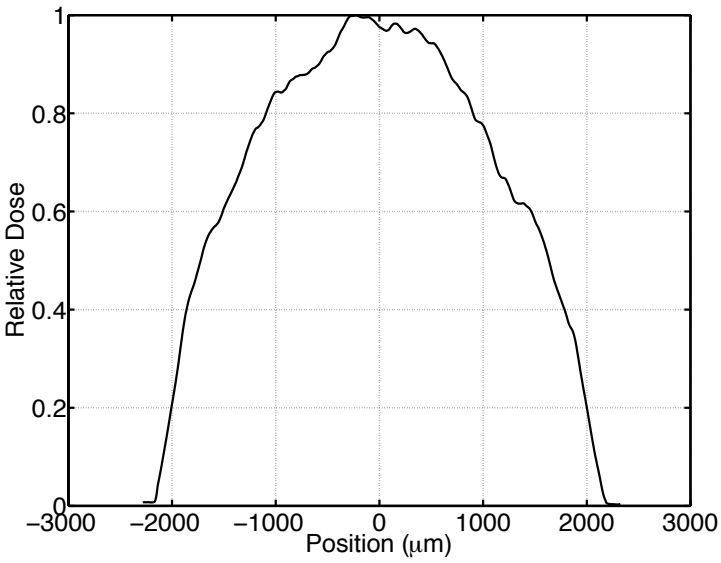

Figure 3.17 Vertical profile over the central microbeam after a 3000 mAs exposure as measured with Gafchromic EBT2 film.

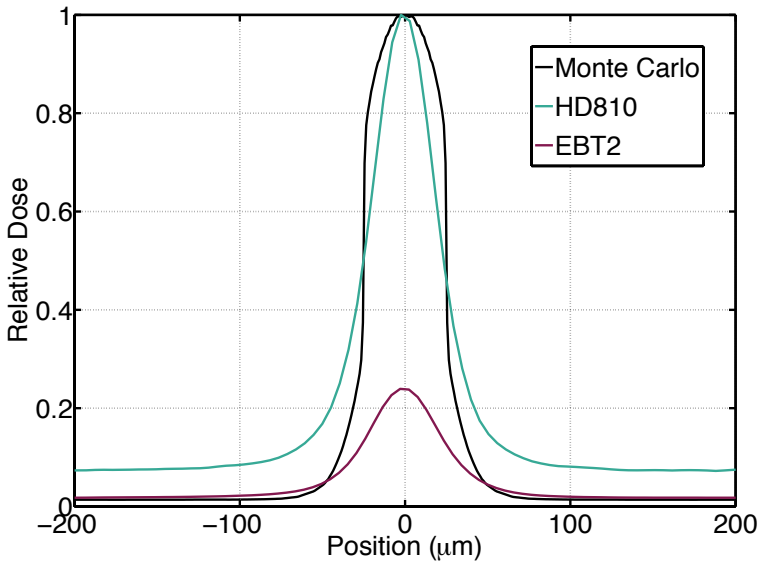

Figure 3.18 The Monte Carlo-generated horizontal dose profile compared to the HD810 and EBT2 film profiles for an exposure of 30000 mAs. The Monte Carlo and HD810 curves have been normalized to 1.

Figure 3.18 compares the shapes of the Monte Carlo simulated horizontal dose profile to HD810 and EBT2 film measurements of a 30000 mAs exposure. Both the high (HD810) and low dose (EBT2) calibrated film measurements were normalized to the maximum measured dose (HD810 peak). The Monte Carlo result is normalized to one. The valley dose (at 200 μm) simulated using Monte Carlo is 1.4% of the peak dose, while the EBT2 measurement is 1.8% of the peak dose. This converts to a PVDR of 72.3 (Monte Carlo) and 56.1 (radiochromic film). Although the PVDRs differ by more than 20%, the discrepancy is not particularly surprising given that Crosbie *et al.* reported PVDR uncertainties of up to 35% using this two-film method.[21] This was dominated by uncertainties in the valley dose. Further measurements would be required to investigate the repeatability of this measurement, as well as to determine the optimal dose range given the sensitivities of the HD810 and EBT2/EBT3 films.

The film and Monte Carlo profiles provide nearly the same FWHM, but differ in shape. The latter is likely due to two issues: first, the Monte Carlo simulations modeled an ideal beam, ignoring the physical beam's divergence, scattering from the MSC, and scattering in air. Secondly, the digitization of the film using a flat bed scanner has limited resolution.

3.3.13 Microbeam array: Horizontal profiles, microbeam width and peak dose (05B1-1)

The Gafchromic EBT2 horizontal dose profiles for the central microbeam at several depths between 0 and 10 cm in Solid Water are plotted in Fig. 3.19(a). The profiles are normalized to the highest dose, which was measured at the "*dmax*" depth of 1 mm. Based on our Monte Carlo results (Fig. 3.14(a)), the enhanced dose at 1 mm depth is unexpected. A dose buildup has been demonstrated by other authors performing simulations of microbeam PDDs with finer depth bins. However, the buildup regions were very small: ~ 20 μm for a beam with mean energy of 125 keV[24] and ~ 10 μm for a beam with mean energy of 107 keV.[17] Thus, at the 54 keV mean energy for our 05B1-1 beam, *dmax* would be expected to be smaller still. Nevertheless, a *dmax* beyond the surface of Solid Water was repeatedly observed with both Gafchromic EBT2 and HD810 film in our measurements. Beyond the 1 mm depth, the horizontal dose profiles monotonically decreased in dose.

The corresponding PDD in the microbeam peak is plotted in Figure 3.19(b) as a function of depth. The black circles show the Monte Carlo prediction of the PDD for the microbeam array (50 μm wide microbeams, 400 μm separation). There are discrepancies of up to 8.2% between measured and simulated data points, although the experimental and theoretical curves are quite similar in shape. Uncertainties in the normalization point limit the accuracy of the experimental curve.

The measured microbeam widths are also shown in Figure 3.19(b). Over the first 5 mm depth, the measured width increases slowly, and has an average FWHM of 45.5 ± 0.3 μm. Beyond this, the microbeam width increases more rapidly with depth, until it reaches 57.9 μm at 10 cm depth. The results depicted in Fig. 3.16 suggest we would expect an increase in width of only approximately 0.4 μm due to beam divergence over this 10 cm. The increase of 12.4 μm is thus primarily attributed to scatter in the water phantom.

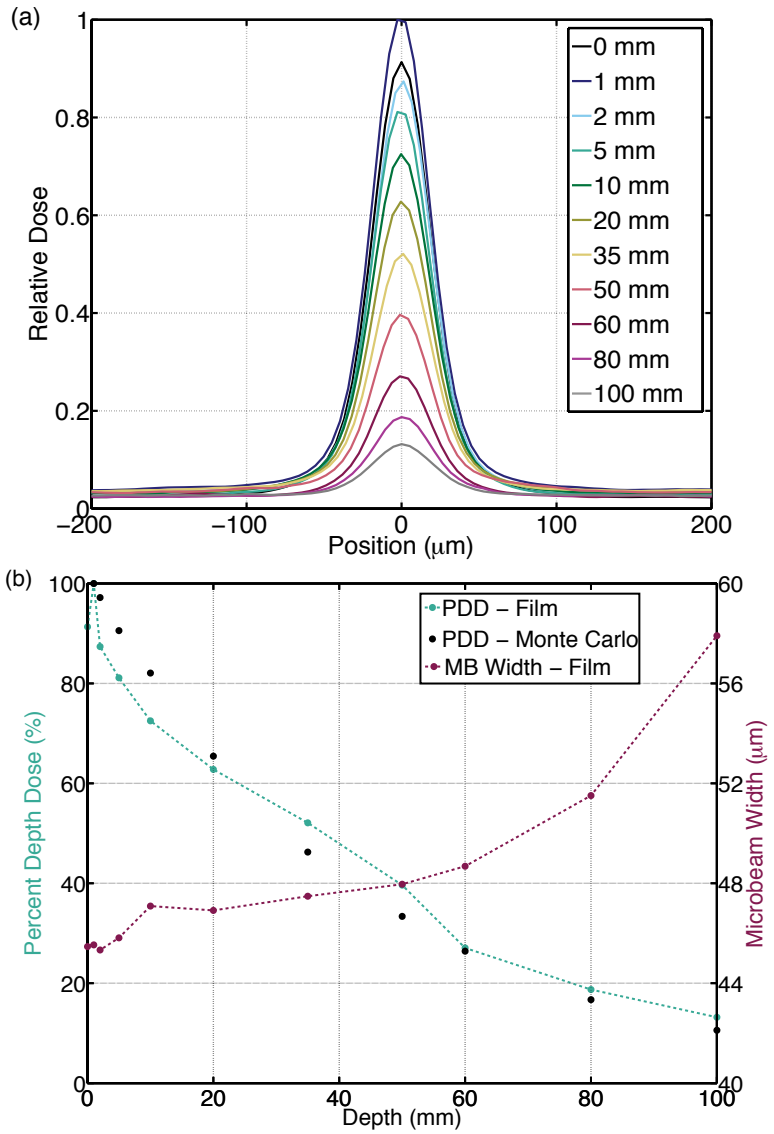

Figure 3.19 (a) Horizontal dose profiles of the 50 × 400 μm array measured with EBT2 film for various depths in Solid Water on the 05B1-1 beamline filtered with 0.938 mm Cu. (b) The corresponding microbeam (MB) width and percent depth dose (PDD) from (a). The Monte Carlo–generated PDD (Fig. 3.14(a)) is also plotted (black circles, no line) to compare to the film measurements.

The relative peak and valley doses measured at the surface of Solid Water for each of the 75 microbeams in the microbeam array are plotted in Fig. 3.20(a) and 3.20(b), respectively. The curves are all normalized to the mean value. Both plots demonstrate the fall off in peak and valley dose at the edges of the 3.2 cm wide array. This fall off is attributed to the loss of scatter radiation from either of the edges of the array. Because the MSC and the incident x-ray beam were not altered between successive film

measurements, the variation between the different exposures can be attributed to variation in the film response or digitzation, or nonuniform uncertainties in film calibration at different dose levels. The variation in the peak dose of individual microbeams was most extreme for the lowest exposure of 25 mAs, which had a standard deviation of 0.072. The standard deviation for the four higher exposures fell between 0.034 and 0.042. There was a much greater variation in relative valley dose over the whole microbeam array. The standard deviation across the microbeam array was lowest for the 100 mAs exposure at 0.155, and highest again for the 25 mAs exposure at 0.227.

The average surface peak to valley dose ratio was also determined from these measurements. The results further highlight the uncertainty of the radiochromic film measurements of the microbeams. Because the PVDR depends only on geometry and depth, its value should not change with exposure, yet the measured results in Table 3.10 superficially suggest otherwise. The PVDRs measured with exposures of 25 and 100 mAs are much lower than expected based on Monte Carlo results (Fig. 3.14(b)). This is likely because the very low doses in the valley region are approaching the minimal dose measurable with EBT2 (e.g., less than approximately 1 cGy), in combination with greater uncertainties in the calibration curve at these low doses. The PVDRs measured at 1000 and 3000 mAs with EBT2 are within 5% of the PVDR value using the two-film technique with a 30000 mAs exposure. As mentioned above, the lower measured PVDR compared to the theoretical value is partially explained by the Monte Carlo calculations not taking into account the divergence of the microbeams, or the scattering off the collimator or in air before the water phantom.

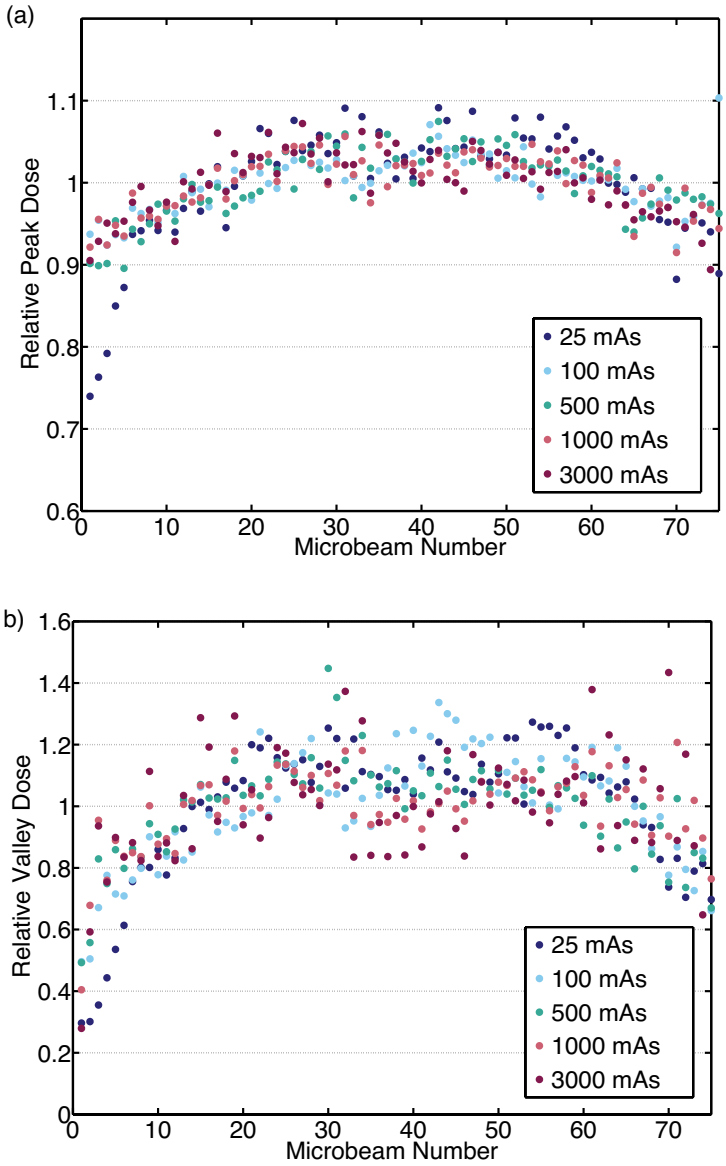

Figure 3.20 The relative peak (a) and valley (b) doses for each microbeam in the array measured using Gafchromic EBT2 film.

Table 3.10 The peak-to-valley dose ratio (PVDR) averaged over the whole microbeam array and measured with Gafchromic EBT2 film at various exposures on the filtered 05B1-1 beamline.

Exposure (mAs)	Average PVDR
25	7.3
100	23.1
500	51.0
1000	58.7
3000	58.5

3.4 Conclusions

The characterization of the BMIT beamlines is important to validate the input needed for analytical calculations (*e.g.*, correction factors for dosimetric measurements (Chapter 4)), and for Monte Carlo simulations. Many measurements have been performed on the 05B1-1 beamline to investigate its output, beam energy quality, broad beam geometry, and microbeam geometry. The comparison of theoretical prediction of energy with half-value layer and percent depth dose measurements suggest that the calculated energy is slightly greater than is measured, with greater discrepancies in less filtered (lower energy) beams. A description of the broad beam geometry for varying energy and beamline collimator settings was presented. This experimental data will be important for experimental dosimetry as will be described in Chapter 5. A series of measurements was also taken for the beam collimated by the MSC. The measurements, predominantly using radiochromic film, were compared to Monte Carlo simulations. Despite many uncertainties and approximations in the experimental and theoretical data, the microbeam array studies showed reasonable similarity between the measurements and simulations. Our Monte Carlo simulations are limited by the absence of divergence, photon fluence non-uniformities over the broad photon beam,[22] scattering and transmission due to the MSC, and scattering in air. Radiochromic film measurements are potentially valuable in providing verification of delivery, and quantifying the spatial distribution of microbeam deliveries. However, the use of film for relative dosimetry is challenging at these high resolutions. The largest challenges to overcome are the spatial resolution of the digitization method, as well as the intrinsic response variation across a sheet of film,[27] which are difficult to correct for at microbeam resolutions.

The features of the recently available, more complex 05ID-2 beamline have only begun to be investigated. The CT monochromator was used to create monoenergetic beams, whose quality was investigated through HVL measurements and Compton spectroscopy. Additional measurements were limited by the instability of the CT monochromator, but this will likely be corrected in the future through the implementation of a feedback system to control the monochromator angle with changing heat loads.

3.5 References

[1] "BioMedical Imaging and Therapy Facility (BMIT) at the Canadian Light Source," http://ex.lightsource.ca/bmit/images/Trifold-Poster-WEB.pdf Accessed 2/23/2015.

[2] F.H. Attix, *Introduction to Radiological Physics and Radiation Dosimetry* (John Wiley & Sons, Inc., New York, 1986).

[3] S. Devic, Y. Wang, N. Tomic, E.B. Podgorsak, "Sensitivity of linear CCD array based film scanners used for film dosimetry," Med. Phys. **33**, 3993-3996 (2006).

[4] S. Devic, "Radiochromic film dosimetry: Past, present, and future," Physica Medica-European Journal of Medical Physics **27**, 122-134 (2011).

[5] International Specialty Products, "GAFCHROMIC EBT2: Self-developing film for radiotherapy dosimetry," (2010).

[6] H. Morrison, G. Menon, R. Sloboda, "Radiochromic film calibration for low-energy seed brachytherapy dose measurement," Med. Phys. **41**, 15-16 (2014).

[7] "Gafchromic EBT2," http://www.ashland.com/Ashland/Static/Documents/ASI/Advanced%20materials/ebt2.pdf Accessed 4/19/2015.

[8] "Gafchromic EBT3," http://www.ashland.com/Ashland/Static/Documents/ASI/Advanced%20materials/gafchromic-ebt3.pdf Accessed 4/192015.

[9] A. Niroomand-Rad, C.R. Blackwell, B.M. Coursey, K.P. Gall, J.M. Galvin, W.L. McLaughlin, A.S. Meigooni, R. Nath, J.E. Rodgers, C.G. Soares, "Radiochromic film dosimetry: Recommendations of AAPM Radiation Therapy Committee Task Group 55," Med. Phys. **25**, 2093-2115 (1998).

[10] "GAFCHROMIC HD-810 Radiochromic Dosimetry Film," http://www.meditest.ft/pdf/GAFCHROMIC%20HD-810.pdf Accessed 4/19/2015.

[11] D.F. Lewis, "A Guide to Radiochromic Film Dosimetry with EBT2 and EBT3," http://www.fimecorp.com/pdfs/A%20Guide%20for%20Using%20Radiochromic%20Film.pdf Accessed 9/5/2015.

[12] T. Tanaka and H. Kitamura, "SPECTRA: a synchrotron radiation calculation code," Journal of Synchrotron Radiation **8**, 1221-1228 (2001).

[13] J. Corbett and C. Wermelskirchen, "Chapter 9: Accelerator Controls and Modeling," in *Synchrotron Radiation Sources: A Primer, Vol. 1*, 1st ed., edited by H. Winick (World Scientific Publishing Co. Pte. Ltd., Singapore, 1994), pp. 215.

[14] F.M. Khan, *The Physics of Radiation Therapy*, 4th ed. (Lippincott Williams & Wilkins, Philadelphia, PA, USA, 2010).

[15] H.E. Johns and J.R. Cunningham, *The Physics of Radiology*, 4th Edition ed. (Charles C Thomas, Springfield, IL, USA, 1983).

[16] F. Salvat, J.M. Fernandez-Varea, J. Sempau, "PENELOPE-2008, a code system for Monte Carlo simulation of electron and photon transport," Issy-les-Moulineaux France, OECD NEA (2009).

[17] E.A. Siegbahn, J. Stepanek, E. Brauer-Krisch, A. Bravin, "Determination of dosimetrical quantities used in microbeam radiation therapy (MRT) with Monte Carlo simulations," Med. Phys. **33**, 3248-3259 (2006).

[18] J. Spiga, Y. Prezado, E. Braeuer-Krisch, V. Fanti, P. Randaccio, A. Bravin, "The Effect of Beam Polarization in Microbeam Radiation Therapy (MRT): Monte Carlo Simulations Using Geant4," 2009 IEEE Nuclear Science Symposium Conference Record, Vols 1-5, 2170-2173 (2009).

[19] I. Martinez-Rovira and Y. Prezado, "Monte Carlo dose enhancement studies in microbeam radiation therapy," Med. Phys. **38**, 4430-4439 (2011).

[20] I. Martinez-Rovira, J. Sempau, J.M. Fernandez-Varea, A. Bravin, Y. Prezado, "Monte Carlo dosimetry for forthcoming clinical trials in x-ray microbeam radiation therapy," Phys. Med. Biol. **55**, 4375-4388 (2010).

[21] H. Nettelbeck, G.J. Takacs, M.L.F. Lerch, A.B. Rosenfeld, "Microbeam radiation therapy: A Monte Carlo study of the influence of the source, multislit collimator, and beam divergence on microbeams," Med. Phys. **36**, 447-456 (2009).

[22] S. Bartzsch, M. Lerch, M. Petasecca, E. Braeuer-Krisch, U. Oelfke, "Influence of polarization and a source model for dose calculation in MRT," Med. Phys. **41**, 041703 (2014).

[23] I. Martinez-Rovira, J. Sempau, Y. Prezado, "Development and commissioning of a Monte Carlo photon beam model for the forthcoming clinical trials in microbeam radiation therapy," Med. Phys. **39**, 119-131 (2012).

[24] J.C. Crosbie, I. Svalbe, S.M. Midgley, N. Yagi, P.A.W. Rogers, R.A. Lewis, "A method of dosimetry for synchrotron microbeam radiation therapy using radiochromic films of different sensitivity," Phys. Med. Biol. **53**, 6861-6877 (2008).

[25] L.O. Dallin, "Synchrotron Light Source Magnets," CLS Design Note 5.2.31.2 Rev.0 (2001).

[26] J.M. Vogt, J.C. Bergstrom, S. Hu, "Accurate measurement of the beam energy in the CLS storage ring," Proceedings of PCaPAC 2010, 36-37 (2010).

[27] B. Hartmann, M. Martisikova, O. Jaekel, "Technical Note: Homogeneity of Gafchromic (R) EBT2 film," Med. Phys. **37**, 1753-1756 (2010).

4 ABSOLUTE AIR KERMA RATE MEASUREMENTS USING A CYLINDRICAL FREE-AIR IONIZATION CHAMBER ON THE 05B1-1 BEAMLINE

4.1 Introduction

The BMIT beamlines were constructed with the intention of imaging and therapy applications for live animals, and ultimately, for human trials. With this end goal in mind, the availability of dosimetry for the BMIT beamlines is vital. It is preferable (and for human studies, required) to use dosimeters traceable to a standards laboratory.

As discussed in Section 1.3, there are many challenges in experimental synchrotron radiation dosimetry. A synchrotron beam is small (< 1 cm) and non-uniform; both intensity and relative energy spectrum vary over the beam's height. Synchrotron x-ray beams are also relatively low in energy (~10s – 100s of keV). These unique characteristics result in uncertainties when using dosimeters calibrated for clinical beams for measurements in a synchrotron beam. An absolute dosimeter, which does not require calibration, can be used to mitigate the uncertainties introduced by calibrating and measuring dose in clinical versus synchrotron x-ray beams. Free-air ionization chambers (FACs) offer accuracy and absoluteness for air kerma measurements.[1]

There have been relatively few publications describing the use of FACs for absolute air kerma measurements at synchrotron light sources. Nariyama *et al.* reported the development of a small (8.5 cm plate separation) parallel plate FAC for the measurement of air kerma rates at the SPring-8 synchrotron light source in Japan.[2] More recently, as described in Section 1.3.2.1, Crosbie *et al.* reported on the evaluation of two parallel plate chambers for air kerma rate measurements at the Australian Synchrotron's Imaging and Medical Beamline.[3]

In this chapter, the process of obtaining absolute air kerma rate measurements using a cylindrical free air ionization chamber on the 05B1-1 beamline is described. This includes the measurements of ionization produced in air by the photon beam for various degrees of filtration, and the determination of correction factors, which are obtained from Monte Carlo methods, calculations based on the theoretical energy spectrum, values provided in the literature, and experimental methods.

4.2 Theory

4.2.1 Free-air ionization chamber

Ionization chambers are one of the most trusted dosimeters in radiation therapy. The majority of ion chambers in the clinic are used as reference dosimeters after calibration at a national standards laboratory (*e.g.*, the National Research Council of Canada (NRC)). However, certain ionization chambers are one of the few types of dosimeters capable of absoluteness, meaning they "can be used to measure the absorbed dose deposited in its own sensitive volume without requiring calibration in a known field of radiation."[1] These FACs require a large active volume, and are typically too bulky and fragile to be regularly used outside of national standards laboratories. They are the standard instrument used for air kerma rate measurements, and the calibration of other dosimeters, in medium energy x-ray beams (energies in range ~10 – 400 kV[4]).

FACs are designed to measure exposure, X, which is defined as dQ/dm where dQ is the total charge of the ions of one sign produced in air when all the electrons liberated by photons in air of mass dm are completely stopped in air.[1] There are two general FAC designs: plane parallel and cylindrical geometry. The more popular, parallel plate design is shown in Fig. 4.1. The x-ray beam enters the chamber through the chamber's aperture, then passes between two parallel plates. A high voltage is applied between the parallel plates which creates an electric field to collect the ionization produced in the volume, V. The length, L, of this volume, V, is defined by the electric field lines at the edges of the collecting plate, and the area of the beam. The collecting volume, V', in which the ions are collected is defined by the edges of the electric field lines, the width of the electrodes, and the separation of the electrodes. The guard plates and wires are used to optimize the position and uniformity of the length-defining electric field lines. A connection between the collector plate and an electrometer allows quantification of the collected ion pairs. A lead-lined box surrounds the active volume to only allow photons to enter the chamber through the aperture. In this configuration, for both parallel[1] and divergent[5] beams, exposure is determined by

$$X = \frac{dQ}{dm} = \frac{Q}{\rho A_{ap} L} \tag{4.1}$$

where ρ is the density of air, A_{ap} is the area of the aperture, and L is the length of the collecting volume.

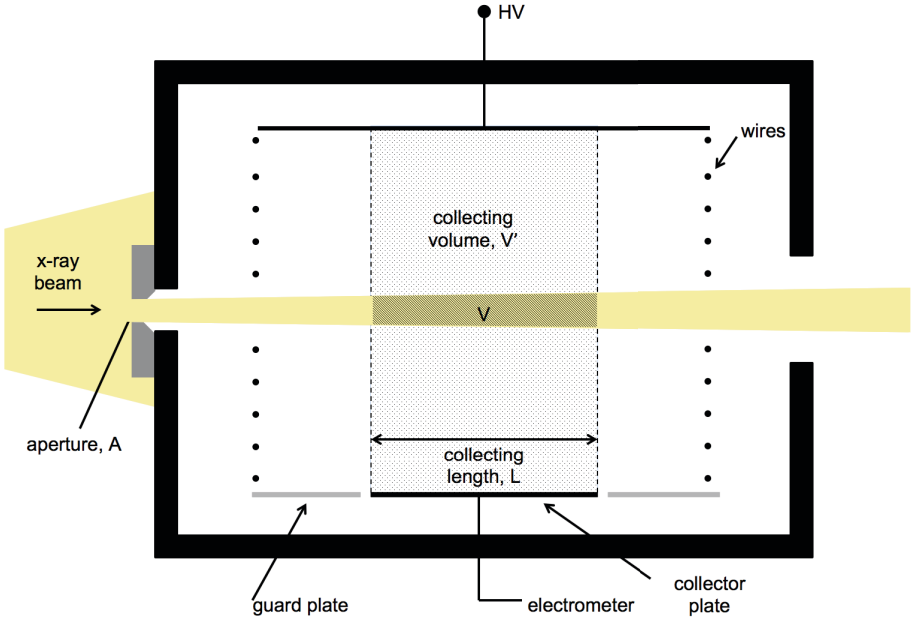

Figure 4.1 A schematic for a typical plane-parallel FAC. The area of the x-ray beam entering the chamber is defined by an aperture. The beam passes between a high voltage plate and grounded, co-planar guard and collector plates. The ionization produced by electrons liberated in volume V is collected from volume V'. The wires and guard plates improve electric field uniformity.

For a FAC to strictly measure exposure according to its definition, certain conditions must be met. These conditions are to ensure the electrons produced by the x-ray beam in the active volume spend all their energy between the two plates. First, the separation of the plates must be large enough such that the range of the liberated electrons is less than the distance between the volume *V* and the electrodes. Additionally, charged-particle equilibrium is required. This is so electrons produced outside of *V* (and thus not to be included in the definition or measurement of exposure), but scattered into *V'* before losing all their energy, are compensated by electrons produced in *V*, but scattered out of *V'* before expending all their energy. For charged particle equilibrium to exist, the beam intensity must be uniform over the length of the collecting volume, and

the distance between the diaphragm and the collecting volume must be greater than the range of the electrons in air.

There are a few drawbacks of the parallel plate design. First, electronic equilibrium is required, but it is never strictly present due to the attenuation of the beam across the collecting length, L. Secondly, for the accurate determination of exposure, the mass of air must be accurately known. The volume of air is determined by the width of the chamber, the area of the aperture, and the length of the collecting volume. The length of the collecting volume, V', depends on the electric field lines at the edges of the collector plate, and it is difficult to know with high accuracy. Finally, due to these constraints on the electric field, parallel plate chambers are fairly fragile and cannot be easily shipped without concern for changes that could cause uncertainties in the electric field.

The Attix-type, cylindrical, variable-length FAC (Fig. 4.2) is a novel design that offers some advantages over the parallel plate design. Like the parallel plate design, the active volume is surrounded by a lead-lined box to attenuate scattered x-rays. The beam enters the FAC through an area-defining aperture, and traverses the central axis along the longitudinal axes of the cylindrical electrodes. Thin windows cover the ends of the cylindrical electrodes where the beam enters and exits the active volume. The windows are present to keep out electrons created outside of the active volume.[1] A high potential (several kV) is applied to the chamber shell. The charge released through ionization is collected at an off-centre collecting rod. The collecting rod is small and located far from the beam (the central axis) to minimize the loss of measured charge due to electrons striking the rod (< 0.01 %[1]).

The two telescoping cylindrical electrodes facilitate the determination of air kerma through a difference measurement. Two ionization measurements are taken, one with the chamber in its collapsed configuration, and the second taken in the extended configuration that is achieved by movement of the telescoping electrodes (Fig. 4.2). The positions of both electrodes are adjusted, such that the center (or midline) of the collecting volume is kept fixed relative to the aperture and x-ray source. For the two

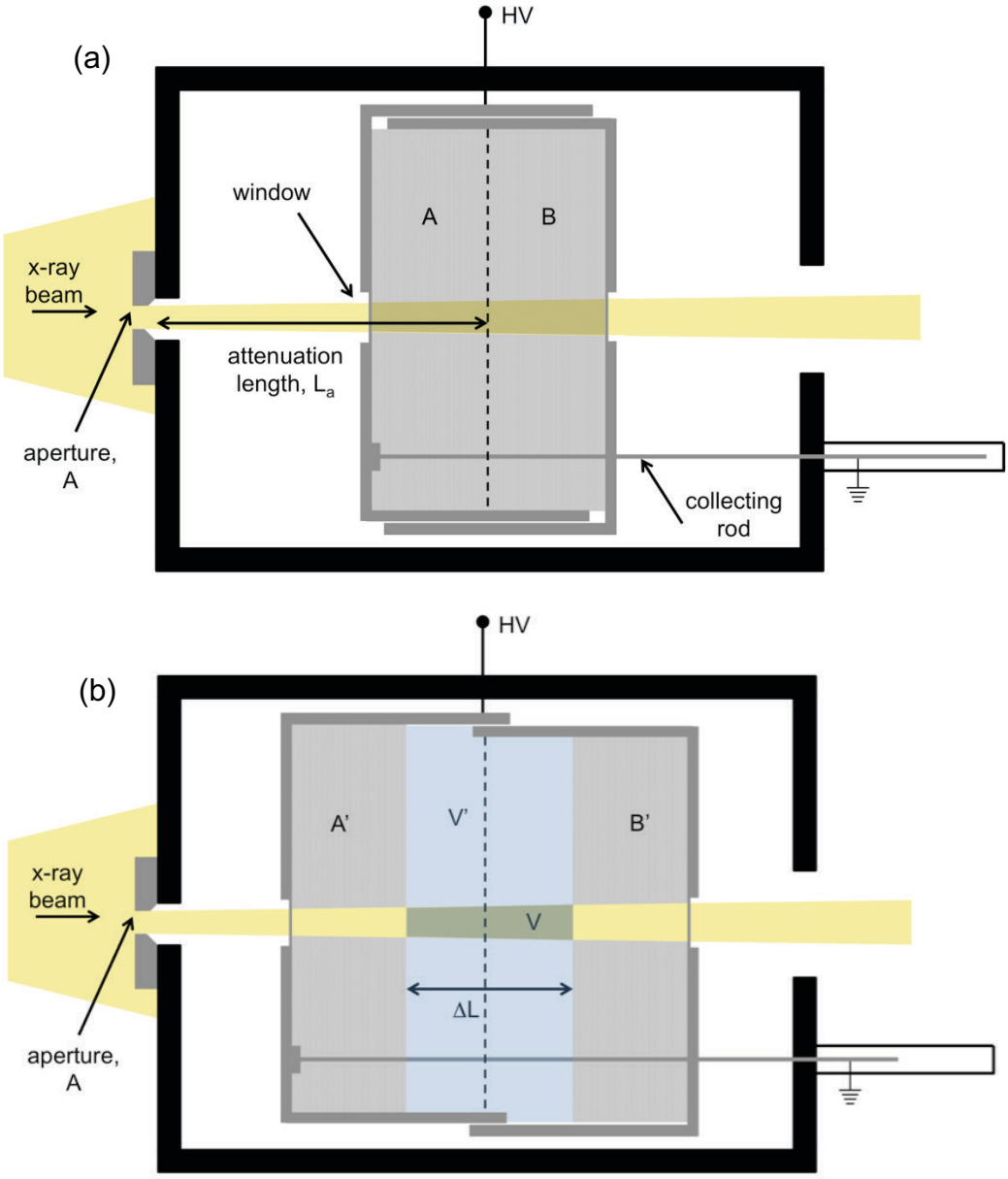

Figure 4.2 A schematic of a variable-length FAC. (a) The collapsed configuration showing the FAC's diaphragm, Pb-lined box, telescoping electrodes, entrance and exit windows, and collecting rod. (b) The extended configuration showing the change in length between the two configurations, ΔL, the effective charge collection region V' (blue region), and the effective volume in which measured charge is created, V.

configurations, the only difference in the measured ionization from A and A' is a slight increase due to less attenuation for A' (Fig. 4.2). The same is true for B and B', except there is a slight decrease in the charge collected from B'. If the attenuation is linear,

which is a good approximation for a small degree of attenuation, the change from A to A' and B to B' will cancel. In this case, the difference in charge collected between the collapsed and extended configurations, ΔQ, is due entirely to charge produced in volume V. With this variable-length cylindrical chamber, exposure is determined as

$$X = \frac{dQ}{dm} = \frac{\Delta Q}{\rho A_{ap} \Delta L} \tag{4.2}$$

where ΔL is the change in length between the extended and collapsed configurations.

There are three advantages of the cylindrical, variable-length design over the plane-parallel design. First, there is no dependence on CPE. The difference technique allows the measurement of the ion pairs created in the volume V only. Secondly, the strict requirements for the electric field uniformity for the parallel plate design do not exist for the Attix-type FAC. Finally, the air mass can be defined more accurately since it is dependent on the change in length between the collapsed and extended configurations of the FAC, which can be determined very accurately. This eliminates the uncertainty involved in the determination of ΔL for plane parallel FACs, which relies on the homogeneity of the electric field.

Air kerma, K_{air}, can be determined from exposure as measured by a FAC as follows

$$K_{air} = \frac{\Delta Q}{\rho_{air} \cdot A_{ap} \cdot \Delta L} \cdot \left(\frac{W}{e}\right)_{air} \cdot \frac{1}{1-g} \cdot \prod_i k_i \tag{4.3}$$

where ΔQ, ΔL, ρ_{air}, and A_{ap} are defined above. This conversion from exposure, a measure of charge released per mass of air, to air kerma, which relates energy released to the air per mass of air, requires the conversion factor $(W/e)_{air}$. This factor is the mean energy spent per unit charge produced in dry air. Additionally, there is a correction required for the mean energy given to photons emitted via radiative processes. The energy carried away by these photons is not included in the definition of exposure, but is included in the definition of air kerma. The correction is given by $(1 - g)$, where g is the fraction of energy lost by radiative processes.[6] Finally, several other correction factors, k_i, are required.

4.2.2 Correction factors

A series of correction factors are required to determine absolute air kerma using a FAC. Most of these correction factors are shared between the parallel plate and cylindrical design. These include corrections that are specific to FACs, as well as factors common to all ionization chambers.

4.2.2.1 Attenuation in air correction, k_a

A correction is applied for attenuation of the primary photon fluence in air between the plane of definition (located at the downstream plane of the diaphragm) to the point of measurement at the mid-point of the chamber. This distance is referred to as the attenuation length, L_a. The magnitude of this correction will increase with increasing attenuation length and decreasing incident x-ray energy.

4.2.2.2 Photon scatter correction, k_{sc}

Any measured ionization produced from any secondary photon interactions is not included in the definition of exposure or air kerma. Scattered primary photons and fluorescence photons contribute most to the required correction.[4] In general, the correction for photon scatter increases with decreasing energy, and increases with increasing attenuation length and increasing collecting volume dimensions laterally.

4.2.2.3 Electron loss correction, k_e

The definition of exposure requires that all released electrons be stopped in air, thus a correction is required to account for those electrons that do not expend all of their kinetic energy before being stopped by the collecting rod, electrodes or chamber walls. The energy-loss correction varies inversely with the diameter of the electrodes, but has a more complicated relationship with energy due to the variation in the range of electrons produced during photoelectric versus Compton interactions, and the relative probability of these interactions.

4.2.2.4 Window attenuation correction, k_w

The correction for attenuation of the primary photons in the thin entrance window of the FAC is denoted by k_w. As expected, this correction increases with decreasing photon energy, and increasing window thickness, and changes with window material.

4.2.2.5 Diaphragm transmission and scatter correction, k_{dia}

A correction is required to account for transmission through and scatter within the diaphragm. The transmission depends on the diaphragm material, the distance to the source, and the shape of the aperture.[7] Scatter from the surface of the aperture requires a greater correction than diaphragm transmission, and is inversely related to the aperture radius.[7,8]

4.2.2.6 Ionic recombination correction, k_{ion}

After an ion pair is produced, it may recombine before reaching the electrodes. A correction is required to account for the lack of complete collection efficiency. The correction for ion recombination depends on radiation quality, dose rate, chamber geometry and applied voltage.

4.2.2.7 Polarity correction, k_{pol}

The polarity correction is common to all ionization chambers and can be determined experimentally. The polarity effect accounts for a change in measured charge with a reversal of the applied potential polarity. Typically for free air chambers the polarity correction is less than 0.1%.[4]

4.2.2.8 Temperature, pressure and humidity corrections, k_{TPH}

Corrections for ambient conditions are required to adjust for the density of air. Attenuation coefficients are tabulated for dry air near sea level conditions, but this does not describe the conditions at the time of measurement. Humidity correction is required to account for its effect on both *W/e* and stopping powers.

4.3 Materials and methods

4.3.1 The cylindrical, variable-length free air ionization chamber

The commercially manufactured Victoreen Model 480 FAC (Fig. 4.3, The Victoreen Instrument Co., Cleveland, OH (no longer available)) was used to perform absolute air kerma rate measurements. The FAC was donated to the National Research Council of Canada (NRC) by Atomic Energy of Canada, Ltd in 2007. The chamber is an Attix-type FAC (Fig. 4.2), with two cylindrical electrodes that define the length of the collecting volume. The aluminum electrodes have a diameter of 30 cm. The two telescoping cylinders allow a variable length, while maintaining a fixed distance between the source and the midline of chamber. The ends of the cylindrical electrodes are capped with PMMA, and have entrance and exit windows (of unknown thickness and composition) along the axis of the chamber (Fig. 4.4(a)).

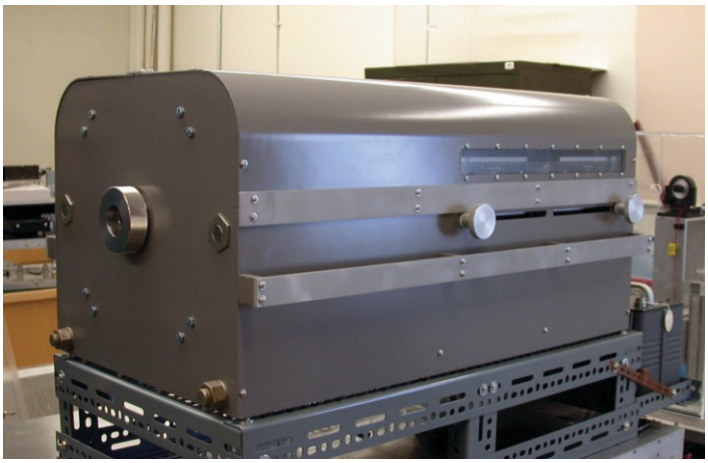

Figure 4.3 The Victoreen 480 FAC. The screw holding the diaphragm in place is visible on the front face of the chamber. The electrode position adjustments are shown on the side of the FAC. Image taken during refurbishment at the NRC.

In its fully collapsed state, the collecting volume is 32 cm in length, and expands up to 62 cm. The FAC's plane of definition (the point of measurement) is located at the back plane of the diaphragm, and is 40.12 cm from the mid-plane of the FAC. The aluminum collecting electrode is 8 cm below the central axis of the chamber, and has a diameter of 0.95 cm (Fig 4.4(b)). The chamber was designed for effective energies between 40 and

250 keV. The FAC has a maximum operating voltage of 5000 V. The volume in which the measured ionization is produced (*V* in Fig. 4.2(b)) is defined by the area of the photon beam traversing the chamber, which itself is defined by a tungsten alloy (Hevimet) diaphragm with a cylindrical aperture. The diaphragm was designed and fabricated at the NRC specifically for use on the BMIT beamlines.

The aluminum housing surrounding the cylindrical electrodes has dimensions of 45.0 cm wide x 38.7 cm high x 81.2 cm long. The FAC's front wall is shielded with approximately 25.4 mm of lead (Fig. 4.4(c)) housing to limit the detection of transmitted x-rays through the FAC wall. The total structure is thus quite large and heavy (~150 kg), which causes challenges in transporting, positioning and alignment of the FAC. At the rear of the chamber there are connections for the high voltage to be applied, and a connection between the collecting rod and the electrometer (Fig. 4.4(d)).

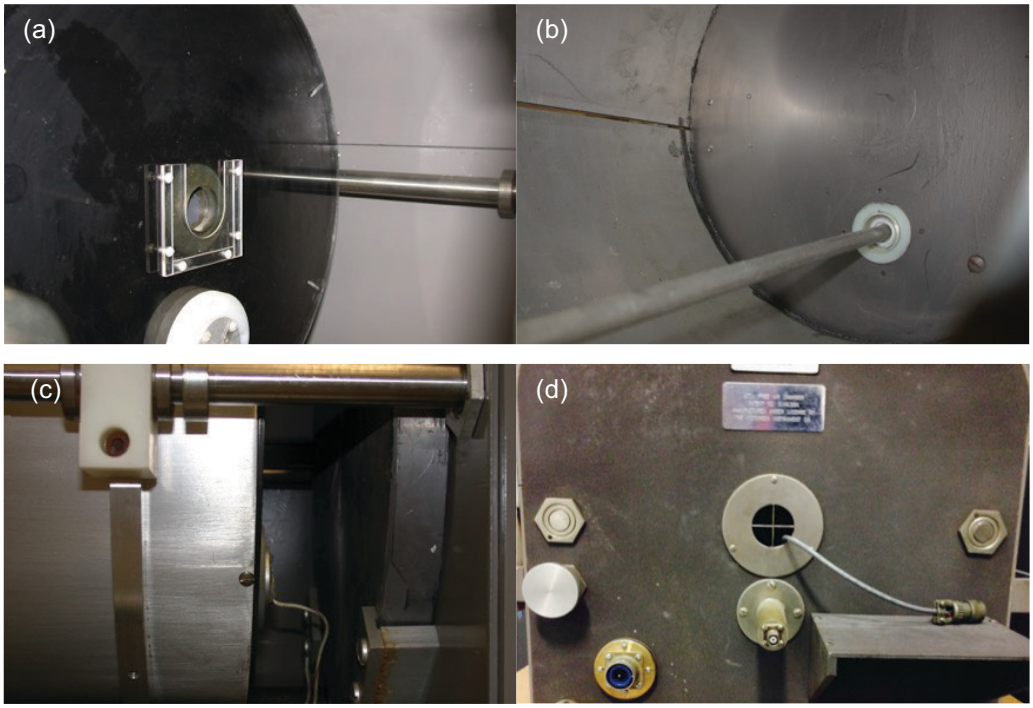

Figure 4.4 Details of the Victoreen 480 FAC structure. (a) The flat end of the upstream cylindrical electrode, including the entrance window. (b) Inside the cylindrical electrodes and the collecting rod. (c) A side view of the cylindrical electrode and the lead shielding behind the front wall of the FAC. (d) The rear of the chamber showing the HV connection (lower left), the electrometer connection (center), and the cross hairs for alignment (center).

4.3.2 Preliminary testing and benchmarking against primary standards at the National Research Council of Canada

Refurbishment and initial testing was performed at the NRC x-ray facility. Two beam qualities (produced by an x-ray tube) were used to benchmark the refurbished Victoreen chamber against two primary standard FACs: (1) a 135 kVp beam with a half-value layer (HVL) of 0.488 mm Cu, and a 60 kVp beam with a HVL of 1.03 mm Al. This Attix-type chamber was compared against two NRC primary standard FACs, the Low Energy Exposure Standard (LEES) and the Medium Energy Exposure Standard (MEES), which are both parallel plate chambers. The LEES has a plate separation of 6.1 cm, and a collecting length of 4.6 cm;[9] the MEES has a plate separation of 35.0 cm and a collecting length of 10.2 cm.[9]

4.3.3 Irradiation conditions at the 05B1-1 beamline

Measurements were performed at the CLS (Section 2.5) on the 05B1-1 beamline (Section 2.6.1). Five filtrations were used to adjust the energy spectrum of the polyenergetic photon beam: 0.552 mm Cu, 13 mm Al + 0.552 mm Cu, 1.103 mm Cu, 2.210 mm Cu, and 6.102 mm Cu. In addition, two monoenergetic beams (20.0 and 33.3 keV, each with 0.1103 mm Al filtration) were produced using a double crystal Bragg monochromator. These filtrations were chosen to reduce the dose rate in the polyenergetic beam to a level with correctable ion recombination, or to match common experimental conditions for imaging and therapy experiments. The beam was uncollimated in the vertical direction and 70 mm in the horizontal direction.

The FAC was placed on three motorized stages (Fig. 4.5(a)) that allowed fine (~ 25 μm) vertical adjustments. The FAC's plane of definition was placed 25.17 m from the bending magnet source, and 5.68 m from the beamline's Be window defining the exit of the vacuum system. Alignment was an iterative process using progressively smaller apertures, and both a fluorescence screen (Fig. 4.5(b)) and radiochromic film to verify the position and size of the beam spot on the exit window of the FAC with respect to its built-in crosshairs (Fig. 4.4(d)).

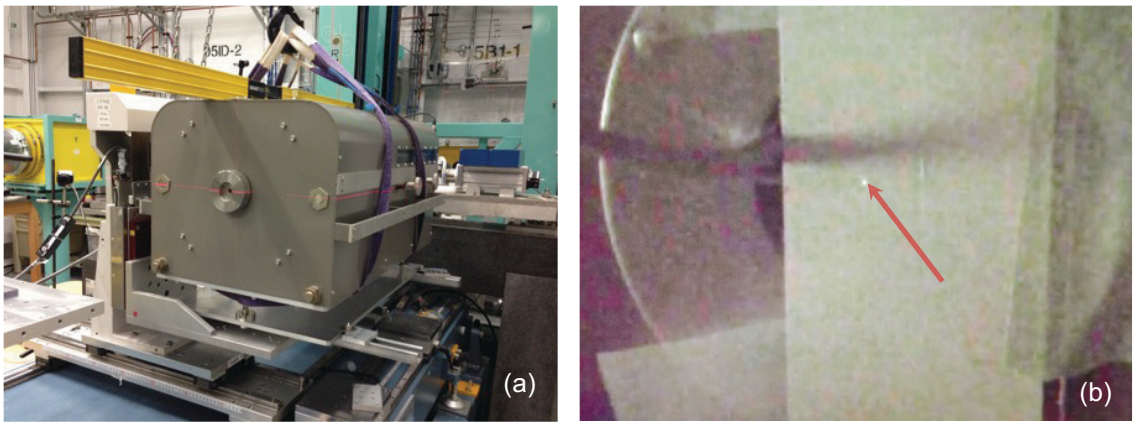

Figure 4.5 (a) The Victoreen 480 positioned on the 05B1-1 beamline's motorized stages. (b) A screen shot showing the beam spot on a fluorescent screen at the rear of the chamber used for alignment.

4.3.4 Air kerma rate determination using the Attix-style FAC

The air kerma rate measurement using the variable-length FAC requires a differential reading of collected charge or current between the expanded and collapsed positions. The air kerma, K_{air} (Gy), is given by Eq. 4.3. An alternative to taking only two charge measurements, one with the electrodes in the fully collapsed and one in the fully extended locations, is to take a series of charge measurements at various locations and apply a linear fit to get a value for $\Delta Q_{air}/\Delta L$. For each beam, $\Delta Q_{air}/\Delta L$ was determined by taking readings with electrode separations of 2, 4, 6 and 8 cm greater than the fully collapsed position. The readings were taken using a Keithley 6517A electrometer (Keithley Instruments, Inc., Cleveland, OH, USA). The high voltage was applied using a Stanford Research Systems PS350 high voltage power supply (Stanford Research Systems, Inc., Sunnyvale, CA, USA). The readings were taken at -5000 V. At each measurement the storage ring current (I_{SR}) was recorded, which was used to normalize the readings. This was necessary because dose rate is directly proportional to the storage ring current. It was assumed the dose per mA did not change during the experimental period, which is a reasonable assumption particularly given the magnitude of other sources of uncertainty.

To relate collected charge to deposited energy we apply $(W/e)_{air,}$ which has a value of 33.97 J/C $\pm$ 0.15 %.[10] The value for ρ_{air} is 1.2048 kg/m^3 at the reference

conditions of 20°C and 101.325 kPa. The fraction of secondary electron energy radiated away, g, is dependent on energy, and is small for the energies of the synchrotron x-ray beams. For energies between 10 and 250 kV, the correction for energy transferred to bremsstrahlung photons, and the component of their energy reabsorbed in the FAC collecting volume, is less than or equal to 0.02 %,[11] and was thus considered negligible for our work.

To determine the mass of air traversed by the beam within the collecting volume, the area of the aperture, A_{ap}, must be known. The specially fabricated diaphragm was imaged using a microscope with a resolution of 0.64 μm per pixel. The aperture area on each face of the diaphragm was measured from these images.

4.3.5 Determination of correction factors

The correction factors used in Eq. 4.3 were determined with a combination of Monte Carlo simulations, analytical calculations, experimental measurements, and interpolation of tabulated factors.

4.3.5.1 The 05B1-1 energy spectra

Analytical calculations and Monte Carlo simulations used to obtain certain correction factors require knowledge of an x-ray beam's energy spectrum. The energy spectra of the polyenergetic 05B1-1 photon beams were calculated using the SPECTRA v. 10.0 software, as described in Section 3.2.6 and reported in Section 3.3.6.[12] The calculations were at the FAC's plane of definition (25.17 m from the source) for a circular aperture with a radius of 260 μm.

As an experimental verification of the theoretical energy spectra, the HVL of all but one of the experimental beams was measured. The procedure is described in Section 3.2.7. The one spectrum not verified experimentally was the 6.103 mm Cu-filtered beam. The beam filtration, mean energy and measured HVLs are repeated here for easy reference in Table 4.1.

Table 4.1 The mono- and polyenergetic beams for which air kerma rates were measured on the 05B1-1 beamline.

Mode	Filtration (mm)	Mean Energy, E (keV)	Measured half-value layer, HVL (mm Cu)
Mono	0.110 (Al)	20.0	0.78 mm Al
Mono	0.110 (Al)	33.3	3.03 mm Al
Poly	0.552 (Cu)	45.3	0.200 mm Cu
Poly	0.552 (Cu) + 13 (Al)	51.7	0.291 mm Cu
Poly	1.103 (Cu)	54.7	0.342 mm Cu
Poly	2.210 (Cu)	65.3	0.557 mm Cu
Poly	6.103 (Cu)	84.0	1.12 mm Cu

4.3.5.2 Monte Carlo simulations (k_a, k_{sc}, k_e, k_w, k_{dia})

The EGSnrc egs_fac user code[13] was developed specifically for performing Monte Carlo simulations to determine the correction factors of a free air chamber. This code requires the chamber geometry, x-ray source information, and material data. The simulation geometry is shown in Fig. 4.6. The images are cross-sections at the center of the chamber in the y,z-plane (vertical plane, Fig 4.6(a)) and the x,z-plane (horizontal plane, Fig. 4.6(b)). The simulation geometry consists of a rectangular box of aluminum (0.32 cm thick), which houses two telescoping cylindrical electrodes. Consistent with the actual FAC dimensions, the outer electrode has a radius, r_{cyl}, of 15 cm, and the collecting electrode has a 0.95 cm diameter and is positioned 8 cm below ($-y$) the central axis of the chamber. The air-filled collecting volume occupies the space within the outer electrode, and is defined by polymethyl methacrylate (PMMA) walls on either side of the cylindrical electrodes. The beam enters and exits the collecting volume through windows in the PMMA. The composition of the windows is unknown, although based on their appearance we have assumed the windows to be composed of beryllium for the purpose of our Monte Carlo simulations. The thickness of the Be windows in the Monte Carlo geometry is 0.22 mm, which was chosen by matching the tabulated window correction factors from the Victoreen 480 manual to the theoretically calculated window correction factors. The 1.29 cm thick tungsten-alloy (Hevimet) diaphragm (modeled as 90% tungsten, 5% nickel and 5% copper) has a 258 μm cylindrical aperture.

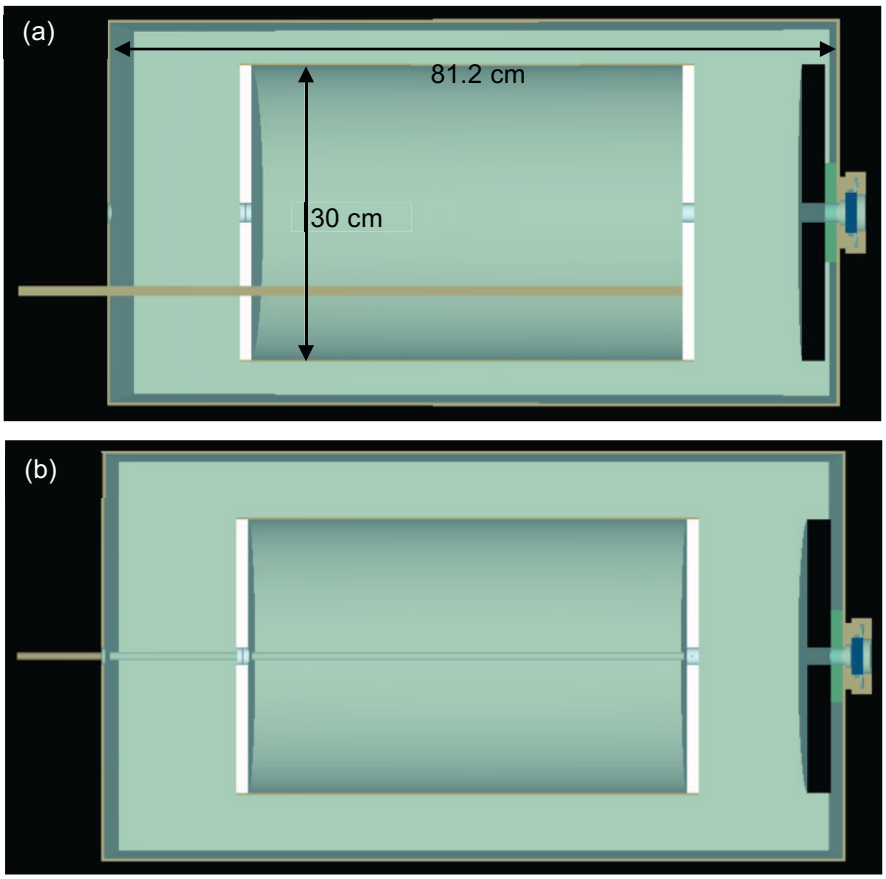

Figure 4.6 The Victoreen 480 geometry used for Monte Carlo simulations. (a) A side view of the chamber (y,z-plane). (b) A top-view of the chamber (x,z-plane). The beam travels from right to left in the image. The air is represented as green, lead shielding as black, the HEVIMET material as dark blue, aluminum as light brown, and PMMA as white.

The modeled beam size was 5 × 5 mm, which is much smaller horizontally than the experimental beam. The small beam was used to minimize simulation time, and because the transmission through the FAC shielding of the relatively low energy beam was expected to be negligible. The angular spread for each beam source was determined using SPECTRA, taking into consideration the small angle subtended by the aperture opening (± 0.01 mrad). The horizontal and vertical divergences were averaged to determine the single input for angular spread in egs_fac. The angular spread ranged from 0.057 mrad for 20 keV to 0.041 mrad for the 6.103 mm Cu-filtered x-ray beam. Although the synchrotron x-ray beam is non-uniform in the vertical direction, the

modeled beam was considered uniform across the small aperture opening. Since the aperture is so small, the non-uniformity over the beam entering the FAC through the aperture is relatively small. Between 0.9 and 1.0×10^9 histories were simulated in each calculation. The calculations were performed using a cluster with 192 AMD Opteron 6276 computation cores. The computation time required for 1.0×10^9 histories per CPU varied with photon energy, and is shown in Fig. 4.7. The uncertainties associated with the Monte Carlo-calculated correction factors are statistical. These uncertainties varied with correction factor and energy, but were less than 0.09 % for all correction factors for all experimental scenarios.

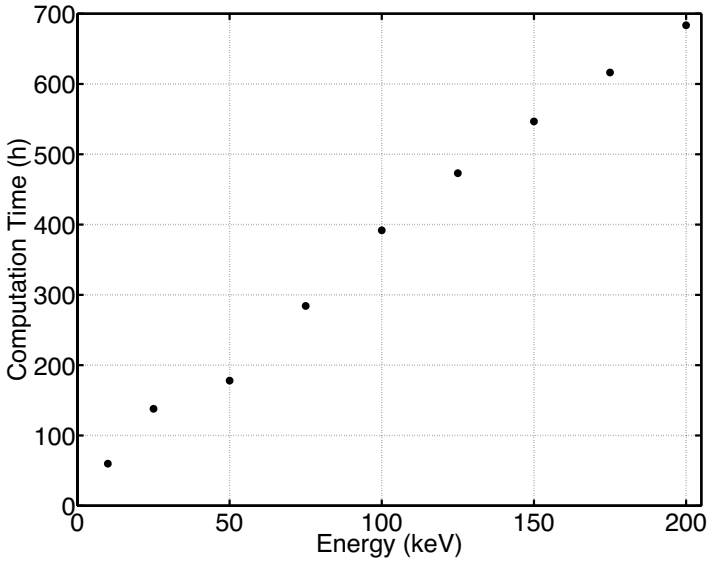

Figure 4.7 The computation time for a single CPU to run 10^9 histories in egs_fac as a function of photon energies between 10 and 200 keV.

The egs_fac code determines each of the correction factors below using the following methodology:

a) k_a (attenuation). The ratio of the air kerma in the collecting volume to the collision kerma at the point of measurement (at the downstream face of the diaphragm) is calculated. This corrects for attenuation in air and in the entrance window.

b) k_{sc} (photon scatter). The code calculates the ratio of the energy deposited in the collecting volume from primary electrons to the total energy deposited in the

same volume. As for k_a, this accounts for photons scattered in air and in the entrance window.

c) k_e (electron loss). This factor corrects for energy lost through interactions with the outer electrodes or collecting rod.

d) k_{dia} (diaphragm transmission and scatter). This factor is given by the ratio of the total energy deposited in the collecting volume to the total energy deposited in the collecting volume excluding energy from particles that have visited a diaphragm region.

e) k_w (window attenuation and scatter). The k_a and k_{sc} factors correct for attenuation and scatter in both air and the entrance window. To better understand the impact of the entrance window, particularly because we are uncertain of its material and thickness, we repeated the simulation, but with an air gap instead of the window. The correction for attenuation and scatter in the window was then determined by taking the ratio of k_a and k_{sc} for the simulations with and without the window. This correction k_w was not included in the final air kerma rate calculations because it is included in the Monte Carlo-determined values for k_a and k_{sc}.

In addition to calculating correction factors for the specific geometry of our experimental measurements, simulations were used to investigate the dependence of these corrections on beam parameters and FAC design. This was done to better understand the influence of individual beam parameters on specific correction factors, and to probe the appropriateness of the Victoreen 480 for air kerma rate measurements on the 05B1-1 beamline. The ranges of values investigated were chosen to explore realistic variations in beam and FAC characteristics (to inform uncertainties), as well as extreme situations to better understand the limits of the beam and/or chamber parameters for which air kerma rates could be determined. The significance of the ranges of the beam and FAC characteristics, and the resulting change in the correction factors, will be examined in the discussion. The relationship between the correction factors and beam energy was investigated by performing the simulations with monoenergetic beams with energies of 10 keV, and 25 – 200 keV in intervals of 25 keV. For a 50 keV monoenergetic beam, the effect of beam divergence (0 – 10 mrad) and beam alignment (0

– 1°) were considered. The dependencies on the FAC dimensions were examined for a monoenergetic beam of 50 keV. Also studied were the impact of altering the radius of the outer cylindrical electrodes (1 – 15 cm), the distance between the collecting rod and the chamber's central axis (2 – 8 cm), the entrance and exit window thickness (0 – 2.5 mm), and the aperture radius (0.0258 – 1.5 cm).

4.3.5.3 Theoretical calculations (k_a, k_w)

The correction for photon attenuation in air over the FAC's attenuation length (L_a = 40.12 cm) was also determined from theory for each beam quality investigated. This was done using the theoretical energy spectrum and the tabulated monoenergetic attenuation coefficients from NIST.[14] With this method the attenuation correction is given by

$$k_a = \frac{dK_{air}^{theor}(0)}{dt} \Big/ \frac{dK_{air}^{theor}(L_a)}{dt} \tag{4.4}$$

where $dK_{air}^{theor}(0)/dt$ is the theoretical air kerma rate at the reference point (at the downstream face of the diaphragm), and $dK_{air}^{theor}(L_a)/dt$ the air kerma rate at the centre of the collecting volume.[1] The air kerma rate at the point L_a is

$$\frac{dK_{air}^{theor}(L_a)}{dt} = \int_{E_{min}}^{E_{max}} \Phi(E,L_a) \cdot E \cdot \left(\frac{\mu_{en}(E)}{\rho}\right)_{air} dE \tag{4.5}$$

where E is the photon energy (keV), $\Phi(E,L_a)$ is the differential flux rate (photons s^{-1} m^{-2} keV^{-1}) at the center of the collecting volume, $(\mu_{en}(E)/\rho)_{air}$ is the mass energy absorption coefficient for dry air in cm^2 g^{-1}, and ρ_{air} is the density of air under experimental conditions (g cm^{-3}). $\Phi(E,0)$ (photons s^{-1} m^{-2} keV^{-1}) is the differential flux rate obtained from the SPECTRA software, and the differential flux rate at the center of the chamber is given by

$$\Phi(E,L_a) = \Phi(E,0) \cdot exp\left(-\left(\frac{\mu(E)}{\rho}\right)_{air} \cdot \rho_{air} \cdot L_a\right). \tag{4.6}$$

The calculations were performed in MATLAB (Mathworks, Natick, MA, USA). The code interpolated the attenuation coefficients for the energy grid of the theoretical energy spectrum to calculate air kerma and the differential flux rate change over the attenuation length. This method is theoretically straightforward, but its accuracy may be limited by

the knowledge of the energy spectrum and the uncertainty of the attenuation coefficients, particularly at the low energies involved. The correction for attenuation in the window material was determined in the same way, but with the attenuation coefficients for beryllium.

4.3.5.4 Measurements (k_a)

A measurement-based method was also used to estimate the photon attenuation correction. The method relies on the unique construction of the variable-length FAC. Two readings are taken, one with the upstream electrode fully expanded and the downstream electrode fully collapsed (M_{up}), and the second with the upstream electrode fully collapsed and the downstream electrode fully expanded (M_{down}). This effectively takes one reading ΔL = 15 cm upstream from the second reading. This provides an experimental value for the mean linear attenuation coefficient in air,

$$\bar{\mu}_{air}^{Q} = \frac{ln(M_{up}/M_{down})}{\Delta L} \tag{4.7}$$

for the given radiation quality, Q. The attenuation correction factor is then

$$k_a = exp\left(\bar{\mu}_{air}^{Q} \cdot L_a\right). \tag{4.8}$$

4.3.5.5 Interpolation of tabulated values (k_a, k_{sc}, k_e, k_w)

Correction factors were also determined by the interpolation, based on the beam quality as specified by the HVL, of experimental values provided in the FAC's manual (Table 4.2). The values of k_a given in the Victoreen manual are for P = 760 mmHg and T = 0 °C. The interpolation of the tabulated values was based on the tabulated and measured HVLs. Similarly, the experimental values from the National Bureau of Standards (NBS) Handbook 64,[15] as fit by Lee *et al.* (2005),[16] were tallied.

Table 4.2 The combined electron loss and photon scatter ($k_e \cdot k_{sc}$), air attenuation (k_a) and window attenuation (k_w) correction factors as a function of HVL provided in the Victoreen 480 manual.

Peak applied voltage, kVp (kV)	Total Filtration	Half-value layer	Correction for electron loss and photon scatter, $k_e \cdot k_{sc}$	Correction for attenuation in air, k_a	Correction for attenuation in window, k_w
60	3 mm Al	0.09 mm Cu 2.6 mm Al	0.995	1.018	1.009
75	3 mm Al	0.11 mm Cu 3.2 mm Al	0.995	1.016	1.008
100	4 mm Al	0.2 mm Cu 5.2 mm Al	0.995	1.012	1.006
150	4 mm Al + 0.23 mm Cu	0.66 mm Cu	0.996	1.009	1.005
200	4 mm Al + 0.5 m Cu	1.26 mm Cu	0.998	1.008	1.004
250	4 mm Al + 1 mm Cu	2.17 mm Cu	0.999	1.006	1.003

4.3.5.6 General ion chamber correction factors (k_{ion}, k_{pol}, k_{TPH})

The high intensity synchrotron x-ray beams have the potential to create a problematic amount of ion recombination during air kerma rate measurements. We have used two methods of investigating the required recombination correction. The first is the two-voltage method for a continuous beam as described in TG51:[17]

$$k_{ion} = \frac{1 - \left(\frac{V_H}{V_L}\right)^2}{\left(\frac{M_H}{M_L}\right) - \left(\frac{V_H}{V_L}\right)^2} \tag{4.9}$$

where $V_{H/L}$ are the higher (H) and lower (L) voltages applied across the chamber, and $M_{H/L}$ are the readings taken at the higher and lower voltages.

It has been reported that the two-voltage method is not valid for large deviations from 1.0 (*e.g.* 1.05 [17] or 1.01 [3,18]). Because of this, we also chose to investigate the recombination correction experimentally by extrapolation based on the expression relating collected current, I_V, saturation current, I_S, and applied voltage, V, given by Boutillon:[18]

$$\frac{I_S}{I_V} = 1 + C_1 \times \frac{1}{V} + C_2 \times \frac{1}{V^2} \times I_S \,. \tag{4.10}$$

For all beam qualities, the inverse of the collected current current, $1/I_V$, was plotted as a function of the inverse of the applied voltage, $1/V$. A quadratic fit was applied to extrapolate to $1/V$=0 to obtain the saturation current, I_s. The recombination correction for each beam quality is then given by

$$k_{ion} = I_V / I_S \,. \tag{4.11}$$

The polarity correction was determined by taking measurements for a single electrode setting with a polarization of +5000 V and – 5000 V. The correction factor was determined according to:[17]

$$k_{pol} = \left| \frac{M^+_{raw} - M^-_{raw}}{2M_{raw}} \right| \tag{4.12}$$

where M^+_{raw} is the reading with the positive applied voltage, M^-_{raw} is the reading with the negative applied voltage, and M_{raw} is the reading at the polarity used for all measurements (negative).

Corrections for ambient conditions are required to adjust for the density of air. The temperature and pressure corrections are those in AAPM's TG51:[17]

$$k_{TP} = \frac{273.2 + T}{273.2 + T_0} \cdot \frac{P_0}{P} \tag{4.13}$$

where T and P are the temperature (in degrees Celsius) and the pressure near the chamber, and T_0 and P_0 are the temperature and pressure at reference conditions. A humidity correction is required to account for its affect on both $(W/e)_{air}$ and stopping powers. The value used for the humidity correction was 0.998 for all measurements. This value is chosen because the value at 50% humidity is 0.998, and only varies approximately 2 parts in 10^3 over the range from 20 – 80%.[4,19] The experimental conditions in the experimental hutch were monitored by built-in beamline monitoring systems, and an independent thermometer, barometer and hygrometer.

4.4 Results

4.4.1 Preliminary testing and benchmarking against primary standards at the National Research Council of Canada

Following restoration, the Victoreen 480 FAC underwent basic testing at the NRC using 60 and 135 kVp x-ray tubes and a 7.03 mm diameter aperture. A measurement of charge per unit length for multiple electrode separations over the range of possible values revealed a standard deviation of 0.16 %, which was deemed acceptable. Polarity and ion recombination corrections were evaluated and found to be consistent with literature values.[20] The results indicated that the chamber was operating correctly, which led to a more detailed comparison between the Attix-type FAC versus two primary standards parallel plate free air chambers. The results are summarized in Table 4.3 for the low energy exposure standard (LEES) and medium energy exposure standard (MEES). At 60 kVp, the agreement between all three chambers is within 0.25 %, which is within the overall uncertainty of the correction factors for the Attix-type chamber. At 135 kVp, the Victoreen 480 and MEES agreed within 0.45 %. The standard uncertainty of each point is estimated to be less than 0.1 %. One disadvantage of the Attix-type chamber is that the required ion recombination correction was much larger than that for the parallel plate design, but it can still be determined with sufficient accuracy at appropriate dose rates.

Table 4.3 Comparison of Victoreen 480 versus the primary standard parallel plate FACs at the NRC.

Chamber	Air kerma rate normalized to Victoreen (%)	
	60 kVp	135 kVp
Victoreen 480	≡1.0000	≡1.0000
LEES	1.0001	---
MEES	1.0025	1.0045

4.4.2 Area of aperture

The diaphragm used for measurements in the small synchrotron beam fabricated at the NRC is shown in Fig. 4.8(a). A microscopy image of the diaphragm opening is shown in

Fig. 4.8(b). Based on this and similar microscopy images, the aperture radius was found to be 255.7 ± 1.1 and 260.7 ± 1.2 μm on the two sides of the diaphragm. The uncertainty describes the standard deviation of multiple contours of the aperture on the images. For the purposes of the calculation of air kerma, the aperture radius was taken to be the average of these two values, 258.2 ± 2.5 μm.

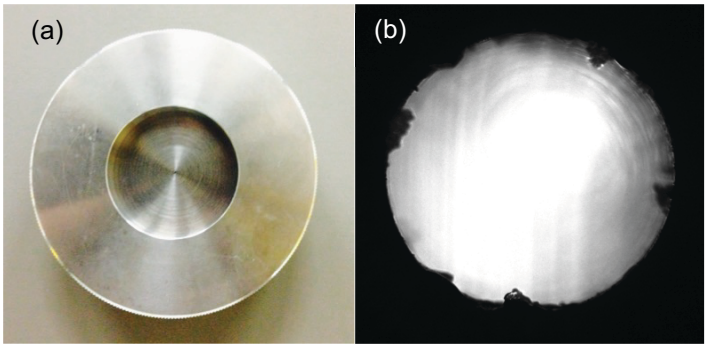

Figure 4.8 The diaphragm and aperture designed for the 05B1-1 beamline measurements. (b) The microscopy images of the aperture.

4.4.3 Dependence of Monte Carlo-determined correction factors on FAC geometry and beam characteristics

4.4.3.1 X-ray energy

The influence of x-ray energy on the Monte Carlo-determined correction factors (photon scatter, electron loss, photon attenuation and diaphragm) is shown in Fig. 4.9. The magnitude of k_{sc} decreases with increasing energy from 0.9818 ± 0.0090 % at 10 keV to 0.9956 ± 0.0274 % at 200 keV. The correction for electron loss, k_e, is unity up to an x-ray energy of 75 keV, reaches a maximum of 1.0059 ± 0.0506 % at 150 keV, then decreases to 1.0041 ± 0.0457% at 200 keV. The attenuation correction, k_a, decreases monotonically with increasing energy from 1.3296 ± 0.0006 % 10 keV (not plotted due to the extreme value) to 1.0113 ± 0.0001 % at 200 keV. The correction for the diaphragm is minimal for all x-ray energies. The magnitude of the correction increases slowly with increasing energy from 1.000 at 10 keV to 0.9994 ± 0.0117 % at 200 keV. For the Victoreen 480, the total correction factor (the product of k_{sc}, k_e, k_a, and k_{dia}) is most strongly influenced by attenuation and photon scatter for the lowest photon energies investigated, and by attenuation and electron loss at the highest photon energies.

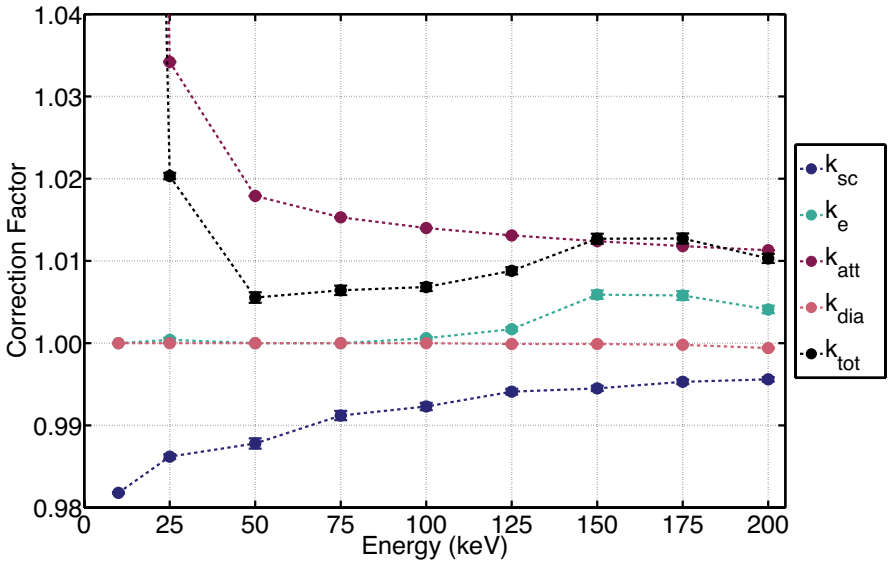

Figure 4.9 The correction factors for photon scatter, electron loss, attenuation, diaphragm, and their product (k_{tot}) as a function of monoenergetic photon energy. The values for k_a and k_{tot} are not shown for 10 keV. The dotted lines are included to guide the eye.

4.4.3.2 Beam divergence

The magnitude of k_{dia} increases with increasing beam divergence, to a maximum of 0.9905 ± 0.0007 at 10 mrad (Fig. 4.10). This is simply due to increasing interactions with the diaphragm. There is also a change in k_{sc} with increasing angular spread. Between 0 to 5 mrad k_{sc} is 0.9921 ± 0.0007. At the maximum divergence investigated, 10 mrad, the correction for photon scatter increases in magnitude to 0.9751 ± 0.0011.

4.4.3.3 Beam alignment

The angle of the incoming x-ray beam was altered with respect to the long axis of the chamber to consider the effect of misalignment between the beam and FAC. The influence of the correction for the aperture gradually increases as k_{dia} decreases from 1.0000 to 0.9814 ± 0.0011 at a misalignment of 1° (Fig. 4.11). The values of k_{sc} are within statistical uncertainty of each other for alignments between 0 and 0.5°, but k_{sc} decreases significantly to 0.9239 ± 0.0021 at 1°.

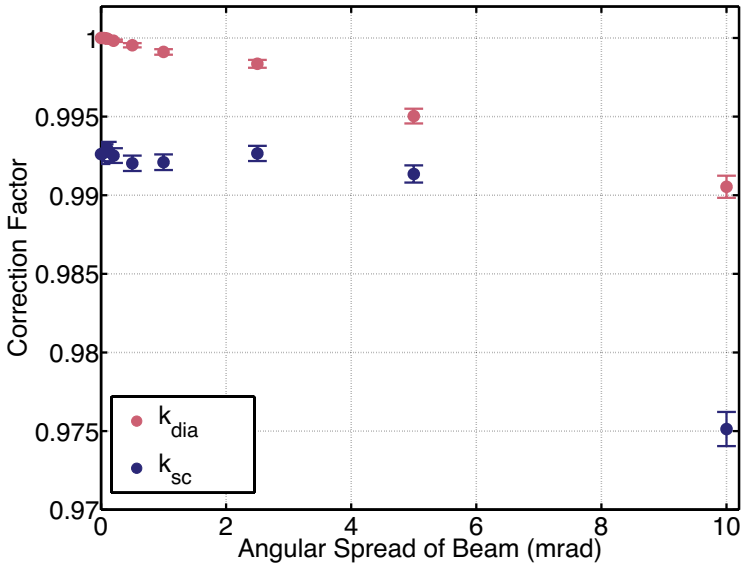

Figure 4.10 The diaphragm (k_{dia}) and photon scatter (k_{sc}) correction factors as a function of x-ray beam angular spread.

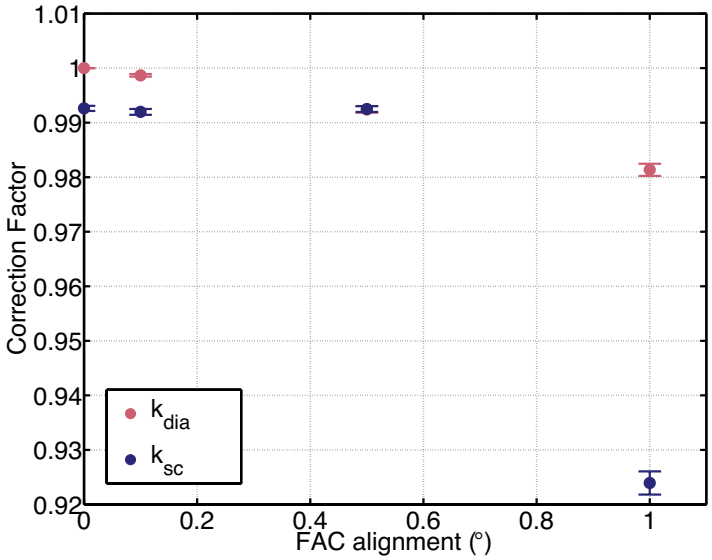

Figure 4.11 The correction for aperture and photons scatter with misalignment between the beam and FAC.

4.4.3.4 Beryllium window thickness

The influence of the window (assumed to be beryllium) on k_{sc} and k_a are shown in Fig. 4.12. As expected, both correction factors increase linearly in magnitude with increasing window thickness. The correction due to attenuation in the window is greater in

magnitude than the extra ionization due to photons scattered in the window. Because the attenuation and scatter corrections have opposing trends (*i.e.*, one increasing and the other decreasing the charge produced in the collecting volume) the combined correction, $k_{sc} \cdot k_a$, correction is lower in magnitude than either k_a or k_{sc} alone.

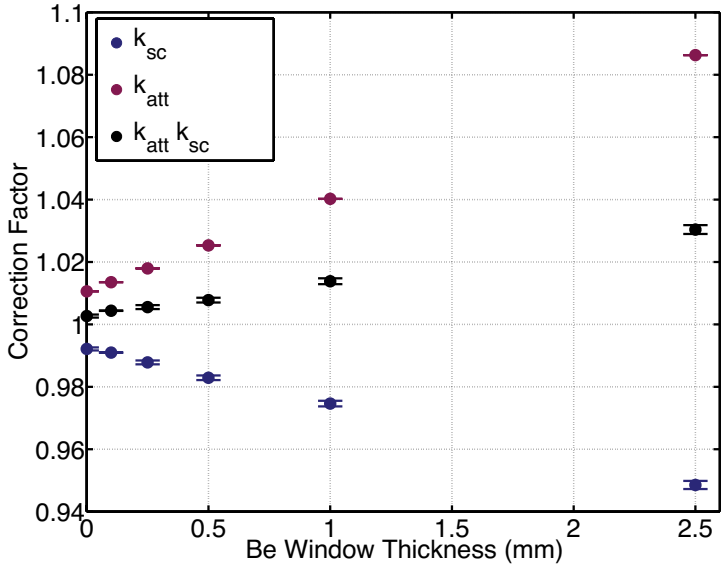

Figure 4.12 The correction factors for photon scatter, attenuation, and the product of the two corrections are plotted as a function of Be window thickness from 0 to 2.5 mm.

4.4.3.5 Outer electrode radius

The relationships between the radius of the outer electrodes and the k_{sc} and k_e corrections are plotted for a 50 and 100 keV monoenergetic beams in Fig. 4.13. The electron loss correction, k_e, decreases as the outer electrodes increase in diameter. Conversely, the magnitude of the scatter correction increases (*i.e.*, k_{sc} becomes smaller and further from unity) with increasing electrode radius as shown. The correction for photon scatter is slightly greater in magnitude for 50 keV versus 100 keV, as expected from Fig. 4.9. For the smallest electrode radius considered, 2.5 cm, k_e is greater for 50 keV (1.2429 ± 0.0027) than 100 keV (1.0994 ± 0.0003). For all greater radii, k_e is greater for 100 keV.

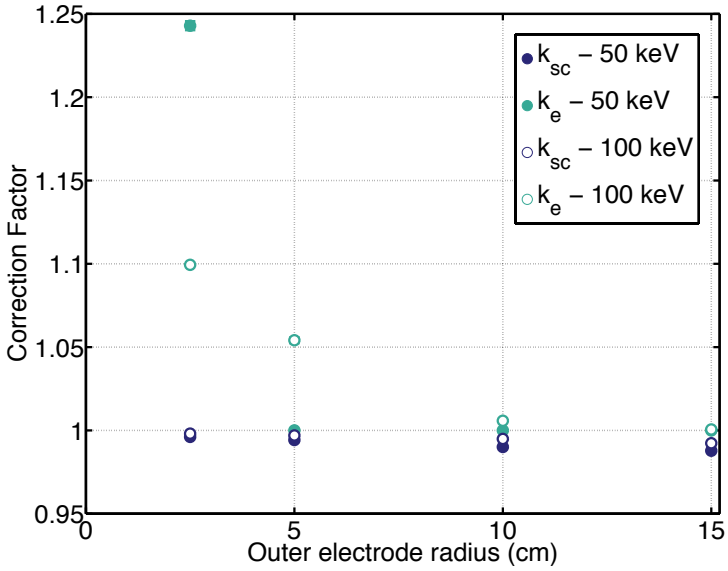

Figure 4.13 The electron loss and photon scatter correction factors as a function of outer electrode radius for 50 (closed circles) and 100 keV (open circles) monoenergetic x-rays.

4.4.3.6 Collecting rod position

The correction for electron loss not only depends on the radius of the outer electrodes, but also on the size and position of the chamber's collecting rod. If the distance between the collecting rod and the central axis of the chamber decreases, the probability of electrons striking the rod before expending all their energy will increase, as shown in Table 4.4. These results show that for a 50 keV beam, the correction for electron loss decreases to unity when the collecting rod is positioned more than 4 cm away from the central axis.

Table 4.4 The change in the electron loss correction factor (k_e) with changing collecting rod position with respect to the FAC central axis.

Collecting Rod Position (cm)	Electron Loss, k_e
2	1.0263 ± 0.0897 %
3	1.0039 ± 0.0298 %
4	1.0001 ± 0.0039 %
6	1.0000 ± 0.0000 %
8	1.0000 ± 0.0000 %

4.4.3.7 Aperture radius

The aperture used in this study is much smaller than typically used for FAC measurements. The effect on k_{dia} was investigated for three aperture sizes, each for a parallel beam, a minimally divergent beam (0.05 mrad) and a more divergent beam (10 mrad). The aperture size had no influence on k_{dia} for the 0 or 0.05 mrad beams. For the beam with 10 mrad of angular spread, k_{dia} increased in magnitude with decreasing aperture radius as shown in Table 4.5.

Table 4.5 The influence of aperture radius on the diaphragm correction factor for an incident x-ray beam with 10 mrad angular spread.

Aperture radius (mm)	Diaphragm correction factor, k_{dia}
0.258	0.9901 ± 0.1492 %
2.58	0.9989 ± 0.0039 %
15.0	1.0000 ± 0.0004 %

4.4.4 Determination of correction factors relevant to our experiments

The Monte Carlo-calculated correction factors are plotted in Fig. 4.14 as a

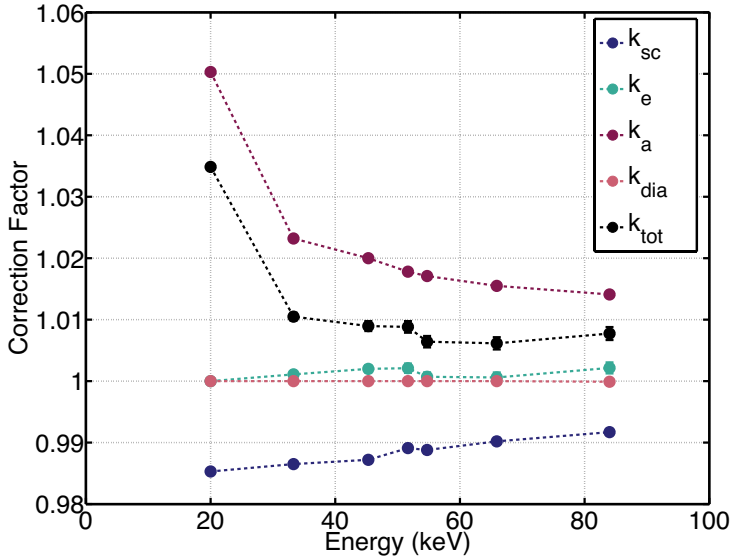

Figure 4.14 The Monte Carlo-calculated correction factors for our experimental beams.

function of mean x-ray beam energy for each beam quality investigated during the experimental beamtime. The dashed lines are included to guide the eye. Each correction factor will be individually discussed below.

4.4.4.1 Photon attenuation in air correction, k_a^{air}

The correction factors for photon attenuation in air determined using four methods are presented in Table 4.6. The values for k_a given in Fig. 4.14 show the same trend as k_a^{air}, but the plotted values also include the attenuation in the entrance window. The tabulated egs_fac corrections were determined from a simulation without the entrance or exit windows to isolate the attenuation in air alone. All egs_fac-determined correction factors have statistical uncertainty of less than 0.01%, and the latter are thus not reported in Table 4.6. The experimental uncertainties are determined from the standard deviation of multiple measurements and error propagation. The theoretical and experimental correction factors are determined for the ambient conditions at the time of measurement.

Table 4.6 The theoretical, experimental, tabulated and Monte Carlo-calculated correction factors for the attenuation correction in air (k_a^{air}) for the synchrotron x-ray beam air kerma measurements. The uncertainty in the egs_fac correction factors is less than 0.01% for all values.

Beam Quality	Theoretical	Experimental	Victoreen manual (corrected for ρ_{air})	egs_fac (corrected for ρ_{air})
20.0 keV	1.035	1.045 ± 0.007	---	1.0371
33.3 keV	1.014	1.025 ± 0.019	1.016	1.0146
0.552 mmCu	1.011	1.018 ± 0.013	1.010	1.0122
0.552 mmCu + 13 mmAl	1.010	1.004 ± 0.008	1.009	1.0105
1.103 mm Cu	1.009	1.003 ± 0.009	1.009	1.0099
2.210 mm Cu	1.008	1.023 ± 0.016	1.009	1.0087
6.103 mm Cu	1.007	0.999 ± 0.050	1.007	1.0077

The values provided by the Victoreen 480 manual and the Monte Carlo-calculated values were corrected to account for the difference in air density at which the values were calculated and the ambient conditions during the air kerma rate measurements on the beamline. This was done by extracting the average attenuation coefficient ($\overline{\mu_{air}}$) from k_a^{air} (Eq. 4.8) for each beam quality, then adjusting $\overline{\mu_{air}}$ by multiplying by the ratio of the air

density at the experimental and calculation conditions. The theoretical, Victoreen 480 manual and Monte Carlo values agree within 0.2% for all beam qualities. The experimental values show the expected trend, except the value at 65.9 keV, but the experimental uncertainty is greater than or similar to the correction for all but the largest value at 20 keV. These results show that the attenuation correction is important at these energies, and ranges from 0.77 to 3.71 %.

4.4.4.2 Photon scatter correction, k_{sc}

The correction factors to account for the excess ionization produced in air by secondary photons are shown in Fig. 4.14 and Table 4.7. The Monte Carlo-generated correction factors do not agree within statistical uncertainty with the interpolated values for the Victoreen 480 manual, or with the expression given by Lee *et al.*[16] The values given by the Victoreen 480 are the product of the photon scatter and electron loss correction factors, but at these low energies, the values are heavily dominated by photon scatter (Fig. 4.9). If the values of k_e from Lee *et al.* (Table 4.8) are used to separate the $k_{sc} \cdot k_e$ correction, only the highest energy beam (6.103 mm Cu filtration) k_{sc} would be affected, and it would decrease to 0.9964.

Table 4.7 The correction factors for photon scatter (k_{sc}). The product ($k_{sc} \cdot k_e$) is expected to be equivalent to k_{sc} for all values except the highest energy (6.103 mm Cu-filtered beam).

Beam Quality	Victoreen 480 Manual ($k_{sc} \cdot k_e$)	Expression from Lee *et al.*[16] (k_{sc})	egs_fac (k_{sc})
20.0 keV	---	---	0.9853 ± 0.0002
33.3 keV	0.9946	0.991	0.9865 ± 0.0004
0.552 mmCu	0.9952	0.993	0.9872 ± 0.0005
0.552 mmCu + 13 mmAl	0.9954	0.994	0.9891 ± 0.0006
1.103 mm Cu	0.9955	0.994	0.9888 ± 0.0006
2.210 mm Cu	0.9959	0.995	0.9902 ± 0.0006
6.103 mm Cu	0.9973	0.995	0.9917 ± 0.0005

The magnitude of the photon scatter correction is between 0.56 and 0.81 %, and 0.33 and 0.58 % greater than the Victoreen 480 manual and values calculated from the

expression given in Lee *et al.*, respectively. The additional photon scatter due to the presence of the entrance window is not directly discussed in either the Victoreen 480 manual or the Lee *et al*. description of the correction factors. If we consider the possibility that neither of these sources consider the scatter from the window in these values, and compare them with k_{sc} determined using egs_fac without modeling the Be window, the egs_fac values are within 0.30 and 0.50 %, and 0.13 and 0.23 % of the Victoreen 480 manual and Lee *et al*. values, respectively.

To investigate changes in k_{sc} with electrode configuration (the extent of expansion), the correction factor was determined for electrode positions of 2, 4, 6, and 8 cm greater than the fully-collapsed configuration. These positions were chosen to match those used experimentally. The results indicate that k_{sc} tends to be greatest in magnitude with the electrode positioned at 2 cm, but in general the values for all four positions are very similar (almost all values agree within statistical uncertainty).

4.4.4.3 Electron loss correction, k_e

The correction factors required to account for electron loss in the FAC are shown in Fig. 4.14 and Table 4.8. For all energies examined, k_e is less than or equal to 0.21 %, and is negligible for the accuracy achieved in this study. As done for k_{sc}, the influence of the

Table 4.8 The correction factors for electron loss (k_e) for the experimental beam qualities.

Beam Quality	Expression from Lee *et al.*[16] (k_e)	egs_fac (k_e)
20.0 keV	1.0000	1.0000 ± 0.0001
33.3 keV	1.0000	1.0011 ± 0.0005
0.552 mmCu	1.0000	1.0020 ± 0.0006
0.552 mmCu + 13 mmAl	1.0000	1.0021 ± 0.0008
1.103 mm Cu	1.0000	1.0007 ± 0.0007
2.210 mm Cu	1.0000	1.0006 ± 0.0008
6.103 mm Cu	1.0009	1.0021 ± 0.0009

outer electrode position with respect to the fully collapsed configuration on k_e was investigated. For all situations, k_e agrees within uncertainty for the four electrode positions examined.

4.4.4.4 Window correction, k_w

As mentioned earlier, the correction for attenuation and scatter produced by the entrance and exit windows is included in k_a and k_{sc}, respectively, by egs_fac. The Monte Carlo-simulated window correction factor was determined by taking the ratio of the correction factors calculated for simulation geometries with and without the Be window. Two separate corrections were calculated. First, the correction due only to attenuation in the window, k_w^a, was determined to compare to theoretically calculated and tabulated factors. The correction including both attenuation and scatter produced in the window, k_w, was also calculated. The uncertainty in the egs_fac correction due to window attenuation alone (k_w^a) is less than 0.01% for all beam qualities, and thus not included in Table 4.9. The agreement between the theoretical values, interpolated values and egs_fac values of k_w^a is within 0.001.

Table 4.9 The correction factors for attenuation in the entrance window, k_w^a, and the correction for attenuation and scatter, k_w.

Beam Quality	Theoretical, (k_w^a)	Victoreen 480 manual (k_w^a)	egs_fac (k_w^a)	egs_fac (k_w)
20.0 keV	1.009	---	1.0097	1.0054 ± 0.0003
33.3 keV	1.007	1.008	1.0073	1.0027 ± 0.0005
0.552 mmCu	1.006	1.006	1.0067	1.0019 ± 0.0006
0.552 mmCu + 13 mmAl	1.006	1.006	1.0064	1.0031 ± 0.0007
1.103 mm Cu	1.006	1.006	1.0063	1.0025 ± 0.0007
2.210 mm Cu	1.006	1.005	1.0060	1.0025 ± 0.0007
6.103 mm Cu	1.005	---	1.0057	1.0025 ± 0.0007

4.4.4.5 Diaphragm transmission and scatter correction, k_{dia}

The correction for photons transmitted through or scattered from the diaphragm is minimal. The correction is 1.0000 for all beam filtrations except the highest energy beam

for which the correction is 1.0001. Like k_e, the Monte Carlo results suggest that the k_{dia} correction is negligible for a properly aligned FAC.

4.4.4.6 Ionic recombination correction, k_{ion}

The recombination correction factors, as determined via two methods, are shown in Table 4.10. The errors associated with the two-voltage method are determined from the standard deviation of multiple measurements and error propagation. For the fitting method, the error was given from the MATLAB curve fitting toolbox. It is expected that k_{ion} should decrease with decreasing beam intensity. The results show that the least filtered polyenergetic beam (0.552 mm Cu) has the highest recombination rate at 1.041 ± 0.015 (two-voltage method). For all higher filtrations, the recombination correction is lower, but the associated uncertainties are too large to see a clear trend. The fitting method of determining k_{ion} is illustrated in Fig. 4.15, where FAC current is plotted versus the inverse of the applied voltage. As expected, with increasing collected current there is an increasing dependence on the applied voltage. While the results of the fitting method shown in Table 4.10 follow the expected trend between air kerma rate and recombination correction, the uncertainties in the fits limit the usefulness of the data. Additionally the fitting method provides k_{ion} values that are less than unity, which is not physical and suggests that the fitting method was not successful.

Table 4.10 The correction factors for ion recombination, k_{ion}.

Beam quality	Collected FAC current / storage ring current (pA/mA)	Two-voltage method	Fitting method
20.0 keV	1.40	1.001 ± 0.001	0.998 ± 0.008
33.3 keV	0.21	0.999 ± 0.001	1.006 ± 0.037
0.552 mmCu	49.6	1.041 ± 0.015	1.083 ± 0.069
0.552 mmCu + 13 mmAl	13.3	1.002 ± 0.018	1.012 ± 0.069
1.103 mm Cu	10.5	1.010 ± 0.004	0.989 ± 0.071
2.210 mm Cu	2.04	1.004 ± 0.004	0.994 ±0.017
6.103 mm Cu	0.05	1.017 ± 0.013	0.990 ± 0.093

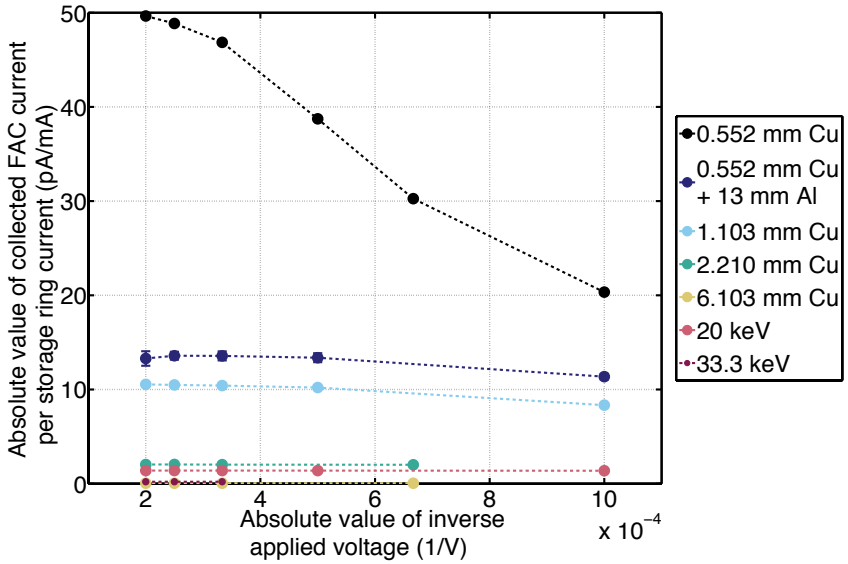

Figure 4.15 The collected current versus the inverse of the applied voltage for all beam qualities. As the inverse applied voltage decreases, the curves are expected to approach the saturation current (Eq. 4.10).

4.4.5 Air kerma rates

The air kerma rates were determined from Eq. 4.3, and the correction factors outlined in Section 4.3.5. The values of k_a, k_{sc}, k_e, and k_{dia} determined using egs_fac, and the two-voltage method-determined k_{ion} values were applied. The experimental values of K_{air} are shown in Table 4.11. The highest air kerma rate measured was 312 Gy/min, and the lowest was 0.27 Gy/min at the highest energy. The experimental air kerma rates are compared to the relative theoretical air kerma rates for the polyenergetic, filtered beams as calculated with SPECTRA. After normalization to the 0.552 mm Cu-filtered beam, the difference between measured and predicted values range between 0.5 and 6.5 % for the other polyenergetic beams. The theoretical air kerma rate was not determined for the monoenergetic beams. To predict the monoenergetic beam intensity would require a thorough understanding of the transportation of the x-rays through the monochromator.

Table 4.11 The measured air kerma rates after correction and the relative theoretical values.

Beam Quality	Experimental air kerma rate (Gy/min)	Relative theoretical air kerma rate	Difference in theoretical and experimental relative air kerma rates (%)
20.0 keV	6.54	---	---
33.3 keV	0.915	---	---
0.552 mmCu	312	1.0000	≡0.0
0.552 mmCu + 13 mmAl	62.4	0.2011	0.5
1.103 mm Cu	63.8	0.1967	4.0
2.210 mm Cu	9.12	0.0298	1.9
6.103 mm Cu	0.270	0.0009	6.5

4.4.6 Uncertainty analysis

The uncertainty analysis for the air kerma rate measurements is shown in Table 4.12 for each beam quality examined. The Type A uncertainty estimates were determined based on standard deviations of experimental values or statistical uncertainties of the Monte Carlo-derived values. Type B uncertainty estimates are based on the potential variability in the measurements, (*e.g.*, manufacturer ratings, tabulated data). The values include neither the uncertainties associated with the lack of knowledge around the composition and thickness of the entrance and exit windows, nor those related to uncertainties in beam and FAC alignment. The majority of the air kerma rate measurements have uncertainties between ~ 2 and 3.5 %, but the highest energy/lowest air kerma rate beam has an uncertainty of 13.6 %.

Table 4.12 The uncertainty analysis for air kerma rate determination with the Victoreen 480 on the 05B1-1 beamline.

	Relative standard uncertainty (%)							
	20.0 keV		33.3 keV		0.552 mm Cu		0.552 mm Cu + 13 mm Al	
	Type A	Type B	Type A	Type B	Type A	Type B	Type A	Type B
Chamber current	1.03	0.02	2.66	0.02	0.68	0.02	2.13	0.02
Aperture area, A_{ap}	1.94		1.94		1.94		1.94	
Collecting volume length, L		0.75		0.75		0.75		0.75
Air density, ρ_{air}		0.40		0.40		0.40		0.40
$(W/e)_{air}$		0.15		0.15		0.15		0.15
Correction factors								
k_a	0.00		0.00		0.00		0.00	
k_{sc}	0.02		0.04		0.05		0.06	
k_e	0.01		0.05		0.06		0.08	
k_{ap}	0.00		0.00		0.00		0.00	
k_{ion}	0.10		0.01		1.44		1.80	
k_{pol}	0.43		0.43		0.43		0.43	
Quadratic sum	2.24	0.86	3.30	0.86	2.51	0.86	3.40	0.86
Combined uncertainty	2.40		3.41		2.65		3.50	

Table 4.12 continued

	Relative standard uncertainty (%)					
	1.103 mm Cu		2.210 mm Cu		6.103 mm Cu	
	Type A	Type B	Type A	Type B	Type A	Type B
Chamber current	0.354	0.02	1.19	0.02	13.32	0.02
Aperture area, A_{ap}	1.94		1.94		1.94	
Collecting volume length, L		0.75		0.75		0.75
Air density, ρ_{air}		0.40		0.40		0.40
$(W/e)_{air}$		0.15		0.15		0.15
Correction factors						
k_a	0.00		0.00		0.00	
k_{sc}	0.06		0.06		0.05	
k_e	0.07		0.08		0.09	
k_{ap}	0.00		0.00		0.00	
k_{ion}	0.40		0.40		1.30	
k_{pol}	0.43		0.43		0.43	
Quadratic sum	2.01	0.86	2.32	0.86	13.52	0.86
Combined uncertainty	2.19		2.47		13.55	

4.5 Discussion and conclusions

In this chapter the first absolute dosimetry performed at the Canadian Light Source BMIT beamlines has been reported. The air kerma rate values were determined using the less common Attix-type FAC. The measurements were supplemented using the EGSnrc code egs_fac for the calculation of correction factors.

Testing of the Attix-type FAC at the NRC determined that the chamber is in good working order. Benchmarking against the NRC primary standards in kV x-ray tube beams indicated the absolute accuracy of the Victoreen FAC in the 60 – 150 kVp range is on the order of 0.3 %. Compared to the more common parallel plate FAC design, the less fragile cylindrical FAC construction allowed the Victoreen to be shipped from the NRC to the CLS without much risk of mechanical damage that could compromise its accuracy. This is primarily because the tight restrictions on the electric field required for the parallel plate FAC are not necessary for a cylindrical-type chamber, as was discussed in section 4.2.1.

To adapt the Attix-type FAC to the small, non-uniform BMIT 05B1-1 beamline, a new diaphragm was fabricated to minimize the aperture opening. The small aperture size is important to reduce the variation in beam intensity over the aperture opening. Unfortunately, the tiny aperture also increases the uncertainty in determining the aperture area. The sub-millimetre aperture requires precision measurements of the radius to minimize the uncertainty in the area. The difference of < 5 μm in the radii between the two diaphragm faces translates to a 1.9 % discrepancy in area, which limits the accuracy at which K_{air} can be determined. Further investigations into the aperture area are important for improving the accuracy of the 05B1-1 beamline air kerma rates in Table 4.11.

The relationships between the correction factors and photon energy are shown in Fig. 4.9. As expected, the attenuation in air and the entrance window, k_a, requires a greater correction at lower x-ray energies. Similarly, the correction for photon scatter, k_{sc}, in the air and entrance window increases with decreasing photon energy, but is smaller in magnitude than k_a. The electron loss correction factor first increases with increasing energy, which is due to the increasing range of released photoelectrons.

Between 150 and 175 keV, the electron loss starts to decrease due to the increasing cross section for Compton scattering and decreasing photoelectric effect cross section, because the Compton electrons have a shorter range than the photoelectrons. Although not shown in Fig. 4.9, if the x-ray energy continues increasing, k_e will reach a local minimum, then again increase when the Compton electrons' range allows them to reach the outer electrodes. The Monte Carlo simulations show that the correction for k_{dia} is negligible for a parallel, properly aligned x-ray beam.

Characterizing the influence of beam and FAC properties on the correction factors is important not only for understanding the magnitude of the corrections for accurate air kerma rate measurements, but also for determining the desired properties of FACs for various beam qualities, and for identifying which beam properties most strongly impact correction factors. Figures 4.10 and 4.11 demonstrate the influence of beam divergence and beam alignment on k_{dia} and k_{sc}. For a beam divergence of up to 5 mrad, which is 10 times higher than the predicted beam divergence for the small opening of the aperture, the change in correction factors is < 0.05%. The change in correction factors is less than 1 % for a misalignment between the photon beam and FAC of up to 0.5°. Based on the beam spot position on the FAC's crosshairs, the maximum misalignment expected is 4 mm or 0.3°, and thus the uncertainty due to improper alignment is expected to be within ~ 0.5 %.

Figure 4.12 informs the potential uncertainties due to the lack of knowledge of the window thickness. In the simulations, the window was chosen to be 0.22 mm to best match the window attenuation correction as tabulated in the Victoreen 480 manual. If we assume that the thickness of the window is between 0.1 and 0.5 mm, the variation in k_a and k_{sc} would be 1.2 % and 0.8 %, respectively. Because the correction factors have opposing trends, the combined variation for a window thickness between 0.1 and 0.5 mm is only 0.3 %. Therefore the lack of knowledge of the window thickness does not have a large impact on our final air kerma measurements when considering the magnitude of other sources of uncertainty. If the window is composed of a material other than beryllium, the change in correction factors could potentially be much greater.

Figures 4.9 and 4.13, and Table 4.3 show that the Attix-type FAC with 30 cm diameter outer electrodes, and its collecting rod positioned 8 cm below the central axis, is

more than sufficient to avoid electron loss for the x-ray energies of interest in this study. In fact, Fig. 4.13 shows that for a 50 keV beam, k_e is above unity only for an outer electrode radius of 2.5 cm for the 50 keV beam. While the large diameter cylindrical electrodes are beneficial for minimizing k_e, the correction for photon scatter and ion recombination increase with increasing outer electrode radius. For the 50 keV beam, the outer electrode radius could be reduced to 5 cm to optimize k_e, k_{sc} and k_{ion}. Figure 4.13 also highlights the importance of understanding the energy dependence of k_e. It may be intuitive to expect a greater value of k_e with higher photon energies, but k_e is greater for the 50 keV incident beam than the 100 keV beam for an outer electrode diameter of 2.5 cm. This is due to the lower cross-section for the photoelectric effect at 100 keV (by an order of magnitude) compared to the 50 keV beam. The mean energy transferred from an incident 100 keV x-ray to a Compton-scattered electron is only 13.8 keV.[14] The range of a 50 keV electron (ignoring the effect of the binding energy, which has a maximum of 3.2 keV for the elements of air) is an order of magnitude larger than a 13.8 keV electron in air; this explains the difference in k_e for the two energies and a 2.5 cm outer electrode radius.[14]

The user code, egs_fac, does not incorporate photon polarization. In Section 1.3.1, the additional dependence on the azimuthal angle of interaction cross-sections is described. For a linear polarization, with the electric field lying in the horizontal axis, there is preferential scattering of photoelectrons in the horizontal plane and of Compton electrons in the vertical plane. Due to the cylindrical geometry of the Victoreen 480 outer electrodes, this additional polarization-dependent azimuthal angle has a minimal effect on electron loss compared to the effect for a parallel plate chamber. The position of the collecting rod along the vertical axis would cause a reduction in the fraction of k_e attributed to photoelectrons and an enhancement in the fraction of k_e due to Compton scattered electrons compared to the value calculated by egs_fac. This suggests that at low energies, where photoelectric effect is more probable than Compton scattering, egs_fac overestimates k_e for the polarized beam. However, this effect would likely be negligible for the accuracy of our measurements. As the energy increases to the point that Compton scattered electrons contribute more to k_e, the egs_fac results may underestimate the electron loss for the polarized beam, as the Compton scattered

electrons are preferentially scattered toward the collecting rod. Nariyama *et al.* showed that for their small parallel plate FAC (plate separation = 8.5 cm), their Monte Carlo-generated k_e decreased by up to 2% for incident x-ray beam energies between 60 and 450 keV when linear polarization was included in the simulations versus no polarization.[2]

The experiment-specific correction factors in Fig. 4.14 demonstrate the expected trends with changing photon energy as established for the monoenergetic beams in Fig. 4.9. We can see that the largest total Monte Carlo-determined correction factor is for the 20 keV beam, and is dominated by the attenuation correction. A FAC with a reduced attenuation length and no entrance window would significantly reduce the required correction. Figure 4.14 also shows that the second most important correction factor is photon scatter. A reduced outer electrode radius would decrease this correction. The preliminary characterization, including correction factors, for the National Institute of Standards (Egypt) Victoreen 480 are provided in a Bureau International des Poids et Mesures (BIPM) report for x-ray energies between 100 and 180 kV.[21] The reported correction factors are similar in magnitude to those calculated in this study, and any differences (which were greatest for the k_{sc}) may be explained by differences in the synchrotron radiation and x-ray tube photon energy spectra.

The values for k_{ion} in Table 4.10 show the corrections for recombination. These values highlight the limitations of the Victoreen 480 for air kerma rate measurements on the 05B1-1 beamline. Even with 0.552 mm of Cu filtration, at an air kerma rate of 5.2 Gy/s, the correction is significant. It is clear that the Victoreen 480 would be severely limited by ion recombination if used to measure air kerma rates with less filtration on the 05B1-1 beamline. Alternative FAC designs can be created to reduce k_{ion}. A reduction in the collecting volume's lateral dimensions and an increase in the applied voltage, both reduce the amount of ion recombination.

The measured air kerma rates range over four orders of magnitude for the poly- and monoenergetic beams. The air kerma rates were measured with uncertainties between 2.2 and 13.6 %. Although this is above the typical uncertainty for a clinical beam, these measurements mark an important accomplishment as the first measurement of *absolute* air kerma rates on the 05B1-1 beamline. These values, with their uncertainties, will provide an important reference for not only microbeam radiation

therapy experimentation, but all other imaging and therapy research programs on this beamline.

A large source of uncertainty is simply due to the extremely small cross-sectional beam area, and the large collecting volume. This results in a considerable amount of noise in the measured current that is manifest as high uncertainties in the measured correction factors (k_{ion} and k_{pol}). The challenge in accurately determining the aperture area also leads to a significant uncertainty in the final air kerma rate. It is important to understand the dependence of the air kerma rate measurements on experimental set-up, particularly the vertical position in the non-uniform beam and the alignment of the FAC with respect to the highly directional beam. Additionally, for the monoenergetic beams, the repeatability is influenced by the state of the monochromator (*e.g.*, angle and temperature of crystals). The set-up of the large, heavy chamber in the small synchrotron beam is tedious and time-consuming, and thus performing this reproducibility investigation with limited experimental beam time would be challenging.

In the future, the method outlined in this chapter will be used for air kerma rate measurements on the BMIT 05ID-2 beamline. This insertion device beamline has the potential of producing much higher air kerma rates, and higher x-ray energies. The Attix-style FAC will not be appropriate for air kerma rates much higher than the maximum of 5.2 Gy/s measured in this study, but it can be used by adding filtration to attenuate the monoenergetic beam, and/or focusing on the higher energy monoenergetic beams which are naturally lower in flux. Additionally, the selection or design of a more appropriate FAC, in terms of collecting volume dimensions and applied voltage, should be investigated. A small, lighter FAC would not only decrease the corrections required for photon attenuation in air, photon scatter in air, and ion recombination, it would also significantly reduce the challenge in transporting and setting up the FAC. A new chamber would require a similar verification by a standards institution, as was performed for the Victoreen 480.

4.6 References

[1] F.H. Attix, *Introduction to Radiological Physics and Radiation Dosimetry* (John Wiley & Sons, Inc., New York, 1986).

[2] N. Nariyama, N. Kishi, S. Ohnishi, "Development of a portable free-air ionization chamber as an absolute intensity monitor for high-energy synchrotron radiation up to 150 keV," Nuclear Instruments & Methods in Physics Research Section A-Accelerators Spectrometers Detectors and Associated Equipment **524**, 324-331 (2004).

[3] J.C. Crosbie, P.A.W. Rogers, A.W. Stevenson, C.J. Hall, J.E. Lye, T. Nordstrom, S.M. Midgley, R.A. Lewis, "Reference dosimetry at the Australian Synchrotron's imaging and medical beamline using free-air ionization chamber measurements and theoretical predictions of air kerma rate and half value layer," Med. Phys. **40**, 062103 (2013).

[4] D.T. Burns and L.B. Bueermann, "Free-air ionization chambers," Metrologia **46**, S9-S23 (2009).

[5] S.M. Seltzer, P.J. Lamperti, R. Loevinger, M.G. Mitch, J.T. Weaver, B.M. Coursey, "New national air-kerma-strength standards for I-125 and Pd-103 brachytherapy seeds," J. Res. Natl. Stand. Technol. **108**, 337-358 (2003).

[6] H.E. Johns and J.R. Cunningham, *The Physics of Radiology*, 4th Edition ed. (Charles C Thomas, Springfield, IL, USA, 1983).

[7] D.T. Burns and C. Kessler, "Diaphragm correction factors for free-air chamber standards for air kerma in x-rays," Phys. Med. Biol. **54**, 2737-2745 (2009).

[8] A.C. McEwan, "Corrections for scattered photons in free-air ionization chambers," Phys. Med. Biol. **27**, 375-386 (1982).

[9] E. Mainegra-Hing, "Efficient Monte Carlo simulations in kilovoltage x-ray beams," (2011).

[10] M. Boutillon and A.M. Perrocheroux, "Reevaluation of the W-Value for Electrons in Dry Air," Phys. Med. Biol. **32**, 213-219 (1987).

[11] D.T. Burns, "Free-air chamber correction factors for electron loss, photon scatter, fluorescence and bremsstrahlung," CCRI(I)/01-36 (BIPM) (2001).

[12] T. Tanaka and H. Kitamura, "SPECTRA: a synchrotron radiation calculation code," Journal of Synchrotron Radiation **8**, 1221-1228 (2001).

[13] E. Mainegra-Hing, N. Reynaert, I. Kawrakow, "Novel approach for the Monte Carlo calculation of free-air chamber correction factors," Med. Phys. **35**, 3650-3660 (2008).

[14] J. Hubbell and S.M. Seltzer, "NISTIR 5632: Tables of x-ray mass attenuation coefficients and mass energy-absorption coefficients from 1 keV to 20 MEV for elements Z = 1 to 92 and 48 additional substances of dosimetric interest," National Institute of Standards and Technology, Gaithersburg, MD, USA Technical Report 5632 (1995).

[15] H.O. Wyckoff and F.H. Attix, "Design of free-air ionization chambers," National Bureau of Standards Handbook 64 (1957).

[16] J.H. Lee, L.H. Kotler, L. Buermann, W.S. Hwang, J.H. Chiu, C.F. Wang, "The performance of the INER improved free-air ionization chamber in the comparison of air kerma calibration coefficients for medium-energy X-rays," Radiat. Measur. **39**, 1-10 (2005).

[17] P.R. Almond, P.J. Biggs, B.M. Coursey, W.F. Hanson, M.S. Huq, R. Nath, D.W.O. Rogers, "AAPM's TG-51 protocol for clinical reference dosimetry of high-energy photon and electron beams," Med. Phys. **26**, 1847-1870 (1999).

[18] M. Boutillon, "Volume recombination parameter in ionization chambers," Phys. Med. Biol. **43**, 2061-2072 (1998).

[19] International Commision on Radiation Units and Measurements, "Average energy required to produce an ion pair," ICRU, Bethesda, MD ICRU Report 31 (1979).

[20] W.L. Chen, S.H. Su, L.L. Su, W.S. Hwang, "Improved free-air ionization chamber for the measurement of x-rays," Metrologia **36**, 19-24 (1999).

[21] D.T. Burns, C. Kessler, P. Roger, A.R. El-Sersy, "Preliminary Characterization of the NIS Free-Air Chamber Standard at the BIPM," BIPM-09/02 (2009).

5 CAVITY IONIZATION CHAMBER REFERENCE DOSIMETRY ON THE 05B1-1 BEAMLINE

5.1 Introduction

In this chapter we develop a technique for using an ion chamber, which has been calibrated in conventional broad-beam conditions, for reference dosimetry in a small, non-uniform synchrotron x-ray beam. In conventional radiation therapy, reference dosimetry is most often performed with a cavity ionization chamber that has been calibrated by a standards institution in a relatively large uniform field. A synchrotron x-ray beam is both non-uniform (in flux and energy) and small (< 1 cm) across the beam's height. Because of this, an ion chamber calibrated for clinical applications requires corrections to provide reference dosimetry in the synchrotron beam. Developing a trusted reference dosimetry protocol using cavity ionization chambers would be an important tool for the characterization of beam output, commissioning of any future treatment planning system, and calibration of other relative dosimeters. In this work, we input the synchrotron x-ray beam's vertical profile, and the radial response of a clinical Capintec PR06C ion chamber in an algorithm that predicts the ion chamber response as a function of collimated beam size. The understanding of ion chamber response in the non-uniform beam allows the determination of the air kerma rate. Two configurations are studied - with the ion chamber stationary and with it scanning vertically across the fixed, horizontal x-ray beam.

5.2 Materials and methods

5.2.1 X-ray source

The measurements were performed on the 05B1-1 beamline at the Canadian Light Source (described in Sections 2.5 and 2.6.1) over two experimental sessions. The measurements were taken with the polyenergetic beam (two filtrations) and the monoenergetic beam (two energies). The experimental session (first or second), mode (polyenergetic versus monoenegetic), filtration, energy (or mean energy), and half-value layer (HVL) are

reported in Table 5.1 for each of the experimental conditions. Details on the measurements of the x-ray beams' effective energy and relative flux, and HVLs are given in Sections 3.2.6/3.3.6 and 3.2.7/3.3.7, respectively. The monoenergetic beams are produced by a double crystal monochromator, and the predicted flux depends on the efficiency of the monochromator, which is not specified.

Table 5.1 The characteristics of the 05B1-1 x-ray beams.

Experimental Session	Mode	Mean Energy, *E* (keV)	Filtration (mm)	Half-value layer, *HVL* (mm)	Predicted relative flux
2	poly	56.0	1.103 (Cu)	0.34 (Cu)	0.69
1	poly	54.0	0.938 (Cu)	0.31 (Cu)	1.00
2	mono	33.3	1.103 (Al)	3.03 (Al)	---
2	mono	20.0	1.103 (Al)	0.78 (Al)	---

5.2.2 Vertical beam profile for various beamline collimator settings

To characterize the beam's non-uniformity in the vertical direction, the profile across the beam was measured at the four beam energies investigated. Radiochromic film was used to measure the beam profile at several beam sizes. The beam size was controlled through adjustment of the built-in beamline jaws. In the first experimental session, the 0.938 mm Cu-filtered beam (Section 3.2.5 and 3.3.4) was characterized using Gafchromic EBT2 film. The film was digitized with an Epson Perfection V700 (Epson, Suwa, NGN, Japan) flat bed scanner at a resolution of 4800 dpi and a pixel depth of 16 bits per colour channel. A calibration curve for this beam energy was generated and fit with a polynomial. At a later experimental session, Gafchromic EBT3 was used to measure the beam profile for all other energies. The film was digitized using an Epson Expression 10000XL flatbed scanner with the same spatial resolution and pixel depth. The calibration curve was created with the Pantak Therapax 3 Series 75 kVp beam. The calibration procedure is a slightly modified version of that described by Morrison *et al.*[1] The calibration fit function has the form $D=(C\cdot 10^{-OD}-A)/(B-10^{-OD})$ where D is the dose; A, B and C are fit functions; and OD is the optical density of the film.

5.2.3 Capintec PR06C: characteristics and radial response function

As described in following sections, Capintec PR06C (Capintec, Inc., Ramsey, New Jersey, USA) ionization chambers were used for air kerma measurements of both relative and absolute output. Two different chambers (S/N C11.69874 and S/N C11.69694) were used for the two different experimental sessions. The PR06C has a cavity volume of 0.65 cm^3, an inner diameter of 6.4 mm, and a central electrode that is 1.6 mm in diameter. The length of the collecting volume is 24.0 mm. The electrode and wall are composed of C-552 (a conducting air-equivalent plastic). The radial wall thickness is 0.050 g/cm^2 or 0.28 mm. All measurements described in this chapter were made with the long axis of the chamber lying in the horizontal plane and perpendicular to the beam direction.

Due to the non-uniformity of the beam over the (vertical) dimensions of the chamber, it was necessary to characterize the radial response function of the Capintec PR06C. This was done by stepping the chamber in 100 μm increments across the central 100 μm of the x-ray beam with the 0.938 mm Cu-filtered polyenergetic beam (Fig. 5.1). The narrow, horizontal beam (> 40 mm wide for all measurements) was defined by a slit between two polished blocks. The radial response function was also measured at a lower resolution for a series of x-ray beams to investigate the energy response of the chamber. Monoenergetic beams ranging in energy from 20 – 150 keV, on both the 05B1-1 and 05ID-2 beamlines, as well as the 05B1-1 beamline's 1.103 mm Cu-filtered polyenergetic beam were used.

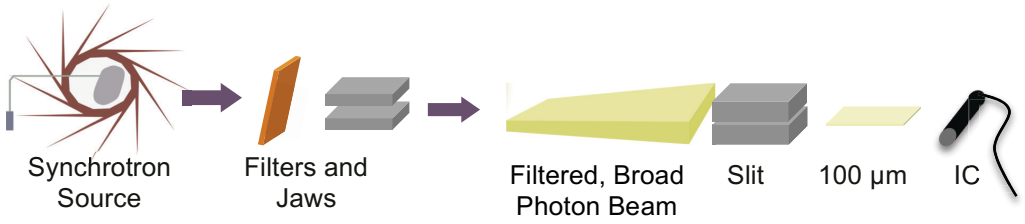

Figure 5.1 A schematic of the experimental set-up for measuring the Capintec PR06C radial response function.

Calibration factors were determined for the Capintec PRO6C chambers to enable absolute quantification of synchrotron beam output. The calibration factors were determined by cross-calibrating on a Pantak Therapax 3 Series orthovoltage unit. The

chamber used for the first experimental session (C11.69874) was cross-calibrated with a Capintec PR06C used for output measurements at the orthovoltage unit. The chamber used for the second experimental session (C11.69694) was cross-calibrated with the primary standard cavity chamber-electrometer system (PTW N30004). The primary standard system has a quoted uncertainty of 1 % at the 95 % confidence level (National Research Council of Canada calibration certificate). The calibration was performed for five orthovoltage x-ray qualities available, and the results are shown in Table 5.2. The calibration factor for the specific ionization chamber and synchrotron x-ray beam was determined by interpolating the calibration factors in Table 5.2 based on the experimental synchrotron HVLs in Table 5.1. If we assume a similar uncertainty in each of the cross-calibrations as stated for the primary standard (1 %), the estimated uncertainties in the calibration factors are 1.4 and 1.7 % for the cross-calibration with the primary standard and the cross-calibration with the quality assurance standard, respectively.

Table 5.2 Calibration factors determined for two Capintec PR06C chambers after cross-calibration with a Pantak orthovoltage unit.

Peak potential, *kVp* (kV)	Additional filtration	Half-value layer, *HVL* (mm)	Calibration factor for air kerma, N_{cal} (cGy/nC)	
			S/N: C11.69874	S/N: C11.69694
75	2.4 mm Al	2.52 (Al) 0.078 (Cu)	3.922	4.088
125	3.12 mm Al	5.0 (Al) 0.19 (Cu)	3.932	4.100
175	1 mm Cu + 2.5 mm Al	0.48 (Cu)	3.965	4.114
200	0.35 mm Cu + 1.5 mm Al	0.92 (Cu)	3.993	4.131
300	0.3 mm Sn + 0.5 mm Cu + 1.5 mm Al	2.86 (Cu)	4.021	4.168

5.2.4 *Measurements and predictions of ion chamber response as a function of beam size*

In conventional scenarios, where the beam is assumed to be uniform over the dimensions of the ion chamber, the charge collected by the chamber (Q) can be expressed as,

$$Q = D\,\overline{R}, \tag{5.1}$$

where D is the uniform dose delivered, $\overline{R}$ is the chamber response (e.g. nC/cGy), and the charge has been appropriately corrected (*e.g.*, ion collection efficiency, temperature/pressure, polarization effect, stem effect, *etc.*). As implied by the nomenclature, $\overline{R}$ represents an average chamber response. More generally, for a non-uniform beam, the collected charge can be formulated as an integral over 2D beam intensity ($B(x,y)$) and chamber response ($R(x,y)$) functions,

$$Q = D \int B(x,y)\, R(x,y) dV_{IC}, \tag{5.2}$$

with the dV_{IC} designating integration over the active dimensions of the chamber. In the above equation, D is chosen to be the maximum dose in the profile, such that $B(x,y)$ becomes a unitless, relative intensity ranging from zero to one. Since $\overline{R} = \int R(x,y) dV_{IC}$, Eq. 5.2 can be rewritten as,

$$Q = D\, f_{vol}\, \overline{R}, \tag{5.3}$$

where

$$f_{vol} = \frac{\int B(x,y)\, R(x,y) dV_{IC}}{\int R(x,y) dV_{IC}} \tag{5.4}$$

represents a weighted fraction of irradiated volume equivalent to when the chamber is uniformly irradiated. Thus, for the small, non-uniform synchrotron beams used in our experiments the effective chamber response ($f_{vol}\,\overline{R}$) is no longer single-valued, but is rather a function of the beam dimensions and profile. A number of experiments were conducted to investigate this dependence.

5.2.4.1 Horizontal beam size dependence

The ion chamber reading as a function of horizontal beam size was investigated by adjusting the horizontal beamline jaws from a nominal size of 1 mm to 80 mm. The measurements were taken at two vertical field sizes: 1 mm and 8.7 mm (nominally).

From theory it is expected that the beam intensity (B_x) is uniform in the horizontal direction. Further, with the long axis of the chamber also in the horizontal direction, the cross-section of the chamber seen by different horizontal beam positions is similar over the majority of the chamber's active volume. (This will not be true near the tip or base of the chamber). If it is thus (to first order) assumed that the chamber response function is also constant horizontally (R_x), then for a given beam height, from Eq. 5.2 it is expected that the collected charge will be proportional to the horizontal length of the chamber irradiated $\int dx$,

$$Q \propto B_x R_x \int dx. \tag{5.5}$$

5.2.4.2 Vertical beam size dependence: stationary ion chamber

The ion chamber response was measured as a function of beam height by varying the nominal vertical setting of the beamline collimators. The chamber was first centered vertically in the beam by finding the maximum ion chamber signal, then remained stationary during the measurements. The nominal vertical beam size was varied between 0.1 and 8.7 mm, with a horizontal beam size of 40 mm, during experimental session 1. For experimental session 2, the vertical beam size was varied between 0.6 and 8.7 mm, with a horizontal beam size of 70 mm. The ion chamber was positioned 26.1 m from the source for experimental session 1 and 25.6 m from the source for experimental session 2.

The analysis of these experiments is complicated because it cannot be assumed that either the beam intensity or the ion chamber response is constant in the vertical direction. A MATLAB (MathWorks, Natick, MA, USA) script was created to predict the ion chamber output using the measured beam profile and ion chamber response functions. Analogous to Eq. 5.2 and 5.3, the charge collected can be expressed as,

$$Q = D \int B(y)\, R(y) dy = D\, f_{vol}\, \overline{R} \tag{5.6}$$

where $R(y)$ is the radial ion chamber response to a vertical slit (collimated vertically, wide horizontally), $B(y)$ is the vertical beam profile for the given collimator settings, and it is assumed that horizontally the beam is uniform and larger than the chamber dimensions. The code aligns, multiplies and integrates the $B(y)$ and $R(y)$ functions to determine the f_{vol} ratio of ion chamber response in the non-uniform, narrow (smaller than the chamber) synchrotron beam compared to the response in a uniform, broad beam (significantly larger than the chamber) that would be used when calibrating the chamber,

$$f_{vol} = \frac{\int B(y)\, R(y)\, dy}{\int R(y)\, dy} \tag{5.7}$$

where the integration is over the height of the chamber. Using Eq. 5.4 and 5.7, and recognizing $1/\overline{R}$ as the dose calibration factor, N_{cal} (*i.e.* cGy/nc) for the ion chamber/electrometer system, the measured maximum dose rate can be calculated from

$$\dot{D}/I_{SR}[Gy \cdot s^{-1} \cdot mA^{-1}] = \frac{Q_{meas} \cdot N_{cal}}{f_{vol} \cdot X_s} \tag{5.8}$$

where Q_{meas} is the electrometer reading (nC) corrected for temperature and pressure, polarity and ion recombination; and X_s is the product of the storage ring current (I_{SR}) in mA and the exposure time in s. Since the ring current decays between ring injections, and the dose rate is directly proportional to the storage ring current, it is convenient to normalize the dose rate with respect to I_{SR}.

5.2.4.3 Vertical beam size dependence: scanning ion chamber

Since many radiotherapy and imaging synchrotron applications, such as microbeam radiation therapy, involve vertically scanning the beam to cover a larger area of the phantom/patient, air kerma rates were measured to replicate these conditions. The integrated charge was measured while the ion chamber was scanned vertically (± 14 mm to ± 20 mm) through the synchrotron x-ray beams at a constant speed (1 or 3 mm/s). As in the stationary measurements, the beam size was varied by adjusting the beamline collimators.

For scanning measurements, at a given instant in time, the current (*i.e.* charge rate) collected is related to the maximum dose rate, $\dot{D}$, via

$$\dot{Q}(a)=\dot{D}\int B(y)\,R(y+a)dy=\dot{D}\,(B\star R)(a) \tag{5.9}$$

where a is the displacement between the centres of the beam and chamber, and the $\star$ indicates cross-correlation. The integrated charge when scanning the chamber through the beam is then

$$Q=\int \dot{Q}(a)\,dt=\dot{D}\frac{\int(B\star R)(a)\,da}{v} \tag{5.10}$$

where v is the constant scan speed in the vertical direction, and thus $dt = da/v$. Analogous to the stationary case, here we define an effective time in a uniform, large beam t_{eff},

$$t_{eff}=\frac{\int(B\star R)(a)\,da}{v\int R(y)\,dy} \tag{5.11}$$

MATLAB code was used to perform the cross-correlation of the relative ion chamber response and beam profile to calculate t_{eff}, and finally, the measured dose or air kerma rate using,

$$\dot{D}/I_{SR}[Gy\cdot s^{-1}\cdot mA^{-1}]=\frac{Q_{meas}\cdot N_{cal}}{t_{eff}\cdot I_{SR}} \tag{5.12}$$

where Q_{meas}, N_{cal}, and I_{SR} are as above.

5.2.5 Reference dosimetry

The reference air kerma rate was determined for the four x-ray beams using Eq. 5.8 and 5.12, but because the scanning response did not have a complete set of data, reference air kerma rates are only reported for the stationary measurement. Additional correction factors (defined in Section 4.3.5) to account for the temperature and pressure (k_{TP}), polarity effects (k_{pol}) and ionic recombination (k_{ion}) were applied. The calibration factors, N_{cal}, are in Table 5.2. Additionally, the measurements from experimental session 1 (0.938 mm Cu-filtered beam) were corrected for attenuation in air to account for the differences in the positions of the ion chambers. The mean air kerma rate and the peak air kerma rate at the center of the x-ray beam were both determined.

5.3 Results and Discussion

5.3.1 PR06C response function

The PR06C's radial slit response function is shown in Fig. 5.2. The response function reveals the structure of the ion chamber, specifically the outer walls and inner electrode of the detector. The full-width at half maximum (FWHM) of the response function is 6.48 mm, which is very close to the ion chamber diameter of 6.4 mm. The FWHM of the inner peaks is 1.64 mm, which again is very similar to the expected electrode diameter of 1.6 mm.

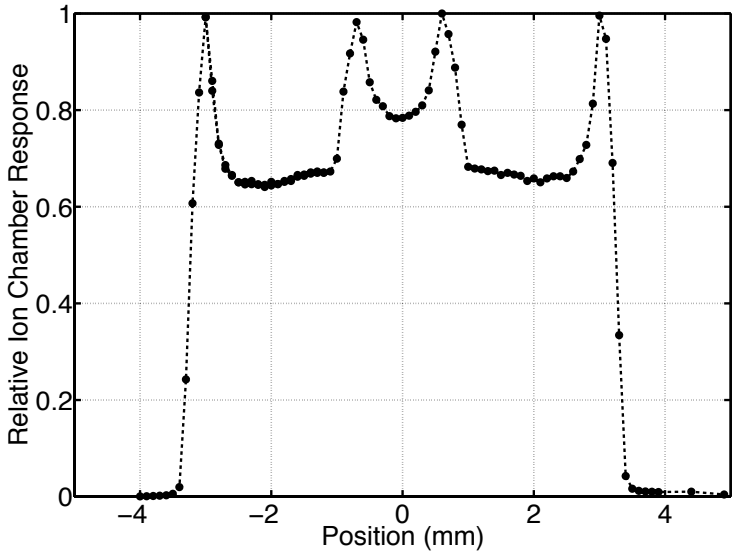

Figure 5.2 The Capintec PR06C response as a function of position across the chamber's diameter (measured with the 0.938 mm Cu-filtered beam). The markers are individual data points and the dashed line is to guide the eye.

The Capintec PR06C response functions for several beam energies are plotted in Fig. 5.3(a). The peaks at the central electrode monotonically decrease with increasing energy. These results suggest a local 30% decrease in the charge collected by the ion chamber for the part of the x-ray beam hitting the central electrode as the x-ray energy increases from 20 keV to 150 keV. Although the chamber wall is composed of the same material, the peaks at the wall do not demonstrate the same monotonically decreasing trend (Fig. 5.3(b)). The mean response over the chamber width is obviously influenced

by both the wall and electrode trends. The broad-beam calibration factors (Table 5.2), representing the spatially-averaged response, show a change in response of less than 5 % over an effective energy range of ~30 – 120 keV. Further investigation is required to fully understand the energy dependence of the chamber, and the potential impact on the air kerma measurements. No corrections for energy dependence were applied for any relative or reference air kerma rate values.

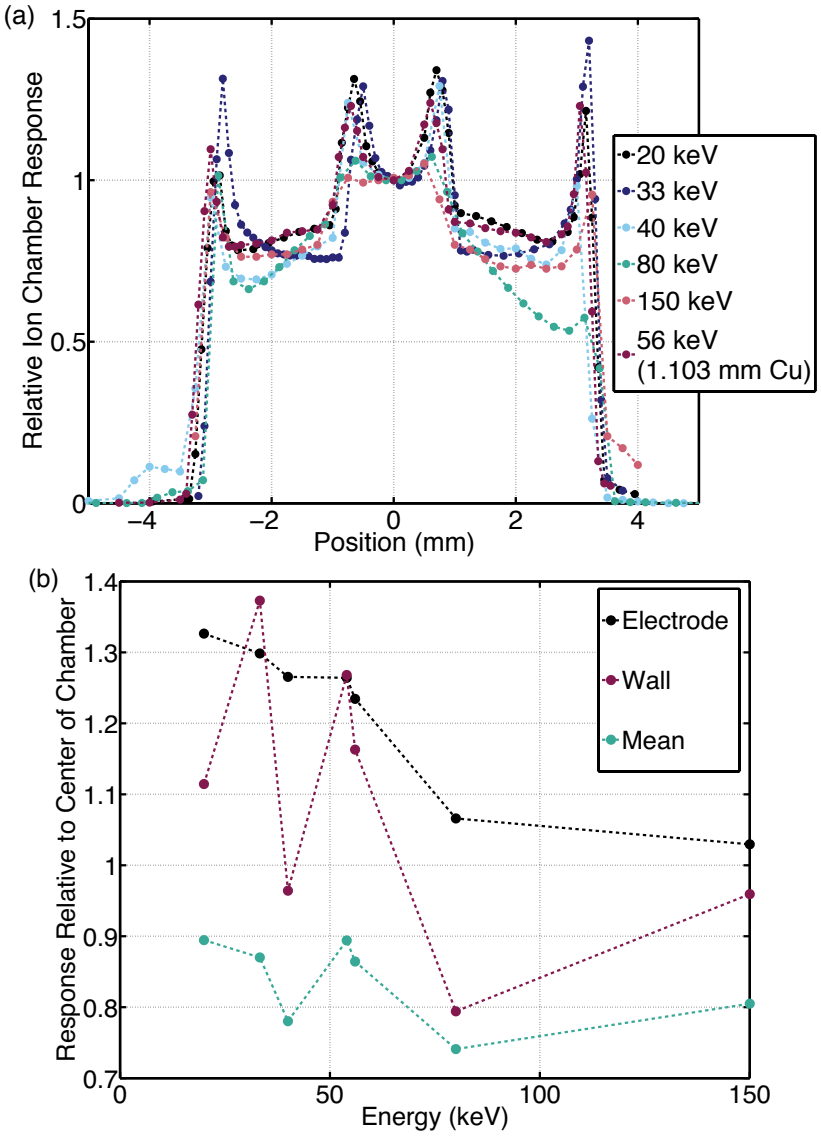

Figure 5.3 (a) The Capintec PR06C response function measured with 5 monoenergetic beams (20 – 150 keV), and the 1.103 mm Cu-filtered polyenergetic beam with a mean energy of 56 keV. (b) The mean of the two outer peaks (ion chamber wall), the two inner peaks (central electrode), and mean across the chamber as a function of x-ray energy.

5.3.2 *Vertical beam profiles*

The vertical beam profiles for the largest collimator setting (8.7 mm) and the collimator setting of 0.6 mm are shown in Fig. 5.4. A more complete representation of the profiles at various collimator settings for the 0.938 mm Cu-filtered beam is shown in Fig. 3.8. The FWHM of the vertical beam profiles are stated in Table 5.3, including all collimator settings measured during experimental session 2 (including 20.0 and 33.3 keV monoenergetic beams, and the 1.103 mm Cu-filtered polyenergetic beams). The set of

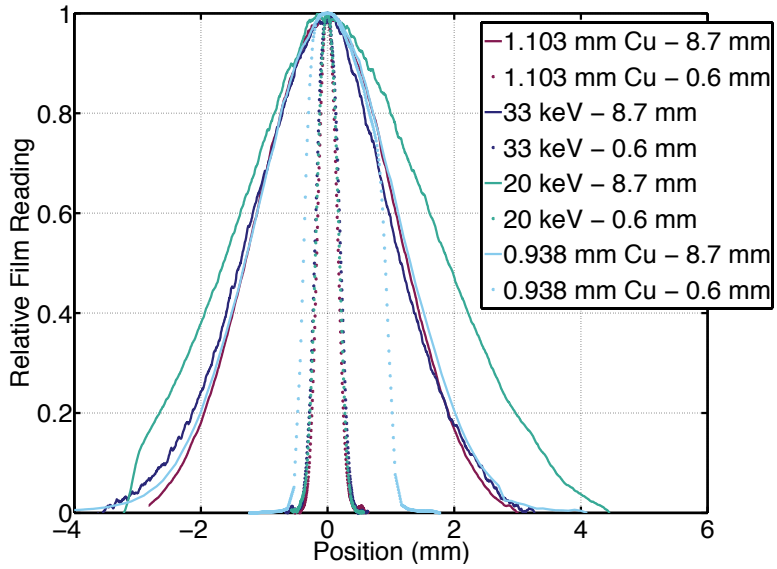

Figure 5.4 The vertical beam profiles measured with Gafchromic EBT2 and EBT3 film for the widest (8.7 mm) and a narrow (0.6 mm) nominal collimator settings for all beam energies investigated.

collimator settings investigated for the 0.938 mm Cu-filtered beam during experimental session 1 were not the same as in session 2. A more complete list of the FWHM for the 0.938 mm Cu filtered beam profiles is given in Table 3.4. At the 8.7 mm collimator setting (i.e. no effective collimation), the lowest energy beam (20.0 keV) is the tallest. This is expected since the opening angle for a given energy decreases as energy increases (Section 2.4.1). The narrowest is the highest energy, most heavily filtered (1.103 mm Cu) beam. As the beamline jaws are brought together to provide collimation, the 0.938 mm Cu-filtered beam appears to be wider than the others. This is attributed to a change

in beamline configuration between the two experimental sessions, and not due to the natural opening angle of the 0.938 mm Cu-filtered beam, which is expected to be quite similar to the 1.103 mm Cu-filtered beam.

Table 5.3 The measured FWHM of the beam profile for nominal collimator settings investigated during experimental session 2 (1.103 mm Cu-filtered, 33.3 keV and 20.0 keV x-ray beams). Some values for the 0.938 mm Cu-filtered beam, measured during experimental session 1, are included for comparison.

Nominal Beam Height (mm)	Measured FWHM of the beam profile (mm)			
	1.103 mm Cu	33.3 keV	20.0 keV	0.938 mm Cu
8.7	2.60	2.59	3.67	2.65
4.0	2.29	2.38	3.12	---
3.0	1.91	1.97	2.52	---
2.0	1.45	1.46	1.70	2.22
1.0	0.73	0.75	0.78	1.63
0.6	0.35	0.42	0.39	1.29

5.3.3 Horizontal ion chamber response

As discussed in Section 5.2.4.1, a linear relationship between chamber response and horizontal beam size was expected because of the uniform profile of the beam and structure of the ion chamber in the horizontal plane. The results, shown in Fig. 5.5, confirmed our expectations. A linear fit (from MATLAB) is also shown over the first 24 mm, and had a coefficient of determination (R^2) of 0.9995. The measurements also confirmed the internal structure of the ion chamber, with a loss in linearity occurring at a beam size of 25 mm. The small, but continued increase in response for field sizes wider than the collecting volume (approximately 25 – 30 mm) is attributed to the additional scatter dose, and potentially stem effects, as the field size grew.

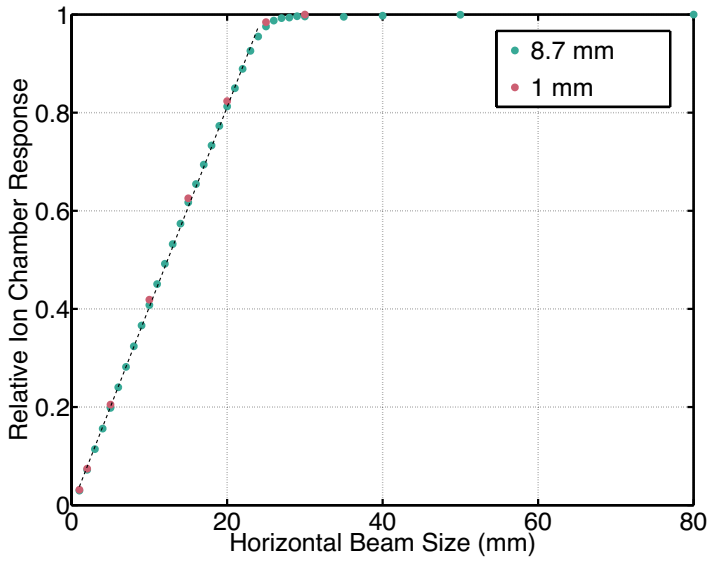

Figure 5.5 The lateral Capintec PR06C response function. Measurements were taken with beam heights of 1.0 and 8.7 mm. The dashed line shows the linear fit.

5.3.4 Vertical ion chamber response - stationary geometry

The predicted relative ion chamber response for the stationary measurements was calculated using Eq. 5.8. Figure 5.6 illustrates the algorithm used to determine the weighted ion chamber volume irradiated (f_{vol}) by integrating the product of the aligned ion chamber response function and the beam profile. The example in Fig. 5.6 is for the 1.103 mm Cu-filtered beam at collimator settings of 8.7 mm (top) and 0.6 mm (bottom).

A comparison between predicted and measured ion chamber response as a function of vertical beam height for the stationary measurements is shown in Fig. 5.7, where the responses have been normalized to the largest vertical beam (8.7 mm). As expected, the predicted and measured ion chamber reading increases as the beam size increases. The chamber response flattens off as the nominal beam size increases, which reflects the Gaussian nature of the beam profile. The 20 keV data demonstrate the least flattening with increasing beam size, and this is because this beam has the largest FWHM, and thus is still affected by collimator changes at the larger beam sizes. The change in the general shape of the 0.938 mm Cu-filtered data (experimental session 1) and the other curves (experimental session 2) is likely due to changes in the beamline's jaws between the two experimental times. If the relative ion chamber response is plotted

with the measured FWHM of the beams instead of the nominal collimator settings, the data sets are more similar.

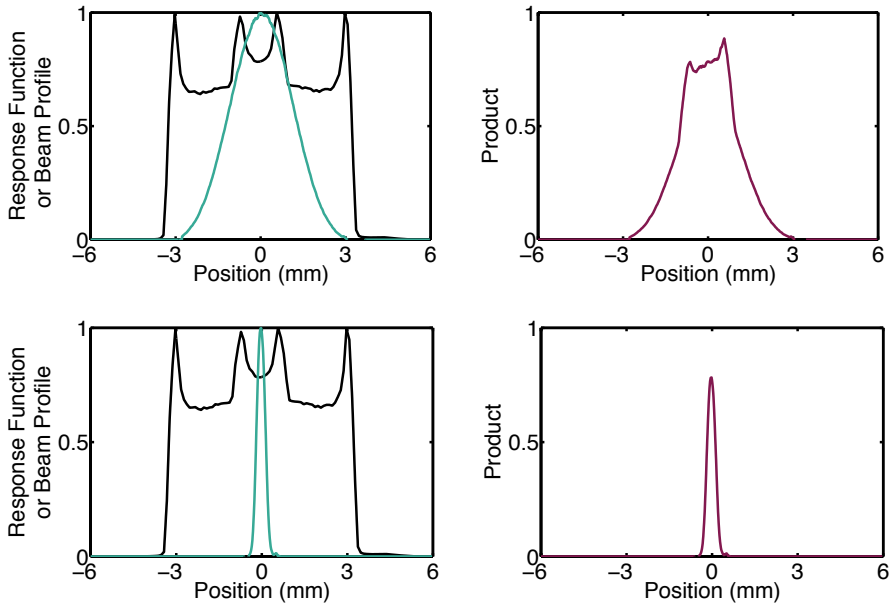

Figure 5.6 A representation of the algorithm used to determine the relative ion chamber response with beam size for the stationary measurement. The left column shows the aligned ion chamber response function and the beam profile, while the right column shows the product of the two functions. The top row is an example for the 1.103 mm Cu-filtered beam and the 8.7 mm collimator setting, and the bottom row is the for 0.6 mm collimator setting.

The maximum difference between the predicted and measured values occurred for the smallest beams (0.1 and 0.6 mm collimator settings). The maximum differences were 4.9, 8.0, 9.0 and 10.2 % for the 0.938 mm Cu-filtered beam, 1.103 mm Cu-filtered beam, 33.3 keV and 20.0 keV, respectively. If the smallest beams are ignored, the average differences between measured and predicted values are 1.4, 0.8, 3.2 and 1.2 % for the four beams in the same order as listed above. The greatest source of uncertainty in the calculated data is probably attributed to the alignment between the beam profile and the ion chamber response function. To investigate the influence of misalignments, the algorithm was re-run with offsets between the ion chamber and beam profiles. For the largest beams, the change in f_{vol} was less than 0.1 % per 100 μm offset near the centered position. The dependence on position was an order of magnitude greater for the smallest

beams, which showed up to a 1.6 % change in f_{vol} per 100 μm misalignment near the centered position.

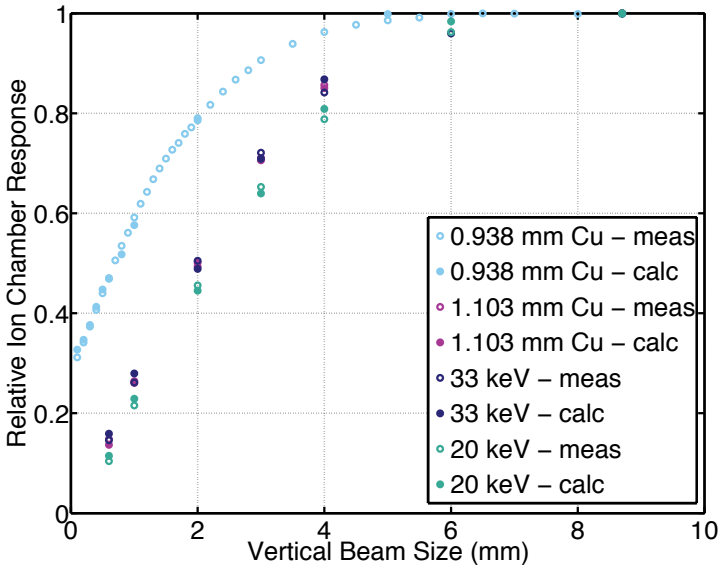

Figure 5.7 The stationary configuration predicted ('calc' – solid circles) and measured ('meas' – open circles) relative ion chamber response as a function of the nominal beam size for all beam energies considered.

5.3.5 Vertical ion chamber response - scanning geometry

Figure 5.8 demonstrates the algorithm for determining the effective time in a uniform beam (Eq. 5.11), which was used to determine the air kerma rate for the scanning measurements. Like Fig. 5.6, the examples shown here are for the 1.103 mm Cu-filtered beam at the 8.7 mm (top) and 0.6 mm collimator settings. The right column shows the cross-correlation between the beam profile and the ion chamber response function, which is integrated to determine t_{eff}.

Figure 5.9 shows that the predicted and measured ion chamber response as a function of beam height for the scanning measurements. The general trends are very similar to the stationary geometry: the rate of change of ion chamber reading with changing beam height is lowest at the widest collimator positions. Again, there is a large difference between the measurements taken during the first (0.938 mm Cu-filtered beam) and second experimental sessions. As above, this is expected to be due to a change in beamline configuration between the two data collection times. Again, the ion chamber

readings in the larger 20 keV beam show more change with collimator setting at the wide settings than any of the other beams.

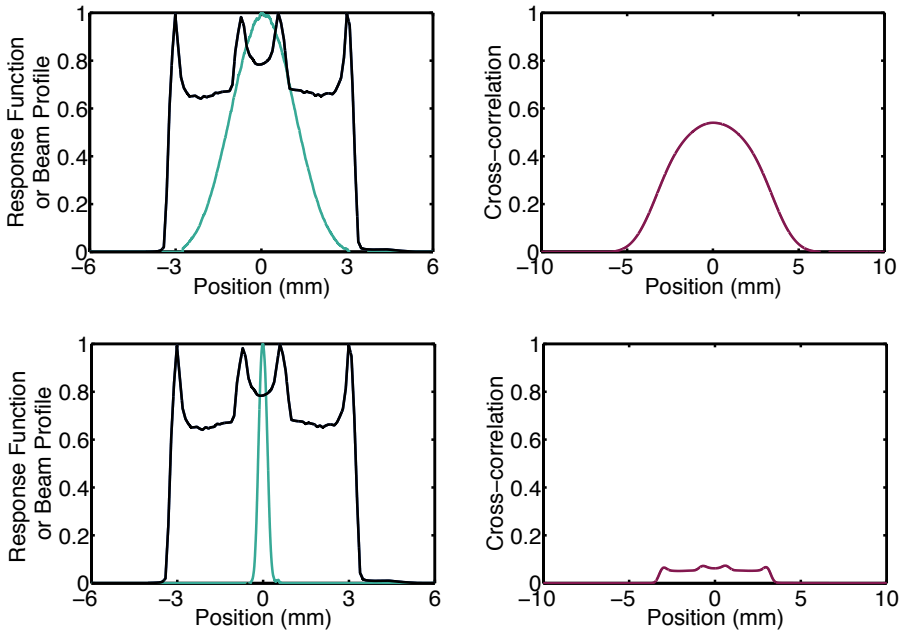

Figure 5.8 A representation of the algorithm used to determine the relative ion chamber response with beam size for the scanning measurement. The left column shows the aligned ion chamber response function and the beam profile, while the right column shows the cross-correlation of the two functions. The top row is an example for the 1.103 mm Cu-filtered beam and the 8.7 mm collimator setting, and the bottom row is for the 0.6 mm collimator setting.

The agreement between measured and predicted values was poorer for the scanning measurements than the stationary measurements. For the beams investigated during the second experimental session, the greatest difference occurred for the 2.0 mm beam, and the values were 9.8, 21.0, and 9.5 % for the 20.0 keV, 33.3 keV, and 1.103 mm Cu-filtered beams, respectively. The mean differences between measured and predicted values are 3.8, 7.4, and 4.9 % in the same order as above. The 0.938 mm Cu-filtered beam, measured in the first experimental session, had a maximum difference between predicted and measured values of 9.0 % (for the 1.0 mm beam), and an average difference of 4.0 %. Although the cause of the large uncertainties is still unknown, it may be influenced by limitations of the electrometer in making effectively instantaneous measurements while the chamber is scanned.

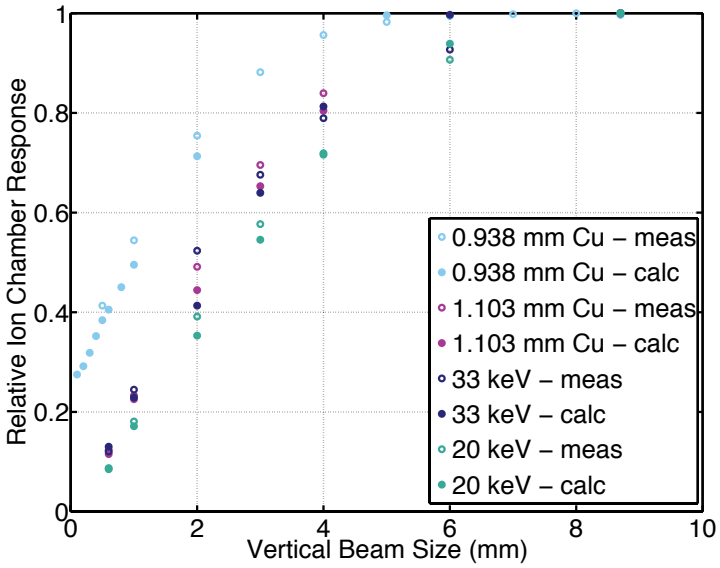

Figure 5.9 The scanning configuration predicted ('calc' – solid circles) and measured ('meas' – open circles) relative ion chamber response as a function of the nominal beam size for all beam energies considered.

5.3.6 Reference dosimetry

The 05B1-1 air kerma rates for two polyenergetic beams (0.938 mm Cu and 1.103 mm Cu filtration) and two monoenergetic beams (20.0 and 33.3 keV) were determined using Eq. 5.8, and are reported in Table 5.4. The interpolated (based on Tables 5.1 and 5.2) calibration factors to convert electrometer reading (nC) to air kerma (Gy) for each beam quality are also tabulated. The correction for additional air attenuation applied to the 0.938 mm Cu-filtered beam measurements was 1.013. The peak and mean air kerma rates at a synchrotron storage ring current of 250 mA (the maximum value) as a function of nominal beam size (collimator setting) are shown in Fig. 5.10. As expected, we see an increase in the mean air kerma rate with increasing vertical beam size. The peak air kerma rate is fairly uniform for collimator positions between 1 and 8.7 mm. It is expected that the least filtered polyenergetic beam will have the highest air kerma rate, which is what is observed. For the uncollimated beams (collimator setting = 8.7 mm), the peak air kerma rate was 1.89 Gy/s for the 0.938 mm Cu-filtered beam. The peak 1.103 mm Cu-filtered beam air kerma rate was determined to be 1.31 Gy/s. The ratio

between these values is 0.70, which is very close to the theoretical relative flux ratio between the two filtrations (0.69; Table 5.1).

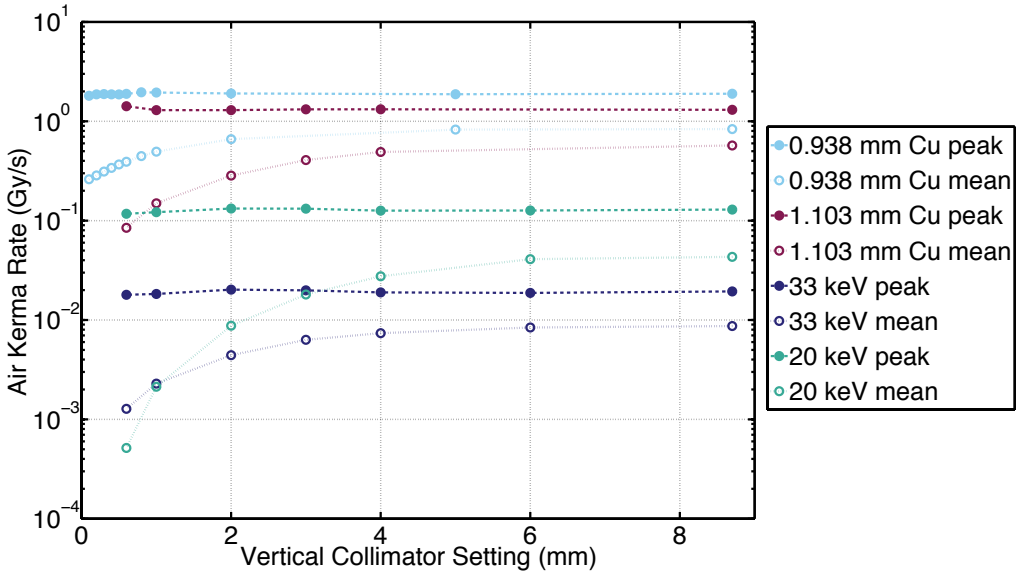

Figure 5.10 Reference air kerma rates as a function of beam size (nominal collimator setting) for the four beam energies investigated. Values include the mean air kerma rate across the varying beam profile, and the air kerma rate in the beam's peak at a storage ring current of 250 mA.

The air kerma rates for the monenergetic beams are significantly lower than the polyenergetic beams. This is because energy selection by the monochromator removes the majority of the photons in the beam. The air kerma rates calculated for the monoenergetic beams depend on the monochromator's crystal angle; small drifts in the angle cause significant changes in the beam's intensity. The monochromator on the 05B1-1 beamline has a feedback system to stabilize its output, but its performance was not investigated. Additionally, the repeatability of the crystal's output after moving between different energies (which requires relatively large changes in the crystal's angle) was not investigated. Because of these unknowns, the repeatability of the air kerma rates reported in Table 5.4 requires investigation.

Table 5.4 The air kerma rates as measured by the Capintec PR06C ionization chamber in the open field (collimator setting = 8.7 mm). The air kerma rates are included for the mean across the non-uniform beam and for the central most intense region of the beam.

X-ray beam	Calibration factor, N_{cal} (cGy/nC)	Air kerma rate, $\dot{K}$ at 250 mAs (Gy/s)	
		Mean	Peak
1.103 mm Cu	4.108	0.57	1.31
0.938 mm Cu	3.945	0.84	1.89
33.3 keV	4.090	0.0087	0.0194
20.0 keV	4.078	0.043	0.129

The air kerma values from experimental session 2 reported above can be compared to values determined through free-air chamber measurements given in Chapter 4. It is not simple to do a direct comparison because the geometry in the two measurements was different. The FAC measurements were taken with a 0.516 mm diameter aperture, while the cavity chamber measurements were performed with wide beams (70 mm) which were collimated vertically by jaws approximately 15 m upstream of the measurements. The cavity chamber peak air kerma rates were 30, 23, and 25 % greater than the FAC measurements for the 20.0 keV, 33.3 keV, and 1.103 mm Cu-filtered beams, respectively. The ratios of air kerma rates at each energy measured by the two chambers agree within ± 4 %, when normalized to the 1.103 mm Cu-filtered air kerma rate.

5.4 Conclusion and future work

Measurements of the ion chamber response function of a clinical, cylindrical ion chamber and of the beam profile enabled development of an algorithm to predict the ion chamber response as a function of beam height in both scanning and stationary geometries. The good agreement between the predicted and measured results for the stationary measurements indicates that the developed model characterizing ion chamber response to the small, non-uniform beam provides a valuable tool in understanding the ion chamber response in the synchrotron x-ray beams. The poorer agreement for the scanning

measurements highlights the limitations of the model and/or experimental method. Peak air kerma rates between 0.019 and 1.89 Gy/s at the maximum storage ring current and the maximum beam size were determined for the filtered BMIT bending magnet beamline at the CLS. This is an important step to allow relatively fast (compared to free-air chamber dosimetry) reference dosimetry on the BMIT beamlines.

Future work will include exploration of the discrepancies observed for the scanning measurement. Monte Carlo simulations of the air kerma delivered to a cavity ionization chamber, such as the Capintec PR06C, by a small non-uniform beam will be used to assess the required correction factors for determining air kerma. This will include assessing the influence of the lack of lateral charged particle equilibrium in the beam, the stem effect for this narrow beam, and the influence of energy dependence. The dependence of correction factors (*e.g.*, recombination and polarity corrections) on field size requires investigation. Monte Carlo simulations will be done to establish a relationship between the dose measured with the cavity ion chambers and with the free air ionization chamber (Chapter 4). Additionally, further experimental work would include the use of smaller volume cylindrical and/or parallel plate ionization chambers. The advantage of smaller volume is less recombination as well as less influence of non-uniformity over the chamber diameter, and a parallel plate chamber will have a uniform response function and thus require fewer corrections.

5.5 References

[1] H. Morrison, G. Menon, R. Sloboda, "Radiochromic film calibration for low-energy seed brachytherapy dose measurement," Med. Phys. **41**, 15-16 (2014).

6 MONTE CARLO-GENERATED MRT DOSE DISTRIBUTIONS AND ASSOCIATED DOSE-VOLUME METRICS IN CUBIC HEAD PHANTOMS FOR THE 05ID-2 BEAMLINE

A version of this chapter has been published: D. Anderson, E. A. Siegbahn, R. Serduc, B. G. Fallone, and B. Warkentin, "Evaluation of dose-volume metrics for microbeam radiation therapy dose distributions in head phantoms of various sizes using Monte Carlo simulations," Phys. Med. Biol. ***57****, 3223-48 (2012).*

6.1 Introduction

The geometric and dosimetric characteristics of MRT depart significantly from conventional radiotherapy techniques. Because of this, much research thus far has been directed at determining the optimal parameters for this type of delivery. In a pioneering article on MRT, Slatkin *et al.* calculated dose distributions in water produced by x-ray microbeams.[1] In this article, the authors introduced the peak-to-valley dose ratio (PVDR), which measures the maximum peak dose in relation to the valley dose found between two adjacent peaks, to quantify differences between microbeam array configurations. It was argued that this ratio would be a parameter of potential therapeutic importance in MRT, with a high PVDR believed to be advantageous for tissue tolerance. Since the inception of MRT, researchers have also investigated more complex irradiation geometries, such as cross-hatched irradiation,[2,3] intersecting cross-firing,[4,5] or interlaced cross-firing,[6-8] (Fig 1.8) as a means of increasing the dose to the target over simple unidirectional irradiation.[3,5,9-11] In reports of animal experiments attempting to optimally balance tumor palliation and normal tissue sparing,[2,4,5,10,12] the parameters varied experimentally have included beam filtration, microbeam widths, center-to-center (c-t-c) distance between microbeams and absolute peak doses delivered at the skin surface. Despite this considerable work, definitive answers to these optimization questions remain elusive.

Although the PVDR has been a standard metric for MRT, it has limitations in its ability to predict tissue response to MRT dose distributions. The PVDR only uses the global minimum and maximum doses. It does not describe the influence of the microbeam shape, which changes with geometry and photon energy. It also does not consider absolute dose: the same PVDR at different dose levels will give different biological results.[10] A larger PVDR, traditionally considered better for normal tissue sparing, has been shown to cause more normal tissue damage with extreme peak doses, compared to geometries with a lower PVDR and lower peak dose.[12] Even extremely high PVDRs will not lead to normal tissue sparing if either the peak or valley dose is high enough, again not reflected in this metric. Results from biological studies related to MRT do indicate, however, that very high peak doses can be given without causing substantial damage in some scenarios.[9,13,14] It has therefore for some time been believed that the valley dose may be a determining factor of the treatment toxicity. When the valley dose has been considered in the planning of an experiment, it has normally been the *local minimum* dose between the centermost microbeam peaks, which is a point dose metric.

In this chapter, we investigate potential metrics of toxicity and/or efficacy that characterize the MRT dose distributions from a more volumetric perspective. Such metrics have not traditionally been assessed in MRT studies. Since we surmise that the valley dose over the full distance between two peaks, and not just the minimum dose, may be of importance because of the significant dose variations within the valley region, we introduce a modified PVDR based on measures of the mean dose within the peak and valley regions. We also examine the mean dose within the different regions of interest within simulated treatment volumes individually. The separation between the microbeam peaks affects the dose distribution, and may have biological consequences: for example smaller separations may increase damage due to destructive signalling between cells. The fractional volume receiving greater than a given threshold dose for the different regions of interest is also assessed.

The study of dosimetric (and eventually radiobiological) metrics for MRT is potentially of interest also to conventional radiotherapy, as it may provide insights into more fundamental aspects of radiation response. Better understanding of the therapeutic effects of the extremely inhomogeneous dose distributions of MRT may inform how to

distribute normal tissue dose during optimization of conventional treatment plans, as well as helping elucidate the principles underlying the use of grid therapy[15-18] (grid sizes of millimeter, described in Section 1.1.4) with conventional x-ray sources. Eventually, quantifying the response to MRT dose distributions, in conjunction with further animal and cell studies, may explain the role of biological factors such as cellular migration, intercellular communication and vascularization[3,19-21] in response to not only MRT, but also conventional radiotherapy modalities.

The primary aim of this work is to prepare for the preclinical biological studies at the Canadian light source (CLS) by evaluating a variety of metrics using dosimetric data as input. Since trials are foreseen for both small and large tumor-bearing animals, we have generated dose distributions with the Monte Carlo simulation method of radiation transport in three model heads of different sizes: (1) a 16 cm cubic phantom for a larger animal (*e.g.* a dog), (2) an 8 cm phantom for a medium-sized animal (*e.g.* a cat), and (3) a 2 cm cubic phantom for a small animal (*e.g.* a mouse). Head phantoms were chosen since the context of this work is potential use of MRT for brain treatments: lesions in the central nervous system in children were given priority when MRT research began[1,5,9,13,22] since the prognosis is in general poor for this patient group (Section 1.1.5) and the depth-dose characteristics of MRT were less limiting in pediatric patients. (Targets in other parts of the body may also be of interest in the future, however.) For each of these different head sizes, we will evaluate the standard PVDR metric, as well as three new ones based on a more volumetric analysis. Trends in the values of these metrics as a function of head size and beam geometry (beam width, beam spacing, unidirectional versus cross-firing) will be evaluated and discussed. These results will provide a framework for eventual comparison with future biological experimental results, which can be used to assess the validity of the metrics in predicting the effect of the treatment, and a first step in developing more robust radiobiological indices.

6.2 Materials and methods

6.2.1 Simulation geometry and details

The 2008 version of the Monte Carlo code PENELOPE[23] was used for the calculation of MRT dose distributions, as it has in many past studies.[6,8,12,24,25] PENELOPE is a general-purpose Monte Carlo simulation package for the modeling of coupled electron– photon transport through arbitrary media. The code is applicable for energies between a few hundred eV to approximately 1 GeV, with developers placing a special emphasis on the implementation of accurate low-energy electron cross sections, which makes it suitable for calculating the required high-resolution dose distributions for MRT. PENELOPE has been benchmarked against experimental data with energies ranging from a few keV to approximately 1 GeV and has shown consistent results between simulation and measurement.[26] Additionally, PENELOPE has been compared with other Monte Carlo packages (EGS4, GEANT4, EGSnrc and MCNPX) for simulating MRT dose distributions.[27-29] The results showed overall agreement, with the largest differences (up to approximately 20 %) occurring in the high gradient regions just outside the primary photon beam.[28] Photon transport is simulated in detail, with the interactions of all photons being simulated explicitly (*i.e.* no grouping of interactions) until the photon cut-off energy for local absorption is reached. Photoelectric effect, Rayleigh scattering, Compton scattering and pair production are all modeled in PENELOPE, and all but pair production are relevant in calculating MRT dose distributions. In the 2008 version of this code, the x-ray polarization is taken into consideration in the simulation of Compton and Rayleigh scattering, which are the most important interactions in brain tissue due to its low atomic number. The charged particle simulation algorithm employs a 'mixed' simulation approach: 'hard' interactions with scattering angles or energy losses greater than pre-selected threshold values are simulated in detail, while 'soft' interactions with scattering angles or energy losses less than these thresholds are modeled with a condensed history (i.e. grouped interactions) multiple scattering approach.

Simulations were performed using the characteristics of the BMIT 05ID-2 (Section 2.6.2) beamline at the CLS (Section 2.5). The energy spectrum of the filtered, collimated x-ray beam produced by the 4.3 T wiggler was calculated using the

SPECTRA[30] program. The program and its results were described in more detail in Chapter 3. The energy spectrum used for the Monte Carlo simulations in this chapter is shown in Fig. 6.1. The initial energy of the primary photons in the simulations was sampled from this calculated energy spectrum, which is normalized to the peak energy. The BMIT wiggler produces an energy spectrum with a most probable energy of 83 keV and a mean energy of 99 keV, which is slightly lower compared to the mean energy of 107 keV [24] of the ID17 biomedical beamline at the ESRF, where the majority of MRT studies have thus far been performed. The Stokes polarization vector (0.997, 0, 0) was used in the simulations, and was based on the output of SPECTRA. The vector indicates almost complete linear polarization in the horizontal plane. Since the CLS 05ID-2 beamline has not yet been fully commissioned, neither the energy spectrum nor the degree of polarization of the x-ray beam produced by its wiggler has been measured. However, initial measurements of the penetrability of the CLS 05B1-1 beam indicate reasonable agreement between this beam's energy and that calculated with SPECTRA (Sections 3.3.7 and 3.3.9). For all simulations, parameters for the cut-off energy loss for hard elastic collisions (W_{CC}) and hard bremsstrahlung emission (W_{CR}) for electrons and photons were set to 1 keV. For electrons, the cut-off energy of 1 keV corresponds to an electron range of approximately 0.1 μm based on tabulated stopping power data from the National Institute of Standards and Technology (NIST).[31] The mixed simulation parameters for electron scattering in PENELOPE — C1, which is the 'average angular deflection produced by multiple elastic scattering along a path equal to the mean free path between consecutive hard elastic events', and C2, which 'defines the maximum average fractional energy loss between consecutive hard elastic events'[23] —were set to small values (0.01) so that the simulations were almost completely done in the detailed collision mode. This was done to minimize possible errors related to limitations of the multiple scattering theory implemented in the code, and is feasible since the secondary electrons generated are low in energy and therefore undergo a relatively small number of collisions before being absorbed. Since our geometry does not contain thin bodies, as discussed in the PENELOPE manual, the step-length control could be switched off by setting DSMAX (the parameter restricting the maximum step length for electrons and positrons) to a large value (1.0×10^{10}). The suitability of this choice was confirmed by

the fact that results from a simulation with the step-length control switched off and a simulation with DSMAX set to one-tenth the thickness of the thinnest body were equivalent within statistical uncertainty. The simulation parameters (W_{CC}, W_{CR}, C1, C2 and DSMAX) were the same for all materials.

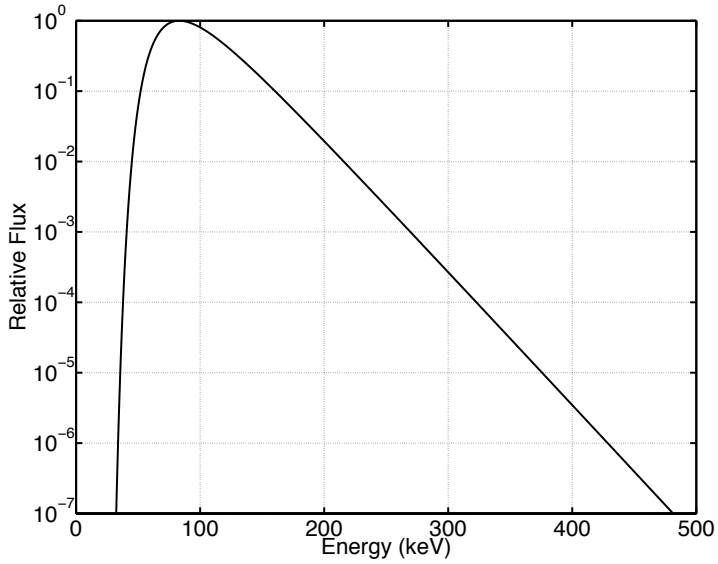

Figure 6.1 The theoretical CLS BMIT 05ID-2 energy spectrum used in the Monte Carlo simulations. The spectrum was estimated using the SPECTRA[30] computer program, and is normalized to the peak energy.

Dose distributions were calculated in head phantoms of sizes representing three different animal sizes. Each phantom consists of three concentric cubes. The outermost layer is composed of skin, the next layer of bone and the innermost cube consists of brain material (Table 6.1 and Fig. 6.2). The compositions of brain, bone and skin were taken from ICRU Report 44. The smallest phantom, representing a small animal head (i.e. a mouse), has a 2 cm cubic brain region, a bone thickness of 0.5 mm and a skin thickness of 0.5 mm, chosen to match the geometry in Serduc *et al.* (2008).[32] An 8 cm cubic brain region was used to represent a medium-sized animal (i.e. a cat) head, and a 16 cm cubic brain region was used to represent a large-sized animal (*i.e.* a dog) head. In addition to the skin, bone and brain, a lesion, also composed of brain material, was imagined at the center of the brain. A lesion represented by a cube with sides measuring 4 mm was considered for the 2 cm mouse, 8 cm cat and 16 cm dog phantoms. To represent the

larger tumors more likely to be found in larger animals, a 16 mm lesion in the 8 cm cat phantom, and a 32 mm lesion in the 16 cm dog phantom were also studied. The thicknesses of skin, bone and brain in these simple phantoms are convenient approximations for the purpose of these simulations; although the values may not necessarily be the most physiologically representative for the 'average' mouse, cat and dog, the dimensions selected fall within ranges quoted in the literature for these dimensions.[33-37] The dose to medium (*i.e.* physical dose) is calculated in the different tissues traversed by a microbeam array. As it is normally the dose to water that is reported in radiotherapy, the dose to the bone appears exaggerated because of the large absorption at these kilovoltage energies.

Table 6.1 Dimensions of the various materials making up the three phantoms corresponding to Fig. 6.2. All simulations done in the larger phantoms (8 cm cat and 16 cm dog heads) considered both a small lesion (4 mm) and a larger lesion scaled up according to the dimensions of the phantom.

	2 cm Mouse Head Phantom	8 cm Cat Head Phantom	16 cm Dog Head Phantom
Skin	0.5 mm	2 mm	4 mm
Bone	0.5 mm	4 mm	8 mm
Brain	20 mm	80 mm	160 mm
Lesion	4 mm	4 mm & 16 mm	4 mm & 32 mm

For each of the five different treatment scenarios summarized in Table 6.1, dose distributions were generated for nine different combinations of microbeam widths and c-t-c spacings between the microbeams. The widths of 25, 50 and 75 μm and spacings of 100, 200 and 400 μm investigated in this study are values that have been used in previous MRT experiments. Since the primary motivation of this work is to identify general trends in the dependences of several dose-volume metrics (described below in Section 6.2.3) on MRT geometry, rather than calculation of the precise values of the metrics, somewhat simplified simulation geometry was used to achieve a reasonable computational efficiency for the number of simulations required, and their spatial resolution.

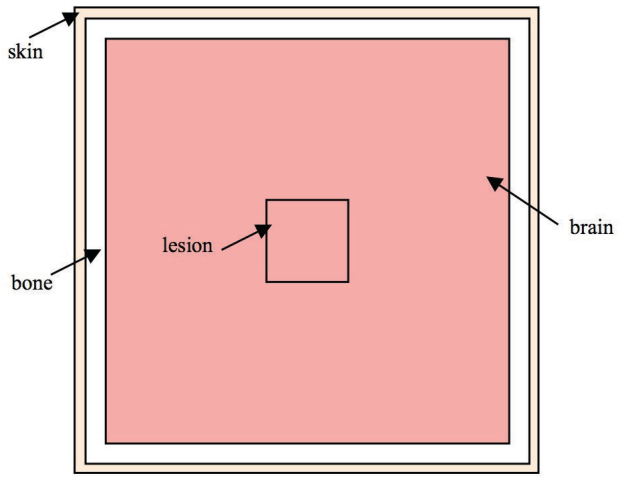

Figure 6.2 The head phantoms used in the simulations consisted of three concentric cubes composed of brain, bone and skin. Different sizes were used to represent animals of varying sizes – a 2 cm brain of a mouse, an 8 cm brain of a cat, and a 16 cm brain of a dog. Dimensions of the various materials are listed in Table 6.1.

As done in several previous MRT Monte Carlo studies,[8,24,38,39] and briefly described previously in Section 3.2.10, a single, rectangular, parallel microbeam incident at the surface of the phantom was simulated. The x-ray energy of the photons was sampled from the theoretical spectrum (Fig. 6.1), and their direction was perfectly perpendicular to the phantom surface. Our simulations thus did not include the source size or the small divergence of the x-ray beam (~ 4 mrad in the horizontal direction), nor the MRT collimator and the effects of the propagation distance between the source and collimator and the collimator and phantom.[40] In each simulation the dose distribution resulting from the incident microbeam was scored in parallelepipeds as a function of depth and lateral displacement from the center of the microbeam. The scoring in the depth direction was in slices of 0.5, 2 and 4 mm thicknesses for the 2 cm mouse, 8 cm cat and 16 cm dog phantoms, respectively. As has been done in previous work,[24] the transversal dose profile at each of these depths was scored in lateral bins of increasing size as the lateral displacement from the center of the microbeam peak increased, in order to reduce the statistical uncertainties as the dose deposition falls off. Doses over the height of the microbeam were integrated. Using the transversal dose profile for a single planar beam, the dose pattern for the number of microbeams in the array size required to

cover the width of the lesion was obtained by using a superposition/convolution procedure:

$$D_{tot}(x) = \sum_{i=1}^{N} D_s(x) \cdot \delta(x - x_i) \qquad (6.1)$$

where $D_s(x)$ is the dose distribution as a function of lateral displacement for a single microbeam (interpolated to a 1 μm spacing to facilitate the convolution), N is the number of microbeams in the array and the x_i's are the relative position of the centers of the different microbeams in the array, spaced at 100, 200 or 400 μm. This approach assumes that the dose profile used in the convolution is position invariant. Nettelbeck *et al.* (2009) showed that modeling of a single microbeam and subsequent superposition is an adequate approximation if the construction of the multi-slit collimator is symmetric.[40] The size of the microbeam array was chosen to match the size of the lesion. A 4×4 mm^2 array was studied for all phantoms, in order to isolate the effect of phantom size alone; to investigate the effects of larger tumors, additional simulations were done with the array scaled up to create a 16×16 mm^2 array in the 8 cm cat head phantom, and 32×32 mm^2 array in the 16 cm dog head phantom.

While in most previous preclinical experiments the animals have been irradiated unidirectionally in the direction from ear to ear (note that the choice of entrance would be more crucial for dogs than mice since beam attenuation is accentuated for deeper seated tumors), some previous and many future experiments will employ a cross-firing technique using a second perpendicular microbeam (*e.g.* in the anterior–posterior direction). Thus, our Monte Carlo simulations of the unidirectional irradiation geometry were also used to derive dose distributions for the cross-fired (CF) array geometry. First, a linear interpolation for intervals of 1 μm in the depth direction was performed between the transversal dose profiles scored at the different depths, which resulted in a two-dimensional (2D) matrix of the dose distribution on a 1×1 μm^2 grid for unidirectional irradiation. This 2D dose matrix was duplicated then rotated 90°, to mimic a second, orthogonal array of microbeams, and added to the original 2D matrix to create a cumulative 2D dose distribution matrix for a CF region at the center of the head phantoms. A matrix corresponding to a $4 \times 4 \times 4$ mm^3 CF region was generated for each

of the three phantoms; in addition, a 16 × 16 × 16 mm^3 array for the 8 cm cat head phantom and a 32 × 32 × 32 mm^3 array for the 16 cm dog head phantom were created. These mathematical operations (interpolation and matrix rotation and summation) were performed using MATLAB. Use of the above approach to generate the CF dose distributions was possible because of the symmetry of the head phantoms simulated, and would not be applicable to an anatomically correct data set.

In the mouse head phantom, 10^9 histories were used for each simulation, while 10^8 histories were used for simulations in the cat and the dog head phantoms. Statistical uncertainties (2σ) were tallied and propagation of errors was used to determine the errors on the interpolated values within the dose distributions. Uncertainties due to the choice of interpolation method were ignored. The resulting statistical uncertainties were 0.2–0.9 % in the microbeam path, and 0.5–2.0 % between microbeams at the center of the array in the center of the phantom for all simulations.

6.2.2 Description of dose-volume metrics

Despite its limitations as a dose-volume metric for MRT, the PVDR was calculated for all simulations because it has been the most commonly used metric in previous MRT research, and is useful to compare our results for the new biomedical beamline at the CLS to past studies. The PVDR was calculated for the central microbeam in the array at the center of the head phantom in the following manner:

$$PVDR = \frac{D_{peak}}{D_{valley}} \tag{6.2}$$

where D_{peak} is the dose at the center of the peak of the central microbeam, and D_{valley} is the dose at the center of the valley on one side of the central microbeam (Fig. 6.3(a)). The uncertainty in the PVDR was determined by conventional propagation of errors for a ratio of two values.

To extend the definition of the PVDR, we devised the peak-to-mean valley dose ratio (PMVDR) to take into account that it is not only the minimum dose between two peaks which is important for the toxicity of MRT, but also the dose in the valley closer to the edges of the microbeams. A biological rationale for such averaging is that the doses

produced by MRT vary significantly, particularly in the valley region, over the biological scales involved. There is evidence from earlier research on MRT that repair becomes more difficult if several neighbouring endothelial cells (typically 10–20 μm in diameter) are damaged in the valley.[24] For a blood vessel, such severe cellular damage can lead to ischemia, for example. In this scenario, looking solely at the absolute minimum dose in the valley may underestimate the potential biological damage since neighbouring endothelial cells in the valley but closer to the peak will receive a higher dose — an overestimation of the expected normal tissue tolerance may result. MRT tumour control and normal tissue toxicity would seem less sensitive to the absolute peak dose, within certain limits, compared to the valley dose, so averaging over the peak may not be as important as averaging over the valley. The mean peak dose is, however, more representative, especially for narrow microbeams, since there is still significant dose falloff at the edges of the microbeams. Evaluating the mean valley and peak doses instead of simply the minimum valley and maximum peak dose is thus a first step to a more complete dose-volume analysis of MRT dose distributions that accounts for dose gradients.

We calculated the PMVDR using the mean dose over the nominal microbeam width (25, 50 or, 75 μm) and the mean dose over the nominal valley width, which is the microbeam spacing (100, 200, or 400 μm) minus the microbeam width (Fig. 6.3(b)) as follows:

$$PMVDR = \frac{\frac{1}{N_{i,peak}} \Sigma_{i,peak} D_{i,peak}}{\frac{1}{N_{i,valley}} \Sigma_{i,valley} D_{i,valley}} \tag{6.3}$$

where the D_i's are the dose in the bins which fall in either the peak or valley region as shown in Fig. 6.3(b), and the N_i's are the number of bins within each region. The uncertainty in the PMVDR is calculated by adding the statistical uncertainties in quadrature when averaging dose in the peak and valley regions, and again using propagation of errors when taking the ratio of the mean values. Using the nominal peak and valley widths to calculate the PMVDR is somewhat arbitrary since it would be expected that if the biological rationale discussed above is realistic, the spatial windows used for averaging should be absolute distances. However, at this point there is not yet

nearly sufficient experimental evidence to inform limiting peak and valley doses or distances for MRT. A superior definition will hopefully be revealed following further cellular and animal studies, or revision of previous studies, allowing comparison of biological outcome with the metrics defined in this and other studies. The PMVDR also does not consider absolute dose, and therefore shares this shortcoming with the PVDR. A better understanding of MRT dose limits is required so that they too can be incorporated into new metrics.

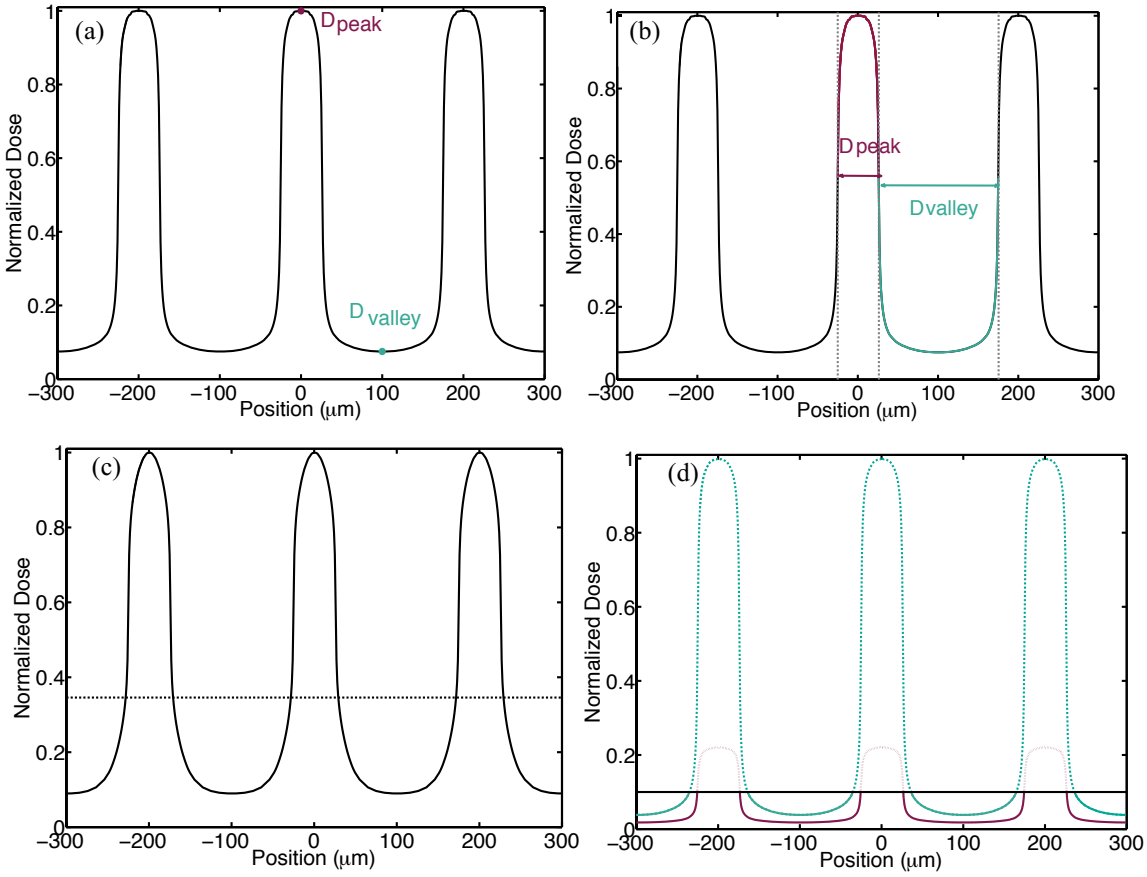

Figure 6.3 Schematics showing the four metrics explored in this study. (a) The PVDR is the ratio between the dose at the center of the peak and the center of the adjacent valley for the central microbeam. (b) PMVDR is the ratio between the mean dose in the peak region and the mean dose in the valley region. (c) The mean dose (dashed line) is calculated in the typical manner, and is normalized to the maximum absorbed dose in the phantom. (d) The *percentage volume under 10 % of the entrance skin dose* was also calculated. The bold section of the curves indicate the bins included in this volume, and the dashed curves indicate bins excluded from this metric.

In addition to the PVDR and PMVDR, we also calculated two other metrics, the first being the mean dose to the different tissues (skin, bone, brain and tumour). The mean dose can be compared to conventional equivalent uniform dose (EUD)[41] methods, since the mean dose is equal to EUD when a volume parameter of 1 is chosen (Fig. 6.3(c)). The value of $a = 1$ was selected for now because values relevant to the extreme spatial fractionation of MRT are unknown, with the volume parameter values typically chosen for tumours and normal tissue likely being unsuitable. Adding the errors in each dose bin in quadrature was again used to estimate the uncertainty in the mean dose. The mean dose was expressed as a percentage of the maximum dose in the array, which occurs in the bone at the side of the head nearest the entrance surface. The second additional metric investigated is the percentage volume of brain, within the volume traversed by the microbeam array path, receiving a dose below 10 % of the peak entrance dose (Fig. 6.3(d)). The error in the volume was taken as the average of the volume lying above or below 2σ of the threshold dose. The *percentage volume below 10 %* was chosen because it is a way of quantifying the dose distribution in terms of its volumetric damage—the greater the volume below a given critical threshold (again chosen arbitrarily since the threshold is unknown) in the normal tissue, the better the sparing expected. Reducing this volume in the lesion is desired to ensure maximal cancer cell death. This metric can easily be adjusted to consider absolute dose, given the knowledge of a threshold valley dose, which in turn depends on geometry (microbeam width and spacing). The analysis of the MRT unidirectional and CF dose distributions with respect to the four different dose metrics was performed using MATLAB.

We hypothesize that one metric may be appropriate for assessing normal tissue damage, while another may be better suited for predicting tumour control. It is hoped that the analysis of preclinical trials will identify which metrics are most useful in predicting the MRT outcomes.

6.3 Results

6.3.1 Dose distributions in head phantoms and the effect of phantom size

To illustrate the general characteristics of the simulated MRT dose distributions in a cubic head phantom, the dose distribution in the 2 cm mouse head when irradiated with an array of 25 μm wide microbeams, separated by 200 μm, is shown in Fig. 6.4(a). The prominent dose near the entrance and exit walls of the phantom is due to the elevated dose to bone. The plot shows the fairly gradual decay in dose with depth in this, the

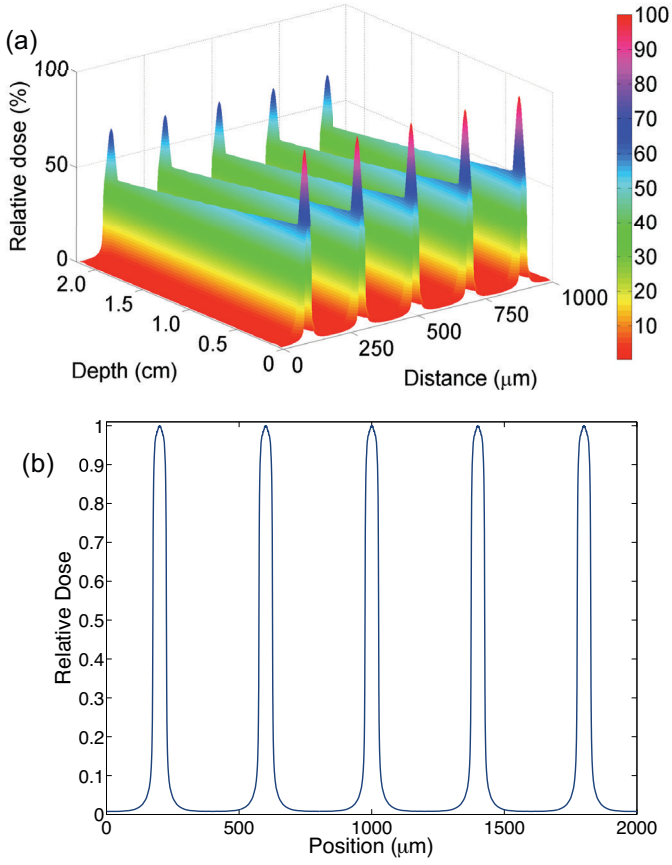

Figure 6.4 (a) Surface plot displaying dose as a function of depth in the phantom and distance perpendicular to the direction of the microbeam array propagation for a microbeam width of 25 μm and a c-t-c spacing of 200 μm. b) A plot showing a lateral dose profile for a 50 μm wide microbeam separated by 400 μm in the 2 cm mouse head phantom with a PVDR of 123. The dose was scored between 10.0 and 10.5 mm in the cubic brain region.

smallest, head phantom. Figure 6.4(b) shows a normalized lateral dose profile, demonstrating the variation in dose in the direction perpendicular to microbeam propagation, for a 50 μm microbeam separated by 400 μm in a 2 cm mouse head phantom scored over 0.5 mm in the depth direction near the center of the phantom. The PVDR in this particular case is 123.

The peak and valley doses, along with the PVDR (also in Table 6.3), are shown as a function of relative depth (since the phantoms have different sizes) for the three head phantoms in Fig. 6.5 for a microbeam width of 50 μm and a c-t-c spacing of 400 μm. All data in Fig. 6.5(a) and (b) are normalized to the maximum peak dose for a given phantom–array combination. The effects of the greater attenuation between the entrance and exit surfaces of the phantom as the phantom size increases are illustrated in Fig. 6.5(a). The 8 cm cat head phantom with the 4 mm array and the 16 cm dog head with the 4 mm array data lie directly under those for the 8 cm cat head with the 16 mm array and the 16 cm dog head with the 32 mm array, indicating that there is very little change in the relative peak dose between the smaller $4 \times 4\text{mm}^2$ array to the larger $16 \times 16\text{mm}^2$ and $32 \times 32\text{mm}^2$ arrays for the 8 cm cat head and 16 cm dog head, respectively. Figures 6.5(a) and (b) show that the valley dose more strongly depends on array size than the peak dose does. The valley dose is higher (more than double for both 8 cm cat and 16 cm dog heads) for the larger arrays due to more scattered dose.

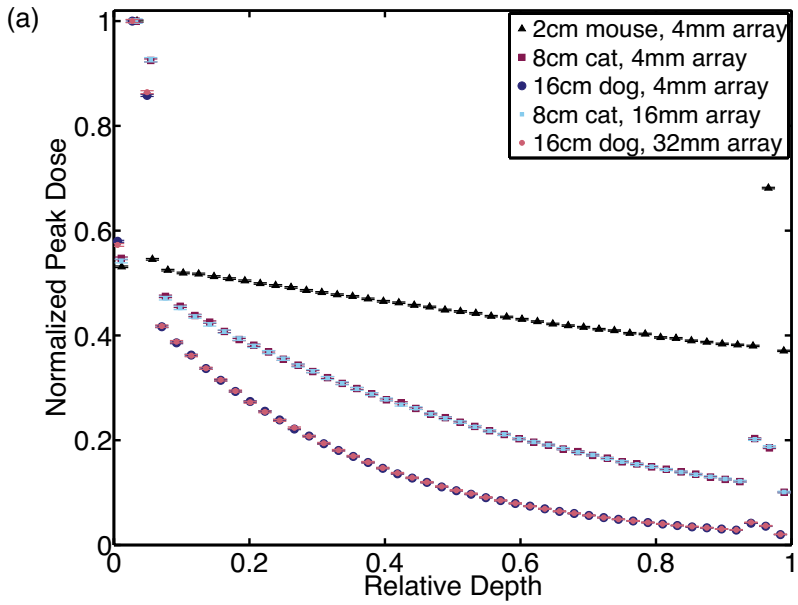

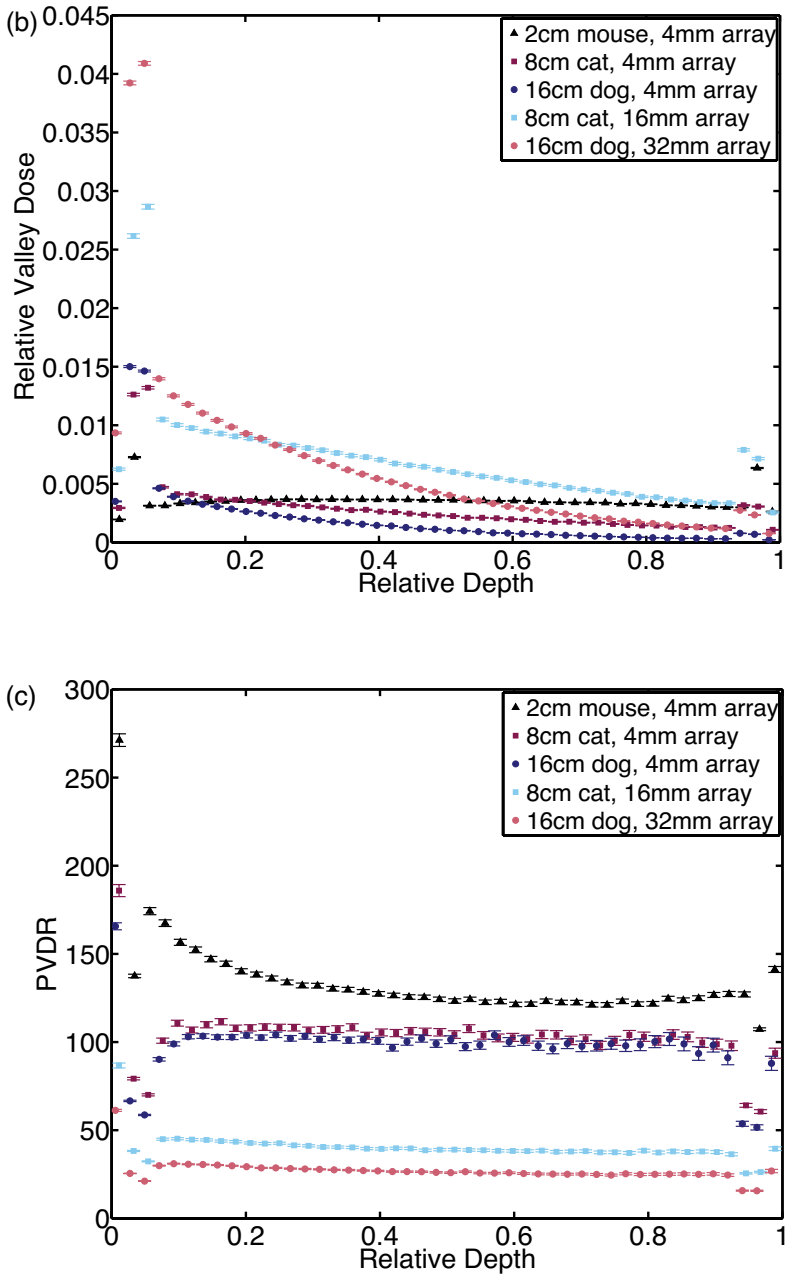

Figure 6.5 a) Normalized peak dose, b) relative valley dose (plotted relative to the peak mean dose for each phantom-array combination) and c) PVDR as a function of relative depth (1.0 corresponds to the full length of the head phantom – 2.2, 9.4 or 18.4 cm depending on the animal) in the three head phantoms for a 50 μm wide microbeam and a spacing of 400 μm. The values are plotted for the 4 mm array for each phantom, and also for the larger array sizes (16 mm and 32 mm) for the 8 cm cat and 16 cm dog head phantoms.

Figure 6.5(c) shows the PVDR for each phantom. The PVDR decreased with increasing phantom size due to the decrease in peak dose and increase in valley dose. For the 4×4 mm^2 array, the PVDR at the center of the 2 cm mouse phantom is 123.8, for the 8 cm cat head phantom it is 104.9 and for the 16 cm dog head it is 100.2. There was also a more significant drop in PVDR when considering the different array sizes for the two larger phantoms. At the center of the phantom, the PVDR dropped to 39.0 in the 8 cm cat head and 26.0 in the 16 cm dog head, which were reductions of 62.8 % and 74.1 %, respectively, compared to data obtained for the smaller arrays. Since in future experiments spontaneous tumours in larger animals will generally be larger in size (larger than 1 cm), results using the larger arrays for the 8 cm cat head and 16 cm dog head are likely more representative of what could be expected in preclinical animal trials. Figure 6.5(c) also shows that the PVDR is lowest in bone and highest in the skin at the entrance side of the phantom, which is beneficial for skin sparing.

6.3.2 Dose-volume metrics for unidirectional irradiation

6.3.2.1 Peak-to-valley dose ratio (PVDR) and peak-to-mean valley dose ratio (PMVDR)

Our Monte Carlo simulated PVDRs are compared to the results of similar studies published in the recent literature in Table 6.2. For this comparison, we selected those previous studies that used microbeam array geometries, phantoms and depths that were most similar to those investigated in this work. As shown, there is generally good agreement between our study and these previous ones, particularly considering that the geometries and phantoms are still not identical. Comparisons with other publications representing calculations performed in dissimilar phantoms showed considerable discrepancies.

Table 6.3 lists the PVDR and our new metric, the PMVDR, calculated at the center of the head phantom and the center of the array for all combinations of array size, phantom size, c-t-c spacing and microbeam widths. The data show that an increase in the microbeam width or decrease in the microbeam spacing will cause a decrease in both the PVDR and PMVDR (due to an increase in valley dose). However, there is a nonlinear relationship between PMVDR and PVDR, with the ratio, PMVDR/PVDR, ranging from

0.21 to 0.79 for different geometries. The PMVDR and PVDR are most similar for low PVDRs, which are produced by wide microbeams and narrow c-t-c spacings. The PVDR for the small array varies more rapidly with changing geometry than both the PVDR for the larger arrays and the PMVDR. In the 16 cm dog head, for example, the largest and smallest values among the nine collimation configurations (beam width/c-t-c spacing) differ by a factor of 37.2 for the PVDR, but only a factor of 13.3 for the PMVDR with the 4×4 mm^2 array; for the larger 32×32 mm^2 array, the PVDRs and PMDRs range by factors of 14.8 and 10.1, respectively. The PMVDR predicts a different dependence (in terms of magnitude) on irradiation geometry parameters than does PVDR: it is thus plausible that the results of biological experiments may be able to establish the superiority of one of the metrics over the other.

Table 6.2 Comparison of PVDR between this work with past publications for unidirectional and cross-fired (CF) irradiations.

Reference	Phantom	Microbeam Width (μm)	Microbeam Spacing (μm)	Array Size	Energy Spectrum	PVDR
This work	2 cm mouse head	25	200	4x4 mm^2	CLS 05ID-2	80.2±0.4
Serduc *et al.* 2008[32] (Fig. 5)	2 cm mouse head	25	211	4x4 mm^2	ESRF ID 17	~80
This work	16 cm dog	50	200	32x32 mm^2	CLS 05ID-2	12.2±0.1
Prezado *et al.* 2009[25](Table 3)	18 cm ellipsoidal head	50	200	20x20 mm^2	ESRF ID 17	11.0±0.3
This work	16 cm dog head	50	400	32x32 mm^2	CLS 05ID-2	26.0±0.2
Martinez-Rovira & Prezado 2011[39] (Table 2)	12 cm slab head	50	400	20x20 mm^2	ESRF ID 17	21.1±0.1
Martinez-Rovira *et al.* 2010[42] (Fig. 2)	16 cm slab head	50	400	20x20 mm^2	ESRF ID 17	~25
This work	2 cm mouse head	25	200	4x4 mm^2 CF	CLS 05ID-2	40.6±0.3
Serduc *et al.* 2009[12] (Table 2)	7 x7x10cm^3 PMMA	25	211	14x10 mm^3 CF	ESRF ID 17	~48
This work	2 cm mouse head	50	200	4x4 mm^2 CF	CLS 05ID-2	21.1±0.2
Serduc *et al.* 2009[12] (Table 2)	7 x7x10cm^3 PMMA	50	211	14x10 mm^3 CF	ESRF ID 17	~27
This work	2 cm mouse head	75	200	4x4 mm^2 CF	CLS 05ID-2	13.6±0.2
Serduc *et al.* 2009[12] (Table 2)	7 x7x10cm^3 PMMA	75	211	14x10 mm^3 CF	ESRF ID 17	~18

Table 6.3 PVDR and PMVDR in the center of the head phantoms for unidirectional irradiation and all combinations of array size, microbeam width, and microbeam spacing.

Phantom	Array Size	Microbeam spacing (μm)	Beam width (μm)	PVDR	PMVDR	Ratio of PMVDR to PVDR
2 cm Mouse Head	4x4 mm^2	100	25	20.33 ± 0.10	10.566±0.003	0.52
			50	9.94 ± 0.05	5.977±0.002	0.60
			75	5.28 ± 0.03	3.601±0.002	0.68
		200	25	80.20 ± 0.37	23.408±0.007	0.29
			50	41.25 ± 0.20	15.184±0.004	0.37
			75	26.28 ± 0.13	11.840±0.003	0.45
		400	25	229.53 ± 1.63	49.208±0.014	0.21
			50	123.75 ± 0.90	33.667±0.009	0.27
			75	84.96 ± 0.63	28.051±0.008	0.33
8 cm Cat Head	4x4 mm^2	100	25	19.67 ± 0.21	10.232±0.008	0.52
			50	9.69 ± 0.10	5.822±0.005	0.60
			75	5.21 ± 0.06	3.525±0.006	0.68
		200	25	71.25 ± 0.69	22.512±0.015	0.32
			50	37.15 ± 0.38	14.575±0.009	0.39
			75	23.80 ± 0.25	11.321±0.007	0.48
		400	25	192.56 ± 2.69	47.099±0.031	0.24
			50	104.90 ± 1.51	32.031±0.020	0.31
			75	71.07 ± 1.06	26.417±0.016	0.37
8 cm Cat Head	16x16 mm^2	100	25	11.87 ± 0.08	7.558±0.006	0.64
			50	6.27 ± 0.05	4.431±0.004	0.71

			75	3.76 ± 0.03	2.874±0.005	0.76
		200	25	31.57 ± 0.18	15.816±0.010	0.50
			50	17.06 ± 0.11	9.948±0.006	0.58
			75	11.60 ± 0.08	7.551±0.005	0.65
		400	25	71.89 ± 0.51	32.382±0.021	0.45
			50	39.01 ± 0.31	20.826±0.013	0.53
			75	27.04 ± 0.23	16.228±0.010	0.60
16 cm Dog Head	4x4 mm^2	100	25	19.14 ± 0.19	10.014±0.008	0.52
			50	9.53 ± 0.11	5.730±0.005	0.60
			75	5.01 ± 0.06	3.465±0.005	0.69
		200	25	67.02 ± 0.68	21.970±0.016	0.33
			50	35.16 ± 0.38	14.272±0.010	0.41
			75	22.69 ± 0.03	11.084±0.007	0.49
		400	25	186.19 ± 2.69	45.929±0.033	0.25
			50	100.23 ± 1.53	31.313±0.021	0.31
			75	68.78 ± 1.07	25.805±0.017	0.38
16 cm Dog Head	32x32 mm^2	100	25	9.25 ± 0.05	6.305±0.005	0.68
			50	5.09 ± 0.04	3.793±0.004	0.75
			75	3.21 ± 0.03	2.552±0.004	0.79
		200	25	22.11 ± 0.11	12.822±0.009	0.58
			50	12.16 ± 0.08	8.052±0.005	0.66
			75	8.44 ± 0.06	6.095±0.004	0.72
		400	25	47.59 ± 0.30	25.858±0.018	0.54
			50	25.96 ± 0.20	16.381±0.011	0.63
			75	18.07 ± 0.15	12.540±0.008	0.69

6.3.2.2 Mean dose

The mean dose was calculated for the different regions of the phantom— skin, bone, brain and lesion. In calculating the mean doses for the skin, bone and brain, only the region of the structure located within the path of the microbeam array was considered (on both entrance and exit sides of the phantom for skin and bone), not the entire volume of the structure. This was done to remove changes in the mean doses resulting solely from differences in the fraction of the regions irradiated, which are dependent on the sizes of the phantoms. (If the whole tissue was considered, the mean doses in the brain, skin and bone would be reduced to between 4 % and 1 % of the values stated for the 2 cm mouse, 8 cm cat and 16 cm dog phantoms with array sizes of 4 × 4, 16 × 16 and 32 × 32 mm^2, respectively; with the larger phantoms and 4 × 4 mm^2 arrays, the mean dose would be reduced to between 0.25 % and 0.02 % of the values given in Table 6.4.) The mean doses for unidirectional irradiation reported in Table 6.4 are expressed as a percentage of the skin entrance peak dose. As an example, an entrance peak dose of 100 Gy given to the 2 cm mouse head with 50 μm wide beams and a beam separation of 200 μm delivers a mean dose of 12.4 Gy to the lesion in the center of the head. As expected, the mean dose increases with decreasing c-t-c spacing and increasing microbeam width. A plot (not shown) of mean lesion dose versus the ratio of microbeam width to c-t-c spacing suggests an approximate linear relationship for a given phantom size, with the slope of the line for the 8 cm cat and 16 cm dog phantoms being roughly one-half and one-fourth, respectively, of the slope for the 2 cm mouse phantom. In the 2 cm mouse phantom, the skin, brain and lesion all receive similar mean doses for a particular microbeam width and spacing, while bone receives nearly double the dose. For the larger phantoms, the bone dose is still about double the dose to the soft tissue, but there is more variation between the skin, lesion and brain doses. The mean dose increases with the larger array size, by between 2.4 % and 12.7 % for the 8 cm cat phantom, and between 6.1 % and 24.5 % for the 16 cm dog phantom.

Table 6.4 Mean dose to skin, bone, brain and the lesion, and *percentage volume below 10 %* of the skin entrance dose for unidirectional irradiation.

Phantom	Array Size	Microbeam spacing (μm)	Beam width (μm)	Mean Dose to Bone (%)	Mean Dose to Skin (%)	Mean Dose to Lesion (%)	Mean Dose to Brain (%)	Volume Under 10% of Peak Entrance Dose (%)
2 cm Mouse Head	4x4 mm^2	100	25	28.59 ± 0.06	14.40 ± 0.03	15.10 ± 0.02	15.17 ± 0.02	59.29 ± 0.10
			50	47.45 ± 0.01	23.99 ± 0.06	24.77 ± 0.04	24.89 ± 0.04	25.37 ± 0.35
			75	66.10 ± 0.19	33.43 ± 0.10	34.32 ± 0.06	34.49 ± 0.06	2.41 ± 0.01
		200	25	14.15 ± 0.03	7.12 ± 0.02	7.47 ± 0.01	7.51 ± 0.01	78.29 ± 0.04
			50	23.68 ± 0.06	11.97 ± 0.03	12.36 ± 0.02	12.42 ± 0.02	65.26 ± 0.06
			75	33.34 ± 0.10	16.86 ± 0.05	17.32 ± 0.03	17.41 ± 0.03	52.64 ± 0.12
		400	25	6.84 ± 0.01	3.44 ± 0.01	3.61 ± 0.01	3.63 ± 0.01	87.08 ± 0.01
			50	11.47 ± 0.03	5.80 ± 0.01	5.99 ± 0.01	6.02 ± 0.01	80.95 ± 0.04
			75	16.19 ± 0.05	8.19 ± 0.02	8.42 ± 0.02	8.46 ± 0.02	75.10 ± 0.03
8 cm Cat Head	4x4 mm^2	100	25	20.24 ± 0.07	10.34 ± 0.03	8.04 ± 0.02	8.76 ± 0.02	69.52 ± 0.08
			50	33.22 ± 0.01	17.04 ± 0.07	13.04 ± 0.03	14.21 ± 0.04	41.25 ± 0.23
			75	45.78 ± 0.02	23.49 ± 0.01	17.89 ± 0.05	19.49 ± 0.06	12.11 ± 0.18
		200	25	10.09 ± 0.03	5.15 ± 0.02	4.01 ± 0.01	4.37 ± 0.01	85.39 ± 0.04
			50	16.76 ± 0.07	8.59 ± 0.04	6.58 ± 0.02	7.17 ± 0.02	72.55 ± 0.04
			75	23.43 ± 0.01	12.01 ± 0.06	9.16 ± 0.03	9.98 ± 0.03	59.86 ± 0.07
		400	25	4.90 ± 0.02	2.49 ± 0.01	1.943 ± 0.005	2.12 ± 0.00	93.02 ± 0.02
			50	8.17 ± 0.04	4.18 ± 0.02	3.21 ± 0.01	3.49 ± 0.01	86.92 ± 0.03
			75	11.48 ± 0.06	5.87 ± 0.03	4.48 ± 0.01	4.89 ± 0.02	80.90 ± 0.02
8 cm Cat Head	16x16 mm^2	100	25	22.02 ± 0.07	10.72 ± 0.03	8.57 ± 0.02	9.27 ± 0.02	67.03 ± 0.15
			50	35.33 ± 0.01	17.28 ± 0.07	13.61 ± 0.04	14.73 ± 0.04	30.34 ± 0.26

			75	47.76 ± 0.02	23.38 ± 0.01	18.32 ± 0.05	19.83 ± 0.06	6.20 ± 0.16
		200	25	11.33 ± 0.04	5.51 ± 0.02	4.39 ± 0.01	4.75 ± 0.01	84.51 ± 0.04
			50	18.56 ± 0.08	9.08 ± 0.04	7.12 ± 0.02	7.71 ± 0.02	70.66 ± 0.08
			75	23.43 ± 0.01	12.01 ± 0.06	9.82 ± 0.03	10.63 ± 0.03	56.50 ± 0.13
		400	25	4.90 ± 0.02	2.49 ± 0.01	2.19 ± 0.01	2.37 ± 0.01	92.48 ± 0.02
			50	9.42 ± 0.04	4.61 ± 0.02	3.60 ± 0.01	3.89 ± 0.01	85.88 ± 0.03
			75	13.17 ± 0.07	6.44 ± 0.03	5.01 ± 0.02	5.42 ± 0.02	79.33 ± 0.04
16 cm Dog Head	4x4 mm^2	100	25	17.04 ± 0.04	9.52 ± 0.02	3.76 ± 0.01	4.94 ± 0.01	80.43 ± 0.13
			50	27.86 ± 0.08	15.63 ± 0.05	6.08 ± 0.01	7.99 ± 0.02	61.26 ± 0.13
			75	38.25 ± 0.01	21.48 ± 0.07	8.30 ± 0.02	10.91 ± 0.03	40.83 ± 0.20
		200	25	8.52 ± 0.02	4.75 ± 0.01	1.877 ± 0.003	2.468 ± 0.004	90.58 ± 0.03
			50	14.12 ± 0.04	7.91 ± 0.02	3.08 ± 0.01	4.05 ± 0.01	81.57 ± 0.08
			75	19.70 ± 0.07	11.05 ± 0.04	4.27 ± 0.01	5.62 ± 0.01	72.52 ± 0.11
		400	25	4.14 ± 0.01	2.31 ± 0.01	0.912 ± 0.003	1.199 ± 0.002	95.51 ± 0.02
			50	6.90 ± 0.02	3.86 ± 0.01	1.50 ± 0.01	1.978 ± 0.004	91.19 ± 0.03
			75	9.69 ± 0.04	5.42 ± 0.02	2.10 ± 0.01	2.76 ± 0.01	86.91 ± 0.06
16 cm Dog Head	32x32 mm^2	100	25	19.55 ± 0.04	9.92 ± 0.02	4.26 ± 0.07	5.94 ± 0.01	78.35 ± 0.08
			50	30.84 ± 0.03	15.74 ± 0.04	6.66 ± 0.01	9.29 ± 0.02	52.57 ± 0.08
			75	40.96 ± 0.01	20.92 ± 0.06	8.81 ± 0.02	12.29 ± 0.02	32.85 ± 0.17
		200	25	10.24 ± 0.02	5.19 ± 0.01	2.230 ± 0.004	3.11 ± 0.01	89.86 ± 0.15
			50	16.63 ± 0.05	8.48 ± 0.03	3.59 ± 0.01	5.01 ± 0.01	79.75 ± 0.07
			75	22.75 ± 0.07	11.62 ± 0.04	4.89 ± 0.01	6.83 ± 0.01	69.11 ± 0.07
		400	25	5.30 ± 0.01	2.69 ± 0.01	1.135 ± 0.002	1.584 ± 0.003	95.06 ± 0.01
			50	8.60 ± 0.03	4.38 ± 0.01	1.854 ± 0.004	2.59 ± 0.01	90.30 ± 0.03
			75	11.93 ± 0.04	6.09 ± 0.02	2.56 ± 0.01	3.58 ± 0.01	85.52 ± 0.08

6.3.2.3 Percentage volume below threshold

The percentage of the volume (in the path of the microbeam array) that has a dose below a certain threshold—chosen arbitrarily as 10 % of the entrance skin dose—is reported in Table 6.4. With increasing c-t-c spacing and decreasing microbeam width (i.e. decreasing ratio of width/spacing), which corresponds to more pronounced spatial fractionation and a lower mean dose, the *percentage of the volume below the dose threshold* increases. Furthermore, since the dose threshold is defined with respect to the entrance dose, the *percentage volume below threshold* also increases with increasing phantom size, due to the larger irradiated volume being exposed to an increasingly attenuated beam: for the 2 cm mouse phantom the range of values for the different collimation configurations is 2.4–87.1 %, for the 8 cm cat phantom it is 6.2–93.0 % and for the largest 16 cm dog phantom it is 32.8–95.5 %. When the ratio of the microbeam width to c-t-c spacing is less than or equal to 0.25, the *percentage of the volume receiving less than the* 10 % *dose threshold* was at minimum 59 %, 67 % and 78 % in the 2 cm mouse, 8 cm cat and 16 cm dog phantoms, respectively. Treating with larger array sizes (for the same phantom) tends to decrease the value of this metric, but the magnitude of the effect is only appreciable for the widest microbeams and smallest spacings. In going from a $4 \times 4 mm^2$ to a $16 \times 16 mm^2$ array in the 8 cm cat phantom, a 49 % decrease from 12.1 % to 6.2 % is observed for the 75 μm width/100 μm spacing; however, for the seven collimation configurations where the width/spacing ratio is less than 0.5, the relative decrease is not more than 6 %. In general, extremely low values of the *percentage volume below threshold* are derived for the simulations performed with the 100 μm spacing: all values below 50 % (for unidirectional irradiations) were obtained with this spacing, and volumes below 15 % were observed with this spacing and the 75 μm wide beams in the 2 cm mouse and 8 cm cat phantoms. This low volume indicates a more uniform coverage of the volume, which is desirable for tumour control, but not for normal tissue sparing. When considering the entire brain, and not just the volume intersected by the path of the beam, the *percentage volume below this* 10 % *threshold* was above 95 % in the 2 cm mouse phantom, above 96 % in the 8 cm cat phantom and

above 97 % in the 16 cm dog phantom, with most geometries resulting in fractional volumes greater than 99 %.

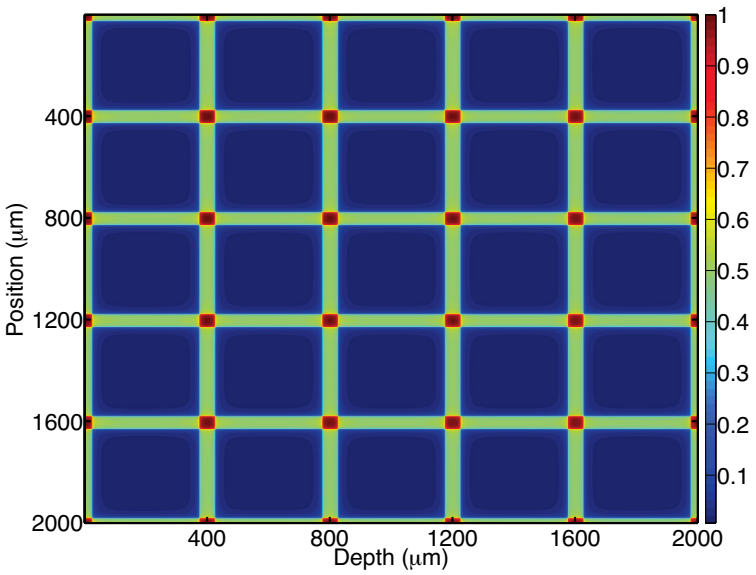

Figure 6.6 Dose distribution in a 2 mm × 2 mm cross-fired region of the 2 cm mouse head phantom for a microbeam width of 50 μm and a spacing of 400 μm c-t-c.

6.3.3 Dose volume metrics for cross-fired irradiation

An example of the simulated CF dose in the 2 cm mouse head phantom is depicted in Fig. 6.6. The percent peak depth dose curve through the 2 cm mouse phantom including a CF array along a microbeam path is shown in Fig. 6.7. The elevated dose in the center of the phantom (alternating with low doses) is due to the intersecting beams at the center of the phantom. The sharp dose profile is due to sampling the dose at only the midpoint of the peaks and valleys. The PVDR and PMVDR are listed in Table 6.5. The CF geometry causes the PVDR and PMVDR to be reduced by nearly half since the valley dose is approximately doubled, while the peak dose remains nearly the same, which is desirable for tumour control. The PVDR and PMVDR have a similar relationship as was discussed in Section 6.3.2.1, namely the PMVDR varies much more slowly than the PVDR with c-t-c spacing and beam width.

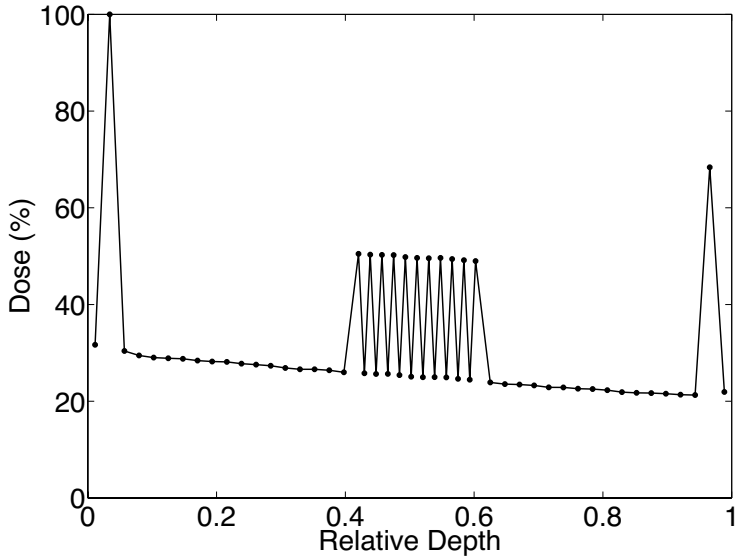

Figure 6.7 The percent depth dose curve for the cross-fired 2 cm mouse head phantom along a microbeam path (peak dose) for a microbeam width of 50 μm and a spacing of 400 μm c-t-c. The elevated dose in the center of the head phantom (which alternates with low dose) is due to the cross-fired array incident from an orthogonal direction.

The mean dose in the lesion (Table 6.5) increases by a factor of approximately 2 between the unidirectional and CF geometries. The error is not included in the table because it is less than 0.01 % for all cases. Higher mean doses occurred for increased microbeam widths and decreased microbeam spacing. This increase is clinically significant and could be enhanced even more by cross-firing from several angles. Figure 6.8 shows that adding a second CF array will enhance the dose at the center of a large animal head to a level that is much more comparable to the dose delivered unidirectionally in a small animal (mouse or rat) head, shown in the past to be biologically effective.[5,10] Adding a second orthogonal array also significantly decreases the *percentage volume less than* 10 % *of the entrance dose* in the lesion (Table 6.5) for certain geometries. The *percentage volume* was as low as 0 % for the widest beams and closest spacings, but nearly 90 % for the narrowest beams and widest spacings. The increase in mean dose and decrease in *volume below the threshold* are advantageous for tumour control since the intersection of the CF beams only occurs in the region of the tumour.

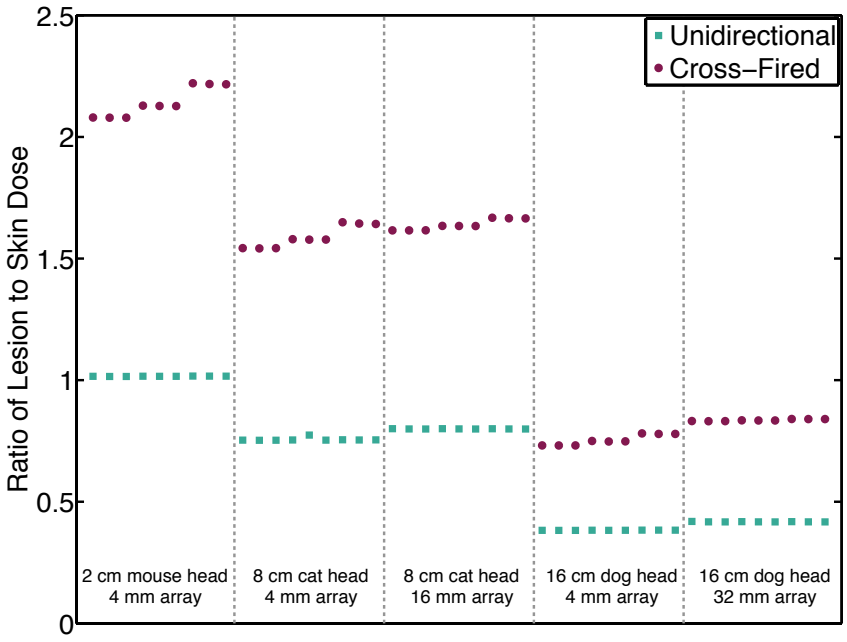

Figure 6.8 Ratio of lesion to skin mean dose for both unidirectional irradiation (squares) and for cross-fired irradiation (circles). The nine points for a given phantom/irradiation geometry each correspond to a c-t-c/beam width combination, and are plotted in the same sequence as presented in Table 6.4.

Table 6.5 PVDR, PMVDR, the mean dose to the lesion, and the *percentage volume of the lesion below 10 %* of the skin entrance dose are shown here for the cross-fired geometry.

Phantom	Cross-fired Array Size	Microbeam spacing (μm)	Beam width (μm)	PVDR	PMVDR	Mean Dose to Lesion (%)	Volume of Lesion Under 10% of Peak Entrance Dose (%)
2 cm Mouse Head	4x4x4 mm^3	100	25	10.67 ± 0.13	4.538 ± 0.009	30.94	18.04 ± 0.24
			50	5.47 ± 0.10	2.819 ± 0.009	50.74	0.00 ± 0.00
			75	3.14 ± 0.07	1.838 ± 0.010	70.30	0.00 ± 0.00
		200	25	40.60 ± 0.27	9.640 ± 0.011	15.67	63.06 ± 0.10
			50	21.13 ± 0.20	6.662 ± 0.010	25.90	38.38 ± 0.13
			75	13.64 ± 0.16	5.359 ± 0.010	36.28	18.28 ± 0.11
		400	25	115.66 ± 0.62	20.055 ± 0.014	7.89	81.71 ± 0.05
			50	62.45 ± 0.45	14.534 ± 0.013	13.07	68.81 ± 0.07
			75	43.07 ± 0.38	12.412 ± 0.012	18.36	57.40 ± 0.07
8 cm Cat Head	4x4x4 mm^3	100	25	10.35 ± 0.19	4.436 ± 0.013	16.48	43.01 ± 0.19
			50	5.35 ± 0.14	2.768 ± 0.013	26.72	6.38 ± 0.33
			75	3.13 ± 0.10	1.818 ± 0.014	36.65	0.00 ± 0.00
		200	25	36.13 ± 0.37	9.365 ± 0.016	8.40	71.24 ± 0.07
			50	19.08 ± 0.26	6.457 ± 0.014	13.78	49.53 ± 0.06
			75	12.46 ± 0.21	5.181 ± 0.014	19.18	31.75 ± 0.11
		400	25	97.20 ± 0.72	19.386 ± 0.020	4.25	85.35 ± 0.04
			50	52.96 ± 0.54	13.957 ± 0.017	6.99	73.49 ± 0.08
			75	36.46 ± 0.43	11.813 ± 0.016	9.76	62.34 ± 0.08
8 cm Cat Head	16x16x16 mm^3	100	25	7.07 ± 0.13	3.734 ± 0.011	17.63	33.83 ± 0.27

			50	3.92±0.09	2.399±0.010	28.00	0.00 ± 0.00
			75	2.51±0.08	1.667±0.012	37.71	0.00 ± 0.00
		200	25	18.73±0.20	7.504±0.012	9.13	69.68 ± 0.09
			50	10.29±0.15	5.070±0.011	14.81	45.53 ± 0.17
			75	7.10±0.12	4.016±0.010	20.41	22.74 ± 0.25
		400	25	42.65±0.35	15.127±0.016	4.65	85.00 ± 0.03
			50	23.38±0.26	10.397±0.013	7.61	72.67 ± 0.07
			75	16.31±0.22	8.419±0.011	10.59	61.27 ± 0.08
16 cm Dog Head	4x4x4 mm^3	100	25	10.17±0.21	4.360±0.016	7.19	54.34 ± 0.02
			50	5.30±0.17	2.736±0.016	11.63	22.12 ± 0.06
			75	3.01±0.12	1.796±0.017	15.88	3.26 ± 0.06
		200	25	34.13±0.44	9.182±0.037	3.68	75.58 ± 0.00
			50	17.90±0.32	6.350±0.017	6.02	54.63 ± 0.01
			75	11.77±0.26	5.089±0.017	8.36	37.08 ± 0.01
		400	25	93.63±0.86	18.980±0.025	1.86	87.36 ± 0.00
			50	51.70±0.64	13.687±0.021	3.06	75.63 ± 0.01
			75	35.00±0.52	11.559±0.020	4.27	64.75 ± 0.01
16 cm Dog Head	32x32x32 mm^3	100	25	5.73±0.12	3.329±0.012	8.51	51.93 ± 0.06
			50	3.35±0.10	2.190±0.012	13.29	15.51 ± 0.15
			75	2.27±0.08	1.578±0.014	17.58	0.05 ± 0.00
		200	25	13.50±0.18	6.473±0.013	4.47	75.11 ± 0.02
			50	7.67±0.14	4.371±0.011	7.19	53.71 ± 0.03
			75	5.43±0.12	3.466±0.011	9.80	35.55 ± 0.05
		400	25	28.95±0.30	12.797±0.017	2.29	87.34 ± 0.01
			50	16.03±0.22	8.656±0.013	3.74	75.46 ± 0.02
			75	11.32±0.19	6.900±0.011	5.17	64.49 ± 0.02

6.4 Discussion

This study stresses the relationships among absolute dimensions of, and doses to, targeted lesions and normal tissues proximal to those lesions at various depths in large and small animals—both in the paths of the microbeams and in between them. When considering the 4 × 4 mm^2 array of unidirectional irradiation, the PVDR ranges between 5 and 230 in the smallest phantom and between 5 and 186 in the largest phantom, with the largest values corresponding to collimation configurations with the narrowest beams and largest c-t-c spacings. The decrease in PVDR between the small 2 cm mouse and large 16 cm dog phantoms when using the 4 × 4 mm^2 array to treat small targets varies between 4 % and 19 %, with the effect of phantom size becoming more pronounced as c-t-c spacing increases. When larger targets (32 × 32 mm^2) are treated in the largest phantom, PVDR reductions of between 36 % and 74 % are calculated, depending on the collimation configuration. The decrease in PVDR with increasing array size is largest for larger phantoms (*i.e.* greater depths), narrower microbeams and larger spacings, with the c-t-c spacing again having the largest impact. These changes in the PVDR are primarily due to the increases in the valley dose between the microbeams. Since the valley dose is an important consideration for toxicity of the treatment,[10,12] any increase must be carefully controlled. Our PVDR results are consistent with previously published values, suggesting that the beam spectrum at the CLS is suitable for MRT research.

The PVDR has been useful in comparing MRT dose distributions, but is limited by its nature as a point dose metric. Since more detailed modeling/metrics are needed to accurately predict tumour control and normal tissue complications for MRT, a number of new dose-volume metrics have been studied in this work: the PMVDR, the mean dose and the *percentage volume below a dose threshold*. The PMVDR has the same general geometrical dependence as the PVDR (decreases with increasing microbeam width and decreasing microbeam spacing), but changes less rapidly with these parameters than the PVDR. Therefore, the PMVDR would predict a different relationship between MRT geometry and biological outcome. When cross- firing is introduced, both the PVDR and PMVDR are nearly halved, but display the same trends as seen for unidirectional

irradiation. The mean doses (calculated only including the tissue volume along the path of the microbeam array) in skin, brain and the central lesions are all very similar in the 2 cm mouse phantom, while the bone receives roughly double the dose to the soft tissue. One interesting possibility is that, in addition to pediatric brain tumors,[43] disease in bone (*e.g.* skull bone and vertebrae) may be an interesting potential primary target for MRT because of this high absorption and the extremely sharp lateral dose falloff that could be exploited to protect a sensitive organ such as the brain or spinal cord. An additional advantage in this case may be the increased relative biological effect in bone due to photoelectron-Auger cascades produced at the x-ray energies used for MRT.[44] As the size of the phantom increases, the dose to the soft tissues becomes less uniform, with the lesion dose being reduced relative to the skin and brain. For a 50 μm beam and 400 μm c-t-c spacing, the mean lesion and brain doses are 78 % and 93 %, respectively, of the mean skin dose for the 8 cm cat head phantom (16×16 mm^2 array), and 42 % and 72 % for the 16 cm dog head (32×32 mm^2 array). The reduction in mean lesion dose in the 16 cm dog phantom is thus considerable. However, the use of cross-firing arrays approximately doubles the mean dose to the lesion in the intersecting regions for the same mean skin dose, which may make irradiation of these larger animals feasible. The *percentage volume below 10 % of the peak entrance dose* to skin increased with increasing phantom size, increasing spacing, decreasing microbeam width and for smaller array sizes. Addition of a second orthogonal array led to the value of this metric in the lesion to as little as 0 % for some of the largest microbeam width/smallest c-t-c spacing combinations, which is advantageous for tumour control.

As mentioned in Section 6.2.1, in starting our simulations at the surface of the phantom, we did not incorporate the effects of source size, beam divergence, nor did we perform explicit modeling of the MRT collimator. Although many previous MRT Monte Carlo studies have used a similar simplified geometry, Nettelbeck *et al.* (2009)[40] and Martinez-Rovira *et al.* (2012)[45] have performed investigations with a more complete simulation geometry. The limitations of the simplified approach are highlighted by Nettelbeck *et al.* who showed that including beam divergence, a finite source size and the multi-slit collimator will all increase penumbral dose, and decrease the dose at the edges of a microbeam.[40] They also showed that including beam divergence will increase the

dose in the valley. These effects would be expected to change the absolute values of the dose-volume metrics, *e.g.* reducing the PVDR and PMVDR. Since the figures in Nettelbeck *et al.* suggest that beam divergence has the most profound impact on the shape of the microbeam profiles, we used the information in Fig. 3(b) of their work[40] to estimate the approximate change in our PVDR and PMVDR values that might result from incorporating a more complete geometric modeling in our simulations. This was done by using their plotted ratio of the doses with and without beam divergence as a function of lateral displacement from the center of a 50 μm wide microbeam to scale our dose profiles. Considering unidirectional irradiation in the 2 cm mouse and 16 cm dog heads, the PVDR was decreased between 0 % and 9 % between our original results and those including divergence, while the reduction in PMVDR was greater at between 5 % and 16 %, with the largest change of 16 % occurring for the smallest 100 μm c-t-c spacing and in the 2 cm mouse phantom. For CF irradiation in the 2 cm mouse head phantom, the impact of beam divergence was smaller, with a decrease of not more than 5 % in PVDR and not more than 8 % in PMVDR. These changes in the PVDR and PMVDR metrics, though not negligible, do suggest that the trends in the metrics we have attempted to elucidate in this study would not essentially change if a more complex modeling of the geometry would have been undertaken in the simulations.

The PMVDR, mean dose and *percentage volume below a given threshold* offer improvement over the PVDR because they progress from a point dose metric to a volumetric measure, which better considers the dose-volume relationship that MRT relies on. It still remains to be proven whether any of these metrics will offer improved prediction of clinical outcome with respect to a given MRT dose distribution. We hope to use future biological studies to correlate dose-volume metrics evaluated for a given MRT dose distribution to biological outcome to refine these metrics. Systematic studies are needed to determine the effect of individual parameters (*i.e.* microbeam width, microbeam spacing, peak dose, valley dose, *etc.*) on tissue toxicity and for reducing tumour size. We suggest that extensive cellular studies are done to determine the geometries and doses that would be most informative for the more complicated animal studies. The vascular response is certainly of importance for the biological effect of radiotherapy in general and for MRT in particular, but can of course only be studied *in*

vivo. A compilation and re-examination of existing animal data in terms of new metrics may also shed light on the best method of scoring MRT dose distributions. We hope that these studies can also further the understanding of the effects of inhomogeneous dose distributions on tumours and critical organs as applied to more conventional radiotherapy modalities.

6.5 References

[1] D.N. Slatkin, P. Spanne, F.A. Dilmanian, M. Sandborg, "Microbeam Radiation-Therapy," Med. Phys. **19**, 1395-1400 (1992).

[2] F.A. Dilmanian, G.M. Morris, N. Zhong, T. Bacarian, J.F. Hainfeld, J. Kalef-Ezra, L.J. Brewington, J. Tammam, E.M. Rosen, "Murine EMT-6 carcinoma: High therapeutic efficacy of microbeam radiation therapy," Radiat. Res. **159**, 632-641 (2003).

[3] J.C. Crosbie, R.L. Anderson, K. Rothkamm, C.M. Restall, L. Cann, S. Ruwanpura, S. Meachem, N. Yagi, I. Svalbe, R.A. Lewis, B.R.G. Williams, P.A.W. Rogers, "Tumor Cell Response to Synchrotron Microbeam Radiation Therapy Differs Markedly from Cells in Normal Tissues," International Journal of Radiation Oncology Biology Physics **77**, 886-894 (2010).

[4] A. Bouchet, B. Lemasson, G. Le Duc, C. Maisin, E. Brauer-Krisch, E.A. Siegbahn, L. Renaud, E. Khalil, C. Remy, C. Poillot, A. Bravin, J.A. Laissue, E.L. Barbier, R. Serduc, "Preferential Effect of Synchrotron Microbeam Radiation Therapy on Intracerebral 9L Gliosarcoma Vascular Networks," International Journal of Radiation Oncology Biology Physics **78**, 1503-1512 (2010).

[5] J.A. Laissue, G. Geiser, P.O. Spanne, F.A. Dilmanian, J.O. Gebbers, M. Geiser, X.Y. Wu, M.S. Makar, P.L. Micca, M.M. Nawrocky, D.D. Joel, D.N. Slatkin, "Neuropathology of ablation of rat gliosarcomas and contiguous brain tissues using a microplanar beam of synchrotron-wiggler-generated X rays," International Journal of Cancer **78**, 654-660 (1998).

[6] E. Brauer-Krisch, H. Requardt, P. Regnard, S. Corde, E. Siegbahn, G. LeDuc, T. Brochard, H. Blattmann, J. Laissue, A. Bravin, "New irradiation geometry for microbeam radiation therapy," Phys. Med. Biol. **50**, 3103-3111 (2005).

[7] F.A. Dilmanian, Z. Zhong, T. Bacarian, H. Benveniste, P. Romanelli, R.L. Wang, J. Welwart, T. Yuasa, E.M. Rosen, D.J. Anschel, "Interlaced x-ray microplanar beams: A radiosurgery approach with clinical potential," Proc. Natl. Acad. Sci. U. S. A. **103**, 9709-9714 (2006).

[8] R. Serduc, E. Braeuer-Krisch, E.A. Siegbahn, A. Bouchet, B. Pouyatos, R. Carron, N. Pannetier, L. Renaud, G. Berruyer, C. Nemoz, T. Brochard, C. Remy, E.L. Barbier, A. Bravin, G. Le Duc, A. Depaulis, F. Esteve, J.A. Laissue, "High-Precision Radiosurgical Dose Delivery by Interlaced Microbeam Arrays of High-Flux Low-Energy Synchrotron X-Rays," Plos One **5**, e9028 (2010).

[9] J.A. Laissue, H. Blattmann, M. Di Michiel, D.N. Slatkin, N. Lyubimova, R. Guzman, W. Zimmermann, S. Birrer, T. Bley, P. Kircher, R. Stettler, R. Fatzer, A. Jaggy, H.M. Smilowitz, E. Brauer, A. Bravin, G. Le Duc, C. Nemoz, M. Renier, W. Thomlinson, J. Stepanek, H.P. Wagner, "The weanling piglet cerebellum: a surrogate for tolerance to MRT (microbeam radiation therapy) in pediatric neuro-oncology," Penetrating Radiation Systems and Applications Iii **4508**, 65-73 (2001).

[10] F.A. Dilmanian, T.M. Button, G. Le Duc, N. Zhong, L.A. Pena, J.A.L. Smith, S.R. Martinez, T. Bacarian, J. Tammam, B. Ren, P.M. Farmer, J. Kalef-Ezra, P.L. Micca, M.M. Nawrocky, J.A. Niederer, F.P. Recksiek, A. Fuchs, E.M. Rosen, "Response of rat intracranial 9L gliosarcoma to microbeam radiation therapy," Neuro-oncology **4**, 26-38 (2002).

[11] B. van der Sanden, E. Braeuer-Krisch, E.A. Siegbahn, C. Ricard, J. Vial, J. Laissue, "Tolerance of Arteries to Microplanar X-Ray Beams," International Journal of Radiation Oncology Biology Physics **77**, 1545-1552 (2010).

[12] R. Serduc, A. Bouchet, E. Braeuer-Krisch, J.A. Laissue, J. Spiga, S. Sarun, A. Bravin, C. Fonta, L. Renaud, J. Boutonnat, E.A. Siegbahn, F. Esteve, G. Le Duc, "Synchrotron microbeam radiation therapy for rat brain tumor palliation-influence of the microbeam width at constant valley dose," Phys. Med. Biol. **54**, 6711-6724 (2009).

[13] D.N. Slatkin, P. Spanne, F.A. Dilmanian, J.O. Gebbers, J.A. Laissue, "Subacute Neuropathological Effects of Microplanar Beams of X-Rays from a Synchrotron Wiggler," Proc. Natl. Acad. Sci. U. S. A. **92**, 8783-8787 (1995).

[14] E. Braeuer-Krisch, R. Serduc, E.A. Siegbahn, G. Le Duc, Y. Prezado, A. Bravin, H. Blattmann, J.A. Laissue, "Effects of pulsed, spatially fractionated, microscopic synchrotron X-ray beams on normal and tumoral brain tissue," Mutat. Res. - Rev. Mut. Res. **704**, 160-166 (2010).

[15] M. Mohiuddin, D.L. Curtis, W.T. Grizos, L. Komarnicky, "Palliative Treatment of Advanced Cancer using Multiple Nonconfluent Pencil Beam Radiation - a Pilot-Study," Cancer **66**, 114-118 (1990).

[16] J.E. Reiff, M.S. Huq, M. Mohiuddin, N. Suntharalingam, "Dosimetric Properties of Megavoltage Grid Therapy," International Journal of Radiation Oncology Biology Physics **33**, 937-942 (1995).

[17] M. Mohiuddin, M. Fujita, W.F. Regine, A.S. Megooni, G.S. Ibbott, M.M. Ahmed, "High-dose spatially-fractionated radiation (GRID): A new paradigm in the management of advanced cancers," International Journal of Radiation Oncology Biology Physics **45**, 721-727 (1999).

[18] J.A. Penagaricano, E.G. Moros, V. Ratanatharathorn, Y. Yan, P. Corry, "Evaluation of Spatially Fractionated Radiotherapy (Grid) and Definitive Chemoradiotherapy with Curative Intent for Locally Advanced Squamous Cell Carcinoma of the Head and Neck: Initial Response Rates and Toxicity," International Journal of Radiation Oncology Biology Physics **76**, 1369-1375 (2010).

[19] F.A. Dilmanian, Y. Qu, L.E. Feinendegen, L.A. Pena, T. Bacarian, F.A. Henn, J. Kalef-Ezra, S. Liu, Z. Zhong, J.W. McDonald, "Tissue-sparing effect of x-ray microplanar beams particularly in the CNS: Is a bystander effect involved?" Exp. Hematol. **35**, 69-77 (2007).

[20] W.N. Rahman, R. Davidson, N. Yagi, M. Geso, I. Darby, "Influence of gold nanoparticles on radiation dose enhancement and cellular migration in microbeam-irradiated cells," BioNanoSci. **1**, 1-13 (2011).

[21] E.C. Mackonis, N. Suchowerska, M. Zhang, M. Ebert, D.R. McKenzie, M. Jackson, "Cellular response to modulated radiation fields," Phys. Med. Biol. **52**, 5469-5482 (2007).

[22] F.A. Dilmanian, G.M. Morris, G. Le Duc, X. Huang, B. Ren, T. Bacarian, J.C. Allen, J. Kalef-Ezra, I. Orion, E.M. Rosen, T. Sandhu, P. Sathe, X.Y. Wu, Z. Zhong, H.L. Shivaprasad, "Response of avian embryonic brain to spatially segmented X-ray microbeams," Cell Mol. Biol. **47**, 485-493 (2001).

[23] F. Salvat, J.M. Fernandez-Varea, J. Sempau, "PENELOPE-2008, a code system for Monte Carlo simulation of electron and photon transport," Issy-les-Moulineaux France, OECD NEA (2009).

[24] E.A. Siegbahn, J. Stepanek, E. Brauer-Krisch, A. Bravin, "Determination of dosimetrical quantities used in microbeam radiation therapy (MRT) with Monte Carlo simulations," Med. Phys. **33**, 3248-3259 (2006).

[25] Y. Prezado, G. Fois, G. Le Duc, A. Bravin, "Gadolinium dose enhancement studies in microbeam radiation therapy," Med. Phys. **36**, 3568-3574 (2009).

[26] J. Sempau, J.M. Fernandez-Varea, E. Acosta, F. Salvat, "Experimental benchmarks of the Monte Carlo code PENELOPE," Nuclear Instruments & Methods in Physics Research Section B-Beam Interactions with Materials and Atoms **207**, 107-123 (2003).

[27] J. Spiga, E.A. Siegbahn, E. Braeuer-Krisch, P. Randaccio, A. Bravin, "The GEANT4 toolkit for microdosimetry calculations: Application to microbeam radiation therapy (MRT)," Med. Phys. **34**, 4322-4330 (2007).

[28] M. de Felici, E.A. Siegbahn, J. Spiga, A.L. Hanson, R. Felici, C. Ferrero, A. Tartari, M. Gambaccini, J. Keyrilaeinen, E. Braeuer-Krisch, P. Randaccio, A. Bravin, "Monte Carlo code comparison of dose delivery prediction for Microbeam Radiation Therapy," International Workshop on Monte Carlo Techniques in Radiotherapy Delivery and Verification - Third McGill International Workshop **102**, 012005 (2008).

[29] E.A. Siegbahn, "Dosimetry for synchrotron x-ray microbeam radiation therapy," , 40-45 (2007).

[30] T. Tanaka and H. Kitamura, "SPECTRA: a synchrotron radiation calculation code," Journal of Synchrotron Radiation **8**, 1221-1228 (2001).

[31] National Institute of Standards and Technology, "ESTAR," http://physics.nist.gov/PhysRefData/Star/Text/ESTAR.html, Accessed 2012.

[32] R. Serduc, Y.V. de Looij, G. Francony, O. Verdonck, B. Van der Sanden, J. Laissue, R. Farion, E. Braeuer-Krisch, E.A. Siegbahn, A. Bravin, Y. Prezado, C. Segebarth, C. Remy, H. Lahrech, "Characterization and quantification of cerebral edema induced by synchrotron x-ray microbeam radiation therapy," Phys. Med. Biol. **53**, 1153-1166 (2008).

[33] D.S. Holder, "Detection of Cerebral-Ischemia in the Anesthetized Rat by Impedance Measurement with Scalp Electrodes - Implications for Noninvasive Imaging of Stroke by Electrical-Impedance Tomography," Clinical Physics and Physiological Measurement **13**, 63-75 (1992).

[34] L.A. Young, J.C. Dodge, K.J. Guest, J.L. Cline, W.W. Kerr, "Age, breed, sex and period effects on skin biophysical parameters for dogs fed canned dog food," J. Nutr. **132**, 1695S-1697S (2002).

[35] A. Gefen, N. Gefen, Q.L. Zhu, R. Raghupathi, S.S. Margulies, "Age-dependent changes in material properties of the brain and braincase of the rat," J. Neurotrauma **20**, 1163-1177 (2003).

[36] A. Diana, C. Guglielmini, F. Fracassi, M. Pietra, E. Balletti, M. Cipone, "Use of high-frequency ultrasonography for evaluation of skin thickness in relation to hydration status and fluid distribution at various cutaneous sites in dogs," Am. J. Vet. Res. **69**, 1148-1152 (2008).

[37] M.W. Slutzky, L.R. Jordan, T. Krieg, M. Chen, D.J. Mogul, L.E. Miller, "Optimal spacing of surface electrode arrays for brain-machine interface applications," Journal of Neural Engineering **7**, 026004 (2010).

[38] J. Spiga, Y. Prezado, E. Braeuer-Krisch, V. Fanti, P. Randaccio, A. Bravin, "The Effect of Beam Polarization in Microbeam Radiation Therapy (MRT): Monte Carlo Simulations Using Geant4," 2009 IEEE Nuclear Science Symposium Conference Record, Vols 1-5, 2170-2173 (2009).

[39] I. Martinez-Rovira and Y. Prezado, "Monte Carlo dose enhancement studies in microbeam radiation therapy," Med. Phys. **38**, 4430-4439 (2011).

[40] H. Nettelbeck, G.J. Takacs, M.L.F. Lerch, A.B. Rosenfeld, "Microbeam radiation therapy: A Monte Carlo study of the influence of the source, multislit collimator, and beam divergence on microbeams," Med. Phys. **36**, 447-456 (2009).

[41] A. Niemierko, "Reporting and analyzing dose distributions: A concept of equivalent uniform dose," Med. Phys. **24**, 103-110 (1997).

[42] I. Martinez-Rovira, J. Sempau, J.M. Fernandez-Varea, A. Bravin, Y. Prezado, "Monte Carlo dosimetry for forthcoming clinical trials in x-ray microbeam radiation therapy," Phys. Med. Biol. **55**, 4375-4388 (2010).

[43] J.A. Laissue, H. Blattmann, H.P. Wagner, M.A. Grotzer, D.N. Slatkin, "Prospects for microbeam radiation therapy of brain tumours in children to reduce neurological sequelae," Dev. Med. Child Neurol. **49**, 577-581 (2007).

[44] H. Nikjoo and L. Lindborg, "RBE of low energy electrons and photons," Phys. Med. Biol. **55**, R65-R109 (2010).

[45] I. Martinez-Rovira, J. Sempau, Y. Prezado, "Development and commissioning of a Monte Carlo photon beam model for the forthcoming clinical trials in microbeam radiation therapy," Med. Phys. **39**, 119-131 (2012).

7 HUMAN CELL CULTURE RESPONSE TO SYNCHROTRON-GENERATED MICROBEAMS USING γH2AX FLUORESCENCE

A version of this chapter has been published in two articles:

D. L. Anderson, R. Mirzayans, B. Andrais, E. A. Siegbahn, B. G. Fallone and B. Warkentin, "Spatial and temporal distribution of γH2AX fluorescence in human cell cultures following synchrotron-generated X-ray microbeams: lack of correlation between persistent γH2AX foci and apoptosis," J. Synch. Rad. ***21****, 801-810 (2014).*

D. Anderson, B. Andrais, R. Mirzayans, E. A. Siegbahn, B. G. Fallone and B. Warkentin, "Comparison of two methods for measuring γ-H2AX nuclear fluorescence as a marker of DNA damage in cultured human cells: applications for microbeam radiation therapy," J. Inst. ***8****, C06008 (2013).*

7.1 Introduction

The mechanisms underlying the biological responses to high-dose microbeams are complex and not yet fully understood. The results for an animal study by Crosbie *et al.* have suggested that the differential responses between normal (skin) and cancerous (mammary) tissues might reflect differences at cellular levels in terms of DNA double-strand break (DSB) repair and apoptotic cell death.[1] The γH2AX assay, a widely used biomarker of DSBs that are detected by the cell,[2-6] has been instrumental in measuring DNA damage after microbeam irradiation in various mammalian cell types both in vitro and in vivo.[1,7-9] Studies with different types of ionizing radiation (*e.g.*, ^{60}Co γ rays) have demonstrated that γH2AX foci detected at early times (~30 min) after irradiation almost exclusively reflect DSBs, whereas foci detected at late times (>24 h) post-irradiation are associated with different responses;[10,11] these include: (i) nuclear fragmentation which is a hallmark of cells undergoing apoptosis; and (ii) persistent DSBs in cells undergoing "permanent" growth arrest which resembles replicative senescence.

In this chapter we describe our semi-automated method of quantifying γH2AX fluorescence within cell nuclei after irradiation, and use this method to assess the responses triggered by high-dose synchrotron microbeam irradiations of varying geometry in cultured normal human fibroblasts and malignant glioma cells (hereafter NHFs and MGCs, respectively). The method of analyzing γH2AX immunofluorescence

images was evaluated using NHFs uniformly irradiated with gamma radiation from a ^{60}Co irradiator at the Cross Cancer Institute in Edmonton. The experiments to assess the response of NHFs and MGCs to microbeam irradiations were conducted on the Biomedical Imaging and Therapy (BMIT) 05B1-1 beamline at the Canadian Light Source (CLS). Our studies employed immunofluorescence assays that could be performed with methanol-fixed samples to facilitate processing and microscopic evaluation at our laboratory in Edmonton. The γH2AX immunofluorescence assay coupled with nuclear counterstaining with DAPI (4′,6-diamidino-2-phenylindole) was used to measure DNA damage and morphological changes associated with apoptotic cell death (*i.e.* nuclear fragmentation) as a function of time after irradiation and beam geometry. Our results provide new insights into microbeam-triggered γH2AX formation, rates of γH2AX clearance and biological outcome (lethality versus growth arrest) in cultured human cells.

7.2 Background

7.2.1 DNA structure and double stand breaks

Deoxyribonucleic acid (DNA) is a double stranded molecule. Each strand consists of a sugar-phosphate backbone, and a series of bases attached to the sugar (deoxyribose). There are four possible bases: adenine, cytosine, thymine and guanine. The order of these bases determines the genetic code. The complementary strands are held together by hydrogen bonding between complementary bases (adenine pairs with thymine, and cytosine pairs with guanine). The two strands are coiled in a double helix. This double helix is packaged with proteins to reduce its length and form chromatin. The double helix is wound around an octamer of proteins called histones. Each octamer contains two molecules each of histones H2A, H2B, H3 and H4.[3] The DNA wraps around the histones 1.7 times to form a nucleosome to give the appearance of beads on a string.[3] Higher order structuring continues to pack the DNA more compactly.[12]

Damage to DNA is the principal cause of the biological effects of ionizing radiation. Ionizing radiation can cause damage to DNA through direct action, when the atoms of DNA itself are ionized or excited. Alternatively, DNA can be damaged through

indirect action. In this case, ionizing radiation interacts with another atom or molecule within the cell to form a free radical (an atom or molecule with an unpaired electron in its outer shell), and that free radical diffuses toward and damages DNA.[12] Approximately two-thirds of x-ray damage to DNA in human cells is caused by the hydroxyl radical (OH·), which is created after radiation interacts with a water molecule.[12]

Ionizing radiation can produce many types of damage to DNA: base damage, sugar damage, single strand breaks (SSBs), DNA-protein crosslinks, DNA-DNA crosslinks, and double strand breaks (DSBs). A dose of ~ 1 – 2 Gy to mammalian cells results in approximately 1000 base damages, 1000 SSBs and 40 DSBs.[12] SSBs can be rapidly repaired by using the undamaged complementary strand as a template.[12] DSBs can lead to cell killing, growth arrest, mutation and/or carcinogenesis if not repaired properly.[12]

7.2.2 Double strand break signaling and repair

Many DNA lesions are produced every day as a result of replication errors, chemical decay of the bases, interactions with reactive oxygen species, or exposure to ionizing radiation.[12] Cells have developed specific pathways to repair the various types of damage (Fig. 7.1).[12] A cell recognizes DNA DSBs via sensor proteins. Transducer proteins are then recruited to the lesion. These transducers may play a role in gathering DNA repair molecules and/or relay signals to effector proteins. Ataxia telangiectasia mutated (ATM) is a protein kinase, and is an important transducer in the DNA damage response.[11] ATM is involved in signalling to the DNA repair molecules, molecules involved cell death and growth arrest, as well as activating cell cycle checkpoints.[12] ATM transmits these signals through the phosphorylation of different targets (*e.g.* p53, checkpoint kinase 2 (CHK2), and H2AX, an H2A histone variant[11]). Other protein kinases similar to ATM are also involved in signalling following DNA damage.[11,12] The molecules phosphorylated by the transducer proteins are referred to as effector proteins, and they are responsible for various responses, including DNA repair processes, activation of cell cycle checkpoints, apoptosis, and growth arrest (senescence) (Fig. 7.1).

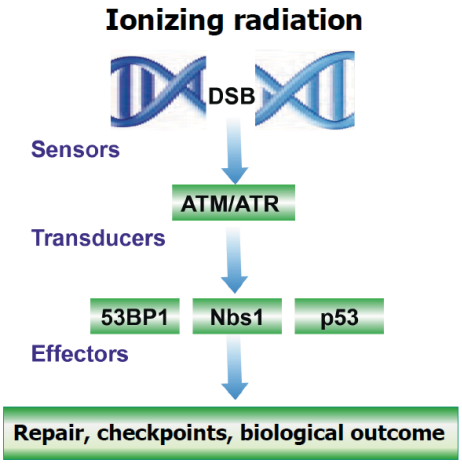

Figure 7.1 The DNA damage response signalling induced by ionizing radiation. DSBs are first detected by sensors that recognize the DNA lesion itself or chromatin alterations caused by DSBs. Next, transducers (*e.g.*, ATM) are recruited to the damage site and convey the DSB signal to the effectors. Effector proteins (*e.g.*, p53) then activate DNA repair mechanisms and cell cycle checkpoints to facilitate repair. DNA lesions that are left unrepaired or are not repaired properly may lead to biological changes such as apoptosis, growth arrest, mutagenesis and malignant transformation.

After the DSBs are detected and repair factors are recruited to the damaged sites in the genome (*e.g.*, by γH2AX foci; see below), their repair is carried out by two well-studied mechanisms: nonhomologous end-joining (NHEJ) and homologous recombination repair (HRR). The NHEJ pathway occurs predominantly in the G1 phase of the cell cycle, when there is only one copy of the cell's DNA, and thus no template for DSB repair.[12] In this pathway, the ends of the DNA breaks are linked together with minimal processing. NHEJ is fast, but error prone.[12] In HRR, the undamaged homologous chromosome serves as a template for repair, and thus occurs predominantly in the late S phase and G2 phase of the cell cycle.[12] The more complex HRR is an error-free process.[12]

7.2.3 The role of H2AX in the cell's DNA damage response

As mentioned above, the phosphorylation of the H2A histone variant H2AX on Ser139 by ATM or other phosphoinositide 3-kinase-related protein kinases (PIKKs) is an

important early event in the response of a cell to ionizing radiation and other genotoxic events that cause DSBs (Fig. 7.2).[2,3,11,13,14] H2A makes up ~ 2 – 20 % of the H2A histones in human cells, depending on cell type.[3,13,15] After phosphorylation, the histone is referred to as a γH2AX. Hundreds or thousands of H2AX on either side of a DSB are phosphorylated and create γH2AX foci; each focus corresponds to about 2 million base pairs in the DNA.[2,3] The phosphorylation of H2AX in response to DNA damage plays many roles in the cellular response. The extensive phosphorylation over a large portion of chromatin around a DSB acts as an amplification of the original DNA damage signal.[14,15] The γH2AX foci are thought to serve as scaffolding for the sustained recruitment of factors involved in DNA repair, including p21,[16] and thus promote DSB repair.[3,14,17] There is also evidence that γH2AX is involved in the physical remodelling of chromatin around a DSB to maintain close proximity of the two broken strands, and thus facilitate end joining, and concentrate repair factors at the lesion.[3,14] If H2AX is absent from mice cells, the cells show an increase in radiosensitivity and decrease in their ability to repair DSBs.[15] Other functions of the phosphorylated H2AX involve the G2 cell cycle checkpoint, recruitment of repair factors in HRR, and to act as a chromatin anchor.[15]

Following repair of DSBs, the DNA damage response must be reset to the constitutive (pre-irradiation) state to allow the cell to re-enter the cell cycle. After the initial exposure to ionizing radiation, γH2AX foci gradually disappear as a function of time post-irradiation. Dephosphorylation of γH2AX via phosphatases and removal of γH2AX from the chromatin have been reported to contribute to foci clearance.[13,17] The principal phosphatase that dephosphorylates γH2AX in response to ionization radiation is WIP1 (wild-type p53-induced phosphatase 1), which functions downstream in the ATM-p53 signaling (Fig. 7.2).[17,18] In addition to γH2AX, WIP1 dephosphorylates other DNA damage response factors (*e.g.*, ATM, Chk1, Chk2, p53), and thus contributes to the "deactivation" of the DNA damage response machinery.[17]

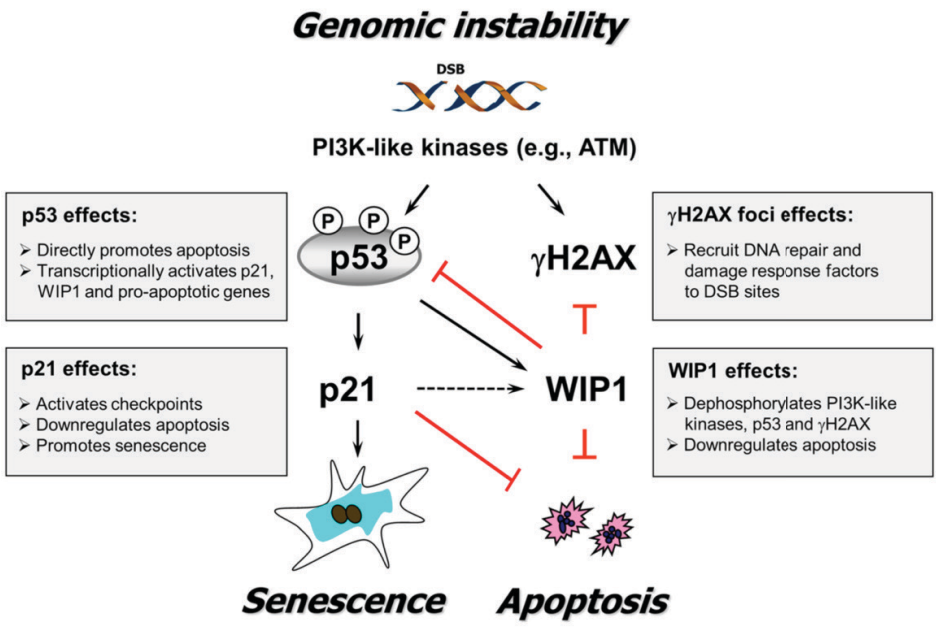

Figure 7.2 A model of the DNA damage response to genotoxic stress (e.g., radiation-induced DSBs) showing the relationships between certain proteins involved in DNA damage response (p53, γH2AX, p21, WIP1) and biological outcomes. Black arrows indicate stimulation, and red T-shaped lines indicate inhibition. Reproduced from Mirzayans *et al.* (2015) with author permission.[10]

7.2.4 γH2AX detection and quantification

The detection of γH2AX foci is possible through the use of a γH2AX-specific antibody and immunostaining techniques. A fluorescence tag can be applied, and the individual foci (composed of hundreds or thousands of γH2AX histones) visualized using immunofluorescence microscopy.[2] Alternatively, the total fluorescence in the cell can be measured using flow cytometry.[15] At early times after DNA damage, there is evidence that γH2AX foci are associated with DSBs with nearly a one-to-one ratio.[2,13,15,19] This method of DNA DSB identification offers orders of magnitude of improvement in sensitivity over alternative methods - a single γH2AX focus (thought to correspond to a single DSB) can be visualized.[15] Other useful features of γH2AX as a method of measuring DNA damage include *in situ* detection, relatively straight-forward quantification, physical localization of the DSBs, and a relatively large dynamic range.[15] Due to these characteristics, the quantification of γH2AX foci through immunostaining has become a widely used marker of DSBs that are detected by the cell.[2-6]

There are approximately 20 – 40 DSBs per cell per Gy of x-rays, and the DSB count increases linearly with dose.[15] A similar linearity in the number of γH2AX foci with dose has been observed over a limited dose range.[15,20] Neumaier *et al.* detected a higher rate of foci appearance per Gy with lower doses.[21] The lowest dose at which foci are detectable depends on the background foci level, which in turn depends on the cell type.[20] The maximum dose at which individual foci can be scored is limited because the foci eventually overlap and cannot be discriminated. After exposure to ionizing radiation, γH2AX foci can be detected within minutes after irradiation.[13,15] The number of phosphorylated H2AX increases with time until a plateau is reached at approximately 10 – 30 min after exposure.[2,13] The foci are initially small, grow with time and intensity after irradiation, and eventually stabilize.[2,15] More persistent breaks lead to larger γH2AX foci and a higher concentration of repair factors.[2] Additionally, higher doses result in more intense γH2AX foci that form faster than foci at lower doses.[21]

The presence of DNA DSBs falls off exponentially with time following their creation.[21] The clearance of γH2AX foci with time is associated with DSB rejoining.[15] The number of foci decrease rapidly to about 50% of the initial level within 1 hour, followed by a slower decline.[15] Rothkamm and Löbrich reported that in both repair-proficient (MRC-5) and repair-deficient (180BR) human skin fibroblast cultures, the loss of foci closely resembles the kinetics of DSB rejoining, suggesting that the rate of γH2AX clearance is similar (if not identical) to the rate of DSB rejoining.[20] Other studies do not support this notion. Suzuki *et al.*, for example, demonstrated that the rate of γH2AX clearance in normal fibroblasts is much slower than the rate of DSB rejoining.[22] It is now understood that the rate of γH2AX clearance post-irradiation depends not only on the rate of DSB rejoining, but also the status of the WIP1 and probably other phosphatases.[10,11]

The γH2AX assay offers a number of useful features, as described above. However, the conventional method of evaluation of γH2AX stained cells by manual counting of the nuclear foci is limited by two important factors. First, the analysis is extremely tedious, time consuming, and operator dependent, which limits the throughput of a large number of samples. Second, exposure to radiation doses greater than ~ 1 Gy results in a high degree of overlap between the majority of γH2AX foci,[23] thus severely

hampering the enumeration of individual foci. This limits the measurement of γH2AX foci to estimate the initial yield of DSBs at early times after irradiation (0.5 h) to relatively low doses (< 5 Gy).[20,23-27] An alternative approach, the scoring of total fluorescence as opposed to individual foci, has advantages. This quantification is much faster than foci counting, and although it is less sensitive than counting individual foci, it is approximately linear with dose till ~ 100 Gy.[20] There have been studies indicating that there is a linearity between foci count and total fluorescence as measured through flow cytometry.[28,29] However, others claim the total fluorescence change lags behind changes in foci numbers, which is most strongly linked to the change in individual foci intensity with time.[15] Additionally, the quantification of total phosphorylation versus individual foci will not differentiate between γH2AX foci caused by DSBs, versus γH2AX fluorescence initiated by other sources.

7.2.5 Radiation-induced cell death and growth arrest mechanisms

There are several types of cell death mechanisms that contribute to the loss of clonogenic survival following exposure to ionizing radiation (*i.e.*, failure of a single cell to multiply several times to form a colony of at least 50 cells within approximately two weeks post-irradiation). Apoptosis and necrosis are the most extensively studied death mechanisms. Apoptosis is a genetically-regulated response which can be identified through a series of morphologic changes: the cells round up and detach from their neighbours; the chromatin condenses and the nuclear envelope fragments; and the cell shrinks further and breaks apart into nuclear-bound fragments called apoptotic bodies (Fig. 7.3).[12,30] Apoptosis can be initiated through either the intrinsic (mitochondrial) or extrinsic (receptors on cell membrane surface) pathway, but both involve the activation of caspases.[12,30] Necrosis, on the other hand, is a passive mode (not genetically regulated) of cell death that most commonly occurs after high doses of ionizing radiation (although a genetically controlled type of necrosis has been identified[31]). It involves cell swelling, disintegration of organelles and the cell membrane, random fragmentation of the DNA, protein denaturation and release of cytoxic materials.[32]

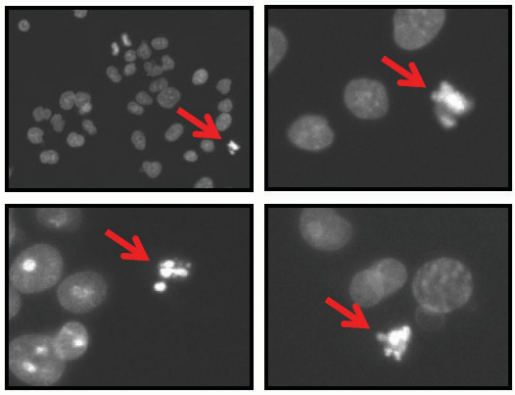

Figure 7.3 Representative images of DAPI-stained cancer cells exposed to ionizing radiation (4 Gy) and incubated for 48 h. Arrows mark some of the small subset of cells with apoptotic morphology. The top two panels are the same image at different magnifications. Reproduced from Mirzayans *et al.* (2015) with author permission.[10]

As extensively reviewed by Mirzayans *et al.*,[11,33] in some cell types, including human skin fibroblasts and solid cancer-derived cells, the primary response triggered by moderate (clinically relevant) doses of ionizing radiation and other cancer therapeutic agents is growth arrest (which would incorrectly be assumed to reflect "death" in the clonogenic assay) and not lethality. The tumour suppressor proteins p53, $p21^{WAF1}$ (p21) and $p16^{INK4a}$ (p16) play important roles in suppressing death and triggering stress-induced premature senescence (SIPS) in some cell types such as skin fibroblasts and epithelial cells within solid cancers.[11,30,33] Radiation-induced growth arrest in p53 wild-type cells is due to p53-mediated upregulation of p21, which blocks apoptosis and induces SIPS (Fig. 7.2); this response is often reversible and contributes to cancer recurrence through a process called induced endopolyploidy-stemness.[30] The growth arrest in p53-deficient but p16-proficient cells is due to upregulation of p16 which, like p21, also suppresses apoptosis and induces SIPS.[30] The growth arrest in cells that do not upregulate p21 and p16 is due to multinucleation which is proven to be reversible and to contribute to cancer recurrence through the endopolyploidy-stemness process.[30,34] In this process, multinucleated giant cells ultimately give rise to rapidly growth progeny which have stem cell-like properties (*i.e.*, rapidly repopulate the tumour).[34,35]

In short, it is now well established that growth arrested cancer cells that do not form macroscopic colonies (each colony containing at least 50 cells) in response to

moderate doses of ionizing radiation (<10 Gy) are not necessarily dead, and have the ability to give rise to stem cell-like progeny, and hence, contribute to radiotherapy failure. This raises an intriguing question as to whether irradiation with very high radiation doses that can be achieved by synchrotron radiation can promote cancer death (*e.g.*, through apoptosis), or would still trigger growth arrest. The results reported in this chapter support the latter response for the cell types under study.

7.3 Materials and methods

7.3.1 Cells and culture conditions

The GM10 normal human fibroblast strain and the p53 wild-type A172 malignant glioma cell line were cultured as monolayers in DMEM/F12 medium supplemented with 10% (vol/vol) fetal bovine serum, 1 mML-glutamine, 100 IU/ml penicillin G, and 100 mg/ml streptomycin sulphate in a humidified incubator under standard conditions (37 °C, 5% CO_2). For experiments, cells were plated in 150 mm tissue culture dishes (2×10^6 cells/30 ml medium/dish) containing 25 × 75 mm sterile microscope slides, and then incubated for two days; under these conditions, cultures of both cell types reached 95–100% confluency (*i.e.*, the proportion of surface covered by cells) prior to irradiation. For the samples to be irradiated at the CLS, the slides were placed in 50 ml tubes filled with fresh growth medium; the tubes were tightly sealed and then transported between a cell culture laboratory at the University of Saskatchewan and the CLS.

7.3.2 X-ray source and irradiation conditions

For the experiments used to compare the two methods of quantifying γH2AX measurement, cell cultures were uniformly irradiated at room temperature. These cultures were irradiated with ^{60}Co gamma-rays in a Gammacell 220 unit at a dose rate of approximately 2.5 Gy/minute. The cells were returned to the incubator immediately following irradiations. After 30 minutes of incubation, the cells were washed with

phosphate-buffered saline (PBS) and then fixed and stored in methanol at -20 °C prior to immunostaining.

A series of cell cultures were also irradiated using microbeam arrays of synchrotron x-rays. These experiments were performed on the 05B1-1 beamline (Section 2.6.1) at the CLS (Section 2.5). The beam was filtered by 0.934 mm Cu to produce a beam with a mean energy of 54 keV and a full width at half-maximum (FWHM) of 23.5 keV, as predicted by the SPECTRA software.[36] The beam profile, theoretical energy spectrum, and penetrability in water are presented in Sections 3.3.6, 3.3.9 and 3.3.3, respectively.[36]

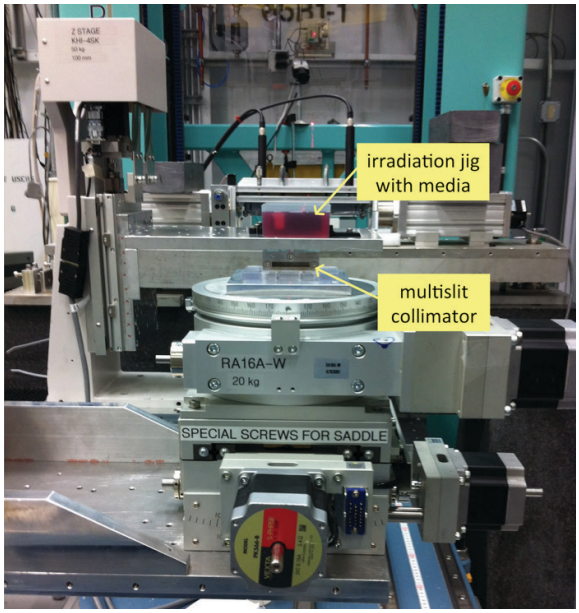

Figure 7.4 A beam's eye view of the experimental set-up showing the collimator that produced the microbeam array and, 1 m downstream, the media-filled irradiation jig containing a sample. Using motorized stages, the collimator and jig are centred in the beam before irradiation.

The cell samples, each on an individual microscope slide, were placed in a media-filled jig that ensured consistent placement of each sample during irradiation (Fig. 7.4). The medium in the jig was changed approximately every 8 h. The samples were positioned 26 m from the source, and 1 m from the multi-slit collimator (MSC). Samples were irradiated with doses of 1.4, 14, 71 or 283 Gy in the microbeam path. In addition, three conditions for the non-irradiated controls were investigated: samples that remained in the incubator until fixation; samples that were transported in tubes to the CLS and back

to the incubator before fixation; and samples that were transported to the CLS and placed in the irradiation jig containing irradiated medium (but were not themselves exposed to x-rays) then subsequently transported back to the incubator. Three beam geometries were considered: (i) an array of 75 microbeams with a centre-to-centre spacing of 400 μm, and each measuring 4 mm tall and 50 μm wide; (ii) single microbeams with a height of 4 mm and widths of 60, 100 or 570 μm; and (iii) a broad beam that was 4 mm vertically and 32 mm horizontally. The microbeam array was created using the 8 mm-thick tungsten MSC (Usinage & Nouvelles Technologies, Moubier, France), while the single microbeams were created using in-house vertical slits, and the broad beam shape was defined by the beamline jaws. Cells were incubated for periods of between 0.5 and 72 h post-irradiation to consider the time evolution of damage.

Following irradiation, for all but the earliest time point of 0.5 h, the samples were returned to their media-filled tubes and transported back to the cell culture laboratory for incubation for their prescribed incubation times. The 0.5 h samples were incubated in medium at room temperature without being returned to the incubator due to time restrictions. At the appropriate time following irradiation, samples were rinsed with PBS and fixed in methanol; slides were stored in 100% methanol at -20 °C. Pilot experiments with ^{60}Co-irradiated cultures demonstrated that storing cells in methanol for several weeks post-irradiation does not influence the quality of γH2AX immunostaining.

7.3.3 γH2AX immunostaining and fluorescence imaging

The γH2AX immunostaining procedure was carried out using well-established techniques that have been published previously.[4] The fixed cells (on microscope slides) were rinsed with PBS then incubated for 45 min with a blocking solution consisting of PBS containing 5% non-fat dry Carnation milk. Subsequently they were incubated with mouse anti-γH2AX antibody (anti-phospho-histone H2AX, Ser139, clone JBW301; Millipore, Billerica, MA, USA) for 1 h. The cells underwent 3 × 10 min washes with PBS containing 0.1% (vol/vol) Tween-20, followed by 60 min incubation with AlexaFluor 488 goat anti-mouse IgG (Life Technologies, Carlsbad, CA, USA). Antibodies were diluted (1:100 for γH2AX and 1:250 for AlexaFluor 488) in PBS

containing 5% non-fat dry milk. Slides were incubated with 170 mL of each antibody on parafilm for 1 h at room temperature in a humidified dark environment. Following incubation with the AlexaFluor 488 antibody, the slides were washed for 2 × 10 min with PBS-Tween-20 and finally 1 × 10min in PBS. DAPI counterstaining was performed to identify the location of the cells' nuclei and to visualize nuclear morphology. To this end, fixed cells on slides were overlaid with a mounting solution (90% glycerol in PBS) containing DAPI (50 mg ml^{-1}), covered with coverslips, and kept in the dark at 4 °C.

Fluorescence microscopy of the immunostained samples was performed using a Zeiss Axioplan 2 microscope (Zeiss, Jena, Germany) in conjunction with an X-Cite 120 PC fluorescent lamp (EXFO, Quebec, QC, Canada) and suitable filters. A Photometrics CoolSnap HQ CCD camera (Photometrics, Tuscon, AZ, USA) and Metamorph software (version 7.7.7.0; Molecular Devices Corporation, Sunnyvale, CA, USA) were used to capture the immunofluorescence images. Two sets of images were taken over any given region of interest: (i) a γH2AX image with a 450 – 490 nm band filter (100 or 600 ms exposure); and (ii) a DAPI image with a band filter of 350 – 400 nm (20 – 50 ms exposure). The resultant images have pixel sizes of either 0.64 μm × 0.64 μm or 0.32 μm × 0.32 μm achieved by using a 10X or 20X objective lens, respectively.

7.3.4 Image analysis

Two methods were used to quantify the γH2AX signal from the acquired fluorescent microscopic images of the uniformly irradiated NHFs. The manual analysis included first processing of the images in Photoshop to optimize the visualization of foci. Examples of inverted grayscale images used for manual analysis are shown in Fig. 7.5. The red, solid circles were placed manually to mark individual foci. The automated analysis was performed using in-house software code developed in the MATLAB (MathWorks, Natick, MA, USA) programming environment. First, DAPI images were used to create a binary mask. This mask was applied to the γH2AX images to isolate the signal in the nuclei from the background signal outside the nuclei. The γH2AX signal within the nuclei was averaged and normalized by the area of nuclear material (number of pixels) contributing to the signal. The average background signal throughout the rest of

the images was also measured and was subtracted from the mean nuclear signal. At least 200 cells (on duplicate slides) were evaluated for each treatment condition for both methods of analysis.

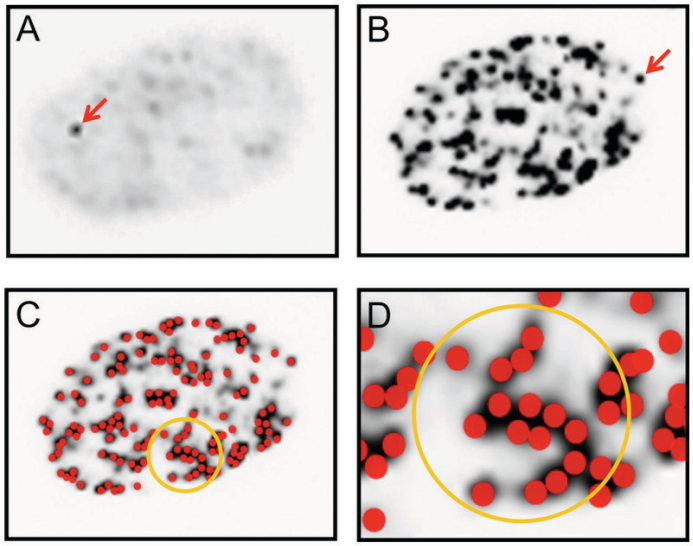

Figure 7.5 Representative immunofluorescence images used for manual foci counting. A: nucleus of a sham-irradiated (0 Gy) NHF. B-D: Nucleus of a fibroblast that was exposed to 10 Gy and incubated for 30 minutes. Arrows show individual γH2AX foci. The red, solid circles in the lower images were placed manually to mark individual foci.

A similar MATLAB code was used for the semi-automatic analysis of the microbeam irradiated samples. The code used both DAPI and γH2AX fluorescence images to map fluorescence intensity as a function of lateral position (orthogonal to the beam's propagation and to the vertical height of the microbeams). The DAPI images were used to create a binary mask of the DNA material in the image. The mask was applied to the γH2AX images to separate the fluorescence signal in the nuclei from the background signal outside the nuclei. The γH2AX fluorescence was integrated in the vertical direction over a portion of the microbeam's height (67 μm) and normalized by the amount of nuclear material in each of these vertical regions. This produced a profile that was fit to a Gaussian curve[37] to determine the mean intensity in the peak (within the microbeam path), the mean intensity in the valley (between two microbeams) and the FWHM of the peak region (*e.g.*, Fig. 7.6). In some γH2AX images at late times after irradiation, the peak and valley regions could not be identified automatically by the

software. In these situations the peak and valleys were identified by manual inspection of the image; if still not distinguishable, the fluorescence intensities for both peak and valley regions were taken as the mean intensity of the image.

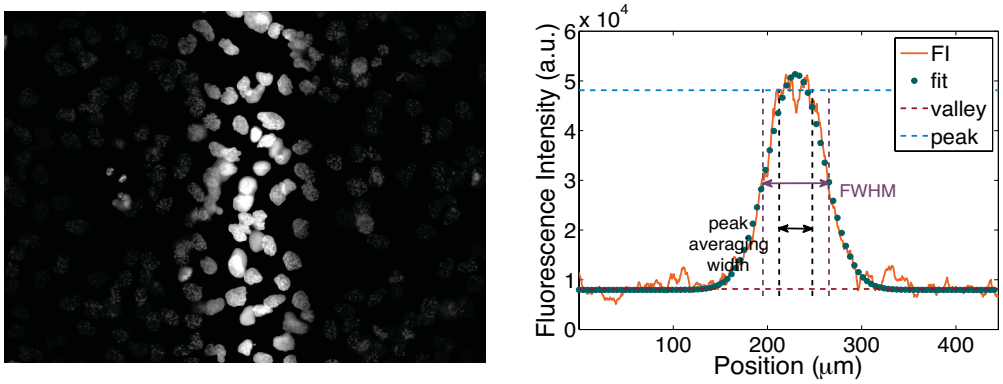

Figure 7.6 The γH2AX image of MGCs following irradiation with a 283 Gy microbeam array (left) and the results from the automated quantification of fluorescence intensity with peak position (right). The plotted results show the normalized raw fluorescence intensity (FI), the Gaussian fit, the mean peak intensity, the mean valley intensity, and the FWHM and the region over which the peak intensity is measured.

Only the automated analysis (supplemented via manual inspection when necessary) was used to extract spatial patterns of γH2AX distributions from the large number of slides irradiated. Each datum point reported herein represents the mean and standard deviation of 15–50 measurements. In addition, high-resolution DAPI images were inspected manually to assess apoptotic morphology (*i.e.*, nuclear condensation and/or fragmentation).

7.3.5 Monte Carlo and experimental dosimetry

The dose rate of the open synchrotron x-ray beam in air was determined using a Capintec PR06C ionization chamber to be 1.9 Gy/s in air at the maximum storage ring current (250 mA) as described in Chapter 5. The Monte Carlo package PENELOPE[38] was used to estimate the decrease in dose rate when moving from the open beam to a 50 μm-wide microbeam, and to simulate the dose distribution delivered by a microbeam array in a water phantom. The energy spectrum was calculated using the SPECTRA software[36]

(Section 3.3.6) and the characteristics of the CLS storage ring and BMIT 05B1-1 beamline described in Sections 2.5 and 2.6. Monte Carlo simulations were performed as described in Section 6.2.1 with a single 50 μm-wide 4 mm-tall x-ray microbeam perpendicularly incident on a water phantom having dimensions of 10.7 cm × 4.8 cm × 12.9 cm, matching those of the medium-filled irradiation jig. The dose distribution was calculated using 10^8 histories; a spatial resolution in the depth direction of 1 mm; and a varying lateral resolution that was 1 μm inside and close to the microbeam, and increased with distance from the microbeam.

7.4 Results

7.4.1 Comparison of quantification methods

Figures 7.5 and 7.7 show representative fluorescence-microscopy images for NHFs before and 30 minutes after exposure to ionizing radiation. The dose-response increase in the number of foci per nucleus is clearly visible (Fig. 7.7). Using our manual method of counting foci, we are able to assess DNA damage up to 10 Gy (Fig. 7.8A). This is a significantly higher dose than reported in previously published approaches for counting γH2AX foci.[20,23-27] Nevertheless, it is apparent in Fig. 7.7 that at 20 Gy, the clustering of foci becomes very dense, making it difficult to distinguish individual foci and thus to count the foci reliably. For this reason, we report quantitative values for the manual counting method only up to 10 Gy. Figure 7.8A compares the manual method to results from the automated method based on fluorescence image intensity. The error bars are the standard deviations of the mean foci per cell, or the mean fluorescence intensity for the two analysis methods. For ease of comparison, the fluorescence intensity values of the automated method were normalized to give the same number of equivalent foci per cell at 2 Gy.

One of the potential advantages of the automated method is the ability to objectively quantify the γH2AX signal at higher doses than is possible with foci counting. In Fig. 7.8B, the average raw pixel values in the nuclei are illustrated up to a dose of 20 Gy. While the signal deviates from linearity at 20 Gy, there remains a large increase in

the intensity value between 10 and 20 Gy. This suggests that useful quantitative information can be obtained from the automated method for significantly higher doses yet, through use of a dose-signal calibration curve.

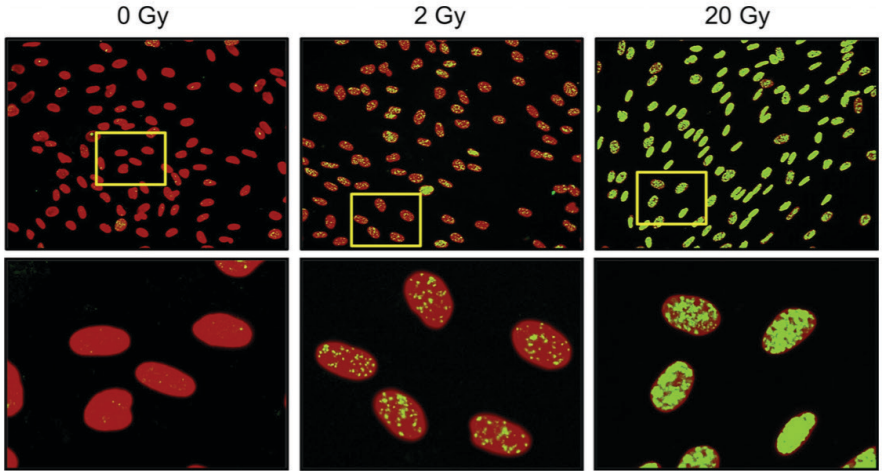

Figure 7.7 Merged DAPI (red) and γH2AX (green) images of the uniformly irradiated NHFs at two magnifications. Magnified view of the boxed regions are shown (lower row) for better visualization of the foci.

The major advantage of the automated analysis over the manual method is the vast increase in speed. Typically a single set of images for a single sample (DAPI and γH2AX images) of uniformly irradiated cells can be analyzed within seconds irrespective of the level of DNA damage. In contrast, the manual analysis of a single image is time consuming, and it becomes particularly tedious and complicated for radiation doses (>2 Gy) that trigger a high frequency of closely spaced DSBs that result in clustered and overlapping γH2AX foci.[23] Another significant advantage is that there is no inter-observer variability, which can occur with the manual method of quantification, specifically for radiation doses above 2 Gy. The automated method does have weaknesses, especially at lower doses when counting individual foci is feasible. For instance, distinctions between true foci and artifacts can be identified by manual evaluation, but are difficult to automate. Artifacts may include pan-stained nuclei (high intensity fluorescence throughout whole nuclei) that do not appear to be associated with DSBs.[39]

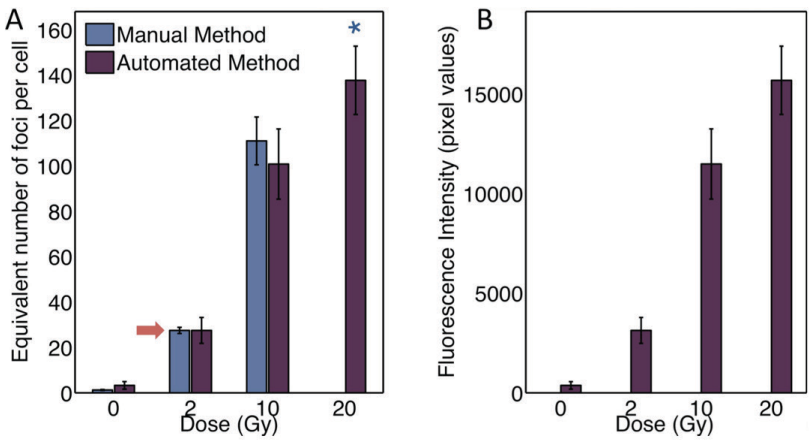

Figure 7.8 Comparison of the two methods of quantifying γH2AX nuclear fluorescence in NHFs. Immunofluorescence was performed before and at 30 minutes after exposure to doses between 0 and 20 Gy. (A) Comparison of the outcome of the manual (foci count number) and automated (mean fluorescence intensity) methods. For ease of comparison, the fluorescence intensity values are normalized to the number of foci per cell at a dose of 2 Gy (arrow). (*) The γH2AX values for 20 Gy irradiated cells were determined by the automated method only. Each datum point represents the mean (±SE) values for at least 200 cells. (B) Actual fluorescence intensity measurements (pixel values for 16 bit depth) obtained by the automated method.

The automated method of analysis (Fig. 7.6) for quantifying the spatial distribution of γH2AX fluorescence intensity following spatially fractionated irradiations enables the rapid quantification of DNA damage distribution with respect to horizontal position in MRT-irradiated cells even at doses considerably higher than what is typically considered with γH2AX quantification. This method of analysis facilitates the investigation of many factors in an efficient and robust fashion, specifically the peak intensity, valley intensity, FWHM and area under the curve, as a function of dosimetric and geometric MRT factors (peak dose, valley dose, microbeam width, microbeam spacing, microbeam array dimensions, and the arrangement of multiple arrays). By varying the time between irradiation and fixation, the clearance of γH2AX foci with time, as well as changes in cell morphology following these high doses, can also be explored. Although linearity between dose and averaged fluorescence intensity is lost for doses above approximately 10 Gy, at higher doses calibration curves can be applied to correct profiles for a more accurate representation of DNA damage. Also, this method of

analysis was developed in MATLAB, which allows for customization based on specific requirements for a given experiment.

7.4.2 Monte Carlo calculated dose distributions

The Monte Carlo simulated dose distribution is shown in Fig. 7.9 for the central three microbeams in the 75 microbeam array. Based on this simulation, the peak-to-valley dose ratio for the geometry considered (50 μm width, 400 μm spacing) at a depth of 2 cm in water is 65 ± 1. This depth was chosen to match the depth in the medium at which the cell culture samples were positioned during irradiations. The peak and valley doses delivered to the cell cultures are reported in Table 7.1.

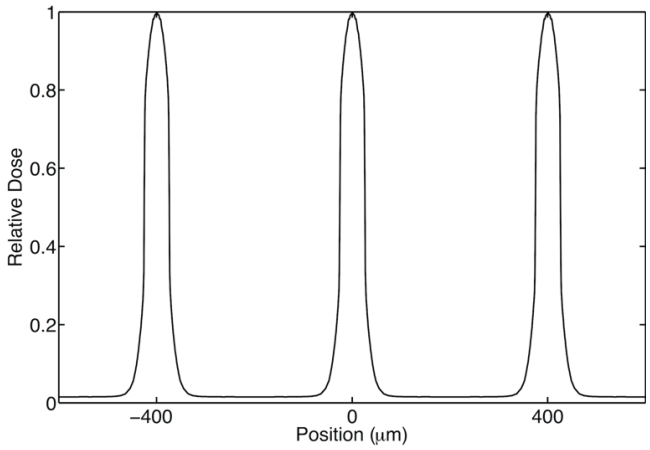

Figure 7.9 The Monte Carlo simulated relative dose distribution at a depth of 2 cm in water resulting from an array of 50 μm–wide microbeams and centre-to-centre (c-t-c) spacing of 400 μm.

Table 7.1 Peak and valley doses delivered at a depth of 20 mm in water for the central microbeam of the microbeam array.

	Peak Dose (Gy)	Valley Dose (Gy)
Dose 1	1.4	0.02
Dose 2	14	0.2
Dose 3	71	1.1
Dose 4	283	4.3

7.4.3 Immunofluorescence signal following irradiation by a synchrotron-generated microbeam array as a function of delivered dose

The presence of γH2AX immunofluorescence in cell cultures was visible at 0.5 h following exposure to the array of synchrotron microbeams for all doses delivered (1.4, 14, 71 and 283 Gy). Fluorescence microscopy images of MGCs and NHFs are shown in Fig. 7.10 for doses of 14, 71 and 283 Gy and different times (between 0.5 and 48 h) following irradiation.

We observed a non-linear increase in peak fluorescence intensity measured 0.5 h after irradiation as a function of delivered peak dose, as plotted in Fig. 7.11. The fluorescence intensity in the peak was measured as the central 25% of the FWHM of the curve. Figure 7.11 also shows the valley fluorescence intensity as a function of dose, where the valley region was defined as the region measured two peak widths (FWHM) away from the peaks on either side of the valley of interest. The 0 Gy data point is the average of the fluorescence intensity in samples from all three control conditions (described in Section 7.3.2), as there was no difference in fluorescence intensity for the three conditions.

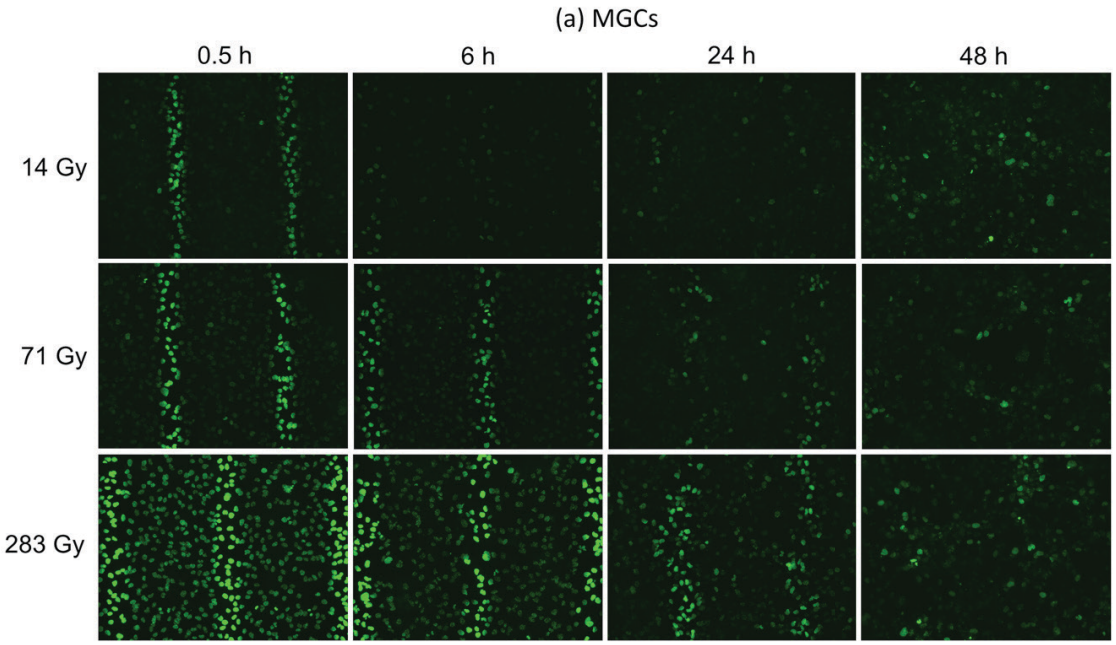

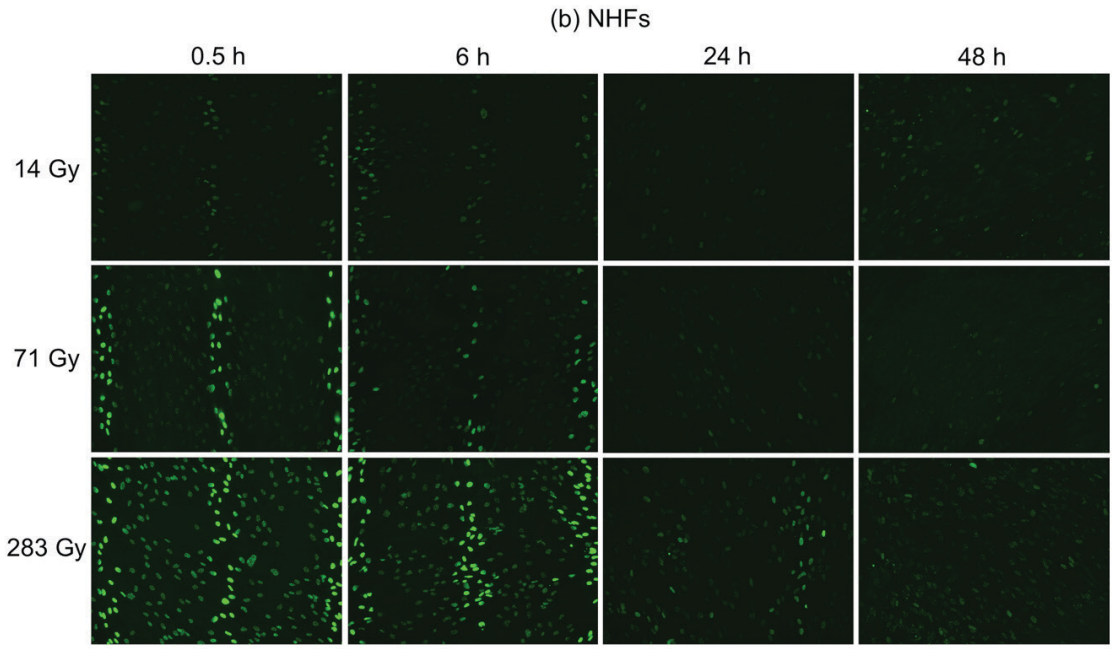

Figure 7.10 The γH2AX immunofluorescence in (a) MGCs and (b) NHFs following irradiation by the microbeam array (50 μm width, 400 μm c-t-c). Samples are shown for doses of 14, 71 and 283 Gy, and times of 0.5, 6, 24 and 48 h after irradiation. Images were taken with a 10X objective lens. The image dimensions are 666 μm vertically × 891 μm horizontally.

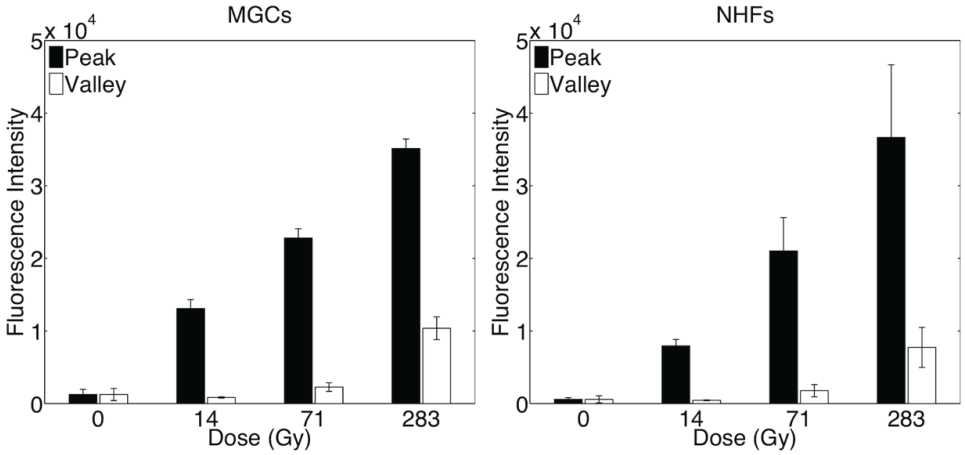

Figure 7.11 The γH2AX immunofluorescence intensity in the peak and valley regions in MGCs (left) and NHFs (right) measured 0.5 h after irradiation with the microbeam array as a function of dose delivered in the peak.

The widths of the peak regions were measured at 0.5 h via the peak-fitting algorithm in both cell types. In NHFs, the peak width was 55.2 ± 5.1 μm, and in MGCs

the width was 56.6 ± 9.3 μm. The ten central peak widths measured at the surface of the irradiation jig (using GafChromic HD810 film (ISP Technologies, NJ, USA)) and at 2 cm depth in media (using GafChromic EBT2 film) were 55.8 ± 2.6 and 57.9 ± 0.9 μm, respectively.

7.4.4 Change in immunofluorescence signal with time after irradiation with a synchrotron-generated microbeam array

Figure 7.10 illustrates the decrease in γH2AX immunofluorescence in both cell types at times of 6, 24 and 48 h after irradiation, as compared with the initial fluorescence measured at 0.5 h. The γH2AX fluorescence intensities in both the peak and valley regions at times up to 24 h following a peak dose of 283 Gy are plotted in Fig. 7.12. In general, the γH2AX fluorescence intensity decreases in a similar manner in both cell

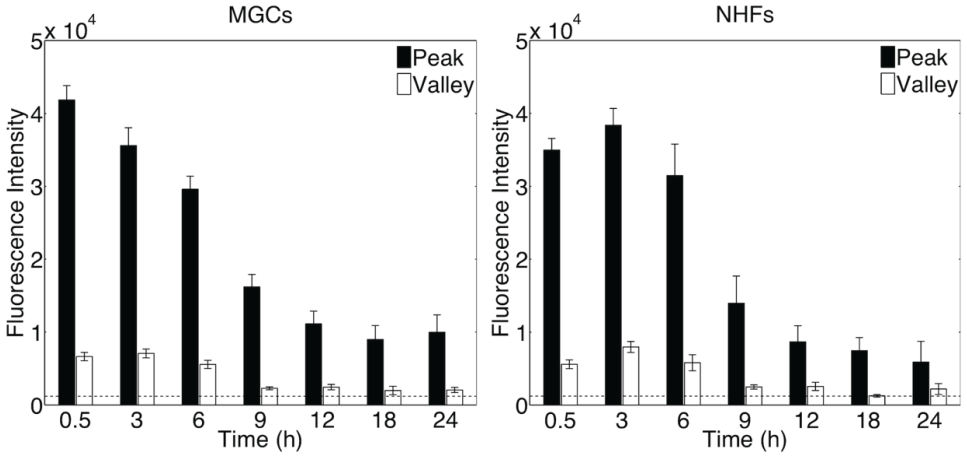

Figure 7.12 The γH2AX immunofluorescence intensity in the peak and valley regions in MGCs (left) and NHFs (right) measured between 0.5 and 24 h after a 283 Gy irradiation with the microbeam array. The dashed line indicates the mean fluorescence intensity in controls.

types. The peak fluorescence decreases most rapidly between 0.5 and 12 h after irradiation, and only minimal changes occur between 12 and 24 h. The valley fluorescence remains relatively constant for the first 6 h, decreases most significantly between 6 and 9 h, then remains relatively constant again until 24 h. The most conspicuous difference in γH2AX fluorescence clearance between MGCs and NHFs is

apparent at 24 h. For a 283 Gy irradiation, the peak and valley structure remains prominent in MGCs up to 24 h, while the fluorescence in these two regions at 24 h in NHFs is either much more similar or even indistinguishable for some samples.

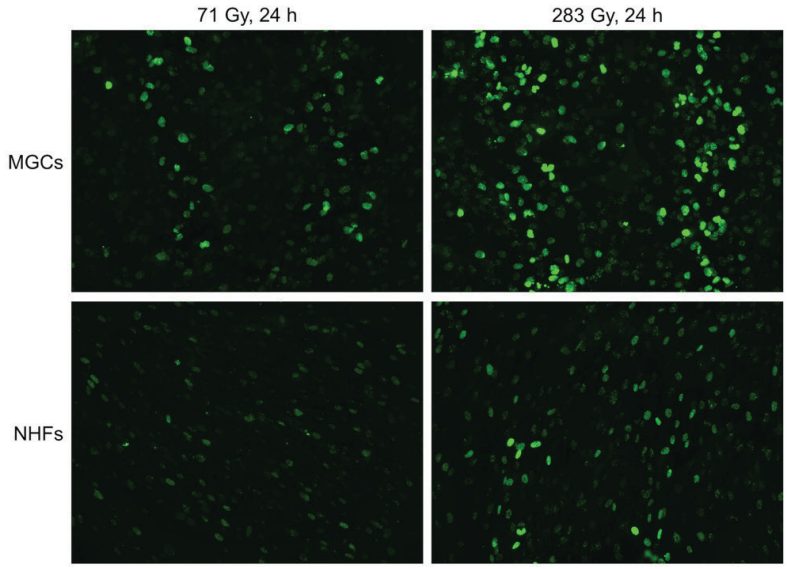

Figure 7.13 γH2AX immunofluorescence in MGCs (top) and NHFs (bottom) at 24 h after a 71 Gy (left) and a 283 Gy (right) irradiation with the microbeam array illustrates the prolonged persistence of peak and valley regions in MGCs compared with NHFs.

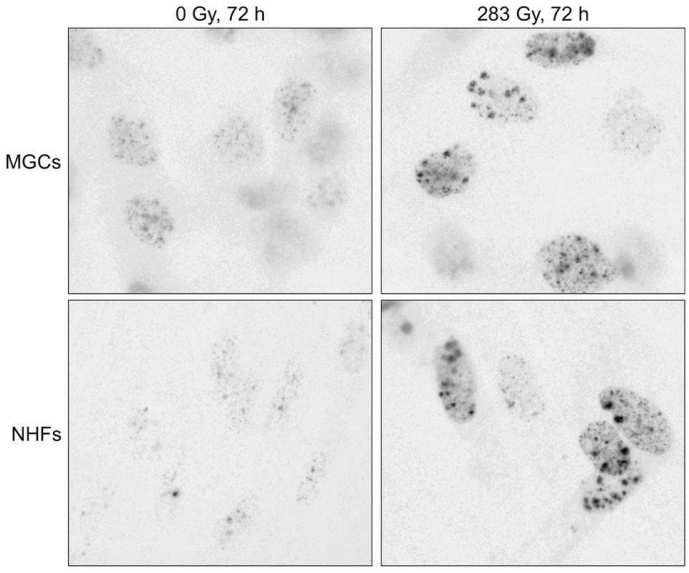

Figure 7.14 γH2AX images at 72 h in control (left) and 283 Gy-irradiated (right) MGCs (top) and NHFs (bottom) show the persistence of γH2AX fluorescence signal in irradiated samples at long times post-irradiation.

The greater difference between peak and valley fluorescence intensity at 24 h evident in MGC samples is readily apparent in the γH2AX images for 71 and 283 Gy doses shown in Fig. 7.13. The time dependence of the cell culture response to lower doses was sampled at a coarser temporal resolution; nevertheless, there appeared to be a similar rate of fluorescence loss between 0.5 and 6 h, and a less defined peak and valley structure at 24 h compared with the 283 Gy samples. At 48 h (data not shown) and 72 h (Fig. 7.14), there are persistent (above background) γH2AX foci visible in the irradiated samples of both cell types. However, at these late times the microbeam pattern is no longer discernible, as the foci are not clustered in distinct peak and valley regions.

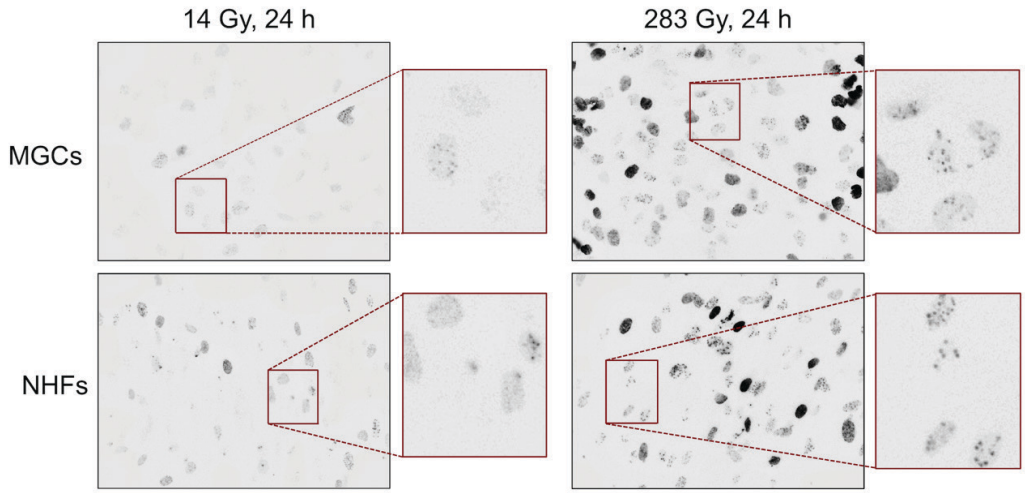

Figure 7.15 The γH2AX immunofluorescence intensity in MGCs (top) and NHFs (bottom) at 24 h after irradiation with the microbeam array. The samples on the left were irradiated with a 14 Gy peak dose and corresponding 0.2 Gy valley dose, while the samples on the right received a 283 Gy peak and 4.3 Gy valley dose. The image dimensions are 333 μm vertically × 445 μm horizontally.

A more detailed examination of the foci present in the valley regions of the cell cultures at 24 h revealed a slower clearance of γH2AX signal than expected based on the valley dose, and the observed clearance in the peak regions. Figure 7.15 shows the results for both cell types at 24 h following peak/valley doses of either 14/0.2 Gy (left) or 283/4.3 Gy (right) delivered via the microbeam array. The MGC-283 Gy image is centred on the valley region (the microbeam paths are along the left and right edges of the image), while the three other images show a mixed zone because the peaks and valleys are indistinguishable in these images. We observed more clearance in directly irradiated

cells receiving 14 Gy than in cells receiving only 4.3 Gy in the valley, but surrounded by 283 Gy peak regions.

7.4.5 Change in immunofluorescence signal with beam width after irradiation with a synchrotron-generated microbeam array, single microbeams and a broad beam

During two experimental sessions at the CLS, the influence of beam size on fluorescence clearance was investigated by comparing samples irradiated using the microbeam array, a single microbeam and a broad beam. Experiment 1 included the 50 μm microbeam from the full array (labelled MSC), and three single microbeams (widths of 60, 100 and 570 μm), all 4 mm tall. Experiment 2 included another 50 μm microbeam from the full array (labelled MSC2) and the response to the 4 mm × 32 mm broad beam (labelled BB). Images of the γH2AX-immunostained nuclei for both cell types are shown in Fig. 7.16 at 24 h after a 71 Gy irradiation. Compared with the microbeam from the full array (MSC), we observed similar γH2AX fluorescence remaining at 24 h with the 60 μm-wide single microbeam, and more fluorescence remaining following exposure to the 570 μm-wide microbeam. Considering the data from experiment 2, we observed less clearance following a broad beam irradiation compared with the microbeam array (MSC2). In general, the nuclei in the wide microbeam (570 μm) or broad beam images contain, on average, a greater number of remaining foci at 24 h compared with the narrow microbeam (50 or 60 μm) images. The residual foci following exposure to the 100 μm microbeam had mixed results. In NHFs, the number of residual γH2AX foci was higher than for the 60 μm-wide microbeam and more similar to the 570 μm-wide microbeam. The opposite was true for MGCs, *i.e.* the response of these cells to the 100 μm microbeam was very similar to the 60 μm microbeam and had fewer remaining foci than the 570 μm microbeam. Differences between the narrow microbeams (50 or 60 μm) compared with the wide microbeam (570 μm) or the broad beam at 24 h were more obvious for NHFs than MGCs. It is possible, however, that this may just reflect the slightly different rates of γH2AX clearance between the two cell types, as was described in Section 7.4.4. Specifically, at 24 h after irradiation, the peak and valley pattern was lost in many NHF samples, but remained visible in MGC samples.

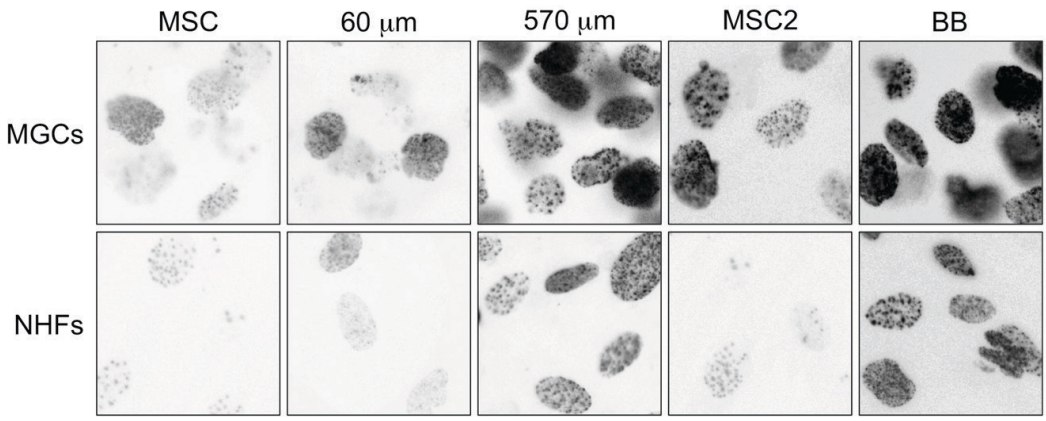

Figure 7.16 Images of MGCs (top) and NHFs (bottom) 24 h after a 71 Gy dose. The first three columns of images were acquired during a first experimental session at the CLS, and correspond to cells irradiated with the microbeam array (MSC), or single microbeams of either 60 or 570 μm width. Images from a second session at the CLS (the last two columns of images) include irradiation using a microbeam array (MSC2) or a broad beam (BB). Images were taken within the peak region (if apparent).

7.4.6 Apoptosis

To investigate cellular fates following high-dose irradiations, cells with apoptotic morphology (see, for example, Fig. 7.3 or the inset in Fig. 7.17) were counted in all microbeam-irradiated samples for times up to 72 h after irradiation, and in broad beam-irradiated samples for times up to 24 h. Since microbeam peaks and valleys are indistinguishable for late time points, for all microbeam samples the apoptotic cells were counted within the entire microbeam array path encompassing both peaks and valleys. Apoptotic cells were identified by morphology (*i.e.*, nuclear fragmentation and/or condensation). The incidence of apoptotic cells is shown in Fig. 7.17 where both subplots have the same scale for comparison between cell types. Even at the high doses considered, very few apoptotic cells were present. For MGCs, the maximum occurrence of apoptotic cells for any time and dose combination following microbeam (MB) irradiation was 0.17 ± 0.03 % (283 Gy, 72 h) and 0.20 ± 0.04 % (283 Gy, 24 h) following broad beam (BB) exposure. In response to the microbeam array, there was a significant difference between the proportion of apoptotic cells at 72 h versus any other time points. There was also an increase in the number of apoptotic cells at 24 h following broad beam irradiation versus the microbeam-irradiated cells at 24 h for 71 and 283 Gy. Overall,

however, MGCs showed an extremely high resistance to undergoing apoptosis following doses up to several hundred Gy.

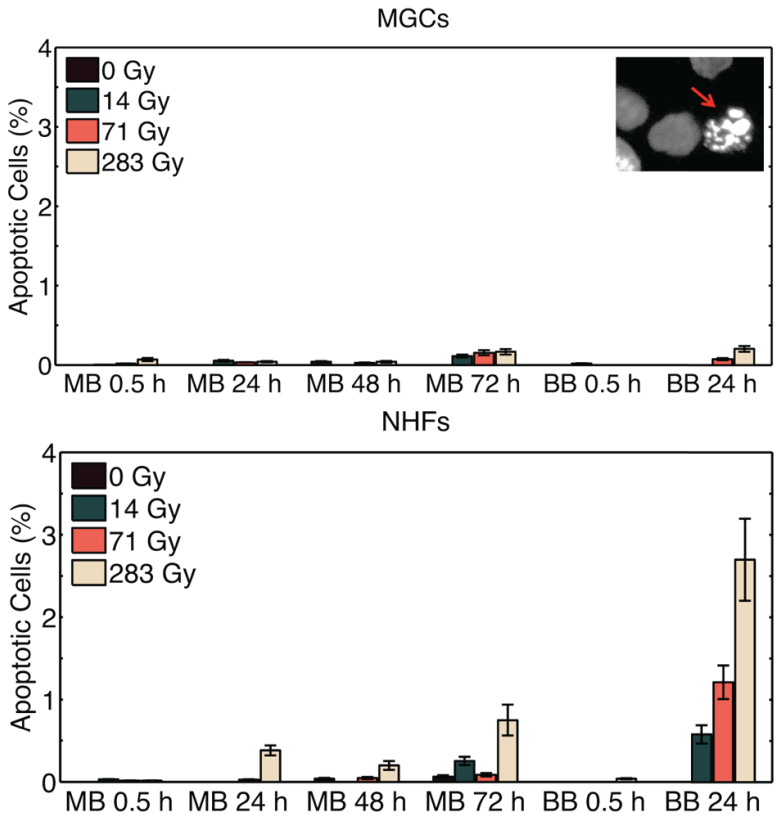

Figure 7.17 The incidence of apoptotic nuclei after irradiation with the microbeam array (labelled MB) or the 4 mm × 32 mm broad beam (labelled BB) at various times after exposure (0.5 – 72 h) and various doses (0 – 283 Gy) for MGCs and NHFs. An example of an apoptotic cell is indicated by the arrow.

The percentage of apoptosis in microbeam-irradiated NHFs was slightly higher than was found for MGCs, but still extremely low, with a maximum incidence of 0.75 ± 0.19 % at 72 h after a 283 Gy dose of irradiation. At any time point, the number of apoptotic cells was highest following the largest dose (283 Gy), and for any dose the most apoptotic cells were found at 72 h after irradiation. There was an increase in the amount of apoptotic NHFs present at 24 h in broad beam-irradiated samples compared with the amount of apoptotic cells present following microbeam irradiations of equivalent doses. After a broad beam dose of 283 Gy, there were 2.7 ± 0.5% apoptotic cells. Despite the higher prevalence of apoptosis in NHFs, particularly for broad beam irradiations, the overall rate of apoptosis is extremely low (<5%). Thus, apoptosis is not

the preferred response of these cultures to ionizing-radiation-induced DNA damage under the conditions we investigated.

7.5 Discussion

The BMIT beamlines at the CLS offer novel techniques using synchrotron x-rays in both imaging and therapy, including the development of an MRT program. Our experiments were performed using the 05B1-1 x-ray beamline at the CLS, the only fully commissioned BMIT beamline at the time of the experiments. Although this beamline provides a lower mean energy (52 keV) and considerably lower dose rate (~1.5 Gy s^{-1}) than typically used in MRT, the minimally divergent (~ 4 mrad) beam is able to provide the highly spatially fractionated dose distribution that is central to MRT's unique biological properties. The cellular response to high-dose synchrotron x-rays of several geometries was assessed using the γH2AX immunostaining assay in conjunction with the examination of apoptotic cell morphology at several time points after irradiation.

To evaluate γH2AX fluorescence, which was used as a surrogate for DNA damage, we employed an automated analysis that tallied fluorescence intensity from the immunostained cell cultures. Total fluorescence intensity was measured, in contrast to the more traditional method of counting individual γH2AX foci, for two major reasons: (i) at these high doses the individual γH2AX foci in the peak regions are too numerous to discern; and (ii) the automated analysis provides a time-efficient method of analysing the large number of samples that were treated. Using this assay we were able to visually identify peak and valley regions of irradiated samples, and quantify the γH2AX fluorescence in a spatially dependent manner in each of these zones in cell cultures. We observed a non-linear increase in γH2AX fluorescence intensity with increasing dose for a range of peak doses between 0 and 283 Gy. The sensitivity of the emitted γH2AX fluorescence with respect to changing dose decreases with increasing dose, most likely due to overlapping individual foci at higher doses. Despite its benefits, this method of analysis does have some limitations. At low valley doses (below ~1 Gy), the automated analysis had insufficient sensitivity to separate the low number of high- intensity γH2AX foci arising spontaneously or induced by ionizing radiation. In the low-dose valley

region it is possible to overcome this issue by manually counting distinct γH2AX foci. It becomes very difficult, however, to distinguish individual γH2AX foci at doses of 14 Gy and above in the peak regions at 0.5 h after irradiation. Despite these challenges, our results show that the distribution of H2AX fluorescence following irradiation faithfully represents the delivered dose distribution, as shown by the agreement within error between the microbeam widths measured via radiochromic film and from the 0.5 h H2AX images. This supports the suggestion by Rothkamm *et al.*[9] that γH2AX immunostaining could be used for biological dose mapping in cell culture and in tissue sections. Even at the high doses typical of MRT, where counting foci to estimate the delivered dose is difficult, this assay could prove useful for verifying difficult irradiation geometries, such as interlaced microbeam arrays[40,41] in animal models at early times after irradiation, and perhaps inform the extent of DNA damage, beyond simply the delivered dose distributions, at late times following microbeam irradiations.

Although limitations of the assay exist, we were able to extract several interesting relationships between the distribution of γH2AX immunofluorescence in cell culture at various times after microbeam irradiations with different doses and geometries. First, in response to the microbeam array, the two cell types had similar overall trends in terms of initial formation and subsequent clearance of γH2AX foci. Specifically, the highest fluorescence signal occurred in the first 0.5–3h in both cell types, and the signal intensity decreased with time. The most significant reduction in valley fluorescence was observed between 6 and 9 h. Although the overall trend of γH2AX fluorescence clearance was very similar for the two cell types, we observed that the rate of clearance in MGCs was slightly slower than in NHFs. At 24 h after irradiation, the peak and valley regions were still easily discernible in MGCs after a dose of 283 Gy, but not in NHFs. This effect was reflected in the constantly widening widths of the peak regions in NHFs with time, while the width in MGCs expanded more slowly. By 48 h after irradiation, the peak and valley regions were completely missing in both cell types. Although the microbeam pattern was lost according to the automated analysis, high-resolution images revealed the persistence of γH2AX foci in both cell types at late times (up to 72 h) following irradiation.

We also observed an interesting effect in the valley clearance at 24 h after exposure. In a valley region exposed to only 4.3 Gy (corresponding to a peak dose of

283 Gy) we observed less clearance by 24 h than we observed in the mixed peak/valley regions that were exposed to a peak and valley dose of 14 and 0.2 Gy and incubation for 24 h. This suggests that the DNA damage response of the cells in the valley region is influenced by the heavily irradiated cells in the peak region. Whether this observation reflects intercellular communication (between cells within peak and valley regions) and/or cell movement (from peak to valley regions) remains to be determined. Additional investigations of this phenomenon are warranted to further the understanding of MRT's potential therapeutic benefit.

The response of MGCs and NHFs to x-ray beams of varying widths was investigated using the full microbeam array, three single microbeams and one rectangular broad beam. We observed more γH2AX clearance for narrower microbeams (the 50 μm-wide microbeam from the full array, and the 60 μm single microbeam) than for the wider microbeam (570 μm) and the broad beam. This difference in response with width was more easily visualized in NHFs. We suspect that this results from the slightly slower rate of H2AX clearance for MGCs discussed above, and not that the overall γH2AX clearance following microbeam irradiation is necessarily better for NHFs over MGCs.

A straightforward interpretation of the γH2AX clearance data is that DSBs induced under these conditions might be rejoined at a faster rate in NHFs than MGCs. However, alternative explanations cannot be ruled out given that radiation-triggered genomic abnormalities other than DSBs are also known to give rise to Ser139-H2AX phosphorylation and formation of γH2AX-associated nuclear foci. Suzuki *et al.*, for example, demonstrated that γH2AX foci persist at times after irradiation when all detectable DSBs are rejoined, and concluded that the residual (persistent) foci indicate an aberrant chromatin structure, but not a DSB itself.[22] In light of this, the only definitive conclusions that can be drawn from our observations are that genomic alterations that give rise to γH2AX foci are induced in these cultures; that such alterations persist for the duration of the experiments (up to 72 h) after synchrotron microbeam irradiation; and that at late times after radiation exposure these foci are distributed uniformly, as opposed to being predominantly present in the peak region as was seen at early times post-irradiation.

The A172 MGCs used in the current study respond to ionizing radiation similarly to NHFs in terms of clonogenic survival[42] and activation of the p53 tumour suppressor,[33,42] a key regulator of the DNA surveillance network.[11] Although these cultures exhibit apoptosis resistance in response to moderate doses of ionizing radiation (*e.g.*, 10 Gy),[33] we considered the possibility that the residual γH2AX foci observed at late times after high-dose (*e.g.*, 283 Gy) irradiation might reflect cells undergoing apoptosis. However, using morphological criteria (i.e. nuclear fragmentation and/or shrinkage), we observed very low frequency (<5 %) of apoptotic cells in cultures of both cell types following high-dose synchrotron-generated x-ray microbeam irradiations. We observed a slightly elevated frequency of apoptosis in NHFs following broad beam irradiation at 2.7 %, but MGCs remained below 0.5 %. Further study would be useful to determine whether the high-dose microbeam conditions alter the frequency of apoptosis for other cell types for which apoptosis has been established as a significant damage response pathway at low to moderate doses.

For the cell types investigated in this work, one hypothesis is that the apoptosis-resistant phenotype of these cultures might be associated with p53-mediated upregulation of p21, a well-characterized anti-apoptotic protein that acts at different levels of the death cascade[11,43] and engages the SIPS response.[11] Cells that undergo the SIPS response enter a prolonged state of growth- arrest in which DNA replication ceases, but the cells remain viable and continue to secrete growth- and tumour-promoting factors.[11] The preference of p53 wild- type human cells for SIPS as opposed to undergoing apoptosis has been previously demonstrated in response to conventional broad beam irradiation.[33,42,44] The residual γH2AX fluorescence observed at late times in this study may be an indicator of cells undergoing SIPS, since this response is also associated with high numbers of γH2AX foci, presumably reflecting genomic instability.[44]

The techniques reported here will facilitate the evaluation of DNA damage response to microbeam irradiation in different types of cultured human cells (*e.g.*, normal versus cancerous) with different genetic background (*e.g.*, TP53 status). Our results give credence to previous work[1,7-9] suggesting that the γH2AX immunofluorescence assay might be used as a reliable biological probe for evaluating DSBs at relatively short times (0.5 h) after synchrotron exposure. We have demonstrated that synchrotron exposure of

p53 wild-type human cell cultures (normal fibroblasts and A172 MGCs) results in a high frequency of genomic instability, which is manifested as γH2AX-associated nuclear foci that persist for long times (*e.g.* 72 h) post-irradiation but are not associated with apoptosis. Our studies motivate further in vitro and in vivo investigations on microbeam-triggered early responses (*e.g.*, DNA repair; cell cycle checkpoints) and late responses (*e.g.*, apoptosis; SIPS) in human cells with differing p53 status.

7.6 References

[1] J.C. Crosbie, R.L. Anderson, K. Rothkamm, C.M. Restall, L. Cann, S. Ruwanpura, S. Meachem, N. Yagi, I. Svalbe, R.A. Lewis, B.R.G. Williams, P.A.W. Rogers, "Tumor Cell Response to Synchrotron Microbeam Radiation Therapy Differs Markedly from Cells in Normal Tissues," International Journal of Radiation Oncology Biology Physics **77**, 886-894 (2010).

[2] D.R. Pilch, O.A. Sedelnikova, C. Redon, A. Celeste, A. Nussenzweig, W.M. Bonner, "Characteristics of γ-H2AX foci at DNA double strand breaks sites," Biochemistry and Cell Biology-Biochimie Et Biologie Cellulaire **81**, 123-129 (2003).

[3] O. Fernandez-Capetillo, A. Lee, M. Nussenzweig, A. Nussenzweig, "H2AX: the histone guardian of the genome," DNA Repair **3**, 959-967 (2004).

[4] R. Mirzayans, D. Severin, D. Murray, "Relationship between DNA double-strand break rejoining and cell survival after exposure to ionizing radiation in human fibroblast strains with differing ATM/p53 status: Implications for evaluation of clinical radiosensitivity," International Journal of Radiation Oncology Biology Physics **66**, 1498-1505 (2006).

[5] L.J. Kuo and L. Yang, "γ-H2AX - A novel biomarker for DNA double-strand breaks," In Vivo **22**, 305-309 (2008).

[6] M. Wang, F. Morsbach, D. Sander, L. Gheorghiu, A. Nanda, C. Benes, M. Kriegs, M. Krause, E. Dikomey, M. Baumann, J. Dahm-Daphi, J. Settleman, H. Willers, "EGF Receptor Inhibition Radiosensitizes NSCLC Cells by Inducing Senescence in Cells Sustaining DNA Double-Strand Breaks," Cancer Res. **71**, 6261-6269 (2011).

[7] G. Kashino, T. Kondoh, N. Nariyama, K. Umetani, T. Ohigashi, K. Shinohara, A. Kurihara, M. Fukumoto, H. Tanaka, A. Maruhashi, M. Suzuki, Y. Kinashi, Y. Liu, S. Masunaga, M. Watanabe, K. Ono, "Induction of DNA Double-Strand Breaks and Cellular Migration through Bystander Effects in Cells Irradiated with the Slit-Type Microplanar Beam of the Spring-8 Synchrotron," International Journal of Radiation Oncology Biology Physics **74**, 229-236 (2009).

[8] C.N. Sprung, M. Cholewa, N. Usami, K. Kobayashi, J.C. Crosbie, "DNA damage and repair kinetics after microbeam radiation therapy emulation in living cells using monoenergetic synchrotron X-ray microbeams," Journal of Synchrotron Radiation **18**, 630-636 (2011).

[9] K. Rothkamm, J.C. Crosbie, F. Daley, S. Bourne, P.R. Barber, B. Vojnovic, L. Cann, P.A.W. Rogers, "In situ Biological Dose Mapping Estimates the Radiation Burden Delivered to 'Spared' Tissue between Synchrotron X-Ray Microbeam Radiotherapy Tracks," Plos One **7**, e29853 (2012).

[10] R. Mirzayans, B. Andrais, A. Scott, Y.W. Wang, R.H. Weiss, D. Murray, "Spontaneous γ-H2AX Foci in Humal Solid Tumor-Derived Cell Lines in Relation to p21WAF1 and WIP1 Expression," Int. J. Mol. Sci. **16**, 11609-11628 (2015).

[11] R. Mirzayans, B. Andrais, A. Scott, Y.W. Wang, D. Murray, "Ionizing Radiation-Induced Responses in Human Cells with Differing TP53 Status," International Journal of Molecular Sciences **14**, 22409-22435 (2013).

[12] E.J. Hall and A.J. Giaccia, *Radiobiology for the Radiologist*, 6th Edition ed. (Lippincott Williams & Wilkins, Philadelphia, PA, USA, 2006).

[13] W.M. Bonner, C.E. Redon, J.S. Dickey, A.J. Nakamura, O.A. Sedelnikova, S. Solier, Y. Pommier, "OPINION γ-H2AX and cancer," Nature Reviews Cancer **8**, 957-967 (2008).

[14] M. Podhorecka, A. Skladanowski, P. Bozko, "H2AX Phosphorylation: Its Role in DNA Damage Response and Cancer Therapy." Journal of nucleic acids **2010** (2010).

[15] K. Rothkamm and S. Horn, " γ-H2AX as protein biomarker for radiation exposure," Annali Dell Istituto Superiore Di Sanita **45**, 265-271 (2009).

[16] M. Koike, Y. Yutoku, A. Koike, "Accumulation of p21 proteins at DNA damage sites independent of p53 and core NHEJ factors following irradiation," Biochem. Biophys. Res. Commun. **412**, 39-43 (2011).

[17] S. Moon, L. Lin, X. Zhang, T. Nguyen, Y. Darlington, A.S. Waldman, X. Lu, L.A. Donehower, "Wild-type p53-induced Phosphatase 1 Dephosphorylates Histone Variant γ-H2AX and Suppresses DNA Double Strand Break Repair," J. Biol. Chem. **285**, 12935-12947 (2010).

[18] L. Macurek, A. Lindqvist, O. Voets, J. Kool, H.R. Vos, R.H. Medema, "Wip1 phosphatase is associated with chromatin and dephosphorylates γH2AX to promote checkpoint inhibition," Oncogene **29**, 2281-2291 (2010).

[19] O.A. Sedelnikova, D.R. Pilch, C. Redon, W.M. Bonner, "Histone H2AX in DNA damage and repair," Cancer Biology & Therapy **2**, 233-235 (2003).

[20] K. Rothkamm and M. Lobrich, "Evidence for a lack of DNA double-strand break repair in human cells exposed to very low x-ray doses," Proc. Natl. Acad. Sci. U. S. A. **100**, 5057-5062 (2003).

[21] T. Neumaier, J. Swenson, C. Pham, A. Polyzos, A.T. Lo, P. Yang, J. Dyball, A. Asaithamby, D.J. Chen, M.J. Bissell, S. Thalhammer, S.V. Costes, "Evidence for formation of DNA repair centers and dose-response nonlinearity in human cells," Proc. Natl. Acad. Sci. U. S. A. **109**, 443-448 (2012).

[22] M. Suzuki, K. Suzuki, S. Kodama, M. Watanabe, "Phosphorylated histone H2AX foci persist on rejoined mitotic chromosomes in normal human diploid cells exposed to ionizing radiation," Radiat. Res. **165**, 269-276 (2006).

[23] W. Bocker and G. Iliakis, "Computational Methods for analysis of foci: validation for radiation-induced γ-H2AX foci in human cells." Radiat. Res. **165**, 113-24 (2006).

[24] P.R. Barber, R.J. Locke, G.P. Pierce, K. Rothkamm, B. Vojnovic, " γ-H2AX Foci Counting: Image processing and control software for high-content screening - art. no. 64411M," Imaging, Manipulation, and Analysis of Biomolecules, Cells, and Tissues V **6441**, M4411-M4411 (2007).

[25] F.A. Cucinotta, J.M. Pluth, J.A. Anderson, J.V. Harper, P. O'Neill, "Biochemical kinetics model of DSB repair and induction of γ-H2AX foci by non-homologous end joining," Radiat. Res. **169**, 214-222 (2008).

[26] Y. Hou, A. Lavaf, D. Huang, S. Peters, R. Huq, V. Friedrich, B.S. Rosenstein, J. Kao, "Development of an Automated γ-H2AX Immunocytochemistry Assay," Radiat. Res. **171**, 360-367 (2009).

[27] Z. Cai, K.A. Vallis, R.M. Reilly, "Computational analysis of the number, area and density of γ-H2AX foci in breast cancer cells exposed to 111In-DTPA-hEGF or -rays using Image-J software," Int. J. Radiat. Biol. **85**, 262-271 (2009).

[28] S.H. MacPhail, J.P. Banath, T.Y. Yu, E.H.M. Chu, H. Lambur, P.L. Olive, "Expression of phosphorylated histone H2AX in cultured cell lines following exposure to X-rays," Int. J. Radiat. Biol. **79**, 351-358 (2003).

[29] S.H. MacPhail, J.P. Banath, Y. Yu, E. Chu, P.L. Olive, "Cell cycle-dependent expression of phosphorylated histone H2AX: Reduced expression in unirradiated but not X-irradiated G(1)-phase cells," Radiat. Res. **159**, 759-767 (2003).

[30] D. Murray and R. Mirzayans, "Role of therapy-induced cellular senescence in tumor cells and its modification in radiotherapy: the good, the bad and the ugly," J. Nucl. Med. Radiat. Ther. **S6:018. doi: 10.4172/2155-9619.S6-018** (2013).

[31] W. Wu, P. Liu, J. Li, "Necroptosis: An emerging form of programmed cell death," Critical Reviews in Oncology Hematology **82**, 249-258 (2012).

[32] P. Golstein and G. Kroemer, "Cell death by necrosis: towards a molecular definition," Trends Biochem. Sci. **32**, 37-43 (2007).

[33] R. Mirzayans, B. Andrais, A. Scott, D. Murray, "New Insights into p53 Signaling and Cancer Cell Response to DNA Damage: Implications for Cancer Therapy," Journal of Biomedicine and Biotechnology, 170325 (2012).

[34] J. Erenpreisa and M.S. Cragg, "Three steps to the immortality of cancer cells: senescence, polyploidy and self-renewal," Cancer Cell International **13**, UNSP 92 (2013).

[35] C. Lagadec, E. Vlashi, L. Della Donna, C. Dekmezian, F. Pajonk, "Radiation-Induced Reprogramming of Breast Cancer Cells," Stem Cells **30**, 833-844 (2012).

[36] T. Tanaka and H. Kitamura, "SPECTRA: a synchrotron radiation calculation code," Journal of Synchrotron Radiation **8**, 1221-1228 (2001).

[37] T.C. O'Haver, Peak Fitter, v. 2.4, http://terpconnect.umd.edu/~toh/spectrum/InteractivePeakFitter.htm, (May 2012).

[38] F. Salvat, J.M. Fernandez-Varea, J. Sempau, "PENELOPE-2008, a code system for Monte Carlo simulation of electron and photon transport," Issy-les-Moulineaux France, OECD NEA (2009).

[39] T.M. Marti, E. Hefner, L. Feeney, V. Natale, J.E. Cleaver, "H2AX phosphorylation within the G(1) phase after UV irradiation depends on nucleotide excision repair and not DNA double-strand breaks," Proc. Natl. Acad. Sci. U. S. A. **103**, 9891-9896 (2006).

[40] E. Brauer-Krisch, H. Requardt, P. Regnard, S. Corde, E.A. Siegbahn, G. LeDuc, H. Blattmann, J. Laissue, A. Bravin, "Exploiting geometrical irradiation possibilities in MRT application," Nuclear Instruments & Methods in Physics Research Section A-Accelerators Spectrometers Detectors and Associated Equipment **548**, 69-71 (2005).

[41] R. Serduc, E. Braeuer-Krisch, E.A. Siegbahn, A. Bouchet, B. Pouyatos, R. Carron, N. Pannetier, L. Renaud, G. Berruyer, C. Nemoz, T. Brochard, C. Remy, E.L. Barbier, A. Bravin, G. Le Duc, A. Depaulis, F. Esteve, J.A. Laissue, "High-Precision Radiosurgical Dose Delivery by Interlaced Microbeam Arrays of High-Flux Low-Energy Synchrotron X-Rays," Plos One **5**, e9028 (2010).

[42] R. Mirzayans, A. Scott, M. Cameron, D. Murray, "Induction of accelerated senescence by gamma radiation in human solid tumor-derived cell lines expressing wild-type TP53," Radiat. Res. **163**, 53-62 (2005).

[43] A.L. Gartel and A.L. Tyner, "The role of the cyclin-dependent kinase inhibitor p21 in apoptosis," Molecular Cancer Therapeutics **1**, 639-649 (2002).

[44] R. Mirzayans, B. Andrais, A. Scott, M.C. Paterson, D. Murray, "Single-Cell Analysis of p16(INK4a) and p21(WAF1) Expression Suggests Distinct Mechanisms of Senescence in Normal Human and Li-Fraumeni Syndrome Fibroblasts," J. Cell. Physiol. **223**, 57-67 (2010).

8 SUMMARY AND CONCLUSIONS

The unique properties of synchrotron radiation offer opportunities for the development of novel imaging and therapy techniques; the BioMedical Imaging and Therapy (BMIT) beamlines at the Canadian Light Source (CLS) enable synchrotron-based biomedical research in Canada. Thus far, BMIT's research has been dominated by imaging experimentation, but there is potential for novel therapy applications to also be explored. Microbeam radiation therapy (MRT), reviewed in Chapter 1, is a synchrotron-based type of therapy that has the potential to treat solid tumours with high dose parallel microbeams. Normal tissues show extreme tolerance, while tumours show a reduction in size and sometimes ablation, in response to these high dose microbeams. Potential applications of MRT include the treatment of solid tumours at particularly radiosensitive sites, with a focus on the difficult to treat pediatric CNS lesions.

The progression of MRT toward clinical trials requires advancement in two fields: (1) dosimetry, and (2) the biological response to high dose microbeams. Like conventional radiation therapy, a complete dosimetric system includes the availability of computational dosimetry for treatment planning and experimental dosimetry for validation of the computational system. Experimental dosimetry in a synchrotron x-ray beam is challenging because of its small dimensions (< 1 cm) in the vertical direction, and non-uniformity in both intensity and energy across its vertical profile. The conditions under which MRT is carried out make dosimetry even more difficult: the dose is delivered at a high rate (1000s of Gy/s), over a wide dose range, with sub-millimetre spatial fractionation, and with relatively low x-ray energies. MRT treatment planning requires high spatial resolution Monte Carlo simulations with high accuracy at low x-ray energies. The assessment of calculated dose distributions is not straight-forward as there are many geometric and dosimetric parameters in MRT that affect biological outcome. A method of scoring dose distributions in a volumetric manner is necessary for optimizing dose distributions. Additionally, it is not completely understood how normal tissue toxicity is so low, yet tumours demonstrate a therapeutic response. This thesis has addressed both of these fields, within the context of preparing for an MRT research program at the CLS.

The majority of this thesis reports experimental dosimetry on the BMIT beamlines. A thorough investigation of beamline characteristics, reported in Chapter 3, was done to provide a basis for further experimental and computational dosimetry. The majority of work was done on the 05B1-1 beamline, which has been available to users since the inception of the thesis work. The more recently available 05ID-2 beamline was assessed by a subset of these measurements. For one or both beamlines the broad beam output, geometry, and energy were investigated through a variety of methods. The beam profile, beam size with beamline collimator setting, and divergence were measured. The theoretical beam energy was determined through analytical calculations. The half-value layer, percent depth dose and spectroscopic measurements, were taken to compare to the theoretical, or nominal (for monoenergetic beams), energy spectra. The microbeam array on the 05B1-1 beamline was also assessed using Monte Carlo methods, and experimentally in terms of geometry (beam profiles and width) and the percent depth dose. The research reported in Chapter 3 provides vital groundwork for the rest of the thesis, and is also useful for BMIT staff and other users.

The only absolute dosimetry performed thus far on the BMIT beamlines was reported in Chapter 4. The Victoreen 480 free-air ionization chamber (FAC), provided and tested in Ottawa by the National Research Council of Canada, was used to determine absolute air kerma rates on the 05B1-1 beamline. The EGSnrc user code egs_fac was used to perform a detailed Monte Carlo analysis of the correction factors for photon attenuation, photon scatter, electron loss, and photon scatter and transmission from the chamber's diaphragm. Air kerma measurements in the broad synchrotron beam are challenging due to the non-uniform beam, which was addressed by using a specially fabricated aperture with a 0.52 mm diameter. Correcting for ion recombination is another challenge in the 05B1-1 x-ray beam. To reduce the magnitude of the recombination correction, the beam was attenuated by between 0.552 and 6.103 mm Cu. This resulted in a maximum dose rate of 5.2 Gy/s for the lowest filtration, and a minimum of 4.5 mGy/s for the maximum filtration. Additionally, the air kerma rates for two monoenergetic beams that are commonly used for imaging applications were measured. The values were 10.9 cGy/s and 1.5 cGy/s for the 20 keV and 33.3 keV beams, respectively.

The air kerma measurements using a FAC are important for providing absolute values in the synchrotron beam. This is particularly important for dosimetry in the synchrotron beam because it departs so drastically from clinical x-ray beams, which brings into question the appropriateness of applying calibration factors determined for clinical beams to the synchrotron x-ray beam. However, the FAC measurements are challenging and time-consuming. The size and weight of the chamber, as well as the small aperture, make simply positioning and aligning the chamber on the beamline a multi-hour process. It is not feasible to perform frequent dosimetry using a FAC. To address this, the use of the PR06C cavity ionization chamber in the small, non-uniform synchrotron beam was investigated. The beam profile and ion chamber response across its diameter were measured and incorporated into a geometric model. This model was used to calculate beam profile correction factors for both a stationary measurement and a scanning measurement of air kerma rates. The agreement between the predicted and measured values was better for the stationary measurements. The greater discrepancy observed for the scanning measurements indicates further work is required to before this method is used for reference dosimetry. The stationary measurements were used to determine reference on-axis air kerma rates between 0.019 for a 33.3 keV beam and 1.9 Gy/s for a 1.103 mm Cu-filtered beam at a maximum storage ring current of 250 mA for four beam filtrations. The differences in geometry between the FAC and cavity chamber measurements limit the ability to directly compare the raw results, but the two dosimeters demonstrate relative air kerma rates for different beam qualities that agree within 4 %.

Almost all imaging and therapy research programs on the 05B1-1 beamlines can benefit from the beamline characterization and dosimetric work described in Chapter 3, 4 and 5. In Chapter 6, theoretical dosimetry using Monte Carlo simulations focusing specifically on MRT at the CLS is reported. The theoretical BMIT 05ID-2 filtered energy spectrum was used to calculate MRT dose distributions in a cubic head phantom. The results of the simulations showed that the dose distributions calculated with the 05ID-2 energy spectra were very similar to those calculated at the European Synchrotron Radiation Facility (ESRF), the synchrotron light source where the majority of MRT research occurs, and thus demonstrated that the 05ID-2 beamline is suitable for supporting MRT research. We also reported a systematic study assessing the change in

dose distribution (quantified with the peak-to-valley dose ratio (PVDR)) with varying phantom size, microbeam width, and microbeam spacing. The study showed the decrease in PVDR and increasing valley dose, with increasing phantom size, increasing microbeam width and decreasing distance between adjacent microbeams. Although the PVDR is helpful for characterizing the dose distribution, as a point dose measurement it is fundamentally limited at describing the highly spatially fractionated dose distributions of MRT. The relationships between phantom and microbeam array geometry were assessed for the PVDR and three alternative dose-volume metrics: the peak-to-mean valley dose ratio (PMVDR), the mean dose, and the percentage volume below a threshold. These metrics all offer advantages over the PVDR due to their volumetric nature, but their usefulness would need to be proven by relating them to biological outcome.

The second major field of MRT research, the biological response to high dose microbeams, was also explored in the thesis. Animal studies have shown strong evidence for a differential vascular response in normal and tumour tissues in response to MRT. Other animal and cell culture studies suggest differential responses involve cell communication, DNA double strand break (DSB) repair and apoptotic cell death. In Chapter 7, the response of human cell cultures of normal human fibroblasts and malignant glioma cells to high dose synchrotron-generated microbeams was examined with the γH2AX immunofluorescence assay, a biomarker for DNA DSBs, and using nuclear counterstaining with DAPI (to assess cellular morphology). A procedure was developed to prepare the cell cultures at the Cross Cancer Institute (CCI), transport the cells to the University of Saskatchewan campus, irradiate the cells at the CLS, and then transport the cells back to the CCI for immunostaining and analysis. Additionally, a MATLAB script was written to facilitate the semi-automatic analysis to measure the spatial and intensity properties of the resulting fluorescence images. The general trends of formation and clearance of γH2AX foci with dose and time were fairly similar between the two cell types. The fluorescence images show evidence of more γH2AX foci in valley regions between two high dose microbeams than expected, which suggests that the highly irradiated peak cells influence the DNA damage response of the valley cells. We also investigated the response of cells in response to single beams of varying

widths. We observed more foci clearance in the narrow microbeams (≤ 60 μm) than wide beams (> 570 μm) at 24 hours after irradiation. Finally, an analysis of the cell morphology showed that there were very low rates of apoptosis (< 5 %) up to 72 hours after irradiation, despite the presence of persistent γH2AX foci (signifying genomic aberrations) up to 72 hours after exposure to the high dose microbeams.

Several future research avenues can be initiated based on the foundations established in this thesis. The air kerma rate on the 05B1-1 beamline was measured using the Victoreen 480, a large cylindrical FAC. The procedure described in Chapter 4 will be used to take air kerma rate measurements on the 05ID-2 beamline, although the energy and filtration will need to be selected carefully to not surpass the correctable limits of ion recombination on this higher flux beamline. Additionally, the FAC measurements and Monte Carlo simulations revealed shortcomings of the Victoreen 480 for air kerma rate measurments on the 05B1-1 beamline. The availability of a smaller, more mobile FAC for the BMIT beamlines would be a beneficial dosimetric tool for the beamlines, particularly as research becomes more heavily focused on live animal experimentation and absolute dosimetry becomes a priority for more research teams. The design of a new FAC would allow the optimization of chamber's geometry (*e.g.*, electrode separation, attenuation length, aperture size) specifically for the 05B1-1 and 05ID-2 beamlines. Additionally, a detailed study of recombination effects is required to maximize the dose rates at which the FAC can be used on these beamlines.

Further improvements upon cavity chamber dosimetry can also be explored. A Monte Carlo study of the cavity chamber response to a small, non-uniform beam would be important for improving the simple geometric model presented in Chapter 5, and investigating the energy response of the chamber. Additionally, dosimetry using smaller (pinpoint) chambers, designed for low energy x-rays, would offer improvements over the Capintec PR06C. The correction for beam profile variation over the chamber's diameter, as well as the recombination correction, would both be reduced with a smaller chamber. As above, the recombination effects of the chamber would need to be well understood to enable dosimetry over a greater range of beam intensities for both the 05B1-1 and 05ID-2 beamlines. This would include both a theoretical description of ion diffusion, as well as experimentally investigating the change in collected current with applied voltage.

For many years, Monte Carlo simulations for MRT consisted of a single beam model, and the full array was approximated through superposition. While this model has been important for showing the capabilities of the BMIT beamlines to deliver the spatially fractionated dose distributions characteristic of MRT, there are improvements that can be made. Analogous to what has been done for the ESRF, a more physically realistic model of the source, beamline and collimator would improve the accuracy of the Monte Carlo simulations. In this work, Monte Carlo simulations were also used to explore dose-volume metrics for MRT. To assess the worth of each of these factors it would be interesting to pursue a retrospective analysis of the literature in which biological outcome for a single type of normal tissue or tumour type was compared against these metrics.

There are still unanswered questions surrounding the biology of MRT, and thus many avenues that may be explored. We demonstrated that even at extreme doses, only a very small fraction of cells undergo apoptosis after microbeam irradiation. The late responses of the p53 wild-type normal human fibroblasts (NHFs) and malignant glioma cells (MGCs) examined in Chapter 7 remains to be confirmed, particularly whether the irradiated cells enter a state of growth arrest (stress-induced premature senescence) as they do after moderate doses. Additionally, the early and late responses of human cells with differing p53 status in response to microbeam irradiations remain to be investigated. The research described in this thesis comprises some of the first and only MRT research in Canada. The work establishes a foundation for many research areas including experimental dosimetry, Monte Carlo dosimetry, and DNA damage response in human cell cultures, all of which support the advancement of an MRT research program on the BMIT beamlines at the Canadian Light Source.

BIBLIOGRAPHY

A.T. Abdul Rahman, E. Brauer-Krisch, T. Brochard, J. Adamovics, S.K. Clowes, D. Bradley, S.J. Doran, "Sophisticated test objects for the quality assurance of optical computed tomography scanners." Phys. Med. Biol. **56**, 4177-99 (2011).

S. Agostinelli, J. Allison, K. Amako, J. Apostolakis, H. Araujo, P. Arce, M. Asai, D. Axen, S. Banerjee, G. Barrand, F. Behner, L. Bellagamba, J. Boudreau, L. Broglia, A. Brunengo, H. Burkhardt, S. Chauvie, J. Chuma, R. Chytracek, G. Cooperman, G. Cosmo, P. Degtyarenko, A. Dell'Acqua, G. Depaola, D. Dietrich, R. Enami, A. Feliciello, C. Ferguson, H. Fesefeldt, G. Folger, F. Foppiano, A. Forti, S. Garelli, S. Giani, R. Giannitrapani, D. Gibin, J.J.G. Cadenas, I. Gonzalez, G.G. Abril, G. Greeniaus, W. Greiner, V. Grichine, A. Grossheim, S. Guatelli, P. Gumplinger, R. Hamatsu, K. Hashimoto, H. Hasui, A. Heikkinen, A. Howard, V. Ivanchenko, A. Johnson, F.W. Jones, J. Kallenbach, N. Kanaya, M. Kawabata, Y. Kawabata, M. Kawaguti, S. Kelner, P. Kent, A. Kimura, T. Kodama, R. Kokoulin, M. Kossov, H. Kurashige, E. Lamanna, T. Lampen, V. Lara, V. Lefebure, F. Lei, M. Liendl, W. Lockman, F. Longo, S. Magni, M. Maire, E. Medernach, K. Minamimoto, P.M. de Freitas, Y. Morita, K. Murakami, M. Nagamatu, R. Nartallo, P. Nieminen, T. Nishimura, K. Ohtsubo, M. Okamura, S. O'Neale, Y. Oohata, K. Paech, J. Perl, A. Pfeiffer, M.G. Pia, F. Ranjard, A. Rybin, S. Sadilov, E. Di Salvo, G. Santin, T. Sasaki, N. Savvas, Y. Sawada, S. Scherer, S. Seil, V. Sirotenko, D. Smith, N. Starkov, H. Stoecker, J. Sulkimo, M. Takahata, S. Tanaka, E. Tcherniaev, E.S. Tehrani, M. Tropeano, P. Truscott, H. Uno, L. Urban, P. Urban, M. Verderi, A. Walkden, W. Wander, H. Weber, J.P. Wellisch, T. Wenaus, D.C. Williams, D. Wright, T. Yamada, H. Yoshida, D. Zschiesche, "GEANT4-a simulation toolkit," Nuclear Instruments & Methods in Physics Research Section A-Accelerators Spectrometers Detectors and Associated Equipment **506**, 250-303 (2003).

G.M. Akselrod, M.S. Akselrod, E.R. Benton, N. Yasuda, "A novel Al2O3 fluorescent nuclear track detector for heavy charged particles and neutrons," Nuclear Instruments & Methods in Physics Research Section B-Beam Interactions with Materials and Atoms **247**, 295-306 (2006).

M.S. Akselrod, R.C. Yoder, G.M. Akselrod, "Confocal fluorescent imaging of tracks from heavy charged particles utilising new Al_2O_3 : C,Mg crystals," Radiat. Prot. Dosimet. **119**, 357-362 (2006).

J. Alder and M. Wright, "Method of performing microbeam radiosurgery," US Patent Application Publication **13/453,338** (2013).

P.R. Almond, P.J. Biggs, B.M. Coursey, W.F. Hanson, M.S. Huq, R. Nath, D.W.O. Rogers, "AAPM's TG-51 protocol for clinical reference dosimetry of high-energy photon and electron beams," Med. Phys. **26**, 1847-1870 (1999).

C. Alric, R. Serduc, C. Mandon, J. Taleb, G. Le Duc, A. Le Meur-Herland, C. Billotey, P. Perriat, S. Roux, O. Tillement, "Gold nanoparticles designed for combining dual modality imaging and radiotherapy," Gold Bulletin **41**, 90-97 (2008).

J. Als-Nielsen and D. McMorrow, *Elements of Modern X-Ray Pysics* (John Wiley & Sons, Ltd., Singapore, 2001).

D. Anderson, E.A. Siegbahn, B.G. Fallone, R. Serduc, B. Warkentin, "Evaluation of dose-volume metrics for microbeam radiation therapy," Med. Phys. **39**, 4645-4645 (2012).

N. Annabell, N. Yagi, K. Umetani, C. Wong, M. Geso, "Evaluating the peak-to-valley dose ratio of synchrotron microbeams using PRESAGE fluorescence," Journal of Synchrotron Radiation **19**, 332-339 (2012).

D.J. Anschel, P. Romanelli, H. Benveniste, B. Foerster, J. Kalef-Ezra, Z. Zhong, F.A. Dilmanian, "Evolution of a focal brain lesion produced by interlaced microplanar X-rays," Minimally Invasive Neurosurgery **50**, 43-46 (2007).

D.J. Anschel, A. Bravin, P. Romanelli, "Microbeam radiosurgery using synchrotron-generated submillimetric beams: a new tool for the treatment of brain disorders," Neurosurg. Rev. **34**, 133-141 (2011).

D.W. Archer, "Collimator for producing an array of microbeams," United States Patent **813,547** (1998).

B. Arjomandy, R. Tailor, A. Anand, N. Sahoo, M. Gillin, K. Prado, M. Vicic, "Energy dependence and dose response of Gafchromic EBT2 film over a wide range of photon, electron, and proton beam energies," Med. Phys. **37**, 1942-1947 (2010).

F.H. Attix, *Introduction to Radiological Physics and Radiation Dosimetry* (John Wiley & Sons, Inc., New York, 1986).

D.T. Attwood, *Soft x-Rays and Extreme Ultraviolet Radiation: Principles and Applications* (Cambridge University Press, New York, NY, USA, 2007).

S. Baird, "Accelerators for Pedestrians," European Organization for Nuclear Research, CERN AB-Note-2007-014 OP (2007).

C.P. Baker, R.G. Woodley, H.J. Curtis, W. Zeman, "Design and Calibration of a Deuteron Microbeam for Biological Studies," Radiat. Res. **15**, 489-& (1961).

A. Balerna and S. Mobilio, "Introduction to Synchrotron Radiation," in *Synchrotron Radiation: Basics, Methods and Applications*, edited by S. Mobilio, F. Boscherini, C. Meneghini (Springer-Verlag Berlin Heidelberg, 2015).

P.R. Barber, R.J. Locke, G.P. Pierce, K. Rothkamm, B. Vojnovic, "γ-H2AX Foci Counting: Image processing and control software for high-content screening - art. no. 64411M," Imaging, Manipulation, and Analysis of Biomolecules, Cells, and Tissues V **6441**, M4411-M4411 (2007).

P. Barnes, J.K. Cockcroft, S. Jacques, M. Vickers, "How do synchrotrons work?" http://pd.chem.ucl.ac.uk/pdnn/inst2/work.htm Accessed 2/23/2015.

J.A. Bartz, G.J. Sykora, E. Braeuer-Krisch, M.S. Akselrod, "Imaging and dosimetry of synchrotron microbeam with aluminum oxide fluorescent detectors," Radiat. Measur. **46**, 1936-1939 (2011).

S. Bartzsch, M. Lerch, M. Petasecca, E. Braeuer-Krisch, U. Oelfke, "Influence of polarization and a source model for dose calculation in MRT," Med. Phys. **41**, 041703 (2014).

S. Bartzsch and U. Oelfke, "A new concept of pencil beam dose calculation for 40-200 keV photons using analytical dose kernels," Med. Phys. **40**, 111714 (2013).

"Beamline Status Update," http://www.lightsource.ca/uso/beamline_status.php Accessed 2/23/2015.

G. Belev, G. Okada, D. Tonchev, C. Koughia, C. Varoy, A. Edgar, T. Wysokinski, D. Chapman, S. Kasap, "Valency conversion of samarium ions under high dose synchrotron generated X-ray radiation," Physica Status Solidi C: Current Topics in Solid State Physics, **8** (2011).

"Biomedical Imaging and Therapy (BMIT-BM) 05B1-1," http://www.lightsource.ca/beamlines/bmit.php Accessed 2/23/2015.

"Biomedical Imaging and Therapy (BMIT-ID) 05ID-2," http://www.lightsource.ca/beamlines/bmit_2.php Accessed 2/23/2015.

"BioMedical Imaging and Therapy Facility (BMIT) at the Canadian Light Source," http://ex.lightsource.ca/bmit/images/Trifold-Poster-WEB.pdf Accessed 2/23/2015.

H. Blattmann, J.O. Gebbers, E. Brauer-Krisch, A. Bravin, G. Le Duc, W. Burkard, M. Di Michiel, V. Djonov, D.N. Slatkin, J. Stepanek, J.A. Laissue, "Applications of synchrotron X-rays to radiotherapy," Nuclear Instruments & Methods in Physics Research Section A-Accelerators Spectrometers Detectors and Associated Equipment **548**, 17-22 (2005).

W. Bocker and G. Iliakis, "Computational Methods for analysis of foci: validation for radiation-induced γ-H2AX foci in human cells." Radiat. Res. **165**, 113-24 (2006).

W.M. Bonner, C.E. Redon, J.S. Dickey, A.J. Nakamura, O.A. Sedelnikova, S. Solier, Y. Pommier, "OPINION γH2AX and cancer," Nature Reviews Cancer **8**, 957-967 (2008).

A. Bouchet, A. Boumendjel, E. Khalil, R. Serduc, E. Braeuer, E.A. Siegbahn, J.A. Laissue, J. Boutonnat, "Chalcone JAI-51 improves efficacy of synchrotron microbeam radiation therapy of brain tumors," Journal of Synchrotron Radiation **19**, 478-482 (2012).

A. Bouchet, B. Lemasson, T. Christen, M. Potez, C. Rome, N. Coquery, C. Le Clec'h, A. Moisan, E. Braeuer-Krisch, G. Leduc, C. Remy, J.A. Laissue, E.L. Barbier, E. Brun, R. Serduc, "Synchrotron microbeam radiation therapy induces hypoxia in intracerebral gliosarcoma but not in the normal brain," Radiotherapy and Oncology **108**, 143-148 (2013).

A. Bouchet, B. Lemasson, G. Le Duc, C. Maisin, E. Brauer-Krisch, E.A. Siegbahn, L. Renaud, E. Khalil, C. Remy, C. Poillot, A. Bravin, J.A. Laissue, E.L. Barbier, R. Serduc, "Preferential Effect of Synchrotron Microbeam Radiation Therapy on Intracerebral 9L Gliosarcoma Vascular Networks," International Journal of Radiation Oncology Biology Physics **78**, 1503-1512 (2010).

M. Boutillon, "Volume recombination parameter in ionization chambers," Phys. Med. Biol. **43**, 2061-2072 (1998).

M. Boutillon and A.M. Perrocheroux, "Reevaluation of the W-Value for Electrons in Dry Air," Phys. Med. Biol. **32**, 213-219 (1987).

E. Braeuer-Krisch, H. Requardt, T. Brochard, G. Berruyer, M. Renier, J.A. Laissue, A. Bravin, "New technology enables high precision multislit collimators for microbeam radiation therapy," Rev. Sci. Instrum. **80**, 074301 (2009).

E. Braeuer-Krisch, A. Rosenfeld, M. Lerch, M. Petasecca, M. Akselrod, J. Sykora, J. Bartz, M. Ptaszkiewicz, P. Olko, A. Berg, M. Wieland, S. Doran, T. Brochard, A. Kamlowski, G. Cellere, A. Paccagnella, E.A. Siegbahn, Y. Prezado, I. Martinez-Rovira, A. Bravin, L. Dusseau, P. Berkvens, "Potential High Resolution Dosimeters For MRT," 6th International Conference on Medical Applications of Synchrotron Radiation **1266**, 89-97 (2010).

E. Braeuer-Krisch, R. Serduc, E.A. Siegbahn, G. Le Duc, Y. Prezado, A. Bravin, H. Blattmann, J.A. Laissue, "Effects of pulsed, spatially fractionated, microscopic synchrotron X-ray beams on normal and tumoral brain tissue," Mutat. Res. - Rev. Mut. Res. **704**, 160-166 (2010).

A. Brahme, "Dosimetric Precision Requirements in Radiation-Therapy," Acta Radiologica Oncology **23**, 379-391 (1984).

E. Brauer-Krisch, A. Bravin, M. Lerch, A. Rosenfeld, J. Stepanek, M. Di Michiel, J.A. Laissue, "MOSFET dosimetry for microbeam radiation therapy at the European Synchrotron Radiation Facility," Med. Phys. **30**, 583-589 (2003).

E. Brauer-Krisch, A. Bravin, L. Zhang, E. Siegbahn, J. Stepanek, H. Blattmann, D.N. Slatkin, J.O. Gebbers, M. Jasmin, J.A. Laissue, "Characterization of a tungsten/gas multislit collimator for microbeam radiation therapy at the European Synchrotron Radiation Facility," Rev. Sci. Instrum. **76**, 064303 (2005).

E. Brauer-Krisch, H. Requardt, P. Regnard, S. Corde, E. Siegbahn, G. LeDuc, T. Brochard, H. Blattmann, J. Laissue, A. Bravin, "New irradiation geometry for microbeam radiation therapy," Phys. Med. Biol. **50**, 3103-3111 (2005).

E. Brauer-Krisch, H. Requardt, P. Regnard, S. Corde, E.A. Siegbahn, G. LeDuc, H. Blattmann, J. Laissue, A. Bravin, "Exploiting geometrical irradiation possibilities in MRT application," Nuclear Instruments & Methods in Physics Research Section A-Accelerators Spectrometers Detectors and Associated Equipment **548**, 69-71 (2005).

E. Brauer-Krisch, E.A. Siegbahn, A. Bravin, "GafChromic film measurements for Microbeam Radiation Therapy (MRT)," IFMBE Proceedings **25**, 174-177 (2009).

A. Bravin, P. Coan, P. Suortti, "X-ray phase-contrast imaging: from pre-clinical applications towards clinics," Phys. Med. Biol. **58**, R1-R35 (2013).

T.A.D. Brown, K.R. Hogstrom, D. Alvarez, K. Ham, J.P. Dugas, K.L. Matthews II, "Dose Response Curve of EBT2 and EBT3 Radiochromic Films to a Synchrotron-Produced Monochromatic X-Ray Beam," Med. Phys. **39**, 3738-3739 (2012).

D.T. Burns, "Free-air chamber correction factors for electron loss, photon scatter, fluorescence and bremsstrahlung," CCRI(I)/01-36 (BIPM) (2001).

D.T. Burns and L.B. Bueermann, "Free-air ionization chambers," Metrologia **46**, S9-S23 (2009).

D.T. Burns and C. Kessler, "Diaphragm correction factors for free-air chamber standards for air kerma in x-rays," Phys. Med. Biol. **54**, 2737-2745 (2009).

D.T. Burns, C. Kessler, P. Roger, A.R. El-Sersy, "Preliminary Characterization of the NIS Free-Air Chamber Standard at the BIPM," BIPM-09/02 (2009).

M.J. Butson, T. Cheung, P.K.N. Yu, "Weak energy dependence of EBT gafchromic film dose response in the 50 kVp-10 MVp X-ray range," Applied Radiation and Isotopes **64**, 60-62 (2006).

M.J. Butson, P.K.N. Yu, T. Cheung, H. Alnawaf, "Energy response of the new EBT2 radiochromic film to x-ray radiation," Radiat. Measur. **45**, 836-839 (2010).

Z. Cai, K.A. Vallis, R.M. Reilly, "Computational analysis of the number, area and density of-H2AX foci in breast cancer cells exposed to 111In-DTPA-hEGF or -rays using Image-J software," Int. J. Radiat. Biol. **85**, 262-271 (2009).

K. Camphausen, M.A. Moses, C. Menard, M. Sproull, W.D. Beecken, J. Folkman, M.S. O'Reilly, "Radiation abscopal antitumor effect is mediated through p53," Cancer Res. **63**, 1990-1993 (2003).

Canadian Cancer Society, "Childhood cancer," http://www.cancer.ca/en/cancer-information/cancer-type/childhood-cancer-information/treatment/radiation-therapy/ Accessed 4/19/2015.

Canadian Cancer Society's Advisory Committee on Cancer Statistics, *Canadian Cancer Statistics 2014* (Canadian Cancer Society, Toronto, ON, 2014).

D. Chapman, "BioMedical Imaging and Therapy Beamline Preliminary Design Report," CLSI Document 26.2.1.2 Rev. 0 (2006).

D. Chapman, N. Gmur, N. Lazarz, W. Thomlinson, "Photon - a Program for Synchrotron Radiation-Dose Calculations," Nuclear Instruments & Methods in Physics Research Section A-Accelerators Spectrometers Detectors and Associated Equipment **266**, 191-194 (1988).

F. Chen, C.F.O. Graeff, O. Baffa, "K-band EPR dosimetry: small-field beam profile determination with miniature alanine dosimeter," Applied Radiation and Isotopes **62**, 267-271 (2005).

W.L. Chen, S.H. Su, L.L. Su, W.S. Hwang, "Improved free-air ionization chamber for the measurement of x-rays," Metrologia **36**, 19-24 (1999).

P. Chtcheprov, L. Burk, H. Yuan, C. Inscoe, R. Ger, M. Hadsell, J. Lu, L. Zhang, S. Chang, O. Zhou, "Physiologically gated microbeam radiation, using a field emission x-ray source array," Med. Phys. **41**, 88-95 (2014).

J.A. Coderre, T.M. Button, P.L. Micca, C.D. Fisher, M.M. Nawrocky, H.B. Liu, "Neutron-Capture Therapy of the 9L Rat Gliosarcoma using the P-Boronophenylalanine-Fructose Complex," International Journal of Radiation Oncology Biology Physics **30**, 643-652 (1994).

F.Z. Company, "Calculation of dose profiles in stereotactic synchrotron microplanar beam radiotherapy in a tissue-lung phantom," Australasian Physical & Engineering Sciences in Medicine **30**, 33-41 (2007).

F.Z. Company and B.J. Allen, "Calculation of microplanar beam dose profiles in a tissue/lung/tissue phantom," Phys. Med. Biol. **43**, 2491-2501 (1998).

F. Coninckx, H. Schonbacher, A. Bartolotta, S. Onori, A. Rosati, "Alanine Dosimetry as the Reference Dosimetric System in Accelerator Radiation Environments," Applied Radiation and Isotopes **40**, 977-983 (1989).

J. Corbett and C. Wermelskirchen, "Chapter 9: Accelerator Controls and Modeling," in *Synchrotron Radiation Sources: A Primer, Vol. 1*, 1st ed., edited by H. Winick (World Scientific Publishing Co. Pte. Ltd., Singapore, 1994), pp. 215.

H. Coutard, "Principles of X ray therapy of malignant diseases," Lancet **2**, 1-8 (1934).

J.C. Crosbie, I. Svalbe, S.M. Midgley, N. Yagi, P.A.W. Rogers, R.A. Lewis, "A method of dosimetry for synchrotron microbeam radiation therapy using radiochromic films of different sensitivity," Phys. Med. Biol. **53**, 6861-6877 (2008).

J.C. Crosbie, R.L. Anderson, K. Rothkamm, C.M. Restall, L. Cann, S. Ruwanpura, S. Meachem, N. Yagi, I. Svalbe, R.A. Lewis, B.R.G. Williams, P.A.W. Rogers, "Tumor Cell Response to Synchrotron

Microbeam Radiation Therapy Differs Markedly from Cells in Normal Tissues," International Journal of Radiation Oncology Biology Physics **77**, 886-894 (2010).

J.C. Crosbie, P.A.W. Rogers, A.W. Stevenson, C.J. Hall, J.E. Lye, T. Nordstrom, S.M. Midgley, R.A. Lewis, "Reference dosimetry at the Australian Synchrotron's imaging and medical beamline using free-air ionization chamber measurements and theoretical predictions of air kerma rate and half value layer," Med. Phys. **40**, 062103 (2013).

F.A. Cucinotta, J.M. Pluth, J.A. Anderson, J.V. Harper, P. O'Neill, "Biochemical kinetics model of DSB repair and induction of γ-H2AX foci by non-homologous end joining," Radiat. Res. **169**, 214-222 (2008).

A. Cullen, M. Lerch, M. Petasecca, A. Rosenfeld, "Monte Carlo modelling of a silicon strip detector for microbeam radiation therapy," Radiat. Measur. **46**, 1646-1649 (2011).

H.J. Curtis, "The use of deuteron microbeam for simulating the biological effects of heavy cosmic-ray particles." Radiation Research Supplement **7**, 250-7 (1967).

L.O. Dallin, "Synchrotron Light Source Magnets**,**" CLS Design Note 5.2.31.2 Rev. 0 (2001).

A. De Felici, R. Felici, C. Ferrero, A. Bravin, A. Tartari, M. Gambaccini, "Monte Carlo assessment of peak-to-valley dose ratio for MRT," Nuclear Instruments & Methods in Physics Research Section A-Accelerators Spectrometers Detectors and Associated Equipment **580**, 489-492 (2007).

M. de Felici, R. Felici, M.S. del Rio, C. Ferrero, T. Bacarian, F.A. Dilmanian, "Dose distribution from x-ray microbeam arrays applied to radiation therapy: An EGS4 Monte Carlo study," Med. Phys. **32**, 2455-2463 (2005).

M. de Felici, E.A. Siegbahn, J. Spiga, A.L. Hanson, R. Felici, C. Ferrero, A. Tartari, M. Gambaccini, J. Keyrilaeinen, E. Braeuer-Krisch, P. Randaccio, A. Bravin, "Monte Carlo code comparison of dose delivery prediction for Microbeam Radiation Therapy," International Workshop on Monte Carlo Techniques in Radiotherapy Delivery and Verification - Third McGill International Workshop **102**, 012005 (2008).

M.F. Desrosiers, J.M. Publ, S.L. Cooper, "An absorbed-dose/dose-rate dependence for the alanine-EPR dosimetry system and its implications in high-dose ionizing radiation metrology," Journal of Research of the National Institute of Standards and Technology **113**, 79-95 (2008).

S. Devic, "Radiochromic film dosimetry: Past, present, and future," Physica Medica-European Journal of Medical Physics **27**, 122-134 (2011).

S. Devic, Y. Wang, N. Tomic, E.B. Podgorsak, "Sensitivity of linear CCD array based film scanners used for film dosimetry," Med. Phys. **33**, 3993-3996 (2006).

A. Diana, C. Guglielmini, F. Fracassi, M. Pietra, E. Balletti, M. Cipone, "Use of high-frequency ultrasonography for evaluation of skin thickness in relation to hydration status and fluid distribution at various cutaneous sites in dogs," Am. J. Vet. Res. **69**, 1148-1152 (2008).

F.A. Dilmanian, G.M. Morris, J.F. Hainfeld, "Methods for implementing microbeam radiation therapy," United States Patent **11/054,001** (2007).

F.A. Dilmanian, T.M. Button, G. Le Duc, N. Zhong, L.A. Pena, J.A.L. Smith, S.R. Martinez, T. Bacarian, J. Tammam, B. Ren, P.M. Farmer, J. Kalef-Ezra, P.L. Micca, M.M. Nawrocky, J.A. Niederer, F.P.

Recksiek, A. Fuchs, E.M. Rosen, "Response of rat intracranial 9L gliosarcoma to microbeam radiation therapy," Neuro-oncology **4**, 26-38 (2002).

F.A. Dilmanian, G.M. Morris, G. Le Duc, X. Huang, B. Ren, T. Bacarian, J.C. Allen, J. Kalef-Ezra, I. Orion, E.M. Rosen, T. Sandhu, P. Sathe, X.Y. Wu, Z. Zhong, H.L. Shivaprasad, "Response of avian embryonic brain to spatially segmented X-ray microbeams," Cell Mol. Biol. **47**, 485-493 (2001).

F.A. Dilmanian, G.M. Morris, N. Zhong, T. Bacarian, J.F. Hainfeld, J. Kalef-Ezra, L.J. Brewington, J. Tammam, E.M. Rosen, "Murine EMT-6 carcinoma: High therapeutic efficacy of microbeam radiation therapy," Radiat. Res. **159**, 632-641 (2003).

F.A. Dilmanian, Y. Qu, S. Liu, C.D. Cool, J. Gilbert, J.F. Hainfeld, C.A. Kruse, J. Laterra, D. Lenihan, M.M. Nawrocky, G. Pappas, C.I. Sze, T. Yuasa, N. Zhong, Z. Zhong, J.W. McDonald, "X-ray microbeams: Tumor therapy and central nervous system research," Nuclear Instruments & Methods in Physics Research Section A-Accelerators Spectrometers Detectors and Associated Equipment **548**, 30-37 (2005).

F.A. Dilmanian, Z. Zhong, T. Bacarian, H. Benveniste, P. Romanelli, R.L. Wang, J. Welwart, T. Yuasa, E.M. Rosen, D.J. Anschel, "Interlaced x-ray microplanar beams: A radiosurgery approach with clinical potential," Proc. Natl. Acad. Sci. U. S. A. **103**, 9709-9714 (2006).

F.A. Dilmanian, Y. Qu, L.E. Feinendegen, L.A. Pena, T. Bacarian, F.A. Henn, J. Kalef-Ezra, S. Liu, Z. Zhong, J.W. McDonald, "Tissue-sparing effect of x-ray microplanar beams particularly in the CNS: Is a bystander effect involved?" Exp. Hematol. **35**, 69-77 (2007).

F.A. Dilmanian, Z. Zhong, T. Bacarian, H. Benveniste, J. Kalef-Ezra, P. Romanelli, R. Wang, T. Yuasa, P.L. Micca, M.M. Nawrocky, M. Testa, M. Worth, E.M. Rosen, D.J. Anschel, "Microbeam radiation therapy in an interlaced geometry: Potential applicability to neuro-oncology and radiosurgery," Neuro-oncology **8**, 484-485 (2006).

S.J. Doran, T. Brochard, J. Adamovics, N. Krstajic, E. Braeuer-Krisch, "An investigation of the potential of optical computed tomography for imaging of synchrotron-generated x-rays at high spatial resolution," Phys. Med. Biol. **55**, 1531-1547 (2010).

S.J. Doran, A.T.A. Rahman, E. Braeuer-Krisch, T. Brochard, J. Adamovics, A. Nisbet, D. Bradley, "Establishing the suitability of quantitative optical CT microscopy of PRESAGE radiochromic dosimeters for the verification of synchrotron microbeam therapy," Phys. Med. Biol. **58**, 6279-6297 (2013).

P.J. Duke, *Synchrotron Radiation: Production and Properties* (Oxford University Press, New York, NY, USA, 2009).

F.R. Elder, A.M. Gurewitsch, R.V. Langmuir, H.C. Pollock, "A 70-Mev Synchrotron," J. Appl. Phys. **18**, 810-818 (1947).

F.R. Elder, A.M. Gurewitsch, R.V. Langmuir, H.C. Pollock, "Radiation from Electrons in a Synchrotron," Physical Review **71**, 829-830 (1947).

L. Ellenberg, L. Qi, G. Gioia, Y. Yasui, R.J. Packer, A. Mertens, S.S. Donaldson, M. Stovall, N. Kadan-Lottick, G. Armstrong, L.L. Robison, L.K. Zeltzer, "Neurocognitive status in long-term survivors of childhood CNS malignancies: a report from the childhood cancer survivor study," Neuropsychology **23**, 705-717 (2009).

B. Emami, J. Lyman, A. Brown, L. Coia, M. Goitein, J.E. Munzenrider, B. Shank, L.J. Solin, M. Wesson, "Tolerance of Normal Tissue to Therapeutic Irradiation," International Journal of Radiation Oncology Biology Physics **21**, 109-122 (1991).

J. Erenpreisa and M.S. Cragg, "Three steps to the immortality of cancer cells: senescence, polyploidy and self-renewal," Cancer Cell International **13**, UNSP 92 (2013).

O. Fernandez-Capetillo, A. Lee, M. Nussenzweig, A. Nussenzweig, "H2AX: the histone guardian of the genome," DNA Repair **3**, 959-967 (2004).

C. Fernandez-Palomo, E. Schueltke, R. Smith, E. Braeuer-Krisch, J. Laissue, C. Schroll, J. Fazzari, C. Seymour, C. Mothersill, "Bystander effects in tumor-free and tumor-bearing rat brains following irradiation by synchrotron X-rays," Int. J. Radiat. Biol. **89**, 445-453 (2013).

P. Fournier, A.H. Clavel, I. Cornelius, P. Berkvens, J.C. Crosbie, M.L.F. Lerch, A.B. Rosenfeld, E. Brauer-Krisch, "Determination of ion recombination for absolute dosimetry in microbeam radiation therapy," European Journal of Medical Physics **29**, e42 (2013).

F. Frommberger, "Particle Accelerators Around the World," http://www-elsa.physik.uni-bonn.de/accelerator_list.html (2014) Accessed 2/23/2015.

"Gafchromic EBT2," http://www.ashland.com/Ashland/Static/Documents/ASI/Advanced%20materials/ebt2.pdf Accessed 4/19/2015.

"Gafchromic EBT3," http://www.ashland.com/Ashland/Static/Documents/ASI/Advanced%20materials/gafchromic-ebt3.pdf Accessed 4/19/2015.

"GAFCHROMIC HD-810 Radiochromic Dosimetry Film," http://www.meditest.fr/pdf/GAFCHROMIC%20HD-810.pdf Accesed 4/19/2015.

"GAFCHROMIC HD-V2 Dosimetry Film," http://www.ashland.com/Ashland/Static/Documents/ASI/Advanced%20materials/gafchromic-hdv2.pdf Accessed 4/19/2015.

A.L. Gartel and A.L. Tyner, "The role of the cyclin-dependent kinase inhibitor p21 in apoptosis," Molecular Cancer Therapeutics **1**, 639-649 (2002).

A. Gefen, N. Gefen, Q.L. Zhu, R. Raghupathi, S.S. Margulies, "Age-dependent changes in material properties of the brain and braincase of the rat," J. Neurotrauma **20**, 1163-1177 (2003).

G. Gokeri, C. Kocar, M. Tombakoglu, "Monte Carlo simulation of microbeam radiation therapy with an interlaced irradiation geometry and an Au contrast agent in a realistic head phantom," Phys. Med. Biol. **55**, 7469-7487 (2010).

P. Golstein and G. Kroemer, "Cell death by necrosis: towards a molecular definition," Trends Biochem. Sci. **32**, 37-43 (2007).

T. Gorjiara, R. Hill, Z. Kuncic, J. Adamovics, S. Bosi, J. Kim, C. Baldock, "Investigation of radiological properties and water equivalency of PRESAGE dosimeters," Med. Phys. **38**, 2265-2274 (2011).

R.J. Griffin, N.A. Koonce, R.P.M. Dings, E. Siegel, E.G. Moros, E. Braeuer-Krisch, P.M. Corry, "Microbeam Radiation Therapy Alters Vascular Architecture and Tumor Oxygenation and is Enhanced by a Galectin-1 Targeted Anti-Angiogenic Peptide," Radiat. Res. **177**, 804-812 (2012).

D.J. Griffiths, *Introduction to Electrodynamics*, 3rd ed. (Prentice-Hall, Inc., Upper Saddle River, NJ, USA, 1999).

M. Hadsell, J. Zhang, P. Laganis, F. Sprenger, J. Shan, L. Zhang, L. Burk, H. Yuan, S. Chang, J. Lu, O. Zhou, "A first generation compact microbeam radiation therapy system based on carbon nanotube X-ray technology," Appl. Phys. Lett. **103** (2013).

E.J. Hall and A.J. Giaccia, *Radiobiology for the Radiologist*, 6th Edition ed. (Lippincott Williams & Wilkins, Philadelphia, PA, USA, 2006).

J.W. Hansen, K.J. Olsen, M. Wille, "The Alanine Radiation Detector for High and Low Let Dosimetry," Radiat. Prot. Dosimet. **19**, 43-47 (1987).

B. Hartmann, M. Martisikova, O. Jaekel, "Technical Note: Homogeneity of Gafchromic EBT2 film," Med. Phys. **37**, 1753-1756 (2010).

P.D. Harty, J.E. Lye, G. Ramanathan, D.J. Butler, C.J. Hall, A.W. Stevenson, P.N. Johnston, "Absolute x-ray dosimetry on a synchrotron medical beam line with a graphite calorimeter," Med. Phys. **41**, 052101 (2014).

R.B. Hayes, E.H. Haskell, J.K. Barrus, G.H. Kenner, A.A. Romanyukha, "Accurate EPR radiosensitivity calibration using small sample masses," Nuclear Instruments & Methods in Physics Research Section A-Accelerators Spectrometers Detectors and Associated Equipment **441**, 535-550 (2000).

J.S. Hendricks, G.W. McKinney, J.W. Durkee, M.R. James, D.B. Pelowitz, H.R. Trellue, "The MCNPX Radiation Transport Code," Los Alamos National Laboratory Report LA-UR-05-0683 (2005).

T. Herrmann, M. Baumann, L. Voigtmann, A. Knorr, "Effect of irradiated volume on lung damage in pigs," Radiotherapy and Oncology **44**, 35-40 (1997).

D.S. Holder, "Detection of Cerebral-Ischemia in the Anesthetized Rat by Impedance Measurement with Scalp Electrodes - Implications for Noninvasive Imaging of Stroke by Electrical-Impedance Tomography," Clinical Physics and Physiological Measurement **13**, 63-75 (1992).

J.W. Hopewell and K.R. Trott, "Volume effects in radiobiology as applied to radiotherapy," Radiotherapy and Oncology **56**, 283-288 (2000).

Y. Hou, A. Lavaf, D. Huang, S. Peters, R. Huq, V. Friedrich, B.S. Rosenstein, J. Kao, "Development of an Automated γ-H2AX Immunocytochemistry Assay," Radiat. Res. **171**, 360-367 (2009).

J. Hubbell and S.M. Seltzer, "NISTIR 5632: Tables of x-ray mass attenuation coefficients and mass energy-absorption coefficients from 1 keV to 20 MEV for elements Z = 1 to 92 and 48 additional substances of dosimetric interest," National Institute of Standards and Technology, Gaithersburg, MD, USA Technical Report 5632 (1995).

R.P. Hugtenburg, A.S. Adegunloye, D.A. Bradley, "X-ray microbeam radiation therapy calculations, including polarisation effects, with the Monte Carlo code EGS5," Nuclear Instruments & Methods in Physics Research Section A-Accelerators Spectrometers Detectors and Associated Equipment **619**, 221-224 (2010).

International Commision on Radiation Units and Measurements, "Average energy required to produce an ion pair," ICRU, Bethesda, MD ICRU Report 31 (1979).

International Specialty Products, "GAFCHROMIC EBT2: Self-developing film for radiotherapy dosimetry," (2010).

A.K. Iyer, G. Khaled, J. Fang, H. Maeda, "Exploiting the enhanced permeability and retention effect for tumor targeting," Drug Discov. Today **11**, 812-818 (2006).

J.D. Jackson, *Classical Electrodynamics* (John Wiley & Sons, Inc., New York, NY, USA, 1962).

D.D. Joel, R.G. Fairchild, J.A. Laissue, S.K. Saraf, J.A. Kalefezra, D.N. Slatkin, "Boron Neutron-Capture Therapy of Intracerebral Rat Gliosarcomas," Proc. Natl. Acad. Sci. U. S. A. **87**, 9808-9812 (1990).

H.E. Johns and J.R. Cunningham, *The Physics of Radiology*, 4th Edition ed. (Charles C Thomas, Springfield, IL, USA, 1983).

M.C. Joiner, B. Marples, P. Lambin, S.C. Short, I. Turesson, "Low-dose hypersensitivity: Current status and possible mechanisms," International Journal of Radiation Oncology Biology Physics **49**, 379-389 (2001).

B. Jolles, "Radiotherapy of Accessible Malignant Tumours by Alternating Chess-Board Method," Lancet **257**, 603-606 (1949).

G.I. Kaplan, A.B. Rosenfeld, B.J. Allen, J.T. Booth, M.G. Carolan, A. Holmes-Siedle, "Improved spatial resolution by MOSFET dosimetry of an x-ray microbeam," Med. Phys. **27**, 239-244 (2000).

H.S. Kaplan, "Basic Principles in Radiation Oncology," Cancer **39**, 689-693 (1977).

G. Kashino, T. Kondoh, N. Nariyama, K. Umetani, T. Ohigashi, K. Shinohara, A. Kurihara, M. Fukumoto, H. Tanaka, A. Maruhashi, M. Suzuki, Y. Kinashi, Y. Liu, S. Masunaga, M. Watanabe, K. Ono, "Induction of Dna Double-Strand Breaks and Cellular Migration through Bystander Effects in Cells Irradiated with the Slit-Type Microplanar Beam of the Spring-8 Synchrotron," International Journal of Radiation Oncology Biology Physics **74**, 229-236 (2009).

F.M. Khan, *The Physics of Radiation Therapy*, 4th ed. (Lippincott Williams & Wilkins, Philadelphia, PA, USA, 2010).

M. Koike, Y. Yutoku, A. Koike, "Accumulation of p21 proteins at DNA damage sites independent of p53 and core NHEJ factors following irradiation," Biochem. Biophys. Res. Commun. **412**, 39-43 (2011).

L.J. Kuo and L. Yang, "γ-H2AX - A novel biomarker for DNA double-strand breaks," In Vivo **22**, 305-309 (2008).

K. Kwang-Je, "Characteristics of Synchrotron Radiation," in *X-Ray Data Booklet*, 2nd ed., edited by A.C. Thompson, D.T. Attwood, E.M. Gullikson, M.R. Howells, J.B. Kortright, A.L. Robinson, J.H. Underwood (Lawrency Berkeley National Laboratory, Berkeley, CA, USA, 2001).

C. Lagadec, E. Vlashi, L. Della Donna, C. Dekmezian, F. Pajonk, "Radiation-Induced Reprogramming of Breast Cancer Cells," Stem Cells **30**, 833-844 (2012).

J.A. Laissue, H. Blattmann, M. Di Michiel, D.N. Slatkin, N. Lyubimova, R. Guzman, W. Zimmermann, S. Birrer, T. Bley, P. Kircher, R. Stettler, R. Fatzer, A. Jaggy, H.M. Smilowitz, E. Brauer, A. Bravin, G. Le Duc, C. Nemoz, M. Renier, W. Thomlinson, J. Stepanek, H.P. Wagner, "The weanling piglet

cerebellum: a surrogate for tolerance to MRT (microbeam radiation therapy) in pediatric neuro-oncology," Penetrating Radiation Systems and Applications III **4508**, 65-73 (2001).

J.A. Laissue, H. Blattmann, H.P. Wagner, M.A. Grotzer, D.N. Slatkin, "Prospects for microbeam radiation therapy of brain tumours in children to reduce neurological sequelae," Dev. Med. Child Neurol. **49**, 577-581 (2007).

J.A. Laissue, G. Geiser, P.O. Spanne, F.A. Dilmanian, J.O. Gebbers, M. Geiser, X.Y. Wu, M.S. Makar, P.L. Micca, M.M. Nawrocky, D.D. Joel, D.N. Slatkin, "Neuropathology of ablation of rat gliosarcomas and contiguous brain tissues using a microplanar beam of synchrotron-wiggler-generated X rays," International Journal of Cancer **78**, 654-660 (1998).

J.A. Laissue, N. Lyubimova, H.P. Wagner, D.W. Archer, D.N. Slatkin, M. Di Michiel, C. Nemoz, M. Renier, E. Brauer, P.O. Spanne, J.O. Gebbers, K. Dixon, H. Blattmann, "Microbeam radiation therapy," Medical Applications of Penetrating Radiation **3770**, 38-45 (1999).

J.A. Laissue, S. Bartzsch, H. Blattmann, E. Braeuer-Krisch, A. Bravin, D. Dallery, V. Djonov, A.L. Hanson, J.W. Hopewell, B. Kaser-Hotz, J. Keyrilainen, P.P. Laissue, M. Miura, R. Serduc, A.E. Siegbahn, D.N. Slatkin, "Response of the rat spinal cord to X-ray microbeams," Radiotherapy and Oncology **106**, 106-111 (2013).

J.A. Laissue, H. Blattmann, D.N. Slatkin, "Alban Kohler (1874-1947): Inventor of grid therapy," Zeitschrift Fur Medizinische Physik **22**, 90-99 (2012).

G. Le Duc, I. Miladi, C. Alric, P. Mowat, E. Braeuer-Krisch, A. Bouchet, E. Khalil, C. Billotey, M. Janier, F. Lux, T. Epicier, P. Perriat, S. Roux, O. Tillement, "Toward an Image-Guided Microbeam Radiation Therapy Using Gadolinium-Based Nanoparticles," Acs Nano **5**, 9566-9574 (2011).

J.H. Lee, L.H. Kotler, L. Buermann, W.S. Hwang, J.H. Chiu, C.F. Wang, "The performance of the INER improved free-air ionization chamber in the comparison of air kerma calibration coefficients for medium-energy X-rays," Radiat. Measur. **39**, 1-10 (2005).

M.L.F. Lerch, M. Petasecca, A. Cullen, A. Hamad, H. Requardt, E. Braeuer-Krisch, A. Bravin, V.L. Perevertaylo, A.B. Rosenfeld, "Dosimetry of intensive synchrotron microbeams," Radiat. Measur. **46**, 1560-1565 (2011).

D.F. Lewis, "A Guide to Radiochromic Film Dosimetry with EBT2 and EBT3," http://www.fimecorp.com/pdfs/A%20Guide%20for%20Using%20Radiochromic%20Film.pdf Accessed 9/5/2015.

R. Lewis, "Medical applications of synchrotron radiation x-rays," Phys. Med. Biol. **42**, 1213-1243 (1997).

F. Liberson, "The Value of a Multi-perforated Screen in Deep X-ray Therapy," Radiology **20**, 186-195 (1933).

A. Mack, S.G. Scheib, J. Major, S. Gianolini, G. Pazmandi, H. Feist, H. Czempiel, H.J. Kreiner, "Precision dosimetry for narrow photon beams used in radiosurgery - Determination of Gamma Knife ® output factors," Med. Phys. **29**, 2080-2089 (2002).

E.C. Mackonis, N. Suchowerska, M. Zhang, M. Ebert, D.R. McKenzie, M. Jackson, "Cellular response to modulated radiation fields," Phys. Med. Biol. **52**, 5469-5482 (2007).

S.H. MacPhail, J.P. Banath, T.Y. Yu, E.H.M. Chu, H. Lambur, P.L. Olive, "Expression of phosphorylated histone H2AX in cultured cell lines following exposure to X-rays," Int. J. Radiat. Biol. **79**, 351-358 (2003).

S.H. MacPhail, J.P. Banath, Y. Yu, E. Chu, P.L. Olive, "Cell cycle-dependent expression of phosphorylated histone H2AX: Reduced expression in unirradiated but not X-irradiated G(1)-phase cells," Radiat. Res. **159**, 759-767 (2003).

L. Macurek, A. Lindqvist, O. Voets, J. Kool, H.R. Vos, R.H. Medema, "Wip1 phosphatase is associated with chromatin and dephosphorylates γH2AX to promote checkpoint inhibition," Oncogene **29**, 2281-2291 (2010).

E. Mainegra-Hing, "Efficient Monte Carlo simulations in kilovoltage x-ray beams," (2011).

E. Mainegra-Hing, N. Reynaert, I. Kawrakow, "Novel approach for the Monte Carlo calculation of free-air chamber correction factors," Med. Phys. **35**, 3650-3660 (2008).

G. Margaritondo, *Elements of Synchrotron Light for Biology, Chemistry, and Medical Research* (Oxford University Press, New York, NY, USA, 2002).

N. Marks, "Chapter 5: Magnet Design," in *Synchrotron Radiation Sources: A Primer, Vol. 1*, edited by H. Winick (World Scientific Publishing Co. Pte. Ltd., Singapore, 1994), pp. 119.

H. Marks, "Clinical Experience with Irradiation through a Grid," Radiology **58**, 338-342 (1952).

T.M. Marti, E. Hefner, L. Feeney, V. Natale, J.E. Cleaver, "H2AX phosphorylation within the G(1) phase after UV irradiation depends on nucleotide excision repair and not DNA double-strand breaks," Proc. Natl. Acad. Sci. U. S. A. **103**, 9891-9896 (2006).

I. Martinez-Rovira and Y. Prezado, "Monte Carlo dose enhancement studies in microbeam radiation therapy," Med. Phys. **38**, 4430-4439 (2011).

I. Martinez-Rovira, J. Sempau, J.M. Fernandez-Varea, A. Bravin, Y. Prezado, "Monte Carlo dosimetry for forthcoming clinical trials in x-ray microbeam radiation therapy," Phys. Med. Biol. **55**, 4375-4388 (2010).

I. Martinez-Rovira, J. Sempau, Y. Prezado, "Development and commissioning of a Monte Carlo photon beam model for the forthcoming clinical trials in microbeam radiation therapy," Med. Phys. **39**, 119-131 (2012).

I. Martinez-Rovira, J. Sempau, Y. Prezado, "Monte Carlo-based treatment planning system calculation engine for microbeam radiation therapy," Med. Phys. **39**, 2829-2838 (2012).

A.C. McEwan, "Corrections for Scattered Photons in Free-Air Ionization Chambers," Phys. Med. Biol. **27**, 375-386 (1982).

T.E. Merchant, H.M. Conklin, S. Wu, R.H. Lustig, X. Xiong, "Late effects of conformal radiation therapy for pediatric patients with low-grade glioma: prospective evaluation of cognitive, endocrine, and hearing deficits," J. Clin. Oncol. **27**, 3691-3697 (2009).

R. Mirzayans, B. Andrais, A. Scott, Y.W. Wang, R.H. Weiss, D. Murray, "Spontaneous γ-H2AX Foci in Humal Solid Tumor-Derived Cell Lines in Relation to p21WAF1 and WIP1 Expression," Int. J. Mol. Sci. **16**, 11609-11628 (2015).

R. Mirzayans, A. Scott, M. Cameron, D. Murray, "Induction of accelerated senescence by gamma radiation in human solid tumor-derived cell lines expressing wild-type TP53," Radiat. Res. **163**, 53-62 (2005).

R. Mirzayans, B. Andrais, A. Scott, D. Murray, "New Insights into p53 Signaling and Cancer Cell Response to DNA Damage: Implications for Cancer Therapy," Journal of Biomedicine and Biotechnology, 170325 (2012).

R. Mirzayans, B. Andrais, A. Scott, M.C. Paterson, D. Murray, "Single-Cell Analysis of p16(INK4a) and p21(WAF1) Expression Suggests Distinct Mechanisms of Senescence in Normal Human and Li-Fraumeni Syndrome Fibroblasts," J. Cell. Physiol. **223**, 57-67 (2010).

R. Mirzayans, B. Andrais, A. Scott, Y.W. Wang, D. Murray, "Ionizing Radiation-Induced Responses in Human Cells with Differing TP53 Status," International Journal of Molecular Sciences **14**, 22409-22435 (2013).

R. Mirzayans, D. Severin, D. Murray, "Relationship between DNA double-strand break rejoining and cell survival after exposure to ionizing radiation in human fibroblast strains with differing ATM/p53 status: Implications for evaluation of clinical radiosensitivity," International Journal of Radiation Oncology Biology Physics **66**, 1498-1505 (2006).

M. Miura, H. Blattmann, E. Brauer-Krisch, A. Bravin, A.L. Hanson, M.M. Nawrocky, P.L. Micca, D.N. Slatkin, J.A. Laissue, "Radiosurgical palliation of aggressive murine SCCVII squamous cell carcinomas using synchrotron-generated X-ray microbeams," Br. J. Radiol. **79**, 71-75 (2006).

M. Mohiuddin, D.L. Curtis, W.T. Grizos, L. Komarnicky, "Palliative Treatment of Advanced Cancer using Multiple Nonconfluent Pencil Beam Radiation - a Pilot-Study," Cancer **66**, 114-118 (1990).

M. Mohiuddin, M. Fujita, W.F. Regine, A.S. Megooni, G.S. Ibbott, M.M. Ahmed, "High-dose spatially-fractionated radiation (GRID): A new paradigm in the management of advanced cancers," International Journal of Radiation Oncology Biology Physics **45**, 721-727 (1999).

S. Moon, L. Lin, X. Zhang, T. Nguyen, Y. Darlington, A.S. Waldman, X. Lu, L.A. Donehower, "Wild-type p53-induced Phosphatase 1 Dephosphorylates Histone Variant γ-H2AX and Suppresses DNA Double Strand Break Repair," J. Biol. Chem. **285**, 12935-12947 (2010).

G.W. Morgan and S.N. Breit, "Radiation and the Lung - a Reevaluation of the Mechanisms Mediating Pulmonary Injury," International Journal of Radiation Oncology Biology Physics **31**, 361-369 (1995).

H. Morrison, G. Menon, R. Sloboda, "Radiochromic film calibration for low-energy seed brachytherapy dose measurement," Med. Phys. **41**, 15-16 (2014).

C. Mothersill and C. Seymour, "Radiation-induced bystander effects: Past history and future directions," Radiat. Res. **155**, 759-767 (2001).

C. Mothersill, C. Fernandez-Palomo, J. Fazzari, R. Smith, E. Schueltke, E. Braeuer-Krisch, J. Laissue, C. Schroll, C. Seymour, "Transmission of Signals from Rats Receiving High Doses of Microbeam Radiation to Cage Mates: an Inter-Mammal Bystander Effect," Dose-Response **12**, 72-92 (2014).

G. Muelhaupt, "Chapter 3: Injector Systems," in *Synchrotron Radiation Sources: A Primer, Vol. 1*, edited by H. Winick (World Scientific Publishing Co. Pte. Ltd., Singapore, 1994), pp. 59.

P.J. Muench, A.S. Meigooni, R. Nath, W.L. Mclaughlin, "Photon Energy-Dependence of the Sensitivity of Radiochromic Film and Comparison with Silver-Halide Film and Lif Tlds used for Brachytherapy Dosimetry," Med. Phys. **18**, 769-775 (1991).

R.K. Mulhern, T.E. Merchant, A. Gajjar, W.E. Reddick, L.E. Kun, "Late neurocognitive sequelae in survivors of brain tumours in childhood," Lancet Oncology **5**, 399-408 (2004).

R.K. Mulhern, H.A. White, J.O. Glass, L.E. Kun, L. Leigh, S.J. Thompson, W.E. Reddick, "Attentional functioning and white matter integrity among survivors of malignant brain tumors of childhood," Journal of the International Neuropsychological Society **10**, 180-189 (2004).

D. Murray and R. Mirzayans, "Role of therapy-induced cellular senescence in tumor cells and its modification in radiotherapy: the good, the bad and the ugly," J. Nucl. Med. Radiat. Ther. **S6:018. doi: 10.4172/2155-9619.S6-018** (2013).

N. Nariyama, N. Kishi, S. Ohnishi, "Development of a portable free-air ionization chamber as an absolute intensity monitor for high-energy synchrotron radiation up to 150 keV," Nuclear Instruments & Methods in Physics Research Section A-Accelerators Spectrometers Detectors and Associated Equipment **524**, 324-331 (2004).

National Institute of Standards and Technology, http://physics.nist.gov/PhysRefData/Star/Text/ESTAR.html, Accessed 2012.

W.R. Nelson, H. Hirayama, D.W.O. Rogers, "The EGS4 Code System," SLAC Report 265 **265** (1985).

H. Nettelbeck, G.J. Takacs, M.L.F. Lerch, A.B. Rosenfeld, "Microbeam radiation therapy: A Monte Carlo study of the influence of the source, multislit collimator, and beam divergence on microbeams," Med. Phys. **36**, 447-456 (2009).

T. Neumaier, J. Swenson, C. Pham, A. Polyzos, A.T. Lo, P. Yang, J. Dyball, A. Asaithamby, D.J. Chen, M.J. Bissell, S. Thalhammer, S.V. Costes, "Evidence for formation of DNA repair centers and dose-response nonlinearity in human cells," Proc. Natl. Acad. Sci. U. S. A. **109**, 443-448 (2012).

A. Niemierko, "Reporting and analyzing dose distributions: A concept of equivalent uniform dose," Med. Phys. **24**, 103-110 (1997).

H. Nikjoo and L. Lindborg, "RBE of low energy electrons and photons," Phys. Med. Biol. **55**, R65-R109 (2010).

A. Niroomand-Rad, C.R. Blackwell, B.M. Coursey, K.P. Gall, J.M. Galvin, W.L. McLaughlin, A.S. Meigooni, R. Nath, J.E. Rodgers, C.G. Soares, "Radiochromic film dosimetry: Recommendations of AAPM Radiation Therapy Committee Task Group 55," Med. Phys. **25**, 2093-2115 (1998).

J. Noonan and D. Walters, "Chapter 8: Vacuum Systems," in *Synchrotron Radiaiton Sources: A Primer, Vol. 1*, 1st ed., edited by H. Winick (World Scientific Publishing Co. Pte. Ltd., Singapore, 1994), pp. 197.

T.C. O'Haver, *Peak Fitter, v. 2.4*, http://terpconnect.umd.edu/~toh/spectrum/InteractivePeakFitter.htm, (May 2012).

G. Okada, B. Morrell, C. Koughia, A. Edgar, C. Varoy, G. Belev, T. Wysokinski, D. Chapman, S. Kasap, "Spatially resolved measurement of high doses in microbeam radiation therapy using samarium doped fluorophosphate glasses," Appl. Phys. Lett. **99**, 121105 (2011).

G. Okada, J. Ueda, S. Tanabe, G. Belev, T. Wysokinski, D. Chapman, D. Tonchev, S. Kasap, "Samarium-Doped Oxyfluoride Glass-Ceramic as a New Fast Erasable Dosimetric Detector Material for Microbeam Radiation Cancer Therapy Applications at the Canadian Synchrotron," J. Am. Ceram. Soc. **97**, 2147-2153 (2014).

J.M. Ordy, W. Zeman, T. Samorajski, H.J. Curtis, R.L. Collins, "Long-Term Pathologic and Behavioral Changes in Mice After Focal Deuteron Irradiation of Brain," Radiat. Res. **20**, 30-& (1963).

I. Orion, A.B. Rosenfeld, F.A. Dilmanian, F. Telang, B. Ren, Y. Namito, "Monte Carlo simulation of dose distributions from a synchrotron-produced microplanar beam array using the EGS4 code system," Phys. Med. Biol. **45**, 2497-2508 (2000).

S.L. Palmer, O. Goloubeva, W.E. Reddick, J.O. Glass, A. Gajjar, L. Kun, T.E. Merchant, R.K. Mulhern, "Patterns of intellectual development among survivors of pediatric medulloblastoma: A longitudinal analysis," Journal of Clinical Oncology **19**, 2302-2308 (2001).

J.A. Penagaricano, E.G. Moros, V. Ratanatharathorn, Y. Yan, P. Corry, "Evaluation of Spatially Fractionated Radiotherapy (Grid) and Definitive Chemoradiotherapy with Curative Intent for Locally Advanced Squamous Cell Carcinoma of the Head and Neck: Initial Response Rates and Toxicity," International Journal of Radiation Oncology Biology Physics **76**, 1369-1375 (2010).

M. Petasecca, A. Cullen, I. Fuduli, A. Espinoza, C. Porumb, C. Stanton, A.H. Aldosari, E. Braeuer-Krisch, H. Requardt, A. Bravin, V. Perevertaylo, A.B. Rosenfeld, M.L.F. Lerch, "X-Tream: a novel dosimetry system for Synchrotron Microbeam Radiation Therapy," Journal of Instrumentation **7**, P07022 (2012).

D.R. Pilch, O.A. Sedelnikova, C. Redon, A. Celeste, A. Nussenzweig, W.M. Bonner, "Characteristics of γ-H2AX foci at DNA double strand breaks sites," Biochemistry and Cell Biology-Biochimie Et Biologie Cellulaire **81**, 123-129 (2003).

M. Podhorecka, A. Skladanowski, P. Bozko, "H2AX Phosphorylation: Its Role in DNA Damage Response and Cancer Therapy." Journal of nucleic acids **2010** (2010).

Y. Prezado, G. Fois, G. Le Duc, A. Bravin, "Gadolinium dose enhancement studies in microbeam radiation therapy," Med. Phys. **36**, 3568-3574 (2009).

K.M. Prise, G. Schettino, M. Folkard, K.D. Held, "New insights on cell death from radiation exposure," Lancet Oncology **6**, 520-528 (2005).

K.M. Prise and J.M. O'Sullivan, "Radiation-induced bystander signalling in cancer therapy," Nature Reviews Cancer **9**, 351-360 (2009).

R.C.U. Priyadarshika, J.C. Crosbie, B. Kumar, P.A.W. Rogers, "Biodosimetric quantification of short-term synchrotron microbeam versus broad-beam radiation damage to mouse skin using a dermatopathological scoring system," Br. J. Radiol. **84**, 833-842 (2011).

W.N. Rahman, R. Davidson, N. Yagi, M. Geso, I. Darby, "Influence of gold nanoparticles on radiation dose enhancement and cellular migration in microbeam-irradiated cells," BioNanoSci. **1**, 1-13 (2011).

C. Regaud and R. Ferroux, "Discordance of the effects of X rays of one part in the skin and of the other part in the testicle, by the fraction of the dosage: Reduction of the efficiency in the skin." C. R. Seances Soc. Biol. Fil. **97**, 431-434 (1927).

P. Regnard, E. Brauer-Krisch, I. Tropres, J. Keyrilainen, A. Bravin, G. Le Duc, "Enhancement of survival of 9L gliosarcoma bearing rats following intracerebral delivery of drugs in combination with microbeam radiation therapy," Eur. J. Radiol. **68**, S151-S155 (2008).

P. Regnard, G. Le Duc, E. Brauer-Krisch, I. Tropres, E.A. Siegbahn, A. Kusak, C. Clair, H. Bernard, D. Dallery, J.A. Laissue, A. Bravin, "Irradiation of intracerebral 9L gliosarcoma by a single array of microplanar x-ray beams from a synchrotron: balance between curing and sparing," Phys. Med. Biol. **53**, 861-878 (2008).

D.F. Regulla and U. Deffner, "Dosimetry by Electron-Spin-Resonance Spectroscopy of Alanine," Int. J. Appl. Radiat. Isot. **33**, 1101-& (1982).

J.E. Reiff, M.S. Huq, M. Mohiuddin, N. Suntharalingam, "Dosimetric Properties of Megavoltage Grid Therapy," International Journal of Radiation Oncology Biology Physics **33**, 937-942 (1995).

T.S. Reimers, S. Ehrenfels, E.L. Mortensen, M. Schmiegelow, S. Sonderkaer, H. Carstensen, K. Schmiegelow, Muller J., "Cognitive deficits in long-term survivors of childhood brain tumors: Identification of predictive factors," Med. Pediatr. Oncol. **40**, 26-34 (2003).

H. Requardt, A. Bravin, Y. Prezado, E. Braeuer-Krisch, M. Renier, T. Brochard, P. Berkvens, F. Esteve, H. Elleaume, J.-. Adam, H. Blattmann, J.A. Laissue, B. Kaser-Hotz, C. Nemoz, G. Berruyer, "The Clinical Trials Program at the ESRF Biomedical Beam line ID17: Status and Remaining Steps," Sri 2009: the 10th International Conference on Synchrotron Radiation Instrumentation **1234**, 161-164 (2010).

K. Ribi, C. Relly, M.A. Landolt, F.D. Alber, E. Boltshauser, M.A. Grotzer, "Outcome of medulloblastoma in children: Long-term complications and quality of life," Neuropediatrics **36**, 357-365 (2005).

M.D. Ris, R. Packer, J. Goldwein, D. Jones-Wallace, J.M. Boyett, "Intellectual outcome after reduced-dose radiation therapy plus adjuvant chemotherapy for medulloblastoma: a Children's Cancer group study," J. Clin. Oncol. **19**, 3470-76 (2001).

A.L. Robinson, "History of Synchrotron Radiation," in *Center for X-Ray Optics Advanced Light Source X-Ray Data Booklet*, Second ed., edited by A.C. Thompson and D. Vaughan (Lawrence Berkeley National Laboratory, University of California, Berkeley, California 94720, 2001).

P. Romanelli, E. Fardone, G. Battaglia, E. Braeuer-Krisch, Y. Prezado, H. Requardt, G. Le Duc, C. Nemoz, D.J. Anschel, J. Spiga, A. Bravin, "Synchrotron-Generated Microbeam Sensorimotor Cortex Transections Induce Seizure Control without Disruption of Neurological Functions," Plos One **8**, e53549 (2013).

A.B. Rosenfeld, "MOSFET dosimetry on modern radiation oncology modalities," Radiat. Prot. Dosimet. **101**, 393-398 (2002).

A.B. Rosenfeld, G.I. Kaplan, T. Kron, B.J. Allen, A. Dilmanian, I. Orion, B. Ren, M.L.F. Lerch, A. Holmes-Siedle, "MOSFET dosimetry of an X-ray microbeam." IEEE Trans. Nucl. Sci. **46**, 1774-1780 (1999).

A.B. Rosenfeld, E.A. Siegbahn, E. Brauer-Krish, A. Holmes-Siedle, M.L.F. Lerch, A. Bravin, I.M. Cornelius, G.J. Takacs, N. Painuly, H. Nettelback, T. Kron, "Edge-on face-to-face MOSFET for synchrotron microbeam dosimetry: MC modeling," IEEE Trans. Nucl. Sci. **52**, 2562-2569 (2005).

C.K. Ross and N.V. Klassen, "Water calorimetry for radiation dosimetry," Phys. Med. Biol. **41**, 1-29 (1996).

K. Rothkamm and M. Lobrich, "Evidence for a lack of DNA double-strand break repair in human cells exposed to very low x-ray doses," Proc. Natl. Acad. Sci. U. S. A. **100**, 5057-5062 (2003).

K. Rothkamm, J.C. Crosbie, F. Daley, S. Bourne, P.R. Barber, B. Vojnovic, L. Cann, P.A.W. Rogers, "In situ Biological Dose Mapping Estimates the Radiation Burden Delivered to 'Spared' Tissue between Synchrotron X-Ray Microbeam Radiotherapy Tracks," Plos One **7**, e29853 (2012).

K. Rothkamm and S. Horn, "γ-H2AX as protein biomarker for radiation exposure," Annali Dell Istituto Superiore Di Sanita **45**, 265-271 (2009).

S. Rutkowski, N.U. Gerber, K. von Hoff, A. Ghekow, U. Bode, N. Graf, F. Berthold, G. Henze, J.E.A. Wolff, M. Warmuth-Metz, N. Soerensen, A. Emser, H. Ottensmeier, F. Deinlein, P.-. Schlegel, R.-. Kortmann, T. Pietsch, J. Kuehl, "Treatment of early childhood medulloblastoma by postoperative chemotherapy and deferred radiotherapy," Neuro. Oncol. **11**, 201-210 (2009).

S. Rutkowski, N.U. Gerber, K. von Hoff, A. Gnekow, U. Bode, N. Graf, F. Berthold, G. Henze, J.E. Wolff, M. Warmuth-Metz, N. Soerensen, A. Emser, H. Ottensmeier, F. Deinlein, P.G. Schlegel, R.D. Kortmann, T. Pietsch, J. Kuehl, German Pediatric Brain Tumor Study Group, "Treatment of early childhood medulloblastoma by postoperative chemotherapy and deferred radiotherapy," Neuro Oncol. **11**, 201-210 (2009).

G.B. Rybicki and A.P. Lightman, *Radiative Processes in Astrophysics* (WILEY-VCH Verlag CmbH & Co. KGaA, Weinheim, 2004).

S. Sabatasso, J.A. Laissue, R. Hlushchuk, W. Graber, A. Bravin, E. Braeuer-Krisch, S. Corde, H. Blattmann, G. Gruber, V. Djonov, "Microbeam Radiation-Induced Tissue Damage Depends on the Stage of Vascular Maturation," International Journal of Radiation Oncology Biology Physics **80**, 1522-1532 (2011).

F. Salvat, J.M. Fernandez-Varea, J. Sempau, "PENELOPE-2008, a code system for Monte Carlo simulation of electron and photon transport," Issy-les-Moulineaux France, OECD NEA (2009).

F. Salvat, J.M. Fernandez-Varea, J. Sempau, "PENELOPE, a Code System for Monte Carlo Simulation of Electron and Photon Transport," OECD NEA France (2003).

S. Sathishkumar, B. Boyanovsky, A.A. Karakashian, K. Rozenova, N.V. Giltiay, M. Kudrimoti, M. Mohiuddin, M.M. Ahmed, M. Nikolova-Karakashian, "Elevated sphingomyelinase activity and ceramide concentration in serum of patients undergoing high dose spatially fractionated radiation treatment - Implications for endothelial apoptosis," Cancer Biology & Therapy **4**, 979-986 (2005).

R.D. Schleuter, "Chapter 14: Wiggler and Undulator Insertion Devices," in *Synchrotron Radiation Sources: A Primer, Vol. 1*, edited by H. Winick (World Scientific Publishing Co. Pte. Ltd., Singapore, 1994), pp. 377.

E.C. Schreiber and S.X. Chang, "Monte Carlo simulation of a compact microbeam radiotherapy system based on carbon nanotube field emission technology," Med. Phys. **39**, 4669-4678 (2012).

E. Schultke, B.H.J. Juurlink, K. Ataelmannan, J. Laissue, H. Blattmann, E. Brauer-Krisch, A. Bravin, J. Minczewska, J. Crosbie, H. Taherian, E. Frangou, T. Wysokinsky, L.D. Chapman, R. Griebel, D. Fourney, "Memory and survival after microbeam radiation therapy," Eur. J. Radiol. **68**, S142-S146 (2008).

O.A. Sedelnikova, D.R. Pilch, C. Redon, W.M. Bonner, "Histone H2AX in DNA damage and repair," Cancer Biology & Therapy **2**, 233-235 (2003).

S.M. Seltzer, P.J. Lamperti, R. Loevinger, M.G. Mitch, J.T. Weaver, B.M. Coursey, "New national air-kerma-strength standards for I-125 and Pd-103 brachytherapy seeds," J. Res. Natl. Stand. Technol. **108**, 337-358 (2003).

J. Sempau, J.M. Fernandez-Varea, E. Acosta, F. Salvat, "Experimental benchmarks of the Monte Carlo code PENELOPE," Nuclear Instruments & Methods in Physics Research Section B-Beam Interactions with Materials and Atoms **207**, 107-123 (2003).

R. Serduc, P. Verant, J.C. Vial, R. Farion, L. Rocas, C. Remy, T. Fadlallah, E. Brauer, A. Bravin, J. Laissue, H. Blattmann, B. Van der Sanden, "In vivo two-photon microscopy study of short-term effects of microbeam irradiation on normal mouse brain microvasculature," International Journal of Radiation Oncology Biology Physics **64**, 1519-1527 (2006).

R. Serduc, A. Bouchet, E. Braeuer-Krisch, J.A. Laissue, J. Spiga, S. Sarun, A. Bravin, C. Fonta, L. Renaud, J. Boutonnat, E.A. Siegbahn, F. Esteve, G. Le Duc, "Synchrotron microbeam radiation therapy for rat brain tumor palliation-influence of the microbeam width at constant valley dose," Phys. Med. Biol. **54**, 6711-6724 (2009).

R. Serduc, E. Braeuer-Krisch, A. Bouchet, L. Renaud, T. Brochard, A. Bravin, J.A. Laissue, G. Le Duc, "First trial of spatial and temporal fractionations of the delivered dose using synchrotron microbeam radiation therapy," Journal of Synchrotron Radiation **16**, 587-590 (2009).

R. Serduc, E. Braeuer-Krisch, E.A. Siegbahn, A. Bouchet, B. Pouyatos, R. Carron, N. Pannetier, L. Renaud, G. Berruyer, C. Nemoz, T. Brochard, C. Remy, E.L. Barbier, A. Bravin, G. Le Duc, A. Depaulis, F. Esteve, J.A. Laissue, "High-Precision Radiosurgical Dose Delivery by Interlaced Microbeam Arrays of High-Flux Low-Energy Synchrotron X-Rays," Plos One **5**, e9028 (2010).

R. Serduc, T. Christen, J. Laissue, R. Farion, A. Bouchet, B. van der Sanden, C. Segebarth, E. Braeuer-Krisch, G. Le Duc, A. Bravin, C. Remy, E.L. Barbier, "Brain tumor vessel response to synchrotron microbeam radiation therapy: a short-term in vivo study," Phys. Med. Biol. **53**, 3609-3622 (2008).

R. Serduc, Y.V. de Looij, G. Francony, O. Verdonck, B. Van der Sanden, J. Laissue, R. Farion, E. Braeuer-Krisch, E.A. Siegbahn, A. Bravin, Y. Prezado, C. Segebarth, C. Remy, H. Lahrech, "Characterization and quantification of cerebral edema induced by synchrotron x-ray microbeam radiation therapy," Phys. Med. Biol. **53**, 1153-1166 (2008).

J. Seuntjens and S. Duane, "Photon absorbed dose standards," Metrologia **46**, S39-S58 (2009).

T.K. Sham and M.L. Rivers, "A brief overview of synchrotron radiation," Reviews in Mineralogy and Geochemistry, **49**, 117-147 (2002).

M. Sharma, J.C. Crosbie, L. Puskar, P.A.W. Rogers, "Microbeam-irradiated tumour tissue possesses a different infrared absorbance profile compared to broad beam and sham-irradiated tissue," Int. J. Radiat. Biol. **89**, 79-87 (2013).

E.A. Siegbahn, "Dosimetry for synchrotron x-ray microbeam radiation therapy," (2007).

E.A. Siegbahn, E. Braeuer-Krisch, A. Bravin, H. Nettelbeck, M.L.F. Lerch, A.B. Rosenfeld, "MOSFET dosimetry with high spatial resolution in intense synchrotron-generated x-ray microbeams," Med. Phys. **36**, 1128-1137 (2009).

E.A. Siegbahn, J. Stepanek, E. Brauer-Krisch, A. Bravin, "Determination of dosimetrical quantities used in microbeam radiation therapy (MRT) with Monte Carlo simulations," Med. Phys. **33**, 3248-3259 (2006).

R. Siegel, D. Naishadham, A. Jemal, "Cancer statistics, 2012," CA Cancer. J. Clin. **62**, 10-29 (2012).

J.H. Silber, J. Radcliffe, V. Peckham, G. Perilongo, P. Kishnani, M. Fridman, J.W. Goldwein, A.T. Meadows, "Whole-brain irradiation and decline in intelligence: the influence of dose and age on IQ score," J. Clin. Oncol. **10**, 1390-1396 (1992).

D.N. Slatkin, P. Spanne, F.A. Dilmanian, J.O. Gebbers, J.A. Laissue, "Subacute Neuropathological Effects of Microplanar Beams of X-Rays from a Synchrotron Wiggler," Proc. Natl. Acad. Sci. U. S. A. **92**, 8783-8787 (1995).

D.N. Slatkin, P. Spanne, F.A. Dilmanian, M. Sandborg, "Microbeam Radiation Therapy," Med. Phys. **19**, 1395-1400 (1992).

M.W. Slutzky, L.R. Jordan, T. Krieg, M. Chen, D.J. Mogul, L.E. Miller, "Optimal spacing of surface electrode arrays for brain-machine interface applications," Journal of Neural Engineering **7**, 026004 (2010).

H.M. Smilowitz, H. Blattmann, E. Brauer-Krisch, A. Bravin, M. Di Michiel, J.-O. Gebbers, A.L. Hanson, N. Lyubimova, D.N. Slatkin, J. Stepanek, J.A. Laissue, "Synergy of gene-mediated immunoprophylaxis and microbeam radiation therapy for advanced intracerebral rat 9L gliosarcomas," J. Neurooncol. **78**, 135-143 (2006).

R.W. Smith, J. Wang, E. Schueltke, C.B. Seymour, E. Braeuer-Krisch, J.A. Laissue, H. Blattmann, C.E. Mothersill, "Proteomic changes in the rat brain induced by homogenous irradiation and by the bystander effect resulting from high energy synchrotron X-ray microbeams," Int. J. Radiat. Biol. **89**, 118-127 (2013).

J. Spiga, Y. Prezado, E. Braeuer-Krisch, V. Fanti, P. Randaccio, A. Bravin, "The Effect of Beam Polarization in Microbeam Radiation Therapy (MRT): Monte Carlo Simulations Using GEANT4," 2009 IEEE Nuclear Science Symposium Conference Record, Vols 1-5, 2170-2173 (2009).

J. Spiga, E.A. Siegbahn, E. Braeuer-Krisch, P. Randaccio, A. Bravin, "The GEANT4 toolkit for microdosimetry calculations: Application to microbeam radiation therapy (MRT)," Med. Phys. **34**, 4322-4330 (2007).

C.N. Sprung, M. Cholewa, N. Usami, K. Kobayashi, J.C. Crosbie, "DNA damage and repair kinetics after microbeam radiation therapy emulation in living cells using monoenergetic synchrotron X-ray microbeams," Journal of Synchrotron Radiation **18**, 630-636 (2011).

C.N. Sprung, Y. Yang, H.B. Forrester, J. Li, M. Zaitseva, L. Cann, T. Restall, R.L. Anderson, J.C. Crosbie, P.A.W. Rogers, "Genome-Wide Transcription Responses to Synchrotron Microbeam Radiotherapy," Radiat. Res. **178**, 249-259 (2012).

J. Stepanek, H. Blattmann, J.A. Laissue, N. Lyubimova, M. Di Michiel, D.N. Slatkin, "Physics study of microbeam radiation therapy with PSI-version of Monte Carlo code GEANT as a new computational tool," Med. Phys. **27**, 1664-1675 (2000).

"Storage Ring Status," http://www.lightsource.ca/operations/storageRing_status.php Accessed 2/23/2015.

W.E. Straile and H.B. Chase, "Use of Elongate Microbeams of X-Rays for Simulating Effects of Cosmic Rays on Tissues - a Study of Wound Healing and Hair Follicle Regeneration," Radiat. Res. **18**, 65-& (1963).

E. Suc, C. Kalifa, R. Brauner, J.L. Habrand, M.J. Terrier-Lacombe, G. Vassal, J. Lemerle, "Brain tumours under the age of three. The price of survival. A retrospective study of 20 long-term survivors," Acta Neurochir. (Wien) **106**, 93-98 (1990).

P. Suortti and W. Thomlinson, "Medical applications of synchrotron radiation," Phys. Med. Biol. **48**, R1-R35 (2003).

M. Suzuki, K. Suzuki, S. Kodama, M. Watanabe, "Phosphorylated histone H2AX foci persist on rejoined mitotic chromosomes in normal human diploid cells exposed to ionizing radiation," Radiat. Res. **165**, 269-276 (2006).

T. Tanaka and H. Kitamura, "SPECTRA: a synchrotron radiation calculation code," Journal of Synchrotron Radiation **8**, 1221-1228 (2001).

W.V. Tenzel, "Experience with Grid Therapy," Radiology **59**, 399-408 (1952).

D.J. Thompson and D.M. Dykes, "Chapter 4: R.F. Systems," in *Synchrotron Radiation Sources: A Primer, Vol. 1*, edited by H. Winick (World Scientific Publishing Co. Pte. Ltd., Singapore, 1994).

B. Timmermann, R.D. Kortmann, J. Kuhl, S. Rutkowski, K. Dieckmann, C. Meisner, M. Bamberg, "Role of radiotherapy in anaplastic ependymoma in children under age of 3 years: Results of the prospective German brain tumor trials HF-SKK 87 and 92," Radiotherapy and Oncology **77**, 278-285 (2005).

S. Vahedi, G. Okada, B. Morrell, E. Muzar, C. Koughia, A. Edgar, C. Varoy, G. Belev, T. Wysokinski, D. Chapman, S. Kasap, "X-ray induced Sm^{3+} to Sm^{2+} conversion in fluorophosphate and fluoroaluminate glasses for the monitoring of high-doses in microbeam radiation therapy," J. Appl. Phys. **112**, 073108 (2012).

B. van der Sanden, E. Braeuer-Krisch, E.A. Siegbahn, C. Ricard, J. Vial, J. Laissue, "Tolerance of Arteries to Microplanar X-Ray Beams," International Journal of Radiation Oncology Biology Physics **77**, 1545-1552 (2010).

A.J. Vanderkogel, "Dose-Volume Effects in the Spinal-Cord," Radiotherapy and Oncology **29**, 105-109 (1993).

J.E. Villarreal-Barajas and R.F.H. Khan, "Energy response of EBT3 radiochromic films: implications for dosimetry in kilovoltage range," Journal of Applied Clinical Medical Physics **15**, 331-338 (2014).

J.M. Vogt, J.C. Bergstrom, S. Hu, "Accurate measurement of the beam energy in the CLS storage ring," Proceedings of PCaPAC 2010, 36-37 (2010).

H.P. Wagner, "Cancer in childhood and supportive care," Supportive Care in Cancer **7**, 293-294 (1999).

E. Waldeland and E. Malinen, "Review of the dose-to-water energy dependence of alanine and lithium formate EPR dosimeters and LiF TL-dosimeters - Comparison with Monte Carlo simulations," Radiat. Measur. **46**, 945-951 (2011).

M. Wang, F. Morsbach, D. Sander, L. Gheorghiu, A. Nanda, C. Benes, M. Kriegs, M. Krause, E. Dikomey, M. Baumann, J. Dahm-Daphi, J. Settleman, H. Willers, "EGF Receptor Inhibition Radiosensitizes NSCLC Cells by Inducing Senescence in Cells Sustaining DNA Double-Strand Breaks," Cancer Res. **71**, 6261-6269 (2011).

"What is a beamline?" http://www.esrf.eu/about/synchrotron-science/beamline Accessed 2/23/2015.

K. Wille, *The Physics of Particle Accelerators, an Introduction* (Oxford University Press, Oxford, U.K., 2000).

H. Winick, "Chapter 1: Introduction and Overview," in *Synchrotron Radiation Sources: A Primer, Vol. 1*, edited by H. Winick (World Scientific Publishing Co. Pte. Ltd., Singapore, 1994).

H.R. Withers, J.M.G. Taylor, B. Maciejewski, "Treatment Volume and Tissue Tolerance," International Journal of Radiation Oncology Biology Physics **14**, 751-759 (1988).

S. Wolff, "The adaptive response in radiobiology: Evolving insights and implications," Environ. Health Perspect. **106**, 277-283 (1998).

M. Wright, "High energy microbeam radiosurgery," US Patent Application Publication **13/492,412** (2013).

W. Wu, P. Liu, J. Li, "Necroptosis: An emerging form of programmed cell death," Critical Reviews in Oncology Hematology **82**, 249-258 (2012).

H.O. Wyckoff and F.H. Attix, "Design of free-air ionization chambers," National Bureau of Standards Handbook 64 (1957).

T.W. Wysokinski, D. Chapman, G. Adams, M. Renier, P. Suortti, W. Thomlinson, "Beamlines of the Biomedical Imaging and Therapy Facility at the Canadian Light Source - Part 2." 11th International Conference on Synchrotron Radiation Instrumentation (Sri 2012) **425**, UNSP 072013 (2013).

T.W. Wysokinski, D. Chapman, G. Adams, M. Renier, P. Suortti, W. Thomlinson, "Beamlines of the biomedical imaging and therapy facility at the Canadian light source - part 3," Nuclear Instruments & Methods in Physics Research Section A-Accelerators Spectrometers Detectors and Associated Equipment **775**, 1-4 (2015).

T.W. Wysokinski, D. Chapman, G. Adams, M. Renier, P. Suortti, W. Thomlinson, "Beamlines of the biomedical imaging and therapy facility at the Canadian light source - Part I," Nuclear Instruments & Methods in Physics Research Section A-Accelerators Spectrometers Detectors and Associated Equipment **582**, 73-76 (2007).

R.J. Yaes and A. Kalend, "Local Stem-Cell Depletion Model for Radiation Myelitis," Math. Comput. Model. **11**, 1041-1046 (1988).

L.A. Young, J.C. Dodge, K.J. Guest, J.L. Cline, W.W. Kerr, "Age, breed, sex and period effects on skin biophysical parameters for dogs fed canned dog food," J. Nutr. **132**, 1695S-1697S (2002).

W. Zeman, C.P. Baker, H.J. Curtis, "Histopathologic Effect of High-Energy-Particle Microbeams on Visual Cortex of Mouse Brain," Radiat. Res. **15**, 496-& (1961).

W. Zeman, H.J. Curtis, E.L. Gebhard, W. Haymaker, "Tolerance of Mouse-Brain Tissue to High-Energy Deuterons," Science **130**, 1760-1761 (1959).

L. Zhang, H. Yuan, L.M. Burk, C.R. Inscoe, M.J. Hadsell, P. Chtcheprov, Y.Z. Lee, J. Lu, S. Chang, O. Zhou, "Image-guided microbeam irradiation to brain tumour bearing mice using a carbon nanotube x-ray source array," Phys. Med. Biol. **59** (2014).

L. Zhang, H. Yuan, C. Inscoe, P. Chtcheprov, M. Hadsell, Y. Lee, J. Lu, S. Chang, O. Zhou, "Nanotube x-ray for cancer therapy: a compact microbeam radiation therapy system for brain tumor treatment," Expert Review of Anticancer Therapy **14**, 1411-1418 (2014).

N. Zhong, G.M. Morris, T. Bacarian, E.M. Rosen, E.A. Dilmanian, "Response of rat skin to high-dose unidirectional X-ray microbearns: A histological study," Radiat. Res. **160**, 133-142 (2003).

R.D. Zwicker, A. Meigooni, M. Mohiuddin, "Therapeutic advantage of grid irradiation for large single fractions," International Journal of Radiation Oncology Biology Physics **58**, 1309-1315 (2004).